

**CONE BEAM OPTICAL COMPUTED TOMOGRAPHY-BASED  
GEL DOSIMETRY**

by

Timothy Russell Olding

A thesis submitted to the Department of Physics, Engineering Physics & Astronomy  
in conformity with the requirements for  
the degree of Doctor of Philosophy

Queen's University

Kingston, Ontario, Canada

September, 2010

Copyright © Timothy Russell Olding, 2010

## **Abstract**

The complex dose distributions delivered by modern, conformal radiation therapy techniques present a considerable challenge in dose verification. Traditional measurement tools are difficult and laborious to use, since complete verification requires that the doses be determined in three dimensions (3D). The difficulty is further complicated by a required target accuracy of  $\pm 5\%$  for the dose delivery. Gel dosimetry is an attractive option for realizing a tissue-equivalent, 3D dose verification tool with high resolution readout capabilities. However, much important work remains to be completed prior to its acceptance in the clinic. The careful development of easily accessible, fast optical readout tools such as cone beam optical computed tomography (CT) in combination with stable and reliable low-toxicity gel dosimeters is one key step in this process.

In this thesis, the performance capabilities and limitations of the two main classes of cone beam optical CT-based absorbing and scattering gel dosimetry are characterized, and their measurement improved through careful matching of dosimeter and scanner performance. These systems are then applied to the evaluation of clinically relevant complex dose distributions. Three-dimensional quality assurance assessments of complex treatment plan dose distributions are shown to be feasible using an optically absorbing Fricke-xylenol-orange-gelatin-based gel dosimeter. Better than 95% voxel agreement is achieved between the plan and the delivery, using 3% dose difference and 3 mm spatial distance-to-agreement gamma function comparison criteria. Small field dose delivery evaluations are demonstrated to be viable using an optically scattering N-isopropylacrylamide (NIPAM)-based polymer gel, with the same comparison criteria. Full treatment process quality assurance is also possible using a NIPAM dosimeter in-phantom, but is limited in its accuracy due to the inherent difficulty of managing the effects of stray light perturbation in the optical attenuation-to-dose calibration.

## **Co-Authorship**

Chapter 2 contains a version of an article published in Physics in Medicine and Biology as:

*Olding T, Holmes O, and Schreiner L J (2010) “Cone beam optical computed tomography for gel dosimetry I: scanner characterization” Phys. Med. Biol. 55 2819-2840.* Tim Olding performed the experiments and data analysis, interpreted the results and wrote the manuscript. Oliver Holmes assisted in some of the experiments and data analysis, advised on data interpretation, and edited the manuscript. John Schreiner supervised the project, advised on data interpretation, and edited the manuscript.

Chapter 3 contains a version of an article submitted to Physics in Medicine and Biology as:

*Olding T and Schreiner L J “Cone beam optical computed tomography for gel dosimetry II: imaging protocols”.* Tim Olding performed the experiments and data analysis, interpreted the results and wrote the manuscript. John Schreiner supervised the project, advised on data interpretation, and edited the manuscript.

Chapter 4 contains a version of an article that has been prepared for submission to Medical Physics as: *Olding T, Darko J and Schreiner L J “Evaluation of IMRT treatment plans using cone beam optical CT-based FXG gel dosimetry”.* Tim Olding performed the experiments and data analysis, interpreted the results and wrote the manuscript. Johnson Darko assisted with IMRT treatment planning and delivery, advised on data interpretation, and edited the manuscript. John Schreiner supervised the project, advised on data interpretation, and edited the manuscript.

Chapter 5 contains a version of an article submitted to the Indian Journal of Medical Physics as: *Olding T, Holmes O, DeJean P, McAuley K, Nkongchu K, Santyr G, and Schreiner L J “Small Field Dose Delivery Evaluations Using Cone Beam Optical Computed Tomography-Based Polymer Gel Dosimetry”*. Tim Olding performed the experiments (except for the initial optical CT-MRI comparison which was completed by Paul DeJean and Ken Nkongchu under the supervision of Giles Santyr and L. John Schreiner), completed the data analysis, interpreted the results and wrote the manuscript. Oliver Holmes assisted in some of the tomotherapy delivery experiments and a portion of the data analysis, advised on data interpretation, and edited the manuscript. Kim McAuley advised on gel formulation and data interpretation, and edited the manuscript. John Schreiner supervised the project, advised on data interpretation, and edited the manuscript.

Chapter 6 contains a version of an article that is in the process of being prepared for submission to Medical Physics as: *Olding T, Holmes O, McAuley K, Darko J, and Schreiner L J “Treatment Process Quality Assurance Using Cone Beam Optical CT-Based Polymer Gel Dosimetry”*. Tim Olding performed the experiments and data analysis, interpreted the results and wrote the manuscript. Oliver Holmes assisted in the conformal delivery experiments and a portion of the data analysis, advised on data interpretation, and edited the manuscript. Johnson Darko assisted with the treatment planning and delivery, advised on data interpretation, and edited the manuscript. Kim McAuley advised on gel formulation and data interpretation, and edited the manuscript. John Schreiner supervised the project, advised on data interpretation, and edited the manuscript.

## Acknowledgements

Throughout my academic and professional career, I have had the opportunity to work under the supervision of three fantastic individuals: Dr. Michael Sayer, Dr. David Barrow, and now, Dr. John Schreiner. Each of them has been enthusiastic and dedicated in their work and taught me a great deal professionally. Perhaps even more importantly from a personal perspective, they have placed a high degree of confidence in me and have consistently demonstrated the high value of believing in and bringing the best out of those around them. John, it has been both a privilege and a pleasure to watch and learn from you. Thank you.

By no means has my doctoral research been completed in isolation. Along the way I have interacted with and received help from: Dr. Steve Babic, Gary Bracken, Jon Chain, Dr. Johnson Darko, Sandeep Dhanesar, Jen Dietrich, Tony DiLabio, Laura Drever, Tom Feuerstake, Jen Fung, Tracy Halsall, Oliver Holmes, Dr. Kevin Jordan, Dr. Chandra Joshi, Dr. Andy Kerr, Valeria Koeva, Dr. Kim McAuley, Justin Lau, Amy MacDonald, Matthew Marsh, Dr. Xiangyang Mei, John Miller, Lynda Mowers, Daxa Patel, Robin Quirt, Nick Rawluk, Dr. Dave Rogers, Dr. Myron Rogers, Bon Ryu, Dr. Greg Salomons, Kevan Welch, and of course, the tolerant radiation therapists in the cancer clinic. Thank you all!

My daughter Joelle has the best summary of my work: “He makes stinky Jello, the kind you can’t eat, and takes pictures of it.” I’m not sure if my kids have kept my sanity intact over the last few years or have driven me close to its edge. Regardless: Joelle, Caleb, Liam, and Erin, I love you with all my heart. You put my work in perspective.

When we were first considering the idea of my going back to school, my wife Joy told me to go for it. Life is an adventure. It is a rare and powerful thing to be loved beyond what you do, for who you are. Joy, words cannot express ...

God, you are so faithful. To you, I owe the ultimate thanks.

## **Statement of Originality**

I hereby certify that all of the work described within this thesis is the original work of the author.

Any published (or unpublished) ideas and/or techniques from the work of others are fully acknowledged in accordance with the standard referencing practices.

Timothy Russell Olding

September, 2010

## Table of Contents

Abstract .....	ii
Co-Authorship .....	iii
Acknowledgements.....	v
Statement of Originality.....	vi
Table of Contents.....	vii
List of Figures .....	xi
List of Tables .....	xiv
Nomenclature.....	xv
Glossary .....	xvii
Chapter 1 General Introduction .....	1
1.1 Radiation Therapy.....	1
1.2 Dose Verification.....	3
1.3 Gel Dosimetry.....	5
1.3.1 Introduction.....	5
1.3.2 Fricke Gels.....	8
1.3.3 Polymer Gels.....	14
1.4 Optical CT Imaging .....	17
1.4.1 Introduction.....	17
1.4.2 Parallel Beam Geometry .....	20
1.4.3 Fan Beam Geometry .....	21
1.4.4 Cone Beam Geometry.....	23
1.4.5 Practical Optical CT Scanners .....	25
1.5 Thesis Outline .....	26
1.6 References.....	29
Chapter 2 Scanner Characterization.....	36
2.1 Abstract.....	36
2.2 Introduction.....	37
2.3 Experiment.....	40
2.3.1 Cone Beam Optical CT Imaging.....	40
2.3.2 Cone Beam Geometry Validation.....	44
2.3.3 Spatial Resolution .....	49
2.3.4 Spatial Distortion .....	51

2.3.5 Scanner Scatter Measurement.....	54
2.3.6 Scanner Absorption Measurement.....	56
2.4 Discussion .....	59
2.4.1 Cone Beam Geometry Validation.....	59
2.4.2 Spatial Resolution .....	61
2.4.3 Spatial Distortion .....	62
2.4.4 Scanner Scatter Measurement.....	63
2.4.5 Scanner Absorption Measurement.....	65
2.5 Conclusions.....	68
2.6 References.....	70
Chapter 3 Imaging Protocols .....	74
3.1 Abstract.....	74
3.2 Introduction.....	75
3.3 Experiment.....	77
3.3.1 Cone Beam Optical CT Imaging.....	77
3.3.2 Scanner Light Source-Detector Stability .....	78
3.3.3 Scan Time Constraints .....	81
3.3.4 Scan Temperature Constraints .....	83
3.3.5 Stray Light Reduction.....	85
3.4 Discussion .....	92
3.4.1 Scanner Light Source-Detector Stability .....	92
3.4.2 Scan Time Constraints .....	93
3.4.3 Scan Temperature Constraints .....	94
3.4.4 Stray Light Reduction.....	96
3.5 Conclusions.....	103
3.6 References.....	104
Chapter 4 IMRT Treatment Plan Quality Assurance Using FXG Gels .....	107
4.1 Abstract.....	107
4.2 Introduction.....	108
4.3 Materials and Methods.....	111
4.3.1 FXG Gel Preparation .....	111
4.3.2 Optical Imaging .....	112
4.3.3 FXG Gel Response Calibration.....	114

4.3.4 IMRT Dose Evaluation .....	115
4.3.5 Modified Dosimeter Characterization.....	117
4.4 Results.....	118
4.4.1 FXG Gel Response Calibration.....	118
4.4.2 IMRT Delivery Evaluation .....	120
4.4.3 Modified Dosimeter Characterization.....	124
4.5 Discussion .....	126
4.5.1 FXG Gel Response Calibration.....	126
4.5.2 IMRT Dose Evaluation .....	129
4.5.3 Modified Dosimeter Characterization.....	132
4.6 Conclusions.....	134
4.7 References.....	135
Chapter 5 Small Field Dose Delivery Evaluations Using Polymer Gels .....	139
5.1 Abstract.....	139
5.2 Introduction.....	140
5.3 Experiment.....	142
5.3.1 Gel Dosimeter Preparation.....	142
5.3.2 Optical CT Imaging .....	144
5.3.3 Initial Optical CT-MRI Comparison.....	145
5.3.4 Scanner Assessment.....	147
5.3.5 Dosimeter Assessment & Modification .....	148
5.3.6 Modified Dosimeter Evaluation & Use .....	148
5.4 Results.....	149
5.4.1 Initial Optical CT-MRI Comparison.....	149
5.4.2 Scanner Assessment.....	151
5.4.3 Dosimeter Assessment & Modification .....	152
5.4.4 Modified Dosimeter Evaluation & Use .....	154
5.5 Discussion .....	157
5.5.1 Initial Optical CT-MRI Comparison.....	157
5.5.2 Scanner Assessment.....	158
5.5.3 Dosimeter Assessment & Modification .....	159
5.5.4 Modified Dosimeter Evaluation & Use .....	161
5.6 Conclusions.....	162

5.7 References.....	163
Chapter 6 Treatment Process Quality Assurance Using Polymer Gels .....	166
6.1 Abstract.....	166
6.2 Introduction.....	167
6.3 Methods and Materials.....	168
6.3.1 Calibration Solution and Gel Dosimeter and Preparation.....	168
6.3.2 Cone Beam Optical CT Imaging.....	170
6.3.3 Stray Light Reduction.....	171
6.3.4 Stray Light Correction .....	172
6.3.5 Treatment Process Quality Assurance .....	173
6.4 Results.....	176
6.4.1 Stray Light Perturbation.....	176
6.4.2 Stray Light Reduction.....	177
6.4.3 Stray Light Correction .....	179
6.4.4 Treatment Process Quality Assurance .....	181
6.5 Discussion .....	182
6.5.1 Stray Light Reduction.....	182
6.5.2 Stray Light Correction .....	184
6.5.3 Treatment Process Quality Assurance .....	187
6.6 Conclusions.....	188
6.7 References.....	190
Chapter 7 Conclusions .....	192
7.1 Viability & Use.....	192
7.2 Future Work .....	196
7.3 References.....	197
Appendices.....	198
A. Permission to reproduce copyrighted material in Chapter 2 .....	198

## List of Figures

1.1: Photographs of a series of FXG and polymer gel dosimeters .....	13
1.2: Understanding the Fourier slice theorem.....	18
1.3: Filtering and backprojection in optical CT image reconstruction.....	19
1.4: Relationship between the parallel beam and fan beam geometry parameters .....	21
1.5: Geometry and notation for a projection in the cone beam detector configuration.....	24
2.1: Photographs of the Vista <sup>TM</sup> cone beam optical CT scanner.....	40
2.2: Geometry of the Vista cone beam optical CT scanner .....	41
2.3: Illustration of the imaging optics for the cone beam CCD-based configuration.....	45
2.4: F-stop selection and cone beam geometry verification of the Vista scanner.....	47
2.5: Establishing the scanner cone beam geometry over the full 2D projection image .	49
2.6: Modulation transfer function data used to set the scanner spatial resolution. ....	50
2.7: Geometric image distortion test phantom .....	52
2.8: Minimizing geometric distortions in the scanner image data .....	53
2.9: Measurement limitations within the image volume.....	54
2.10: Scatter attenuation measurement .....	56
2.11: Absoprtion attenuation measurement .....	57
2.12: Determining the optimal attenuation measurement range .....	59
3.1: Effect of scanner warm up time .....	79
3.2: Instabilities in the mean intensity of the light source.....	80

3.3: Dose development in the FXG gel dosimeter .....	81
3.4: Diffusion effects in the FXG gel dosimeter .....	82
3.5: Temperature dependence of optically scattering and absorbing dosimeters.....	83
3.6: Identifying and managing the source of FXG gel temperature dependence.....	85
3.7: Stray light perturbation due to the PETE jar.....	87
3.8: Stray light perturbation due to the FXG gel matrix. ....	88
3.9: Variation in stray light perturbation with irradiated attenuation.in the FXG gel.....	89
3.10: Side region scatter and glare in the imaging of absorption solutions .....	90
3.11: Side region scatter in the imaging of scatter solutions.....	91
4.1: Photographs of the wax Rando phantom and in-phantom FXG gel irradiation.....	114
4.2: Dose range and auto-oxidation response of the FXG gel .....	118
4.3: Intra-batch dose response and energy dependence of the FXG gel .....	119
4.4: Treatment plan and gel-measured dose for an IMRT plan delivered to the FXG gel dosimeter in-phantom.....	120
4.5: Gamma function analyses of two IMRT plan deliveries .....	121
4.6: Evaluation of a IMRT plan delivery after a normalization.correction.....	122
4.7: Evaluation of the same IMRT plan delivered to a modified FXG gel dosimeter .....	123
4.8: Change in stray light perturbation after modification of the FXG gel dosimeter.....	125
4.9: Characterization of the modified FXG gel dosimeter.....	126
5.1: Test pencil beam plans and photographs of the tomotherapy benchtop apparatus used to deliver the plans to a NIPAM polymer gel dosimeter .....	145

5.2: Initial methodology for NIPAM gel dosimeter calibration.....	149
5.3: Side-by-side comparison of optical CT and MRI for readout of NIPAM.gels.....	151
5.4: Evaluation of phantoms with scattering regions of varied attenuation and size .....	152
5.5: Effect of formulation and preparation on NIPAM gel background scatter attenuation.....	153
5.6: Modified NIPAM gel dosimeter calibration .....	154
5.7: Gamma function evaluations of a 500 cGy pencil beam treatment plan delivered to two modified NIPAM gel dosimeters and to a Gafchromic film in-phantom. ....	155
5.8: Intra- and inter-batch reproducibility of the NIPAM gel dose response.....	156
6.1: Methods for managing scatter-derived stray light perturbation.....	174
6.2: Evaluation of a simple IGART process using NIPAM gel dosimetry .....	171
6.3: Imaging scattering ‘finger’ phantoms.....	181
6.4: Assessment of the polarizing film and fan beam scatter reduction strategies.....	178
6.5: Beam stop array (BSA) correction of uniform scattering phantoms.....	177
6.6: Challenges with BSA correction of non-uniform phantoms.....	178
6.7: Assessment of a geometric miss using NIPAM gel dosimetry .....	179

## List of Tables

2.1: Scanner measurement precision.....	58
4.1: Fricke-based gel atomic compositions.....	129
6.1: Effect of increasing object-to-camera distance.....	178

## Nomenclature

### Symbols

au	arbitrary units
$\Delta c(X)$	change in concentration of chemical species X
%C	percentage of cross-linking monomer by weight
D	dose, source-to-detector distance, object-to-detector distance
e	conversion factor for joules to electron volts ( $1.6 \times 10^{-19}$ J/eV)
$\epsilon$	molar extinction coefficient
f	object function
G	radiation chemical yield in number of species per 100 electron volts
$G(X)$	radiation chemical yield in moles per joule
H, h	frequency filter
I	optical intensity
L	optical path length
$\mu, \Delta\mu$	optical attenuation coefficient, change in optical attenuation coefficient
$N_A$	Avagadro's number
OD	optical density
$\rho$	mass density
P	Radon transform (projection data) of the object function f
Q	filtered projection data function
r	relaxivity
R	relaxation rate, fan & cone beam geometry cosine weighting factor
$R_1$	spin-lattice relaxation rate
$R_2$	spin-spin relaxation rate
S	Fourier transform
%T	total monomer percentage by weight
U	cone beam geometry weighting factor

### Acronyms

1D, 2D, 3D	one, two, three-dimensional
BIS	N,N'-methylene-bis-acrylamide

BSA	beam stop array
CBCT	cone beam x-ray computed tomography
CCD	charge-coupled device
CCSEO	Cancer Centre of Southeastern Ontario
CERR	Computational Environment for Radiotherapy Research
CT	computed tomography
DNA	deoxyribonucleic acid
FXG, FG	Fricke-xylenol orange-gelatin, Fricke-gelatin
IMRT	intensity modulated radiation therapy
IGART	image guided adaptive radiation therapy
LED	light emitting diode
MLC	multi-leaf collimator
MOSFET	metal oxide-semiconductor field effect transistor
MRI	magnetic resonance imaging
MTF	modulation transfer function
NIPAM	N-isopropylacrylamide
NMR	nuclear magnetic resonance
OBI	on-board imaging
OAR	organs at risk
PETE	polyethylene terephthalate
PMMA	polymethyl-methacrylate
PTFE	poly-tetrafluoroethylene
PTV	planning target volume
QA	quality assurance
RI	refractive index
ROI	region(s) of interest
RTAP	resolution, time, accuracy, precision
SNR	signal-to-noise ratio
TLD	thermoluminescent dosimeter
THPC	tetrakis hydroxymethyl phosphonium chloride
wt%	weight percent

## Glossary

**Absorbed dose:** The energy absorbed per unit mass of irradiated material. The SI unit for absorbed dose is the gray (Gy), where  $1 \text{ Gy} \equiv 1 \text{ J/kg}$ .

**Affine transformation:** a transformation that preserves co-linearity (i.e. points along a line remain along a line) and ratios of distances. A solid body affine transformation allows for rotation and translation, but not shear operations.

**Anterior-posterior:** from the front to the back of the body.

**Anthropomorphic:** having the attribute of human characteristics (e.g. shape).

**Apodizing sinc function:** a windowing or tapering ( $\sin x / x$ ) function.

**Auto oxidation effect:** the slow conversion of Fe(II) to Fe(III) ions in the dosimeter, triggered by sources other than high energy radiation.

**Bicubic spline interpolation:** a form of interpolation where the interpolant is a piecewise polynomial function called a spline. The function and its derivatives are matched at the corners of the unit square to satisfy the bicubic specification.

**Brachytherapy:** a form of radiotherapy where a radiation source is placed inside or next to the tumour or area requiring treatment.

**Cancer:** A generic term for more than one hundred different diseases characterized by an uncontrolled, abnormal growth of cells that usually invade and destroy normal tissue and can travel through the bloodstream and lymphatic system to reach other parts of the body.

**Chelator:** a chemical that binds to a central metal ion to form a soluble, complex molecule. After chelation, the central metal ion has lowered reactivity with other elements or ions.

**Coherent scattering:** occurs when a photon interacts with the full electronic structure of an atom and is re-emitted in a new direction with energy conserved.

**Collimator:** A mechanical device used to define the size and shape of a radiation beam, made from a heavily attenuating material such as tungsten.

**Compton scattering:** occurs when an incoming photon interacts with a ‘free’ electron in an atom (i.e. with binding energy less than the photon energy), ejecting the electron from the atom with some amount of kinetic energy, and producing a scattered photon of lesser energy.

**Computed tomography (CT):** an imaging modality in which 2D slices of an object are reconstructed from transmission data through the object space, recorded at multiple angles. One implementation is x-ray CT, typically used to obtain 2D slices of a patient's anatomy.

**Cone beam:** A broad, diverging radiation beam in the geometry of a cone.

**Conformal radiation therapy:** A form of external beam radiation therapy in which the shape of the treatment field(s) closely conform to the defined edges of a target volume.

**Conventional radiation therapy:** A form of external beam radiation therapy employing simple geometric-shaped radiation beams directed at the target volume (but not conforming to its edges) from different orientations around the patient.

**External beam radiation therapy:** A treatment modality using radiation directed at the cancer and surrounding tissue from a machine outside the body.

**Fan beam:** A slit-shaped diverging radiation beam in the geometry of a fan.

**F-stop:** the ratio of the focal length of the lens to the diameter of the entrance pupil. Each full stop increase (e.g. from f4 to f5.6) reduces the light gathering capacity of the aperture by 50%.

**Gantry:** A section of the external beam radiotherapy unit that: (a) houses the radiation source, and (b) can rotate about a horizontal axis.

**Image guided adaptive radiation therapy (IGART):** In an IGART process, treatment planning and delivery modifications (adaptations) are made on the basis of image measurements of the patient's anatomy obtained at some point during the course of the treatment process.

**Intensity modulated radiation therapy (IMRT):** A type of conformal radiation therapy in which the intensity of the the radiation beam is modulated during the delivery of each (fixed angular position) treatment field to boost the dose to the target volume and spare surrounding healthy tissue.

**Inverse treatment planning:** A method of treatment planning for radiation therapy that uses a computer optimization routine to produce the treatment fields for a pre-specified dose distribution.

**Isodose curve:** a line passing through points of equal dose, usually shown for 2D slices in a given dose distribution.

**Ionization chamber:** an instrument consisting of an open air or gas filled enclosure between two conducting electrodes. When gas (or air) between the electrodes is ionized by radioactive emission, the ions and dissociated electrons move to the electrodes of the opposite polarity,

creating an ionization current which may be measured by a galvanometer or electrometer. A bias voltage is applied to facilitate charge collection.

**Left lateral-right lateral:** from the left to the right side of the body

**Linear accelerator (linac):** A high-energy x-ray-generating machine used in external beam radiation therapy. The linac uses microwaves to accelerate electrons to high energy (megaelectron volts, MeV) through a linear waveguide. The high energy electron beam may be used directly, or it can be directed at a high atomic number target material to produce x-rays as an alternative form of radiation for treatment.

**Modulation transfer function:** The modulation transfer function reports a measurement of the imaging system's ability to transfer contrast from the object to the image plane at a specific resolution and is usually normalized to the contrast value from some low spatial frequency periodic variation.

**Multi-leaf collimator (MLC):** A type of collimator typically with two banks of narrow, interleaved metal blocks (leaves). The individual MLC leaves can be independently moved into or out of the radiation beam passing through the primary and secondary collimators of the linac, to block a portion of the radiation beam.

**Optical absorption:** occurs when the electromagnetic energy of a photon is taken up by an interacting atom (typically by the electrons of an atom) and is lost to another form of energy such as heat.

**Optical scattering:** occurs when the electromagnetic field of a photon interacts with a particle, inducing a dipole moment in the particle. The induced dipole moment will then radiate (i.e. scatter) light in all directions. The polarizability is related to a difference in the index of refraction of the scattering particle and the surrounding medium. That is, light scattering only occurs in media that have an inhomogeneous index of refraction. If the particle size is small compared to the wavelength of the photon, then the interaction is treated as a whole particle interaction (Rayleigh scattering). If the particle size is not small compared to the photon wavelength, then the light can scatter from different parts of the particle. The difference in path lengths can then lead to destructive interference that reduces the recorded intensity of the light by varying degrees at each angle of scatter.

**Pair production:** an interaction of a photon with the electromagnetic field of the nucleus of an atom, producing an electron and positron with some amount of kinetic energy.

**Pencil beam:** A radiation beam of small field size, typically on the order of 1-2 cm full width.

**Penumbra:** The fall-off region at the edge of a radiation beam. The physical penumbra width is often defined as the lateral distance between the 90% and 50% isodose curves at a specified depth in the medium.

**Photo-disintegration:** occurs when a high energy photon penetrates the nucleus of an atom, exciting the nucleus such that it undergoes a transmutation (often expelling a neutron).

**Photoelectric effect:** occurs when a photon is absorbed by an atom, transferring energy to other forms, including charged particles (photoelectrons, Auger electrons) and characteristic energy photons.

**Radiation therapy (radiotherapy):** the medical treatment of cancer and other diseases through use of ionizing radiation.

**Radiochromic:** a material that changes in colour with the absorption of radiation.

**Spherical aberration:** image blurring that occurs when light near the edge of a lens with a spherical surface comes to a shorter focus than light from the central region.

**Superficial therapy:** treatment with x-rays produced at potentials of 50-150 kV. A filtration of 1-6 mm of aluminum is usually applied to the radiation beam.

**Superior-inferior:** from the head to the opposite end of the body.

**Target volume:** A three-dimensional (3D) region in the patient's anatomy (e.g. tumour) for which a radiation dose is prescribed.

**Thermochromic:** a material that changes in colour in response to a change in temperature.

**Tissue-equivalent:** a substance that has absorbing and scattering properties for a given radiation that match that of a specified biological tissue to an appropriately defined level of accuracy.

**Tomotherapy:** A rotational form of intensity modulated radiation therapy using a fan beam of radiation that rotates around the patient as he or she is translated through the radiation beam.

**Treatment fraction:** in radiation therapy, the total prescribed dose is usually delivered in multiple, small fractions on different days to improve local tumour control and sparing of normal tissues. The benefits of fractionation are usually summarized by the '4 Rs' of radiobiology: repair, repopulation, redistribution, and reoxygenation, the full details of which are outside the scope of this work. In repair, for example, healthy cells are given a chance to recover, while a larger percentage of cancerous cells are preferentially eliminated, as they have a reduced capacity to recover from radiation-induced damage compared to normal tissue cells.

**Tumour:** An abnormal mass of cancerous tissue.

**Voxel:** A basic volume unit in three-dimensional space.

# **Chapter 1**

## **General Introduction**

### **1.1 Radiation Therapy**

Radiation therapy involves the use of ionizing radiation either as a primary treatment or as part of a treatment regime for cancer that may include surgery, chemotherapy, hormone therapy or a combination of all three to control malignant cell growth. The aim of radiation therapy may be curative, with the disease being irradiated and cure achieved. The scope of radiation therapy also includes adjuvant treatment to keep cancer from returning, neo-adjuvant treatment which is given to shrink a tumour before the main treatment (typically surgery), or palliative treatment for local disease control and symptomatic relief in the cases where cure is not possible (Khan and Potish 1998).

Radiation therapy damages cell DNA. The damage may be due to direct interaction of photons, electrons, protons, neutrons, or ions from a radiation source with atoms in the DNA chain. The damage may also be from indirect interaction, where the radiation interacts with surrounding water to form free radicals, which then damage the cell DNA. In the common forms of electron and photon external beam therapy, most of their effect is indirect, through free radical formation and their resulting damage (Johns and Cunningham 1983, Khan 1994, Hall 2000).

Cancer cells are characteristically undifferentiated and stem cell-like (Hall 2000). Undifferentiated cells are not well developed, have a tendency to multiply very quickly, and do not resemble healthy cells. Stem-like cells have some similar characteristics to those of normal stem cells, particularly the ability to give rise to all cell types found in a particular cancer sample. Because of these characteristics, cancer cells reproduce rapidly and have a reduced capacity to repair non-lethal damage compared to healthy cells (Hall 2000).

Radiation therapy is therefore commonly applied to the cancerous tumour in treatment fractions over time to give healthy cells a chance to recover. A margin of normal tissue around the tumour is included to allow for daily setup uncertainties, as well as tumour movement, either internally or through movement of external alignment fiducial marks on the patient. To spare healthy tissues, shaped (or conformal) radiation beams may be directed at the target volume from different angles of exposure to provide a much larger absorbed dose to the tumour than the surrounding normal tissue. The dose is measured in units of gray (Gy), which is the standard unit of absorbed ionizing-radiation dose, equivalent to one joule per kilogram. It is estimated that more than 50% of the individuals who develop cancer will receive radiation therapy at some point during treatment of their disease (Foroudi *et al* 2002, Foroudi *et al* 2003, Usmani *et al* 2005).

Over the years, there have been significant developments in external beam radiation therapy technology. In the last few decades cobalt-60 irradiators have been replaced as the workhorse of radiotherapy by x-ray linear accelerators producing higher quality and higher energy photon beams, as well as electron beams (Khan 1994). Conventional linear accelerators are capable of depositing dose more effectively to deep-seated tumors with increased sparing of surrounding healthy structure, primarily due to their increased penetration energy and reduced beam penumbra. More recently, multi-leaf collimators (MLCs) with movable leaves capable of controlling the exit shape of the beam have been added to linear accelerators, providing additional options in external beam conformal dose delivery (Ezzell *et al* 2003). Further development has led to the introduction of the next generation of conformal therapy, termed intensity modulated radiation therapy or IMRT (Bortfeld *et al* 1994, Webb 2003, Ezzell *et al* 2003). In IMRT, the treatment is inverse planned (Ezzell *et al* 2003), and the MLC leaves move during irradiation to change the intensity of the radiation beam (at each fixed field position) during treatment to spare more adjoining normal tissue than is spared during conventional or conformal radiation therapy.

Serial and helical tomotherapy have been developed as implementations of IMRT employing a fan beam of radiation delivered along a stepped circular or continuous helical path around the patient as the patient is translated along the superior-inferior (head-to-foot) direction through the beam (Mackie *et al* 1993). Another implementation is intensity modulated arc therapy, in which radiation is delivered while the gantry of a linear accelerator is rotated (Yu 1995). In this form of radiation therapy, the MLC aperture shape is varied over one or more gantry arcs during the delivery. Perhaps the most recent arrival is volumetric arc therapy, where gantry speed, dose rate, MLC aperture shape and MLC orientation are changed dynamically during a single continuous arc treatment, promising both increased versatility in delivery planning as well as shorter treatment times (Otto 2008). The goal in the development of all of these high-tech delivery options is to provide a sufficient and uniform dose to the target volume (to control the disease) with increased sparing of the dose to healthy tissue, and in particular, sensitive tissues (termed organs-at-risk) for ensuing quality of life. The intent in all the above treatment modalities is also to complete the delivery in as short a time as possible.

## 1.2 Dose Verification

Performing a three-dimensional (3D) verification of the complex dose distributions found in external beam radiotherapy, brachytherapy and radioisotope therapy is an increasingly challenging task. The importance of dose verification has been highlighted through results reported by the Radiological Physics Center, which offers a credentialing program to National Cancer Institute centres. A recent update (Ibbott *et al* 2008) still indicates considerable variation in the participating institutions' abilities to deliver planned IMRT dose distributions. Close to 30% of the participating institutions (71 of 250 institutions) to date have failed to deliver a dose distribution to the standardized Radiological Physics Center anthropomorphic head-and-neck

phantom that agrees with their calculated treatment plan to within 7% dose difference or 4 mm distance-to-agreement (between isodose points in the two spatial dose distributions under comparison). Point measurements were acquired using thermo-luminescent dosimeters (TLDs), with agreement required on the first attempt. The recommendation of the International Commission on Radiation Units and Measurements that the accuracy of dose delivery in radiotherapy should be within  $\pm$  5% (International Commission on Radiation Units and Measurements 1999) underscores the importance of validating complex treatment plans in terms of proper spatial dose targeting and the accuracy of the calculated treatment plan dose distribution.

The tools presently used in the clinic for dose verification include ionization chambers, diodes, metal oxide–semiconductor field effect transistors (MOSFETs), and thermoluminescent dosimeters (TLDSS) for point dose measurements. These may be extended to ion chamber and diode arrays to acquire dose information at multiple points, usually in a plane. New flat panel devices, two-dimensional (2D) and three-dimensional (3D) arrays of detectors and scintillation devices are also being developed with a higher level of verification capability and introduced into the clinic (Moran *et al* 2005, Archambault *et al* 2005, Petric *et al* 2006, Archambault *et al* 2006). Radiochromic film provides the highest resolution data of all the 2D dose measurement systems. The film may be stacked to acquire multiple planes of dose data from an irradiation. Unfortunately, while film provides high resolution 2D dose data, its use involves a labor intensive process for accurate volume dosimetry.

Both 2D film and array-based techniques can detect specific features of a delivery (e.g. the fluence pattern from one beam orientation in a complex IMRT treatment) only in a user-specified plane. For this reason, traditional measurement methods are not well-suited for complete verification of spatially complex IMRT dose distributions, which incorporate large

changes in dose over small spatial displacements (Paliwal *et al* 1998, Low *et al* 1998b, Sandilos *et al* 2004). IMRT doses are also delivered dynamically, so that specific points in the irradiated volumes receive their final dose only over a total treatment time. These considerations have been factored into the emergence and development of the fully 3D measurement tool of gel dosimetry (Gore *et al* 1984, Appleby *et al* 1987, Olsson *et al* 1989, Olsson *et al* 1990, Schulz *et al* 1990).

### **1.3 Gel Dosimetry**

#### **1.3.1 Introduction**

Gel dosimetry is a form of chemical dosimetry in which the effects of localized radiation-initiated changes in a volume of aqueous gel material are measured by a suitable imaging modality. The extent of the change that occurs is related to the absorbed dose delivered to a particular point in the volume for a given concentration and reactivity of active chemical species. Depending on the class of dosimeter employed, imaging techniques such as magnetic resonance imaging (MRI), optical computed tomography (CT), x-ray CT and ultrasound can be used to probe the dose-dependent changes in three dimensions over the volume of the gel dosimeter (Schreiner and Olding 2009). This type of dosimetry is termed *fully 3D* dosimetry, distinguishing it from other forms of dosimetry such as film in which two-dimensional planar dose data sets may be combined to form a 3D dose data set.

Gel dosimeters usually are prepared in radiologically near soft-tissue-equivalent formulations. They primarily consist of water, with a balance of gel-forming material such as gelatine or agarose, and a small amount of radiosensitive chemical species providing the dose contrast mechanism. The dosimeters are liquid during their preparation and can be poured into shaped vessels and phantoms (including clinically interesting anthropomorphic phantoms) prior to gelation.

Gel dose response is primarily derived from water radiolysis. Electrons ( $e^-$ ), positively charged water ions ( $H_2O^+$ ) and water molecules in an excited state ( $H_2O^*$ ) are first produced through interaction of ionizing radiation with water in the gel. The basic radiation-water interactions (Khan 1994) producing these species are the photoelectric effect (up to  $\sim 150$  keV), Compton scattering (the dominant interaction over most of the megavoltage treatment energy range), pair production (starting at 1.02 MeV, becoming dominant near  $\sim 15$  MeV), and photo-disintegration (with a threshold energy of 8 MeV). The resultant electrons ( $e^-$ ) lose energy and become hydrated ( $e^- + nH_2O \rightarrow e_{aq}^-$ ), the positively charged water ions ( $H_2O^+$ ) combine with water to form hydronium ions and highly reactive hydroxyl radicals ( $H_2O^+ + H_2O \rightarrow H_3O^+ + OH\cdot$ ), and the excited water molecules ( $H_2O^*$ ) decompose to hydrogen and hydroxyl radicals ( $H_2O^* \rightarrow H\cdot + OH\cdot$ ). Following this, the aqueous electrons, hydronium ions, hydrogen, and hydroxyl radicals react together to form the molecular species water, molecular hydrogen and hydrogen peroxide,  $H_2O_2$ . The reaction of these free radicals and molecular species to form quantifiable dose-dependent chemical species in the dosimeter is the fundamental basis of gel dosimetry (Schreiner and Olding 2009).

The dose response for typical gel dosimeter imaging parameters (nuclear magnetic resonance relaxation rate, optical attenuation, or x-ray CT number) usually has a linear dependence that saturates at high dose (Schreiner and Olding 2009). This can be explained as follows. Some amount of a finite chemical species X formed by the absorption of radiation energy in the system can be related directly to the absorbed dose (D). The relationship between dose and the amount of X formed is usually specified by the radiation chemical yield,  $G(X)$ , or the G-value, which is conventionally designated G (Schreiner and Olding 2009). Both of these parameters specify the yield of the measured product in terms of the energy absorbed by the

dosimeter:  $G(X)$  is the SI unit expressed in moles  $J^{-1}$  while the G-value is a historically used parameter specified as the number of chemical entities produced by the absorption of 100 eV of energy. Although either term would suffice, the historical quantity  $G$  is also included here because most of the gel dosimetry literature still specifies the yield in terms of G-value.

The dose  $D$  absorbed by the chemical dosimeter may be determined (Attix 2004) from the chemical yield and change in concentration of the measured species  $X$  as:

$$D(Gy) = \frac{\Delta c(X)}{G(X)\rho} \quad (1.1)$$

where  $\Delta c(X)$  is the change in the concentration of product  $X$  in mol/L and  $\rho$  is the density of the dosimeter in kg/L. Using the G-value the relationship becomes:

$$D(Gy) = \frac{100 \cdot N_A \cdot e \cdot \Delta c(X)}{G \cdot \rho} = \frac{9.64 \times 10^6 \Delta c(X)}{G \cdot \rho} \quad (1.2)$$

where  $N_A$  is Avogadro's number ( $6.022 \times 10^{23} \text{ mol}^{-1}$ ) and  $e$  is the number of joules per electron volt ( $1.602 \times 10^{-19} \text{ J/eV}$ ). As the amount of un-reacted chemical species in the dosimeter depletes to a critically low concentration level, the dose response begins to saturate.

It should be emphasized, however, that in gel dosimetry the change in the quantity of the species formed under radiation is not directly measured. Instead, one usually measures a related physical property to the change that has occurred. As the imaging parameters are typically unique to the system in use and the dose response sensitivity can change significantly if the chemistry is changed even slightly, for example, by changing chemical suppliers, or by adding oxygen scavengers in polymer gels, a dosimeter batch calibration procedure is usually employed. Since the imaging relies on the macroscopic expression of dosimeter response at the molecular level, reasonably high doses are usually required to provide sufficient changes for a precise and

accurate quantification. This will be discussed in more detail as the common readout techniques for the two main classes of gel dosimeters are considered.

### 1.3.2 Fricke Gels

The first of the two classes of modern gel dosimeter was introduced by Gore *et al* in 1984, termed here as the Fricke gel dosimeter. This dosimeter is based on the well-established aqueous Fricke or ferrous sulphate dosimeter (Fricke and Hart 1966), but additionally incorporates a gel matrix for fixing of spatial dose. In a similar manner to its aqueous (gel-free) counterpart, ferrous  $\text{Fe}^{2+}$  ions interspersed in a gel matrix of the Fricke gel dosimeter are transformed under irradiation to ferric  $\text{Fe}^{3+}$  ions, the physical properties of which can be measured and related to absorbed dose.

It should be noted (before continuing on with a description of the Fricke gel dosimeter) that the concept of gel dosimetry was introduced previous to the report presented by Gore *et al* (1984). For example, experiments in the 1950s showed that aqueous solutions and agar-based gels containing a radiosensitive methylene blue dye experienced a color change under irradiation (Day and Stein 1950, Day and Stein 1957). Following this, a chloral hydrate agar gel formulation was used for measurements of electron depth dose curves (Andrews *et al* 1957).

Returning to the discussion of Fricke gels, the radiation chemical yield (G-value) for carefully prepared aqueous Fricke solution is  $15.5 \text{ Fe}^{3+}/100 \text{ eV}$  (Klassen *et al* 1999). The ferric ion chemical yield in Fricke gel systems, on the other hand, is increased from the aqueous value because of the addition of chemical pathways provided by the gel-based macromolecules for the conversion of  $\text{Fe}^{3+}$  (Audet and Schreiner 1997). The change in the Fricke gel yield is not surprising since it had been known from the onset of Fricke dosimetry that care had to be taken in the preparation of the dosimeter. Any impurity in the formulation would cause a poorly controlled increase in the sensitivity, and sodium chloride was specifically added to aqueous Fricke dosimeters to stabilize the response when low concentrations of impurity were present. With the

addition of gelatin in typical Fricke gels as an alternative source of response-stabilizing impurity, the use of sodium chloride was no longer indicated.

The paramagnetic characteristics of  $\text{Fe}^{2+}$  and  $\text{Fe}^{3+}$  ions are such that they perturb the nuclear magnetic resonance (NMR) spin-relaxation of neighboring water protons differently. The radiation-induced changes in the Fricke gel dosimeter (due to localized variations in the concentrations of ferrous and ferric ions) can consequently be imaged using MRI, and MRI-derived contrast calibrated to absorbed dose. This ability to measure radiation-induced changes in a bulk sample by high resolution MRI generated much interest, and launched the field of gel dosimetry.

The NMR relaxation in aqueous Fricke dosimeters may be described by a fast exchange model in which water is considered to exist in three specific environments (or groups). Water may be found in bulk form or hydrating either the ferrous or the ferric ions. If the environments were isolated, then each would be described by its own relaxation rate. However, since they are coupled by the exchange of water, the observed spin relaxation depends upon the exchange dynamics between the groups (Zimmerman and Brittin 1957). In the fast exchange limit, the observed relaxation rate may be effectively described by the weighted sum of the rates from the different water environments. The dose-dependent relaxation rate  $R_1(D)$  (Audet and Schreiner 1997) then becomes:

$$R_1(D) = \left\{ \left( r^{3+} - r^{2+} \right) \cdot G \cdot \frac{10 \cdot \rho}{e \cdot N_A} \right\} \cdot D + R_1(0) \quad (1.3)$$

where  $G$  is the G-value of  $\text{Fe}^{3+}$ ,  $R_1(0)$  is the relaxation rate of the dosimeter prior to irradiation, and  $r^{3+}$  and  $r^{2+}$  are the NMR relaxivities in the presence of ferrous and ferric ions, respectively. The relaxivity of a paramagnetic ion defines how the relaxation rate changes as a function of the

concentration of the ion (in  $\text{s}^{-1}\text{mM}^{-1}$ ). Eqn. 1.3 includes a factor of 1000 to account for the change in concentration unit convention from M to mM). For a pure aqueous Fricke solution, the  $\text{Fe}^{2+}$  and  $\text{Fe}^{3+}$  relaxivities are well-established and NMR Fricke dosimetry can therefore be used as an absolute dosimeter without a further requirement for calibration (Audet and Schreiner 1997).

The relaxation model increases in complexity as the aqueous Fricke dosimeter is incorporated into a gel matrix, but Eqn. 1.3 still holds true with slight modification. The additional spin environments introduced by the gel component in the dosimeter (one environment associated with the gel itself and another with water hydrating the gel) are incorporated into the relaxation rate of the pre-irradiation dosimeter  $R_1(0)$ . Eqn. 1.3 can be then be rearranged as:

$$D = \frac{N_A \cdot e}{10 \cdot \rho \cdot G} \cdot \frac{R_1(D) - R_1(0)}{\left(r_{\text{eff}}^{3+} - r^{2+}\right)} \quad (1.4)$$

The relaxivity of the ferrous ( $r^{2+}$ ) ion in the Fricke gel dosimeter can be taken directly from measurements in aqueous solution. In the case of the ferric ( $r^{3+}$ ) ion, however, the gelatin component acts to perturb the hydration of  $\text{Fe}^{3+}$  ions through a complexing step which effectively diminishes the hydration layer (Audet and Schreiner 1997). Therefore, the ferric ion environment has an effective relaxivity (hence the subscript *eff* in the Eqn. 1.4) that must be determined for the particular gel system in use (for example, in the presence of gelatin). In a similar manner, the dose response of the NMR relaxation rate for Fricke gels prepared with a chelator such as xylenol orange is also reduced because water hydration of the iron is perturbed by the presence of the chelator (Rae *et al* 1996). Therefore, since the chemical yield and NMR relaxivities of specific Fricke gel dosimeters are usually not well determined, and vary according to the preparation of the dosimeter, the dose response is usually calibrated for each dosimeter gel batch.

The Fricke transformation can also be optically probed. In fact, spectrophotometry is the standard technique of choice for determination of the ferric ion concentration in irradiated aqueous Fricke. The strong absorption by  $\text{Fe}^{3+}$  in the ultraviolet range at wavelengths of 224 and 304 nm enables a change in concentration of the ferric ion in irradiated Fricke gels to be related to the change in the measured optical density  $\Delta\text{OD}$ :

$$\Delta c(\text{Fe}^{3+}) = \frac{\Delta OD}{L \varepsilon_m} \quad (1.5)$$

where  $\varepsilon_m$  is the molar extinction coefficient for  $\text{Fe}^{3+}$  ( $\sim 2200 \text{ M}^{-1}\text{cm}^{-1}$  at 304 nm for aqueous Fricke solution at 25°C), L is the optical path length (width of the sample cuvette) and the change in  $\text{Fe}^{3+}$  concentration is in mM. Optical density ( $\Delta\text{OD}$ ) is a dimensionless quantity defined as the logarithm of the ratio of transmitted light intensity between an irradiated and a non-irradiated sample (i.e.,  $\Delta\text{OD} = \log_{10} I/I_0$ ). This quantity should not be confused with the localized change in optical attenuation ( $\Delta\mu$ ), which follows Beer's Law ( $I = I_0 e^{-\mu_{\text{optical}} X}$ ) along a specified path length through an attenuating media. Optical density is related to attenuation in that it represents the global change in the optical attenuation coefficient along the specified path. The optical equivalent of Eqn. 1.4 can be written either as:

$$\bar{D} = \frac{\Delta OD(D)}{\varepsilon_m \rho L G(X)} \quad (1.6)$$

or

$$D = \frac{\Delta\mu(D)}{\varepsilon_m \rho G(X)_{\text{Fe}^{3+}}} \quad (1.7)$$

It should be noted, however, that only the form of the equation which uses optical attenuation yields localized information on absorbed dose. The form of Eqn. 1.6 is better suited to providing

information on average absorbed dose over a known path length, as would be obtained from standard spectrophotometer cuvette measurements (acquired prior to and following the irradiation of radiosensitive gel-filled cuvettes).

Standard aqueous Fricke or Fricke gel dosimeters do not experience a significant change in optical attenuation coefficient in the visible range. However, there are alternative aqueous Fricke-based dosimeter formulations that exhibit a peak in optical response in the visible range. These formulations (which date back to the late 1970s to early 1980s) originally incorporated additional agents, such as benzoic acid and xylene orange, with the intent of increasing the sensitivity of the dosimeters (Gupta and Gomathy 1974). In addition to increasing the dose sensitivity, these agents also were also observed to shift the absorption bands for the Fricke dosimeter so that the maximum absorption was at 540 nm (green) in the visible range (see figures 1.1a and 1.1b). Following this initial work by Gupta and his colleagues, agar and gelatin-based analogues were introduced for optical CT-based dosimetry (Appleby and Leghrouz 1991, Kelly *et al* 1998).

The introduction of Fricke-xylene orange-based gel formulations addressed one of the original concerns with the Fricke gels, which was the requirement for reasonably high doses for the radiation-induced changes to be readily observed by any 3D probing technique. This concern was not deemed a limitation at the time, as linearly scaled doses into the absolute dose range required for reliable Fricke dosimetry could be readily achieved in a reasonable time with clinical radiation therapy radiation units. However, more recent areas of interest for application of gel dosimetry, such as dynamic treatment deliveries, often involve the investigation of single treatment fractions with absorbed doses of 100-200 cGy. This level of dose is significantly lower

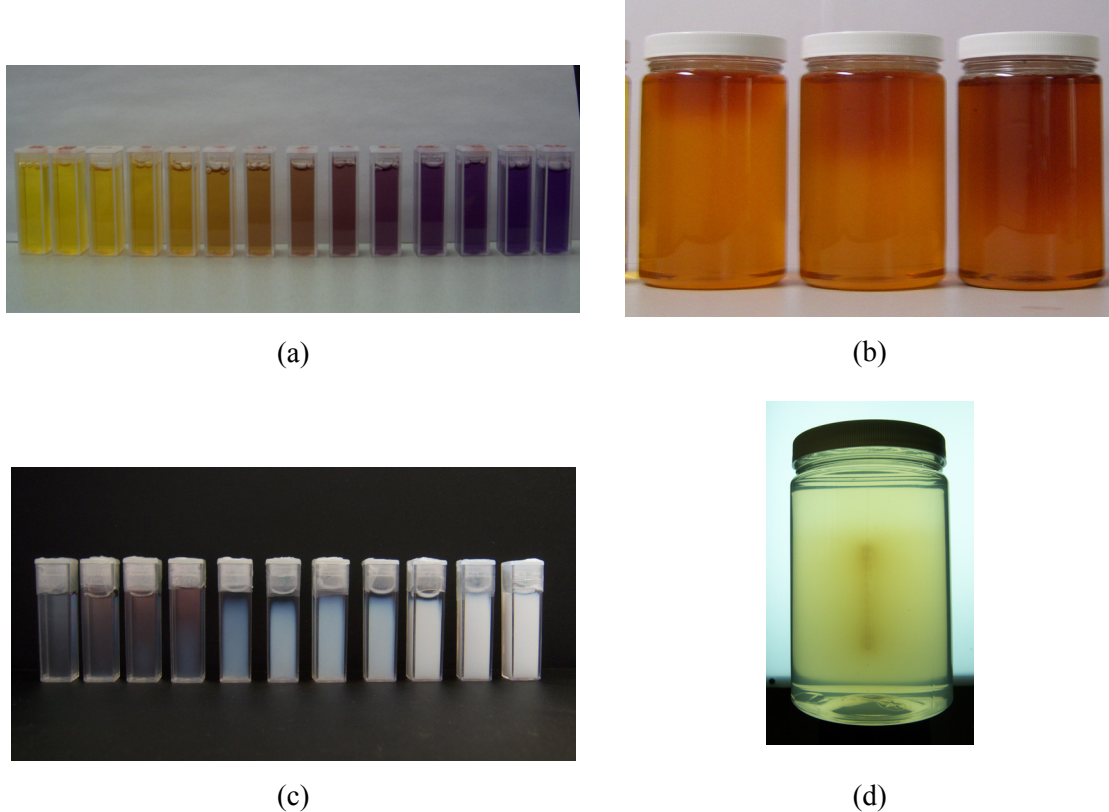


**Figure 1.1:** (a) A series of FXG gel-filled spectrophotometer cuvettes irradiated with doses ranging from 0-50 Gy. (b) Three FXG gel-filled 1 L PETE jar dosimeters irradiated with 6 MeV, 12 MeV and 20 MeV electron beams (from left to right). (c) A series of N-isopropylacrylamide polymer gel-filled cuvettes irradiated with doses ranging from 0-10 Gy. (d) An N-isopropylacrylamide polymer gel-filled 1 L PETE jar dosimeter irradiated with a simple Ir-192 brachytherapy line source treatment delivery.

than the preferred operating range of Fricke gel dosimeters, and due to the dynamic nature of the treatment delivery, dose scaling is not preferable.

The Fricke-xylenol orange-gelatin (FXG) dosimeter introduced by Kelly *et al* (1998) is perhaps most commonly used today (Caldeira *et al* 2007, Calcina *et al* 2007, Babic *et al* 2008b, Babic *et al* 2009). The benzoic acid component has been phased out of most formulations, as the impurities introduced by the gelatin are sufficient on their own to increase chemical yield, as noted earlier. During the 1990s, it was noted that the xylenol orange chelator contributed the

beneficial effect of significantly reducing iron ion diffusion in the gel causing loss of dose localization (Rae *et al* 1996). Follow up studies have subsequently investigated the optimization of the overall gel formulation while incorporating the xylenol orange component (Davies and Baldock 2008, Babic *et al* 2008a). The dose-contrasting optical absorption changes in the FXG gel formulation following irradiation are typically imaged with amber light at a wavelength of 580-590 nm (Kelly *et al* 1998).

In early investigations of Fricke gel dosimetry it became apparent that there were practical concerns that needed to be worked through. One primary challenge was the loss of dose spatial integrity due to diffusion of ferric ions in the gel over a time scale of few hours (Harris *et al* 1996, Rae *et al* 1996, Baldock *et al* 2001a). Some effort was given to the exploration of alternative gelling agents (Chu *et al* 2000) and systems with chelators (Rae *et al* 1996), but these were found to only partially suppress diffusion. Without further improvement in the chemistry, faster imaging techniques would be required to improve the accuracy of FXG gel dosimetry.

### 1.3.3 Polymer Gels

The limitations introduced by diffusion problems in Fricke gels led to the development of the second modern class of gel dosimeter based on radiation-induced polymerization and cross-linking of monomers suspended in a gel matrix (Maryanski *et al* 1993), as shown in figures 1.1c and 1.1d. As a precursor to the report by Maryanski *et al*, it had been shown that irradiated polymers could alter their structure and molecular dynamics, and the degree of change in some of the systems was dose-dependent (Andrews *et al* 1957, Hoecker and Watkins 1958, Boni 1961). In another investigation completed prior to Maryanski's work, it was observed that the radiation-induced dissociation of water molecules into highly reactive radicals then initiated polymerization and cross-linking reactions (Spinks and Woods 1976).

This new class of dosimeter opened the door to new dose readout techniques. The localized radiation-induced copolymerization of monomers suspended within an aqueous gel could not only be imaged via MRI (Maryanski *et al* 1993, Maryanski *et al* 1994, Maryanski *et al* 1996a, De Deene *et al* 1998, Baldock *et al* 2001b) and optical CT (Maryanski *et al* 1996b), but also by x-ray CT (Hilts *et al* 2000) and ultrasound (Mather *et al* 2002).

Over the last decade and a half, a number of different polymer gel formulations have been suggested (see table 30-2 in Schreiner and Olding (2009) for some typical formulations). Some gels incorporate acrylic monomers other than the acrylamide monomer originally used by Maryanski *et al* (Lepage *et al* 2001, Sandilos *et al* 2004, Saion *et al* 2005), while others use non-acrylic variants (Pappas *et al* 1999, Pappas *et al* 2003, Senden *et al* 2006a). The ongoing investigation of new monomer systems is partially due to an expressed concern about the acrylamide monomer (Fong *et al* 2001, McAuley 2004). Acrylamide is a neurotoxin, teratogen, and suspected human carcinogen that is readily absorbed through the skin (MSDS 2005). After irradiation, acrylamide-containing dosimeters usually still contain significant quantities of unreacted monomer, complicating their handling and disposal.

The use of polymer gels has historically been limited both by the toxicity of the initial, most commonly used acrylamide-based formulations, and by the fact that the early dosimeters required specialized preparation facilities. The polymerization and cross-linking reactions in these gel formulations were found to be inhibited by the presence of oxygen (Maryanski *et al* 1993, Salomons *et al* 2002), and glove boxes and an inert gas purging step were therefore required for the preparation of viable (anoxic) dosimeters. Unfortunately, even with the application of these preparation measures, oxygen contamination remains a significant issue in anoxic gels. This problem was substantially reduced by the introduction of anti-oxidants in the polymer gel formulation to reduce their oxygen sensitivity (Fong *et al* 2001, De Deene *et al* 2002a). The

resulting dosimeters are termed *normoxic* polymer dosimeters, as they are prepared and irradiated under normal atmospheric conditions. Both the development of normoxic preparations and the substitution of the toxic monomer components in the gel with less harmful alternatives (Pappas *et al* 1999, Senden *et al* 2006a) have served to advance the possibility of using polymer gels for dosimetry in the clinical environment.

One additional factor to be noted is that gelation and polymerization reactions in polymer gels can continue for many hours after irradiation, causing temporal evolution/instability in the NMR- and optical-dose responses (De Deene *et al* 2000, De Deene *et al* 2002, Fuxman *et al* 2003, Fuxman *et al* 2005, Senden *et al* 2006b). The reproducibility of the dose data is improved after a considerable wait period of roughly 12 hours to one day after irradiation, depending on the dosimeter recipe.

One approach to assigning an effective radiation chemical yield in polymer gel systems uses the concept of a ‘polymer yield’ (Babic and Schreiner 2006), specified in units of %wt Gy<sup>-1</sup> and defined as:

$$G^{poly} = \frac{\%wt(polymer)}{D} \quad (1.8)$$

where D is the dose in Gy and %wt (polymer) is the weight fraction of polymer formed. An effective relaxivity  $r^{poly}$  can also be defined in an analogous manner to the effective Fricke gel relaxivity (Eqn. 1.4) as:

$$r^{poly} = k^{poly} (R_2^{poly} - R_2^{bulk}) \quad (1.9)$$

where the superscripts poly and bulk denote water hydrating polymer and bulk water, and  $k^{poly}$  is the fraction of water protons hydrating the polymer per percent weight of polymer. The term  $(R_2^{poly} - R_2^{bulk})$  is the relaxation enhancement of the polymer-mediated water relative to bulk

water. Note that the NMR spin-spin relaxation rates ( $R_2 = 1/T_2$ ) are specified in Eqn. 1.9, as they are more sensitive than  $R_1$  relaxation rates to the dynamic, structural changes resulting from radiation-induced polymerization in the gels. The  $R_2$ - and optical attenuation-to-dose responses for polymer gels can then be developed from Eqns. 1.4 and 1.7 using Eqns. 1.8 and 1.9 (Schreiner and Olding 2009).

Up to this point, the bases for both MRI and optical CT readout of gel dosimeters have been discussed. However, while Fricke and polymer gels can readily be imaged using MRI, most clinics today cannot ensure timely access to MRI for readout of these two main classes of gel dosimeter. On the other hand, the ongoing improvement of easily accessible, fast optical readout tools promises to remove one of the barriers to acceptance of gel dosimetry as a viable tool in the cancer clinic. With this in mind, further discussion of MRI is considered to be outside of the scope of this work, and the following section, therefore, focuses exclusively on the use of optical CT imaging for 3D readout of gel dosimeters.

## 1.4 Optical CT Imaging

### 1.4.1 Introduction

The mathematical basis for optical CT imaging is well-described in Kak and Slaney (1998) , and hence is only outlined in brief in this section. The starting point for CT image reconstruction is the Fourier slice theorem (graphically shown in figure 1.2), which states that the Fourier transform  $S_\theta(\omega)$  of a line integral projection  $P_\theta(t)$  acquired at an angle  $\theta$  to the x-axis in object space is a radial line in the two-dimensional Fourier transform  $F(u, v)$  of the object at the same angle  $\theta$  to the u axis in frequency space. The object is represented by a two-dimensional function  $f(x, y)$  and each line integral through object space by the  $(\theta, t)$  parameters, where  $t = x \cos\theta + y \sin\theta$ . The parameters  $u = w \cos \theta$  and  $v = w \sin \theta$  account for the relationships between

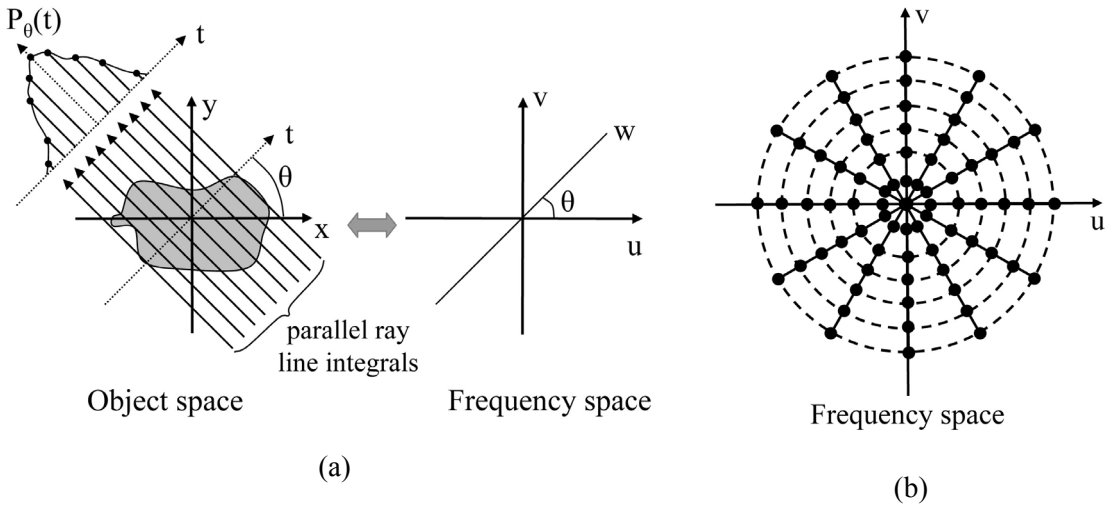


**Figure 1.2:** (a) A graphical representation of the Fourier slice theorem. (b) The radial density of projection image data in frequency space.

rectangular and polar variables in frequency space. The line integral projection data  $P_\theta(t)$  may be expressed as:

$$P_\theta(t) = \int_{-\infty}^{+\infty} \int_{-\infty}^{+\infty} f(x, y) \delta(x \cos \theta + y \sin \theta - t) dx dy \quad (1.10)$$

This equation is termed the Radon transform of the object space function  $f(x, y)$ .

The Fourier transform of the object may be estimated through the acquisition of a set of projections at regular angular intervals along a circular path around the object. Figure 1.2b shows the set of discrete  $F(u, v)$  values obtained from the full projection data set, spaced along radial lines (corresponding to each projection angle) in frequency space. In order to execute the inverse Fourier transform back to object space and reconstruct the object image in rectangular coordinates, the radial points are interpolated to obtain data points on a square grid. Since the density of the radial points decreases with distance from the origin in Fourier space, the interpolation error becomes larger with increasing distance. This means that there will be greater

uncertainty in the calculation of the high frequency components in an image versus the low frequency components, translating into image degradation.

The filtered backprojection algorithm is the primary approach used in most applications of straight ray tomography to obtain an estimate of the object in physical space. In the filtering part of the algorithm, each projection is weighted in the frequency domain to account for the variation in data sampling with frequency illustrated in figure 1.2b. A Shepp-Logan, cosine, or Hamming filter is typically selected for this purpose (figure 1.3a). All of these filters include a ramp in frequency space accounting for the variation in data sampling. The ramp term in the Shepp-Logan filter is then multiplied by a sinc apodizing function to reduce the undesirable amplification of high frequency noise. The other two filters are similar in intent. In the cosine

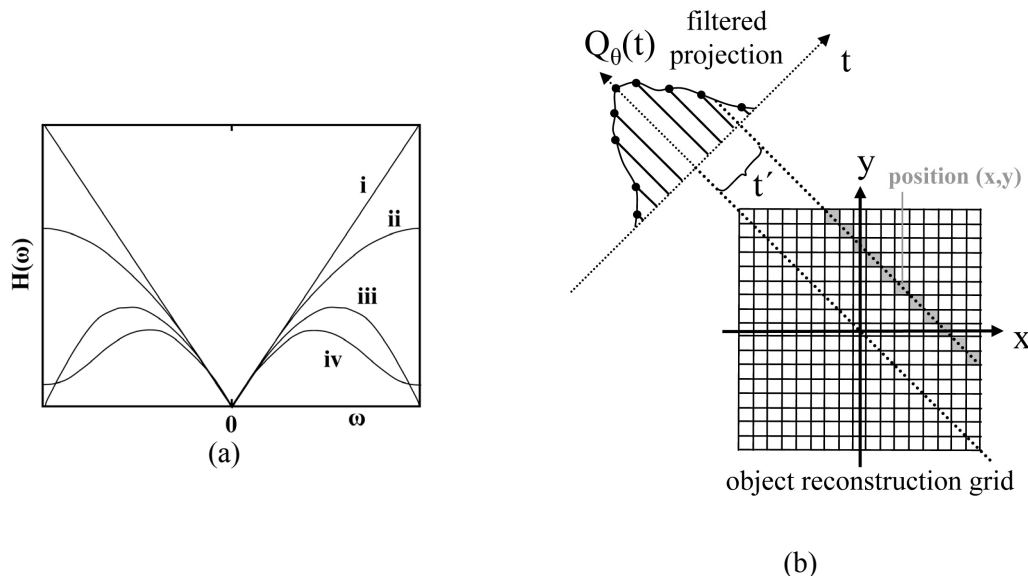


**Figure 1.3:** (a) The types of frequency filters used in CT image reconstruction include the (i) ramp, (ii) Shepp-Logan, (iii) cosine, and (iv) Hamming filter. (b) Backprojection of the filtered projection  $Q_\theta(t)$  onto the object space reconstruction pixel grid.

filter, the sinc term from the Shepp-Logan filter is replaced with a cosine term. A “raised cosine” term is used in the Hamming filter, optimized to minimize the nearest side lobes of the filter.

The final reconstructed image is obtained by adding together the two-dimensional inverse Fourier transforms from each weighted projection. This step can be thought of as the smearing of the data from each filtered projection over the image plane, and hence is referred to as backprojection. Referring to figure 1.3b, the filtered projection data  $Q_\theta(t)$  is interpolated to the correct backprojected position  $t'$  corresponding to each specific pixel in object space, and the interpolated value applied to the pixel(s) backprojected along that line. This operation is repeated for each pixel in object space over all the angles at which projection data was acquired. The final sum of interpolated filtered data values applied to each pixel position is then averaged against the number of projection angles to obtain the final object function  $f(x,y)$ .

#### 1.4.2 Parallel Beam Geometry

The simplest configuration for data acquisition is the parallel beam geometry shown in figure 1.2a. In this case, the backprojection operation used to acquire the original object function  $f(x,y)$  is expressed as:

$$f(x,y) = \int_0^\pi Q_\theta(x \cos \theta + y \sin \theta) d\theta \quad (1.11)$$

and the filtering operation used to obtain the filtered projection data  $Q_\theta(t)$  is:

$$Q_\theta(t) = \int_{-\infty}^{+\infty} S_\theta(w) H(w) e^{j2\pi w t} dw \quad (1.12)$$

where  $H(w)$  is the frequency filter transfer function applied to the Fourier transform  $S_\theta(w)$  of the projection data  $P_\theta(t)$  acquired at each angle  $\theta$  (Kak and Slaney 1998). However, parallel beam

geometry is rarely achieved in x-ray CT practice, except in pencil beam configurations. A fan beam geometry is more efficient and hence, conventional for imaging of 2D slices.

### 1.4.3 Fan Beam Geometry

A coordinate transformation can be applied to the filtered backprojection integral in Eqn. 1.11 to change the acquisition parameters from fan beam to parallel beam geometry (figure 1.4a). The

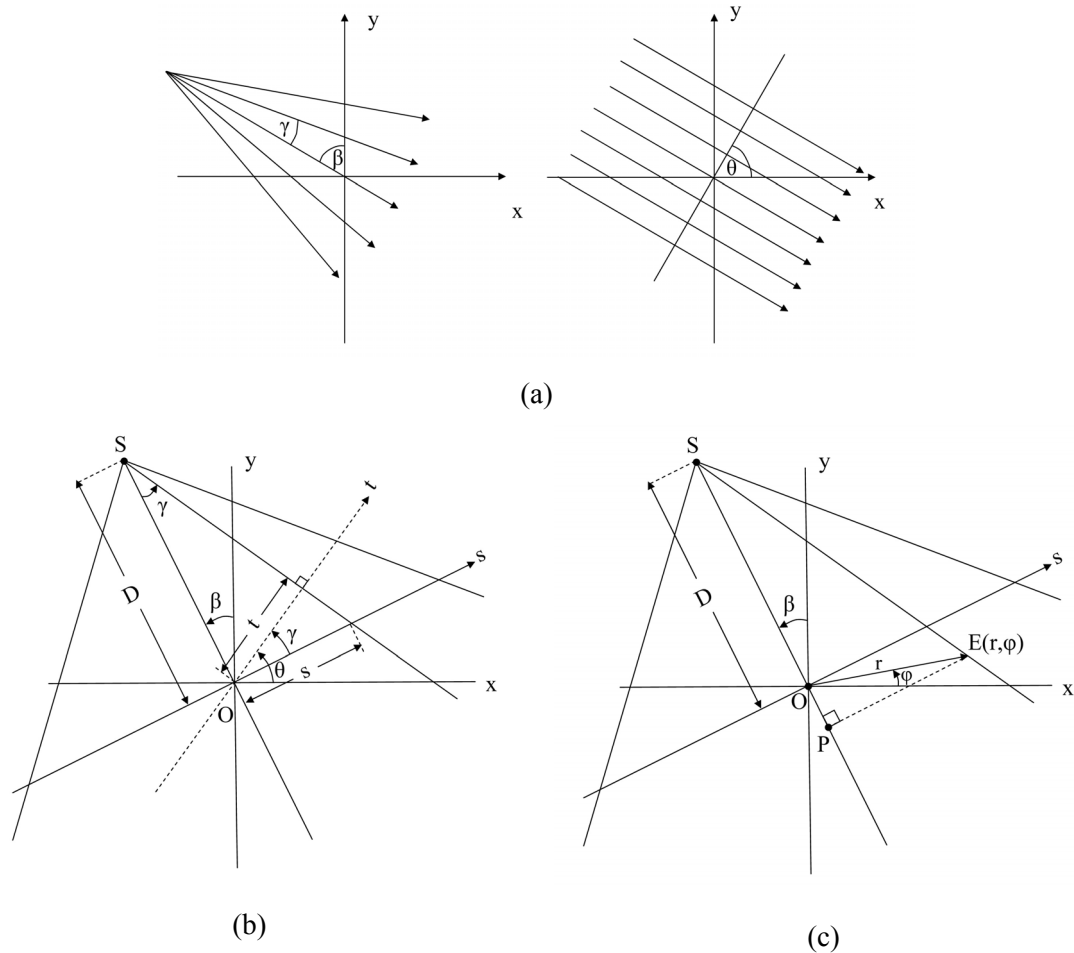


**Figure 1.4:** (a) Fan beam (left) and parallel beam (right) geometries (b) Establishing the relationship between the parallel and fan beam parameters used in the derivation of the fan beam filtered back-projection algorithm for an equi-spaced linear detector configuration (c) Illustration of the back-projection weighting factor ( $U$ ). The illustrations in (b) and (c) are adapted from Kak and Slaney (1998).

geometry for the scenario of a linear detector with regularly spaced pixels is shown in figure 1.4b.

The parallel beam parameters  $(\theta, t)$  can be related to the fan beam parameters  $(\beta, s)$  as:

$$\theta = \beta + \gamma = \beta + \tan^{-1} \frac{s}{D} \quad (1.13)$$

$$t = s \cos \gamma = \frac{sD}{\sqrt{D^2 + s^2}} \quad (1.14)$$

Using these relationships, the fan beam filtered backprojection formula for the linear detector configuration can then be determined from the parallel beam formula as:

$$f(x, y) = \int_0^{2\pi} \frac{1}{U^2} \int_{-\infty}^{+\infty} R_\beta(s) g(s' - s) \frac{D}{\sqrt{D^2 + s^2}} ds d\beta \quad (1.15)$$

where (with reference to figure 1.4c)  $s'$  is the backprojected coordinate of  $(r, \varphi)$  at projection angle  $\beta$ :

$$s' = \frac{\overline{EP}}{\overline{SP}} \overline{SO} = D \frac{r \cos(\beta - \varphi)}{D + r \sin(\beta - \varphi)} \quad (1.16)$$

and  $U$  is a weighting ratio of the projection  $\beta$  onto the central ray SP:

$$U(r, \varphi, \beta) = \frac{\overline{SO} + \overline{OP}}{D} = \frac{D + r \sin(\beta - \varphi)}{D} \quad (1.17)$$

Breaking it down into steps:

1. The projection data is pre-weighted by:

$$R'_\beta(s) = R_\beta(s) \frac{D}{\sqrt{D^2 + s^2}} \quad (1.18)$$

where this weighting factor is the cosine of the angle between each fan beam projection ray and the central ray of the current projection.

2. The projections are then filtered using the discrete filtering kernel

$$g(s) = \frac{1}{2} h(s) \quad (1.19)$$

where  $h(s)$  is the selected frequency filter.

3. The object image is calculated by backprojecting each pixel in object space to obtain the (interpolated) filtered projection data value at the detector plane according to the fan beam geometry (over all the projection angles), and weighting that value by  $1/U^2$ .

With the introduction of flat panel detectors, a select number of applications are undergoing a transition from fan beam to cone beam geometry to achieve a greater volume imaging efficiency. In a cone beam configuration, the image (object) volume is reconstructed from a single set of 2D projections, rather than as a collection of 2D image slices from multiple 1D projection sets (as in the fan beam case).

#### **1.4.4 Cone Beam Geometry**

The most widely used filtered backprojection algorithm for cone beam geometry (Feldkamp *et al* 1984) is similar in its implementation to that for fan beam geometry. Each elevation in the cone is considered separately (figure 1.5a) as a fan beam projection angled out of the source-detector plane of rotation (i.e. a tilted fan). The final three-dimensional reconstructed object is obtained by summing the backprojected contribution from each tilted fan beam to the object space.

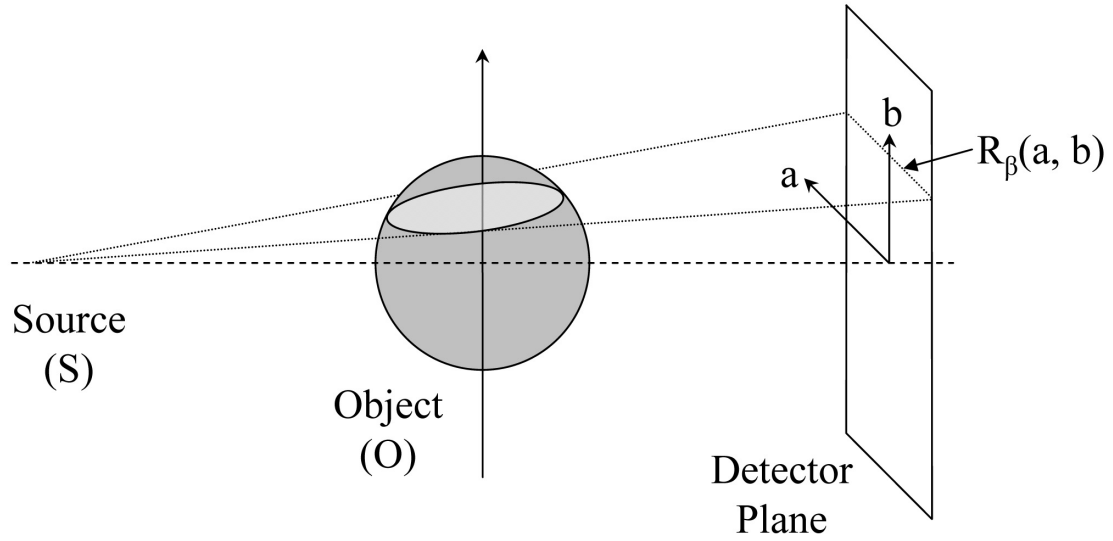


**Figure 1.5:** Geometry and notation for the single projection  $R_\beta(a,b)$  corresponding to a cone-beam 2D linear detector configuration.

As in the case of the fan beam algorithm, three steps are required to perform the reconstruction:

1. The projection rays are pre-weighted according to their position within the 3D cone:

$$R'_{\beta}(a,b) = R_\beta(a,b) \frac{D}{\sqrt{D^2 + a^2 + b^2}} \quad (1.20)$$

where (with reference to figure 1.5)  $a$  and  $b$  are found by back-projecting the voxel position  $(x,y,z)$  into the projection (at angle  $\beta$ ) as:

$$a(x,y,\beta) = D \frac{x \cos \beta + y \sin \beta}{D + x \sin \beta - y \cos \beta} \quad (1.21)$$

$$b(x,y,z,\beta) = \frac{zD}{D + x \sin \beta - y \cos \beta} \quad (1.22)$$

The projection pre-weighting factor can be interpreted as the cosine of the angle between each tilted fan beam projection ray and the central ray of the projection.

2. The projections are then filtered along horizontal detector lines using the same discrete filtering kernel as the one used in the fan beam algorithm.

$$g(a) = \frac{1}{2}h(a) \quad (1.23)$$

$$Q_\beta(a, b) = R'_\beta(a, b)^* g(a) \quad (1.24)$$

3. A weighted backprojection of the filtered projections along the cone is performed with the same weighting factor U as in the 2D fan beam case. Reverting back to the original (x,y,z) coordinates, the filtered projection formula is then:

$$f_{FDK}(x, y, z) = \int_0^{2\pi} \frac{1}{U^2} \int_{-\infty}^{+\infty} Q_\beta((x, y, \beta), b(x, y, z, \beta)) d\beta \quad (1.25)$$

where

$$U(x, y, \beta) = \frac{D + x \sin \beta - y \cos \beta}{D} \quad (1.26)$$

and is expressed this time in rectilinear coordinates. With this foundational theory in place, the discussion can now move on to the implementation of optical CT imaging.

#### 1.4.5 Practical Optical CT Scanners

Optical CT was first introduced as a readout modality for gel dosimetry in the mid 1990s (Tarte and van Doorn 1993, Tarte and van Doorn 1995, Gore *et al* 1996). In Gore's work, a He-Ne laser beam light source-photodiode detector pair in a translate-rotate scan path was used to acquire a set of transmitted light intensity projections through an irradiated acrylamide-based polymer gel

dosimeter at different angles over  $360^\circ$ . Parallel beam optical CT geometry was applied to the data and a reconstructed optical attenuation map of the dosimeter volume was obtained. The initial results from this system were exciting both in terms of measurement accuracy (better than 5%) and spatial resolution (< 2 mm voxels).

The relatively slow scan time (on the order of hours) associated with this initial scanner configuration led to the development of faster optical scanners, including improved translate-rotate scanners (van Doorn *et al* 2005, Lopatiuk-Tirpak *et al* 2008), and cone beam (Wolodzko *et al* 1999, Babic *et al* 2008b) and parallel beam (Doran *et al* 2001, Krstajic and Doran 2006, Krstajic and Doran 2007) charge-coupled device (CCD)-based configurations. While point detection laser-photodiode based systems acquire point-by-point data, CCD cameras obtain a 2D projection at each scan angle of the transmission from an area light source through the imaged object, reducing the total scan time to the order of minutes.

There are advantages and disadvantages associated with each type of scanner configuration. Cone beam scanners, in particular, are low cost, fast, compact, and easily scalable, but are known to be prone to scatter perturbation affecting the imaging accuracy (Doran and Krstajic 2006). If the complicating effects of scatter perturbation could be well-managed, reduced, or even eliminated, cone beam optical CT would become even more attractive for use in gel dosimetry. This is a primary incentive for this work.

## 1.5 Thesis Outline

The goals of this thesis are to: (a) establish the performance capabilities and limitations of the two main classes of cone beam optical CT-based gel dosimetry, (b) improve their measurement, and (c) apply them to the evaluation of clinically relevant complex dose distributions. The motivation behind this work is the belief that the careful development of easily accessible, fast optical

readout tools such as cone beam optical CT, and a deeper case history of gel measurement, will help to improve the acceptance of gel dosimetry in the cancer clinic.

In chapter 2 of this thesis, a basic characterization is performed on a representative cone beam optical CT scanner, establishing its imaging capabilities and limitations for application to gel dosimetry. Basic assessments are completed through use of calibration scattering solutions, absorbing solutions, and gelatin phantoms, which allow the optical measurement to be separated from the uncertainties in dosimeter preparation and dose delivery.

Chapter 3 follows up on imaging issues raised in chapter 2, and is specifically directed at cone beam readout of a Fricke-xylenol-gelatin (FXG) gel dosimeter. In addition to establishing some of the necessary details for reliable cone beam optical CT imaging of an FXG gel dosimeter, this chapter is intended to serve as an illustrative example of the work that is required to move past basic scanner characterization to imaging a specific gel dosimeter chemistry with its own inherent strengths and limitations.

Chapter 4 establishes a calibration basis for FXG gel-based evaluation of complex dose distributions. A series of representative head-and-neck IMRT plan evaluations are completed on a standard FXG gel-filled 1 L polyethylene terephthalate (PETE) jar-in-phantom. A dosimeter modification is then described that reduces stray light perturbation in the optical readout of the dosimeter, and improves the overall 3D dose measurement in the FXG gel.

Chapter 5 explores the use of an N-isopropylacrylamide (NIPAM)-based polymer gel dosimeter for evaluation of small field dose deliveries. Although cone beam optical CT imaging of polymer gels is significantly perturbed by scatter signal, careful matching of the dosimeter response to the scanner's imaging capabilities yields an improved 3D measurement.

In chapter 6, a methodology is described for radiotherapy treatment process quality assurance using a NIPAM-based polymer gel dosimeter in-phantom. Different scatter management and/or correction strategies are investigated in an attempt to improve the cone beam optical CT measurement of dose in polymer gels.

Chapter 7 summarizes the progress made in bringing cone beam optical CT-based gel dosimetry toward the point of clinical viability, and outlines some action steps for future improvements in the system.

## 1.6 References

- Andrews H L, Murphy R E and LeBrun E J 1957 Gel Dosimeter for Depth-Dose Measurements. *Review of Scientific Instruments* 28 329-332.
- Appleby A, Christman E A and Leghrouz A 1987 Imaging of spatial radiation dose distribution in agarose gels using magnetic resonance. *Med Phys* 14 382-384.
- Appleby A and Leghrouz A 1991 Imaging of radiation dose by visible color development in ferrous-agarose-xylenol orange gels. *Med Phys* 18 309-312.
- Archambault L, Arsenault J, Gingras L, Beddar A S, Roy R and Beaulieu L 2005 Plastic scintillation dosimetry: optimal selection of scintillating fibers and scintillators. *Med.Phys.* 32 2271-2278.
- Archambault L, Beddar A S, Gingras L, Roy R and Beaulieu L 2006 Measurement accuracy and cerenkov removal for high performance, high spatial resolution scintillation dosimetry. *Med.Phys.* 33 128-135.
- Attix F H 2004 *Introduction to radiological physics and radiation dosimetry*. Hoboken, NJ: Wiley-VCH.
- Audet C and Schreiner L J 1997 Multiple-site fast exchange model for spin-lattice relaxation in the Fricke-gelatin dosimeter. *Med.Phys.* 24 201-209.
- Babic S, Battista J and Jordan K 2008a An apparent threshold dose response in ferrous xylenol-orange gel dosimeters when scanned with a yellow light source. *Phys.Med.Biol.* 53 1637-1650.
- Babic S, Battista J and Jordan K 2008b Three-dimensional dose verification for intensity-modulated radiation therapy in the radiological physics centre head-and-neck phantom using optical computed tomography scans of ferrous xylenol-orange gel dosimeters. *Int.J.Radiat.Oncol.Biol.Phys.* 70 1281-1291.
- Babic S, McNiven A, Battista J and Jordan K 2009 Three-dimensional dosimetry of small megavoltage radiation fields using radiochromic gels and optical CT scanning. *Phys.Med.Biol.* 54 2463-2481.
- Babic S and Schreiner L J 2006 An NMR relaxometry and gravimetric study of gelatin-free aqueous polyacrylamide dosimeters. *Phys.Med.Biol.* 51 4171-4187.
- Baldock C, Harris P J, Piercy A R and Healy B 2001a Experimental determination of the diffusion coefficient in two-dimensions in ferrous sulphate gels using the finite element method. *Australas.Phys.Eng Sci.Med.* 24 19-30.
- Baldock C, Lepage M, Back S A, Murry P J, Jayasekera P M, Porter D and Kron T 2001b Dose resolution in radiotherapy polymer gel dosimetry: effect of echo spacing in MRI pulse sequence. *Phys.Med.Biol.* 46 449-460.

- Boni A L 1961 A Polyacrylamide gamma dosimeter. *Radiat.Res.* 14 374-380.
- Bortfeld T, Boyer A L, Schlegel W, Kahler D L and Waldron T J 1994 Realization and verification of three-dimensional conformal radiotherapy with modulated fields. *Int.J.Radiat.Oncol.Biol.Phys.* 30 899-908.
- Calcina C S, de Oliveira L N, de Almeida C E and de Almeida A 2007 Dosimetric parameters for small field sizes using Fricke xylenol gel, thermoluminescent and film dosimeters, and an ionization chamber. *Phys.Med.Biol.* 52 1431-1439.
- Caldeira A M, Neto A M, Bento A C, Baesso M L, Silva M A and de Almeida A 2007 Behavior of oxidation in the radiochromic gel dosimeter through photoacoustic technique measurements. *Appl.Radiat.Isot.* 65 605-609.
- Chu K C, Jordan K J, Battista J J, Van Dyk J and Rutt B K 2000 Polyvinyl alcohol-Fricke hydrogel and cryogel: two new gel dosimetry systems with low Fe<sup>3+</sup> diffusion. *Phys.Med.Biol.* 45 955-969.
- Davies J B and Baldoock C 2008 Sensitivity and stability of the Fricke-gelatin-xylan orange gel dosimeter. *Radiation Physics and Chemistry* 77 690-696.
- Day M J and Stein G 1950 Chemical effects of ionizing radiation in some gels. *Nature* 166 146-147.
- Day M J and Stein G 1957 The action of ionizing radiations on aqueous solutions of methylene blue. *Radiat.Res.* 6 666-679.
- De Deene Y, De Wagter C, Van Duyse B, Derycke S, De Neve W and Achten E 1998 Three-dimensional dosimetry using polymer gel and magnetic resonance imaging applied to the verification of conformal radiation therapy in head-and-neck cancer. *Radiother.Oncol* 48 283-291.
- De Deene Y, Hanselaer P, De Wagter C, Achten E and De Neve W 2000 An investigation of the chemical stability of a monomer/polymer gel dosimeter. *Phys.Med.Biol.* 45 859-878.
- De Deene Y, Venning A, Hurley C, Healy B J and Baldoock C 2002 Dose-response stability and integrity of the dose distribution of various polymer gel dosimeters. *Phys.Med.Biol.* 47 2459-2470.
- Doran S and Krstajic N 2006 The history and principles of optical computed tomography for scanning 3-D radiation dosimeters. *J.Phys.: Conf.Ser.* 56 45-57.
- Doran S J, Koerkamp K K, Bero M A, Jenneson P, Morton E J and Gilboy W B 2001 A CCD-based optical CT scanner for high-resolution 3D imaging of radiation dose distributions: equipment specifications, optical simulations and preliminary results. *Phys.Med.Biol.* 46 3191-3213.

- Ezzell G A, Galvin J M, Low D, Palta J R, Rosen I, Sharpe M B, Xia P, Xiao Y, Xing L and Yu C X 2003 Guidance document on delivery, treatment planning, and clinical implementation of IMRT: report of the IMRT Subcommittee of the AAPM Radiation Therapy Committee. *Med.Phys.* 30 2089-2115.
- Feldkamp L A, Davis L C and Kress J W 1984 Practical cone-beam algorithm. *J.Opt.Soc.Amer.* 1 612-619.
- Fong P M, Keil D C, Does M D and Gore J C 2001 Polymer gels for magnetic resonance imaging of radiation dose distributions at normal room atmosphere. *Phys.Med.Biol.* 46 3105-3113.
- Foroudi F, Tyldesley S, Barbera L, Huang J and Mackillop W J 2003 Evidence-based estimate of appropriate radiotherapy utilization rate for prostate cancer. *Int.J.Radiat.Oncol.Biol.Phys.* 55 51-63.
- Foroudi F, Tyldesley S, Walker H and Mackillop W J 2002 An evidence-based estimate of appropriate radiotherapy utilization rate for breast cancer. *Int.J.Radiat.Oncol.Biol.Phys.* 53 1240-1253.
- Fricke H and Hart E J 1966 Chemical Dosimetry. In: Attix, F H and Roesch, W C *Radiation Dosimetry Vol.II*. New York: Academic Press.
- Fuxman A M, McAuley K B and Schreiner L J 2003 Modeling of Free-radical Crosslinking Copolymerization of Acrylamide and N,N'-methylene-bisacrylamide for Radiation Dosimetry. *Macromol.Theory Simul.* 12 647-662.
- Fuxman A M, McAuley K B and Schreiner L J 2005 Modelling of polyacrylamide gel dosimeters with spatially non-uniform radiation dose distributions. *Chemical Engineering Science* 60 1277-1293.
- Gore J C, Kang Y S and Schulz R J 1984 Measurement of radiation dose distributions by nuclear magnetic resonance (NMR) imaging. *Phys.Med.Biol.* 29 1189-1197.
- Gore J C, Ranade M, Maryanski M J and Schulz R J 1996 Radiation dose distributions in three dimensions from tomographic optical density scanning of polymer gels: I. Development of an optical scanner. *Phys.Med.Biol.* 41 2695-2704.
- Hall E J 2000 *Radiobiology For The Radiologist*. Lippincott: Williams & Wilkins.
- Harris P J, Piercy A and Baldock C 1996 A method for determining the diffusion coefficient in Fe(II/III) radiation dosimetry gels using finite elements. *Phys.Med.Biol.* 41 1745-1753.
- Hilts M, Audet C, Duzenli C and Jirasek A 2000 Polymer gel dosimetry using x-ray computed tomography: a feasibility study. *Phys.Med.Biol.* 45 2559-2571.
- Hoecker F E and Watkins I W 1958 Radiation polymerization dosimetry. *Int.J.Appl.Radiat.Isot.* 3 31-35.

- Ibbott G S, Followill D S, Molineu H A, Lowenstein J R, Alvarez P E and Roll J E 2008 Challenges in credentialing institutions and participants in advanced technology multi-institutional clinical trials. *Int.J.Radiat.Oncol.Biol.Phys.* 71 S71-S75.
- International Commission on Radiation Units and Measurements 1999 Prescribing, Recording and Reporting Photon Beam Therapy (Supplement to ICRU Report 50). 62 .
- Johns H E and Cunningham J R 1983 *The Physics of Radiology*. Illinois: Charles C Thomas.
- Kak A C and Slaney M 1998 *Principles of Computerized Tomographic Imaging*. Philadelphia: Society for Industrial and Applied Mathematics. 107
- Kelly B G, Jordan K J and Battista J J 1998 Optical CT reconstruction of 3D dose distributions using the ferrous- benzoic-xylenol (FBX) gel dosimeter. *Med.Phys.* 25 1741-1750.
- Khan F M 1994 *The Physics of Radiation Therapy*. Baltimore: Williams & Wilkins.
- Khan F M and Potish R A 1998 *Treatment Planning in Radiation Oncology*. Baltimore: Williams & Wilkins.
- Klassen N V, Shortt K R, Seuntjens J and Ross C K 1999 Fricke dosimetry: the difference between G(Fe<sup>3+</sup>) for 60Co -rays and high-energy x-rays. *Phys.Med.Biol.* 44 1609-1624.
- Krstajic N and Doran S J 2006 Focusing optics of a parallel beam CCD optical tomography apparatus for 3D radiation gel dosimetry. *Phys.Med.Biol.* 51 2055-2075.
- Krstajic N and Doran S J 2007 Characterization of a parallel-beam CCD optical-CT apparatus for 3D radiation dosimetry. *Phys.Med.Biol.* 52 3693-3713.
- Lepage M, Jayasakera P M, Back S A J and Baldock C 2001 Dose resolution optimization of polymer gel dosimeters using different monomers. *Phys.Med.Biol.* 46 2665-2680.
- Lopatiuk-Tirpak O, Langen K M, Meeks S L, Kupelian P A, Zeidan O A and Maryanski M J 2008 Performance evaluation of an improved optical computed tomography polymer gel dosimeter system for 3D dose verification of static and dynamic phantom deliveries. *Med.Phys.* 35 3847-3859.
- Low D A, Mutic S, Dempsey J F, Gerber R L, Bosch W R, Perez C A and Purdy J A 1998 Quantitative dosimetric verification of an IMRT planning and delivery system. *Radiother.Oncol.* 49 305-316.
- Mackie T R, Holmes T, Swerdloff S, Reckwerdt P, Deasy J O, Yang J, Paliwal B and Kinsella T 1993 Tomotherapy: a new concept for the delivery of dynamic conformal radiotherapy. *Med.Phys.* 20 1709-1719.
- Maryanski M J, Gore J C, Kennan R P and Schulz R J 1993 NMR relaxation enhancement in gels polymerized and cross-linked by ionizing radiation: a new approach to 3D dosimetry by MRI. *Magn.Reson.Imaging* 11 253-258.

- Maryanski M J, Ibbott G S, Eastman P, Schulz R J and Gore J C 1996a Radiation therapy dosimetry using magnetic resonance imaging of polymer gels. *Med.Phys.* 23 699-705.
- Maryanski M J, Schulz R J, Ibbott G S, Gatenby J C, Horton D and Gore J C 1994 Magnetic resonance imaging of radiation dose distributions using a polymer-gel dosimeter. *Phys.Med.Biol.* 39 1437-1455.
- Maryanski M J, Zastavker Y Z and Gore J C 1996b Radiation dose distributions in three dimensions from tomographic optical density scanning of polymer gels: II. Optical properties of the BANG polymer gel. *Phys.Med.Biol.* 41 2705-2717.
- Mather M L, Whittaker A K and Baldoock C 2002 Ultrasound evaluation of polymer gel dosimeters. *Phys.Med.Biol.* 47 1449-1458.
- McAuley K B 2004 The chemistry and physics of polyacrylamide gel dosimeters: why they do and don't work. *J.Phys.: Conf.Ser.* 3 29-33.
- Moran J M, Roberts D A, Nurushev T S, Antonuk L E, El Mohri Y and Fraass B A 2005 An Active Matrix Flat Panel Dosimeter (AMFPD) for in-phantom dosimetric measurements. *Med.Phys.* 32 466-472.
- MSDS 2005 Material Safety Data Sheet acrylamide, version 1.10, <http://www.sigma-aldrich.ca/>.
- Olsson L E, Fransson A, Ericsson A and Mattsson S 1990 MR imaging of absorbed dose distributions for radiotherapy using ferrous sulphate gels. *Phys.Med.Biol.* 35 1623-1631.
- Olsson L E, Petersson S, Ahlgren L and Mattsson S 1989 Ferrous sulphate gels for determination of absorbed dose distributions using MRI technique: basic studies. *Phys.Med.Biol.* 34 43-52.
- Otto K 2008 Volumetric modulated arc therapy: IMRT in a single gantry arc. *Med.Phys.* 35 310-317.
- Paliwal B R, Ritter M A, McNutt T R, Mackie T R, Thomadsen B R, Purdy J A and Kinsella T J 1998 A solid water pelvic and prostate phantom for imaging, volume rendering, treatment planning, and dosimetry for an RTOG multi- institutional, 3-D dose escalation study. Radiation Therapy Oncology Group. *Int.J.Radiat.Oncol.Biol.Phys.* 42 205-211.
- Pappas E, Angelopoulos A, Kipouros P, Vlachos L, Xenofos S and Seimenis I 2003 Evaluation of the performance of VIPAR polymer gels using a variety of x-ray and electron beams. *Physics in Medicine & Biology* 48 N65-N73.
- Pappas E, Maris T, Angelopoulos A, Paparigopoulou M, Sakelliou L, Sandilos P, Voyatzzi S and Vlachos L 1999 A new polymer gel for magnetic resonance imaging (MRI) radiation dosimetry. *Phys.Med.Biol.* 44 2677-2684.
- Petric M P, Robar J L and Clark B G 2006 Development and characterization of a tissue equivalent plastic scintillator based dosimetry system. *Med.Phys.* 33 96-105.

- Rae W I, Willemse C A, Lotter M G, Engelbrecht J S and Swarts J C 1996 Chelator effect on ion diffusion in ferrous-sulfate-doped gelatin gel dosimeters as analyzed by MRI. *Med.Phys.* 23 15-23.
- Saison E, Shaari A H, Rahman M, Zaman M., Kadni T, Doyan A and Susilawati A 2005 The effects of crosslinker and monomer to the polymerization of polymethacrylamide gel dosimeters by direct and indirect methods. *Am.J.Appl.Sci* 2 1248-1255.
- Salomons G J, Park Y S, McAuley K B and Schreiner L J 2002 Temperature increases associated with polymerization of irradiated PAG dosimeters. *Phys.Med.Biol.* 47 1435-1448.
- Sandilos P, Angelopoulos A, Baras P, Dardoufas K, Karaikos P, Kipouros P, Kozicki M, Rosiak J M, Sakellou L, Seimenis I and Vlahos L 2004 Dose verification in clinical IMRT prostate incidents. *Int.J.Radiat.Oncol.Biol.Phys* 59 1540-1547.
- Schreiner L J and Olding T 2009 Gel Dosimetry. In: Rogers, D. W. and Cygler, J. E. *AAPM Medical Physics Monograph No. 34: Clinical Dosimetry Measurements in Radiotherapy*. Madison, WI, USA, Medical Physics Publishing.
- Schulz R J, deGuzman A F, Nguyen D B and Gore J C 1990 Dose-response curves for Fricke-infused agarose gels as obtained by nuclear magnetic resonance. *Phys.Med.Biol.* 35 1611-1622.
- Senden R J, De Jean P, McAuley K B and Schreiner L J 2006a Polymer gel dosimeters with reduced toxicity: a preliminary investigation of the NMR and optical dose-response using different monomers. *Phys.Med.Biol.* 51 3301-3314.
- Senden R J, DeJean P, McAuley K B and Schreiner L J 2006b Polymer gel dosimeters with reduced toxicity. *J.Phys.: Conf.Ser.* 56 156-159.
- Spinks J and Woods R 1976 *An Introduction To Radiation Chemistry*. New York: John Wiley & Sons.
- Tarte B J and van Doorn T 1995 Laser based tomographic scanning of gel volumes for applications in ionising radiation dosimetry. *10th Conference of the Australasian Optical Society, University of Queensland* .
- Tarte B J and van Doorn T 1993 Optical scanning of ferrous sulphate gels for radiotherapy treatment dosimetry. *APSEM/BECON Australasian Conference on Physical Science and Engineering in Medicine /Biomedical Engineering Conference* .
- Usmani N, Foroudi F, Du J, Zakos C, Campbell H, Bryson P and Mackillop W J 2005 An evidence-based estimate of the appropriate rate of utilization of radiotherapy for cancer of the cervix. *Int.J.Radiat.Oncol.Biol.Phys.* 63 812-827.
- van Doorn T, Bhat M, Rutten T P, Tran T and Costanzo A 2005 A fast, high spatial resolution optical tomographic scanner for measurement of absorption in gel dosimetry. *Australas.Phys.Eng Sci.Med.* 28 76-85.

- Webb S 2003 The physical basis of IMRT and inverse planning. *Br.J.Radiol.* 76 678-689.
- Wolodzko J G, Marsden C and Appleby A 1999 CCD imaging for optical tomography of gel radiation dosimeters. *Med.Phys.* 26 2508-2513.
- Yu C X 1995 Intensity-modulated arc therapy with dynamic multileaf collimation: an alternative to tomotherapy. *Phys.Med.Biol.* 40 1435-1449.

## **Chapter 2**

### **Scanner Characterization**

A version of this chapter with content formatted for publication has been published as: Olding T, Holmes O, and Schreiner L J (2010) Cone beam optical computed tomography for gel dosimetry I: scanner characterization *Phys. Med. Biol.* **55** 2819-2840 (see Appendix A for copyright permission; abstract found at <http://iopscience.iop.org/0031-9155/55/10/003>).

#### **2.1 Abstract**

The ongoing development of easily accessible, fast optical readout tools promises to remove one of the barriers to acceptance of gel dosimetry as a viable tool in the cancer clinic. This paper describes the characterization of a number of basic properties of the Vista<sup>TM</sup> cone beam CCD-based optical scanner, which can obtain high resolution reconstructed data in less than 20 minutes total imaging and reconstruction time. The suitability of a filtered back projection cone beam reconstruction algorithm is established for optically absorbing dosimeters using this scanner configuration. The system was then shown to be capable of imaging an optically absorbing media-filled 1 L polyethylene terephthalate (PETE) jar dosimeter to a reconstructed voxel resolution of 0.5 x 0.5 x 0.5 mm<sup>3</sup>. At this resolution, more than 60% of the imaged volume in the dosimeter exhibits minimal spatial distortion, a measurement accuracy of 3-4% and the mean to standard deviation signal-to-noise ratio greater than 100 over an optical absorption range of 0.06-0.18 cm<sup>-1</sup>. An inter-day scan precision of 1% was demonstrated near the upper end of this range. Absorption measurements show evidence of stray light perturbation causing artifacts in the data, which if better managed would improve the accuracy of optical readout. Cone beam optical attenuation measurements of scattering dosimeters, on the other hand, are nonlinearly affected by angled scatter stray light. Scatter perturbation leads to significant cupping artifacts and other

inaccuracies that greatly limit the readout of scattering polymer gel dosimeters with cone beam optical CT.

## 2.2 Introduction

Modern radiation therapy has been a rapidly evolving field over the last few decades, involving increasingly sophisticated treatment planning and delivery options toward the goal of delivering sufficient and uniform dose to a target volume while sparing surrounding healthy tissue, in as short a treatment time frame as possible. While conventional one- and two- dimensional (1D, 2D) dosimetry tools such as ion chambers, diodes, arrays of ion chambers or diodes, film, etc available in the clinic are well suited to the task of regular quality assurance, there are particular circumstances (e.g. when bringing a new treatment on-line, or verifying small field deliveries) where a fully three-dimensional (3D) dosimetry tool would be a useful addition to the task of spatial dose verification of these sophisticated delivery options (Schreiner 2009).

Since the early development of gel dosimetry (Gore *et al* 1984, Olsson *et al* 1990), it has been recognized as a potential high resolution, tissue-equivalent, 3D dosimeter for clinical use, but a number of factors have limited the uptake of this tool into the clinical environment (Schreiner and Olding 2009). One of the major limiting factors has been the lack of access to the first developed gel dosimeter readout modality of magnetic resonance imaging (Gore *et al* 1984, Olsson *et al* 1990).

An alternative modality of optical readout was introduced in the mid 1990s (Tarte and van Doorn 1993, Tarte and van Doorn 1995, Gore *et al* 1996) which employed a He-Ne laser beam light source-photodiode detector pair in a translate-rotate scan path to acquire a set of transmitted light intensity projections through an irradiated cylindrical polymer gel dosimeter (Maryanski *et al* 1993, Maryanski *et al* 1996b) at different angles over 360°. Optical computed

tomography (CT) techniques were then applied to obtain a reconstructed 3D optical attenuation map of the gel which could be calibrated against absorbed dose. The initial results from this system were exciting both in terms of measurement accuracy (better than 5%) and spatial resolution (< 2 mm voxels).

The long scan time associated with the first generation translate-rotate scanner in order to obtain a high resolution 3D data set has spurred the development of faster optical scanners, from improved translate-rotate scanners (van Doorn *et al* 2005, Lopatiuk-Tirpak *et al* 2008), to cone beam (Wolodzko *et al* 1999, Babic *et al* 2008b) and parallel beam (Doran *et al* 2001, Krstajic and Doran 2006, Krstajic and Doran 2007) charge-coupled device (CCD)-based configurations. While point detection laser-photodiode based systems acquire point-by-point data, digital CCD detectors obtain a complete 2D area intensity transmission projection at a time. This introduces a tradeoff between the two systems. At present, point detection schemes can easily incorporate a collimator that rejects stray light from sources not along the primary ray path between the light source and the detector (Oldham and Kim 2004), but they may have scan times on the order of hours. CCD-based area detection schemes cannot easily incorporate physical collimation at the detector end of the scanner, and hence they accept stray light into the ray bundle passing through the lens aperture(s) and falling on the CCD detector, but can have a total scan time under 10 minutes. This fast scan time is particularly advantageous with the use of Fricke-based gel dosimeters, which exhibit a degradation of spatial integrity of dose information over time through diffusion of iron or chelated iron-dye complex ions (Olsson *et al* 1992, Kelly *et al* 1998).

Important work has been completed on the characterization on the parallel beam CCD scanner (Krstajic and Doran 2006, Krstajic and Doran 2007), and there have been several studies of different rotate-translate scanners, for example, the investigations by Oldham *et al* (Oldham *et al* 2001, Oldham *et al* 2003, Oldham and Kim 2004) and Islam *et al* (Islam *et al* 2003). Some

literature also exists on cone beam CCD scanners, primarily describing the commercial VISTA<sup>TM</sup> cone beam optical CT unit available from Modus Medical Devices Inc (London, ON, Canada) (Wolodzko *et al* 1999, DeJean *et al* 2006a, Jordan and Battista 2006a, DeJean *et al* 2006b, Jordan and Battista 2006b, Bosi *et al* 2007, Bosi *et al* 2009). The cone beam system brings the advantages of being low cost, compact, and easily scalable, but early results indicate that this readout modality is particularly prone to scatter perturbation (Doran and Krstajic 2006).

This paper presents an investigation of the performance capabilities and limitations of the Vista cone beam optical CT scanner for use in the field of gel dosimetry. Results are reported to provide a basic understanding of the effect of camera lens aperture selection, to validate the assertion of cone beam optical CT imaging geometry, and to experimentally establish the high spatial resolution optical CT image reconstruction. The effects of geometric distortion in cone beam optical CT are then examined and the scanner measurement capabilities assessed through volume imaging of optically scattering and absorbing media in standard-sized 1 L polyethylene terephthalate (PETE) jars (obtained from Modus Medical Devices Inc, London, ON, Canada). These measurements were quantified over a range of mean optical scatter and absorption attenuation values in terms of attenuation linearity, accuracy, mean-to-standard deviation signal-to-noise ratio (SNR) and inter-day scan precision. While this work is particularly directed toward optical cone beam imaging of standard-sized 1 L PETE dosimeter jars, the results could be applied to other container sizes. The investigation presented in this paper is distinguished from previous reports (describing some of the basic properties listed above) by its broad scope of evaluation using a standard-sized gel dosimeter container, and its justification of some of the basic assumptions fundamental to the use of cone beam optical CT.

## 2.3 Experiment

### 2.3.1 Cone Beam Optical CT Imaging

The basic details of the optical CT imaging performed in this study and the preparation of scanner calibration solutions are outlined in this section. A Vista<sup>TM</sup> cone beam optical CT scanner (figure 2.1) was used for volume imaging, with either 633 or 590 nm LED diffuse light panel illumination (specified in each experiment) filtered by an optical band pass filter placed at the camera. Calibration parameters for the geometry shown in figure 2.2 ( $H_F$ ,  $H_R$ ,  $W_F$ ,  $W_R$ ,  $L$ , and  $D_{SA}$ ) were determined or calculated to better than  $\pm 0.5$  mm using a metric ruler and a printed transparency checkerboard line grid, with 1 cm spacing between lines, inserted at the front and rear of the matching tank.

The normal practice was to let the scanner warm up for at least 1 h prior to performing a scan. For each scan, a set of 410 light intensity transmission projections was acquired over 360° to ensure adequate sampling in Fourier space during image reconstruction (Robb 1982, Guan and Gordon 1996). A 1024 x 768 pixel, 12-bit CCD camera (Dragonfly2 DR2-HIBW, Point Grey

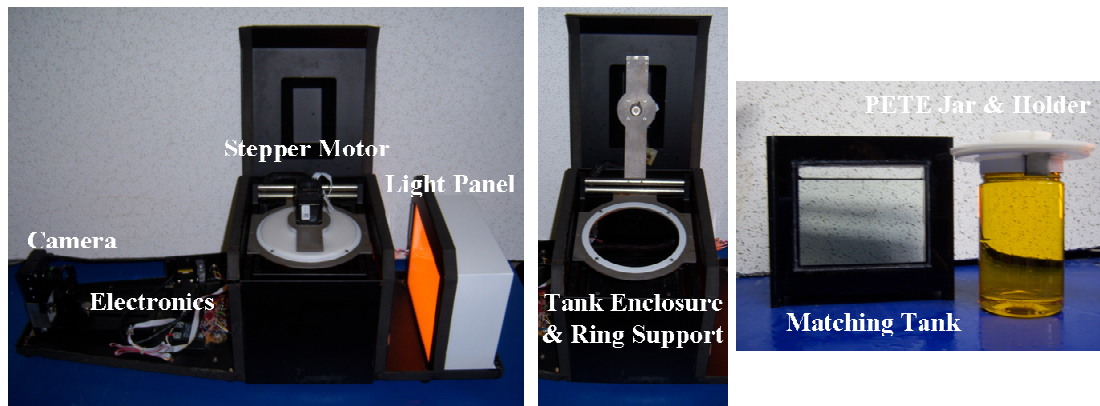


**Figure 2.1:** The Vista<sup>TM</sup> cone beam optical CT scanner used for volumetric imaging. This scanner contains a CCD camera with a 6.4° half cone imaging angle, a precision stepper motor for rotating the dosimeter jar, a dosimeter matching tank, and an acrylic sheet-diffused light LED area light panel providing illumination at wavelengths of 590 nm and 633 nm. Standard-sized 1 L PETE jars are suspended on the ring support in the matching tank.

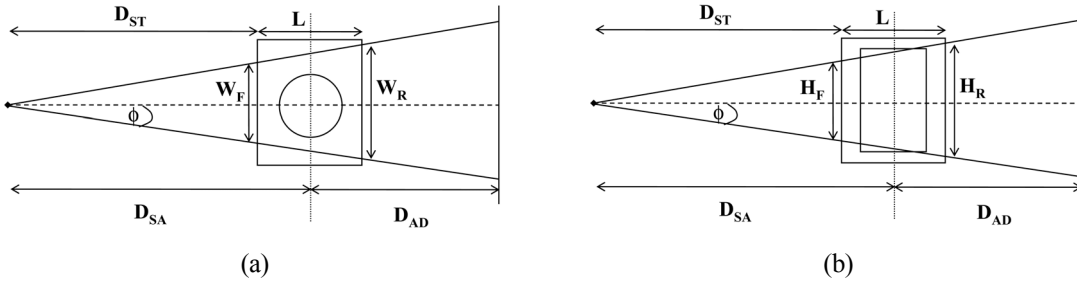


**Figure 2.2:** (a) Top and (b) side views of the Vista cone beam optical CT scanner geometry (adapted from the VistaRecon manual produced by Modus Medical Devices Inc).

Research, Richmond, BC, Canada) using a 2/3" diameter, 12 mm focal length lens (Computar M-1214-MP, Commack, NY, USA) set to an aperture setting of f5 (unless otherwise stated) was used in the scanner. Reference scans were completed on a 1 L PETE jar containing matching tank solution held by a custom holder in the ring support, at the longest shutter exposure time possible (without inducing camera pixel saturation) and the lowest gain setting. Data scans were acquired at the same camera settings as the reference scan on the absorbing solutions, scattering solutions, and gelatin phantoms. Reconstructed 3D linear optical attenuation data sets were obtained using the natural logarithmic ratio of the data and reference scans (note that a dark field image is acquired and subtracted from each scan) through use of the VistaRecon software. A Feldkamp filtered back-projection reconstruction algorithm with a Hamming filter (Feldkamp *et al* 1984) was used in the image reconstruction. A standard 4 x 4 pixel binning routine was applied to the projection data by the software for reconstruction to 0.5 mm cubic voxel resolution, while 8 x 8 pixel binning was employed for 1.0 mm cubic voxel resolution. The default resolution for scanner characterization data was 0.5 mm, unless otherwise specified.

The matching tank solution for the scanner consisted of 10-12 wt% propylene glycol-water mixtures, the refractive index (RI) of which (1.344-1.346  $\pm$  0.001 at 590 nm) was monitored over time at room temperature ( $21 \pm 1$  °C) using a handheld refractometer with a central

measurement wavelength of 589 nm ( $r^2$  mini refractometer, Reichert Analytical Instruments, Depew, NY, USA). Temperature measurements were taken using a digital temperature probe (TM99A-NA Digital Thermometer, Nuclear Associates, Carle Place, NY, USA).

Note that one of the primary goals for using a cone beam charge-coupled-device (CCD)-based configuration is to improve the scan time over that of the point-detection schemes. For an aperture setting of f5 and a maximum shutter speed of 133.2 ms (gain set to zero) under 590 nm illumination, reference and data scans are acquired in just over 4 minutes each and a 12.8 x 12.8 x 12.8 cm<sup>3</sup> sized volume image of 0.5 mm cubic voxel size resolution is reconstructed in 10 minutes, using a standard desktop computer. The hardware and software configurations for this total imaging time under 20 minutes are not optimized. While it is outside the scope of this paper, further imaging time reduction is certainly achievable.

To test the performance of the cone beam scanner under scattering conditions, scattering solutions and gelatin phantoms were employed that allowed the characterization of the range of optical measurement integrity and accompanying performance limitations of the scanner to be separated from the uncertainties in dose delivery and gel dosimetry. Previous studies employing calibration scattering solutions and phantoms for optical CT scanner characterization (Bosi *et al* 2007, Bosi *et al* 2009) have involved the use of a turbid colloidal suspension of Dettol<sup>TM</sup> antiseptic (Reckitt Benckiser, West Ryde, Australia) in water-gelatin mixtures. In this work, an alternative acrylic latex scattering emulsion (Duramax B-1000, Rohm & Haas, Philadelphia, PA, USA) was identified for use. This scattering emulsion can be diluted by water, and maintains uniformity and stability of colloidal distribution in heated, refrigerated, and room temperature formulations of water, propylene glycol and gelatin. These features were important for the preparation of scattering solutions and gel phantoms that mimic the scattering and refractive index properties of typical Fricke-xylenol and polymer gel-based dosimeter recipes. The

Duramax-based solution is similar in performance to the Dettol-based solution prepared by Bosi *et al*, but was preferred as (1) the solution comes pre-formulated as an emulsion and only requires a simple dilution step to achieve different concentrations with high accuracy, (2) the particle size distribution does not vary during preparation, whereas Dettol produces a variable particle size distribution each time it is mixed with water, and (3) acrylic has a similar refractive index to the acrylamide monomer commonly used in polymer gel dosimetry.

Calibration scattering solutions were prepared through addition of small amounts of Duramax B-1000 to mixtures of 12 wt% propylene glycol (Cat.No.134368, Sigma-Aldrich Ltd, Oakville, Canada) in water. These solutions were then poured into 1 L PETE containers and stored at room temperature prior to optical measurement. A diluted sample of the Duramax B-1000 acrylic latex emulsion was independently assessed using a Fritsch particle sizer (Fritsch GmbH, Germany) and the particle size distribution determined to have a mean particle size of  $370 \pm 140 \mu\text{m}$ , which is on the same order as the size of polymerized particles in polymer gel dosimeters (Maryanski *et al* 1996b, Oldham *et al* 2003). The refractive index of the calibration scattering solutions was verified at a room temperature ( $21 \pm 1^\circ\text{C}$ ) using the  $r^2$  mini refractometer over a period of 16 months and found to be consistent within a measurement uncertainty of  $\pm 0.001$ .

A gelatin phantom was prepared by adding 5 wt% gelatin (300 bloom Type A porcine gelatin, Cat.No.G2500, Sigma-Aldrich Ltd) to room temperature distilled, de-ionized water. The mixture was allowed to swell for 15 minutes, and then heated to  $45^\circ\text{C}$  for 5 minutes to dissolve the gelatin. The heated solution was poured into a 1 L PETE container and placed in the refrigerator overnight to set the gelatin. The gelatin-filled container was brought to room temperature conditions prior to optical scanning.

To test the performance of the cone beam scanner under absorbing conditions, calibration absorbing solutions were prepared by adding small amounts of patent blue violet dye (Cat.No.198218, Sigma-Aldrich Ltd) to mixtures of 12 wt% propylene glycol in water, poured into 1 L PETE containers and stored at room temperature prior to optical scanning.

Line profiles and regions of interest (ROI) in absorbing, scattering and gelatin phantom projection data and optical CT reconstructed 3D data sets were evaluated using ImageJ (National Institute of Health, Bethesda, MD, USA), Microview 2.1.2 (GE Healthcare, United Kingdom) or MatLab (Mathworks, Newark, NJ, USA) software.

### **2.3.2 Cone Beam Geometry Validation**

The first step in acquiring a basic understanding of cone beam optical imaging is to validate the geometry under optically absorbing conditions. The typical scenario in x-ray cone beam computed tomography (CBCT) involves the measurement of the x-rays along ray paths projected in a 3D solid angle from a point source (Kak and Slaney 1998). Optical CT imaging with a cone beam optical scanner, on the other hand, employs projection images acquired using a digital camera with a finite detector area from diffuse light source illumination through a 3D semi-transparent (or attenuating) volume. The validity of the cone beam reconstruction algorithm in this scenario is therefore not inherently obvious. Referring to figure 2.3 (which is not drawn to scale for purpose of illustration), there is a small ray bundle of light centered on each primary ray path from the diffuse light source to the CCD detector chip that is actually focused through the camera lens onto each CCD pixel. The size of this ray bundle (the edges of which are termed ‘marginal’ rays) is affected by properties of the lens such as focal length, aperture settings within the lens (i.e. the f-stop), the distances between the light source, imaging volume and detector, the depth of field, etc. In the ideal scenario, the signal acquired at each detector pixel would come from light attenuated along a single cone beam geometry ray path through the object space.

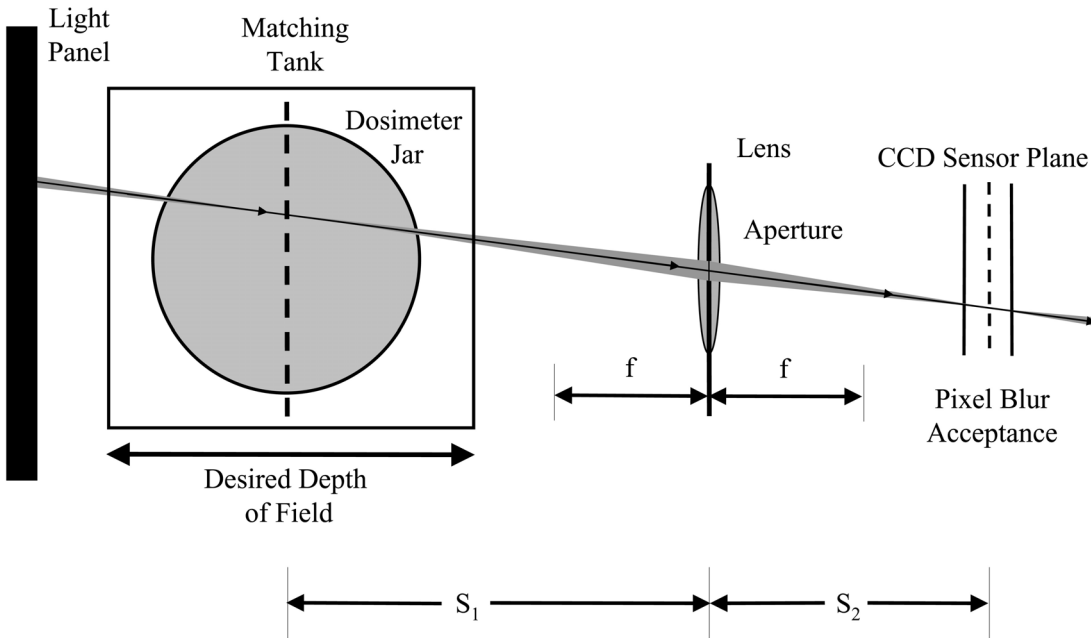


**Figure 2.3:** Illustration of the imaging optics for the cone beam CCD-based configuration (not to scale).

However, while the acceptance of a single ray path at each detector pixel is not a practical reality, the lens-based camera approximately adheres to the cone beam geometry by only focusing light that has travelled in a tight ray bundle along cone beam primary ray path geometry to the CCD detector. This approximation becomes less valid as the ‘angle of acceptance’ of light reaching each point (or pixel) in the detector array increases. That is, individual ray bundles can be thought of as occupying a volume ‘light cone’ with the base of the cone at the light source and vertex ‘angle of acceptance’ at the corresponding detector pixel. The approximation to cone beam geometry can be given a mathematical description (Marks *et al* 2001), and depends on the camera settings being optimized toward a small acceptance angle light cone, such that the base of the cone decreases toward a point source of light and the volume of the cone toward encompassing a single cone beam ray path.

The thin lens law states that a given object plane will be in focus at the CCD sensor plane when  $(S_1)^{-1} + (S_2)^{-1} = f^{-1}$ , where  $S_1, S_2 \geq f$ . For a given pixel area and camera lens setting, there is a detector-to-object distance range for which points on the cone beam primary ray path through the object space in that range will focus to a finite sized point ‘blur’ accepted to the area of a single pixel on the CCD sensor image plane, a range that is termed the depth of field. Outside that range, points on the primary ray path will be imaged as a blurred circle on the image plane, termed the ‘circle of confusion’. Therefore, it is important to maintain a depth of field that covers the entire imaged volume to satisfy the cone beam geometry, otherwise the image acquired by the camera will be blurred, and hence there will be a degradation of spatial information. For a given source-detector geometry and camera lens, the f-stop setting influences several variables. High f-stops can result in diffraction-related aberrations and low f-stops may allow spherical aberrations from the lens to affect the projection image (for example, see (Hillier 1949). Raising the f-stop narrows the ray bundle (or light cone angle of acceptance), but also reduces the collection efficiency of the lens. This necessitates an increased shutter time and raised camera gain, which can increase scan time and noise level respectively of the scan measurements. To investigate the balance of these parameters further and verify the assertion of cone beam geometry, some basic experiments were performed on the Vista scanner.

The effect of camera lens aperture (f-stop) setting on cone beam geometry was investigated through analysis of transmission projection images taken at 590 nm of a 1 L PETE jar containing 12 wt% propylene glycol-water matching tank solution. Images were acquired over the range of camera lens f-stops under open field illumination (figure 2.4a) and with a single 1 mm diameter pinhole blocker (machined in 1/32” matte-coated aluminum sheet) inserted at the light source side of the matching tank (figure 2.4b). The peak ‘centre pixel’ intensity with the pinhole blocker in place (i.e. the intensity value at the centre pixel in the circular area of

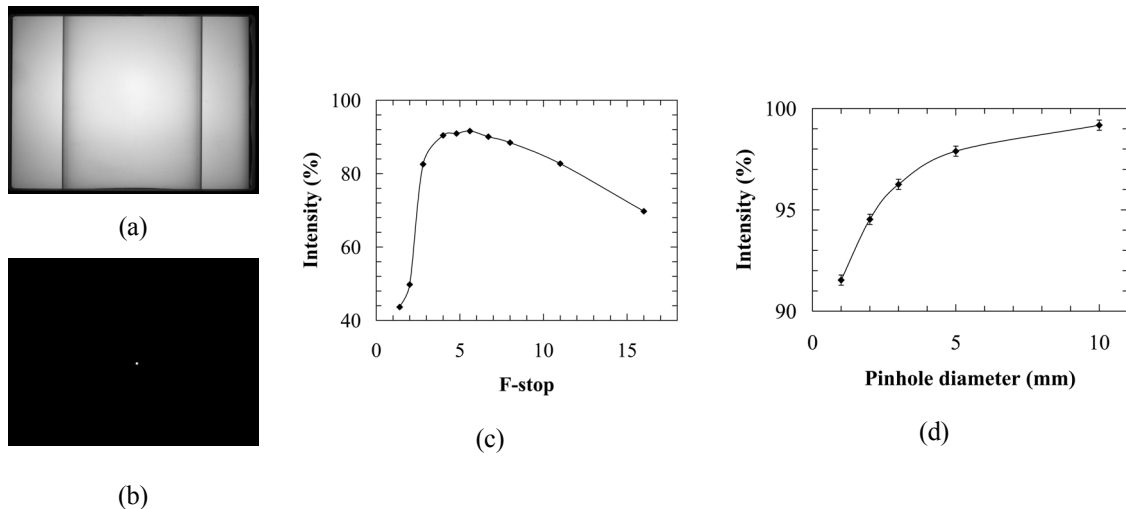


**Figure 2.4:** (a) Open field and (b) 1 mm pinhole blocker projection images from the Vista scanner with a 1 L PETE jar in the matching tank. Pinhole blocker ‘centre pixel’ intensity is extracted from the ‘blocked’ projection image and expressed as a percentage of open field intensity at the same pixel from the open field projection image for: (c) a 1 mm diameter pinhole at varied camera aperture, and (d) for varied diameter single pinholes at f5 with the single pinhole beam pass insert placed at the light source side of the matching tank. Lines are included to aid the eye. Some of the error bars are smaller than symbol size.

illuminated detector pixels) was compared to the light intensity recorded at the same ‘centre pixel’ location under open field illumination. The percentage of centre pixel pinhole-to-open-field intensity reaches a maximum value above 90% over a relatively broad f-stop range of f4-f6.7 (figure 2.4c).

Figure 2.4d shows results from a second set of transmission projection images taken at 590 nm of a 1 L PETE jar containing the same 12 wt% propylene glycol-water solution as used in the Vista scanner. In this experiment, images were acquired under open field illumination and for single pinhole blockers of varying diameter inserted at the light source side of the matching tank at an f-stop of f5. The centre pixel intensity through the pinhole blocker for pinhole diameters in the range of 1-10 mm ranged from approximately 91% to 99%+ of the value for the same pixel under open field illumination. That is, over 99% of the light received at the detector pixel falls

within a light cone volume described by a cone vertex angle of  $\sim 0.9^\circ$  at the detector pixel and 10 mm diameter base at the light source, and approximately 90% of that light originates from an even more restricted vertex angle of  $\sim 0.1^\circ$ , as calculated using the pinhole diameter and the pinhole blocker-to-detector distance of  $66.0 \pm 0.1$  cm.

The results in figure 2.4 were extended to two dimensions by using the same scanner setup and replacing the single pinhole grid blocker with a pinhole grid blocker machined with 2 mm diameter pinholes spaced 11 mm apart in 1/32" matte-coated aluminum sheet and inserted at the light source side of the matching tank. The objective of the pinhole grid blocker experiment was to validate the cone beam geometry at regularly spaced points over the full two-dimensional area of the projection at the chosen f-stop of f5. This blocker grid (or beam pass array) approach has previously been used in the evaluation of optical CT projection images (Olding *et al* 2009, Jordan and Battista 2009a), but has been extended to a full two-dimensional analysis in this work. Open field (figure 2.5a) and pinhole grid projection images (figure 2.5b) were acquired, and each pinhole ‘centre pixel’ intensity was extracted from the ‘blocked’ projection image and expressed as a percentage of open field intensity at the same pixel from the open field projection image. A bi-cubic spline function in MatLab was used to interpolate between measured grid points to obtain a 2D percentage map for the full projection image (figure 2.5c). The reported values in the map then indicate how much of the light intensity recorded at each pixel in the detector travels in the ‘tight ray bundle’ or light cone volume that is centered on the primary cone beam ray path, and defined by the 2 mm diameter pinhole opening and the pinhole blocker-to-detector distance of  $66.0 \pm 0.1$  cm. Hence, this percentage map represents a measure of adherence to cone beam geometry across the full 2D projection image. The 2 mm grid measurement was then repeated, replacing the jar containing matching tank solution with two jars containing a 12 wt% propylene-glycol mixture and 0.74 mg/L and 1.48 mg/L of patent blue violet absorbing dye respectively.

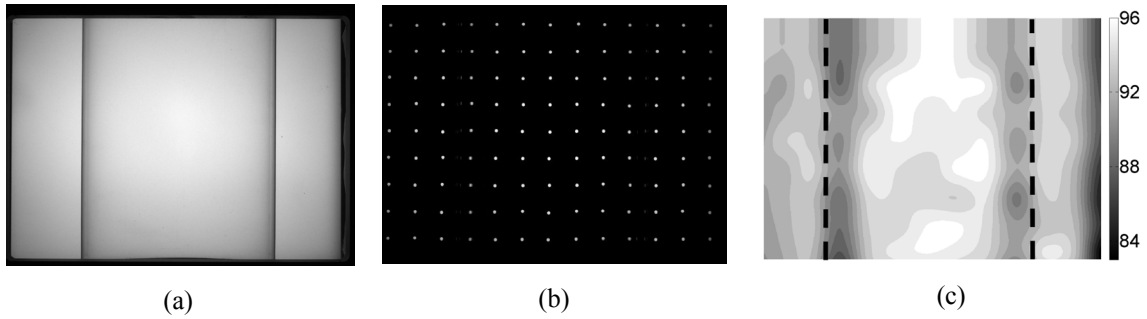


**Figure 2.5:** (a) Open field and (b) pinhole grid projection images from the Vista scanner with a 1 L PETE jar in the matching tank. Each pinhole blocker ‘centre pixel’ intensity is extracted from the ‘blocked’ projection image and expressed as a percentage of open field intensity at the same pixel from the open field projection image. These values were used to calculate (c) an interpolated percentage map over the full 2D region. The dashed lines show the approximate location of the jar edges from the projection data.

Percentage maps were obtained as before and found to be approximately equivalent to that obtained for the matching tank fluid-filled jar.

### 2.3.3 Spatial Resolution

The ability of an imaging system to distinguish between two closely spaced objects (i.e. the spatial resolution of the scanner) can be described by the modulation transfer function (MTF), which is a measure of spatial frequency response in terms of contrast at a given spatial frequency relative to a well-defined low frequency. Reconstructed optical CT image MTFs have previously been evaluated for a laser-based and a parallel-beam CCD scanner using the wire method (Oldham and Kim 2004, Doran *et al* 2004). In their investigations, a thin wire was scanned and the line spread function of the reconstructed CT image was determined, with a de-convolution correction accounting for the finite wire diameter. In-depth studies evaluating the MTF of the actual (irradiated) polymer gel with an MRI system have also been completed (Berg *et al* 2004, Bayreder *et al* 2008). Projection MTFs have also been obtained for the parallel beam CCD system

using a high quality test target with an MTF sinusoidal test pattern (from Edmund Optics) located at different detector-target distances (Krstajic and Doran 2007).

In order to establish the spatial resolution and depth of field of the Vista scanner, an imaging test target (the 2003 Koren lens test chart) similar to the high quality test target used by Krstajic *et al* (2007) was obtained from [www.normankoren.com](http://www.normankoren.com). Projection images were taken at 590 nm with the test target positioned in the matching tank fluid along the optical axis at the front, center and rear of the matching tank (camera-to-target distances of  $49.9 \pm 0.1$  cm,  $57.5 \pm 0.1$  cm and  $65.1 \pm 0.1$  cm respectively). Projection MTFs were then derived from the sinusoidal MTF test pattern data in the image (figure 2.6). A projection image and calculated MTF were also obtained for the test target inserted at the rear of the tank as before, but with a 1L PETE jar containing a 5 wt% gelatin-water mixture inserted in the matching bath. In this case, the MTF decreased to 50% at a spacing of approximately 1.6 line pairs  $\text{mm}^{-1}$ . This is slightly more than a 10% reduction in projection image resolution from the previous experiment, which showed the MTF decreasing to 50% at approximately 1.8 line pairs  $\text{mm}^{-1}$  (at the rear of the tank, see figure

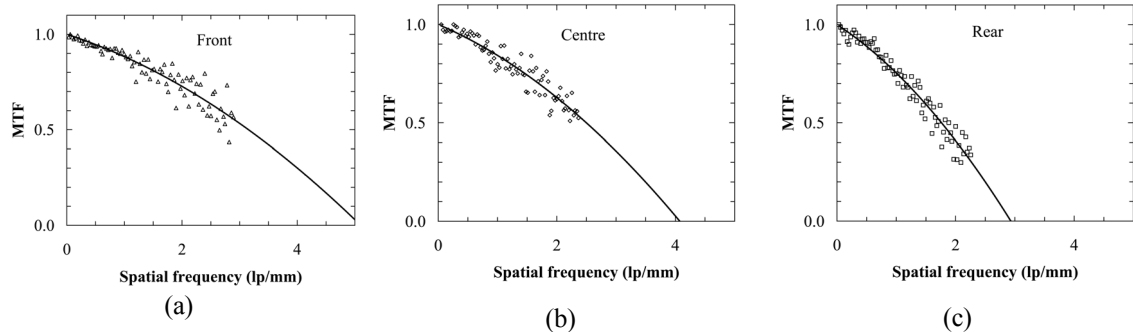


**Figure 2.6:** Modulation transfer function of the projection data obtained from imaging a sinusoidal test pattern on the 2003 Koren lens test chart ([www.normankoren.com](http://www.normankoren.com)) located along the central axis at the (a) front, (b) centre and (c) rear of the Vista scanner matching tank, referenced against the camera position. The MTF for each data set was fit with a third-order polynomial to aid the eye. Error bars are smaller than the symbol size.

2.6c). The scatter in the measured data reported in figure 2.6 can partially be attributed to the print quality of the test target.

The depth of field criterion for satisfying the cone beam geometry condition (Kak and Slaney 1998) of the scanner was set to be the axial range (distance from detector to object plane) over which the image contrast of a square wave pattern at 2 line pairs  $\text{mm}^{-1}$  on the 2003 Koren lens test chart was 50% of the maximum imaged contrast at the lowest frequency line spacing on the test chart. The necessary data were acquired by imaging the test target at 590 nm over a range of f-stops in the matching tank fluid at the front and rear of the tank. An MTF of 50% (or more) at 2 line pairs  $\text{mm}^{-1}$  was obtained from the square wave pattern image data for f-stops of f4 or greater.

#### 2.3.4 Spatial Distortion

The effect of index of refraction mismatch on geometric distortion of optical CT reconstructed images was investigated through use of a custom in-house built pin phantom. The phantom consisted of a spiral pattern of stainless steel pins supported by an acrylic frame similar in concept to the needle phantom employed by Oldham and Kim (2004), but designed to be inserted into a standard 1 L PETE dosimeter jar (see figure 2.7). In this way, the index of refraction, scattering and absorbing properties of the media within the jar could be easily adjusted, to explore their individual effects on the imaging of pin positions.

Two different matching tank solution formulations based on propylene glycol and glycerol were investigated. Both of these chemicals have previously been used for index matching, depending on the dosimeter being imaged. Glycerol has the advantage of a wider refractive index range for imaging high refractive index dosimeters, while propylene glycol is generally preferred as it is not degraded by biological activity over time. For the propylene glycol trial, the tank media was kept at 10 wt% propylene glycol in water, corresponding to an optical

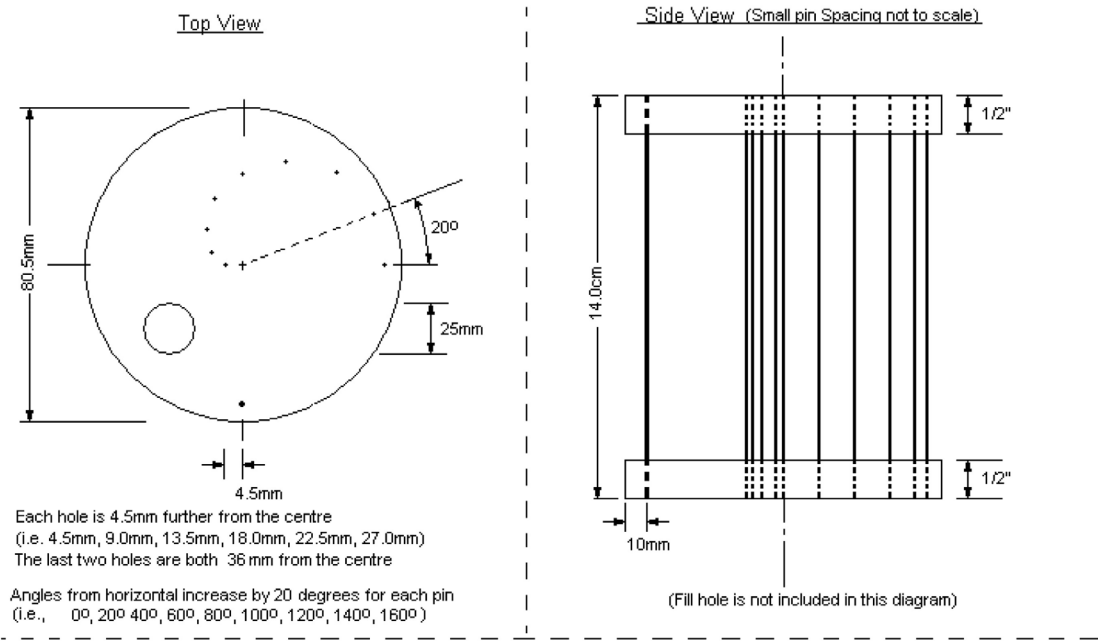


**Figure 2.7:** A pin phantom consisting of a series of stainless steel pins supported by an acrylic frame, designed to be inserted into a standard 1 L PETE dosimeter jar.

index of refraction of  $1.344 \pm 0.001$  at  $21^\circ\text{C}$ , while the jar concentration was adjusted from 0-12 wt% propylene glycol in water. A 3D image of the pin phantom was reconstructed from optical CT measurements for each concentration. Similar measurements were performed for the glycerol trial, with the exception that the range of jar concentrations corresponded to 0-20% wt% glycerol. The concentration of the tank media for the glycerol trial was 19.4 wt% in water, corresponding to an optical index of refraction of  $1.356 \pm 0.001$  at  $21^\circ\text{C}$ . Measurements were acquired for the distance between the central pin positioned at the scanner axis of rotation and each of the other 8 pins in the phantom using: (1) the optical CT volume image data and (2) vernier calipers, which are considered to be accurate to  $\pm 0.1$  mm. The percentage radial compression was then calculated from the ratio of optical CT-measured distance to vernier caliper-measured distance for

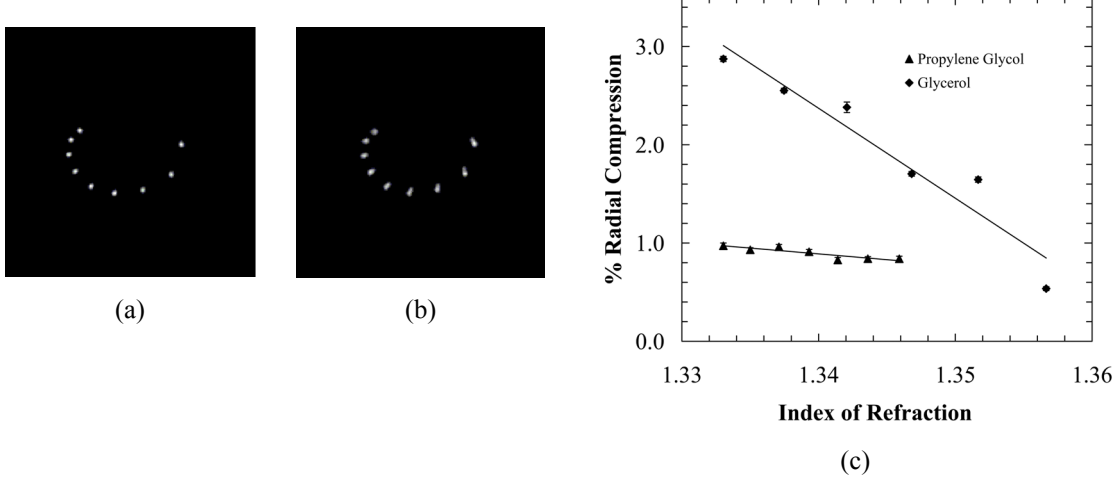


**Figure 2.8:** (a), (b) 2D slices of 3D optical CT images of the pin phantom. One image (b) exhibits the case of mismatch in index, while the other (a) shows the matching case. (c) Mean radial compression of pin positions in cone beam optical CT measurements at various jar concentrations of propylene glycol or glycerol and water. For most of the data points the errors bars are smaller than symbol size.

each of the 8 pin separations for each slice in the optical CT data set, obtaining an average percentage radial compression for each pin (a total of 800 measurements in the optical CT image volume) relative to the ‘true’ vernier caliper measurement.

Matching the bath and jar media refractive indices reduces reconstructed image blurring, as seen through a visual comparison of the reconstructed image slices shown in figures 2.8a and 2.8b. In the matched condition, the average radial compression under room temperature conditions was found to be  $0.54 \pm 0.02\%$  for glycerol and  $0.84 \pm 0.02\%$  for propylene glycol, corresponding to geometric distortions in the range of 0.2-0.3 mm. The average radial distortions for the full range of tank media concentrations are indicated in figure 2.8c. The maximum radial compression observed in all trials was 4.5% at the third pin away from the centre pin.

### 2.3.5 Scanner Scatter Measurement

The starting point for assessment of scanner scatter measurement linearity was to acquire reference and data scan projection data sets of the matching tank containing 12 wt% propylene glycol-water mixture in the Vista scanner at 633 nm. Three 8 cm diameter, 1 cm high cylindrical regions of interest (ROI) were evaluated at the top, middle and bottom of the reconstructed volume (figure 2.9a) and found to have values of  $0.000 \pm 0.003 \text{ cm}^{-1}$ ,  $0.0000 \pm 0.0005 \text{ cm}^{-1}$ , and  $0.000 \pm 0.001 \text{ cm}^{-1}$  respectively. A second projection data set was then acquired with a 5 wt% gelatin in water-filled 1 L PETE jar in the matching tank. Three 8 cm diameter, 1 cm high ROI centered in the PETE jar near the top, middle and bottom of the reconstructed volume were evaluated as before, and found to have mean attenuation values of  $0.04 \pm 0.01 \text{ cm}^{-1}$ ,  $0.044 \pm 0.001 \text{ cm}^{-1}$ , and  $0.045 \pm 0.006 \text{ cm}^{-1}$  respectively (figure 2.9b).

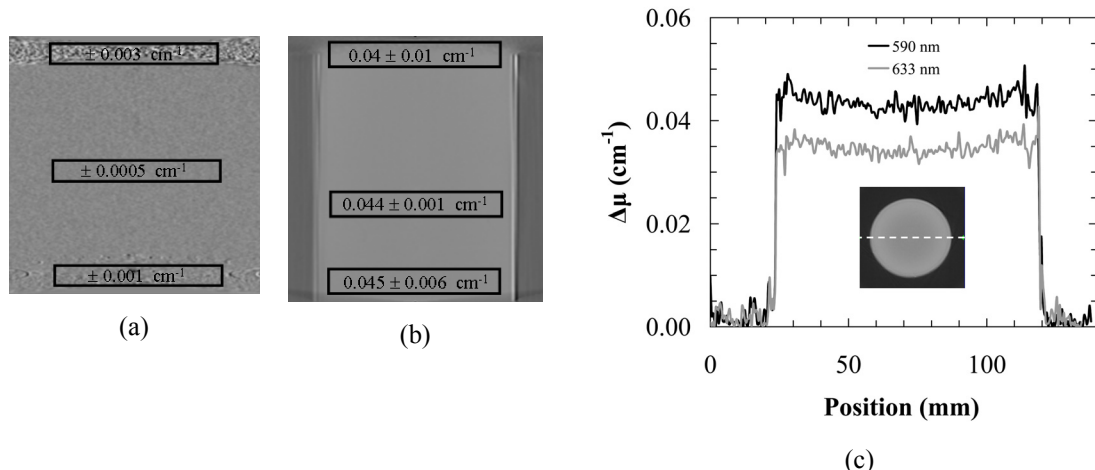


**Figure 2.9:** Reconstructed volume cross-sections showing standard deviation in mean attenuation for selected cylindrical regions of interest (ROI) in (a) the fluid-filled matching tank, with (b) a 5 wt% gelatin-in-water-filled 1 L PETE jar inserted in the fluid-filled tank. High uncertainty regions are observed at the top and bottom of the volume in both cases. The results in (c) show reconstructed attenuation profiles through a 5 wt% gelatin-in-water-filled 1 L PETE jar imaged at 590 nm and 633 nm.

Most of the dosimeters used in gel dosimetry have a gelatin or agarose matrix used to fix the dose data spatially after irradiation. Hence, imaging a gelatin ‘blank’ can be thought of as the next step beyond imaging a PETE jar containing matching tank solution. Profiles through the reconstructed optical CT image of the 5wt% gelatin-in-water-filled 1 L PETE jar phantom (figure 2.9c) under 590 nm and 633 nm illumination reveal additional data perturbation seen as cupping in the reconstructed data when the scattering media is introduced.

To further investigate the limitations imposed by cupping and other effects arising from optical cone beam readout of scattering polymer gel dosimeters, a series of calibration scattering solutions in 1 L PETE jars were then imaged using the Vista scanner. Small portions of the varied concentration scattering solutions were also separated into 10 mm polymethyl-methacrylate (PMMA) cuvettes and evaluated using an Ultrospec 1000 UV/visible spectrophotometer (Biochrom Ltd, Cambridge UK). As the spectrophotometer provides better than 0.5-1.0% accuracy in transmission measurement, the spectrophotometer results were considered to be a ‘true’ assessment of calibration solution attenuation. Figure 2.10a shows that spectrophotometer-measured optical attenuation values obtained under room temperature conditions at 633 nm are linear with scatter concentration in the range of 0.01-0.08 g/L. The measurements showed reasonable long term stability in mean optical attenuation coefficient and refractive index over 16 months of measurement. However, when the Vista scanner is used to image the full set of calibration scattering solutions in 1 L PETE jars (from which the 10 mm cuvettes were filled), the measured mean optical attenuation values in a 8 cm diameter, 10 cm high ROI centered in the jar volume image clearly depart in a nonlinear fashion from the corresponding spectrophotometer values over the full range of jar scatter concentration (figure 2.10a). The variation in mean ROI attenuation value between the three scan trials completed at different times in the sixteen month period ranged from 2-6% for the different

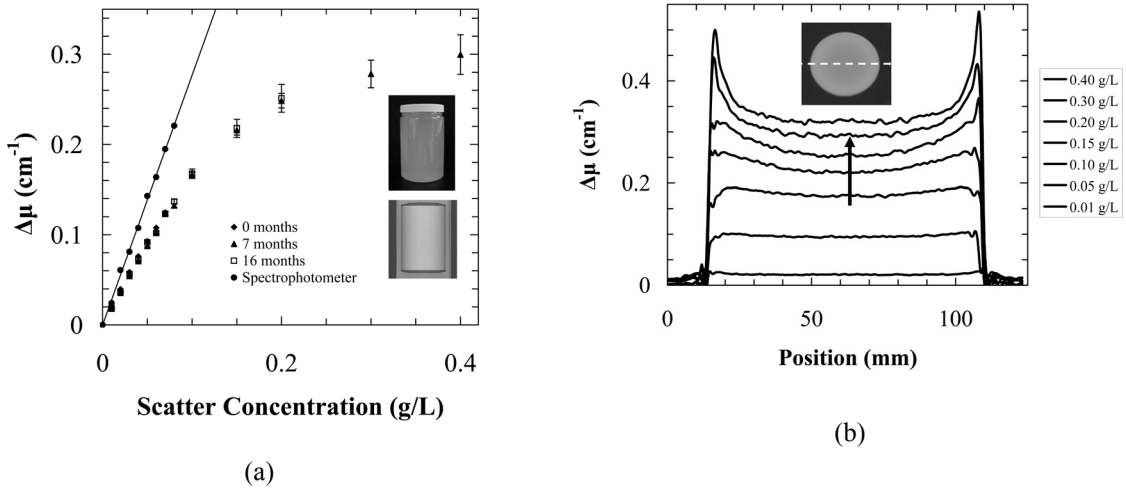


**Figure 2.10:** (a) Mean attenuation coefficients of uniform acrylic scattering solutions in 1 L PETE jars (top right inset) from the Vista scanner, measured from a 8 cm diameter, 10 cm high cylindrical ROI in the image data (bottom right inset) and spectrophotometer measurements using 10 mm PMMA cuvettes. A linear fit to the spectrophotometer data is shown in the plot. (b) Reconstructed (1.0 mm cubic voxel resolution) profiles across the scattering solutions (arrow in direction of increasing scatter concentration).

concentrations. Figure 2.10b shows profiles across 1.0 mm cubic voxel resolution reconstructed optical CT volume images of the calibration scattering solutions, indicating an increase in cupping of the data with scatter concentration. The profiles are reconstructed at a lower voxel resolution than the data in figure 2.10a in order to observe underlying artifacts with reduced noise.

### 2.3.6 Scanner Absorption Measurement

While the dose contrast mechanism in polymer gel-based dosimeters is scattering of visible light, Fricke-based dosimeters contrast dose by light absorption. To investigate the performance of the Vista scanner under absorbing conditions, a series of calibration absorbing solutions in 1 L PETE jars were imaged using the Vista scanner. Small quantities of the varied concentration absorbing solutions were also separated into 10 mm PMMA cuvettes for spectrophotometer measurement.

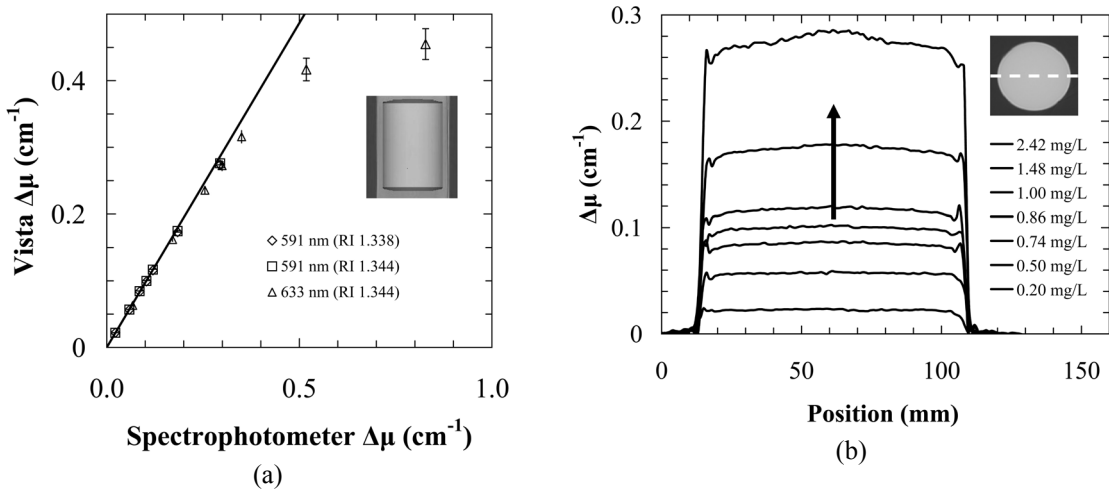


**Figure 2.11:** (a) Comparison of mean attenuation values (ROI as in figure 10) from 1 L PETE jars and 10 mm PMMA cuvettes filled with uniform absorbing dye solutions, 1) at two wavelengths and two different matching bath refractive indices (RI) using the cone beam Vista scanner, and 2) at 590 nm and 633 nm using a UltraSpec 1000 UV-Vis spectrophotometer. A linear fit to the 590 nm (RI 1.344) data in the range of 0.0-0.2 cm<sup>-1</sup> is shown in this plot. (b) Reconstructed (1.0 mm cubic voxel resolution) profiles across the uniform absorbing solutions imaged at 590 nm and a refractive index of 1.344 (the arrow indicates the direction of increasing dye concentration).

In contrast to the scattering solutions, the mean attenuation measurements of absorbing solutions from the Vista scanner (from the same ROI as in figure 2.10a) can be fit to a linear relationship against spectrophotometer measurement under both measurement wavelengths of 590 nm and 633 nm (figure 2.11a). The slope of the fit is slightly less than unity at  $0.973 \pm 0.004$  (with an  $R^2$  value of 0.9994) for the 590 nm (RI 1.344) data in the range of 0.0-0.2 cm<sup>-1</sup>. A linear fit to the 590 nm (RI 1.338) data over the same attenuation range was found to have only a slightly lower slope at  $0.967 \pm 0.004$ . The slope was not determined from the 633 nm data, as there were only two data points falling in the same 0.0-0.2 cm<sup>-1</sup> attenuation range. At mean jar attenuations greater than roughly 0.2 cm<sup>-1</sup>, the Vista measurement starts to depart from linearity. A bowing artifact is observed in the reconstructed profiles of the absorbing solutions (figure 11b); this becomes more pronounced at higher absorption values.

Mean attenuation values are recorded in table 2.1 for a representative 25 mm diameter ROI slice centered on the jar axis in the reconstructed volume of a 1.48 mg/L absorbing solution. The recorded values are from 5 different scans acquired over a period of time spanning 6 hours each on two separate days (designated trials 1 and 2) with careful attention to scanner warm-up time, as well as keeping the light source on throughout both scans and using the optional Vista software projection normalization region. Same day and inter-day measurement precisions better than 0.1% and 1.0% are indicated for this absorbing solution concentration/attenuation.

To determine the mean-to-standard deviation signal-to-noise ratio (SNR) for varied concentrations of scattering and absorbing media-filled 1 L PETE jars in the Vista scanner, a 5 x 5 x 1 voxels<sup>3</sup> (i.e. 25 voxels) SNR-ROI was set for evaluation of both image resolutions. Each data point shown in figure 2.12a represents the average of 9 SNR-ROI measurements at different positions in the jar region of the optical CT image (three positions at each of three heights within the cylindrical ROI used in figure 2.10a). The 0.5 mm cubic voxel resolution data were acquired under 633 nm illumination, and the 1 mm cubic voxel resolution data under 590 nm illumination.

**Table 2.1:** Scanner Measurement Precision

Scan #	Trial 1 mean attenuation (cm <sup>-1</sup> )	Trial 2 mean attenuation (cm <sup>-1</sup> )
1	0.1743 ± 0.0022	0.1730 ± 0.0022
2	0.1742 ± 0.0022	0.1727 ± 0.0023
3	0.1742 ± 0.0022	0.1728 ± 0.0023
4	0.1742 ± 0.0022	0.1728 ± 0.0022
5	0.1741 ± 0.0022	0.1729 ± 0.0022

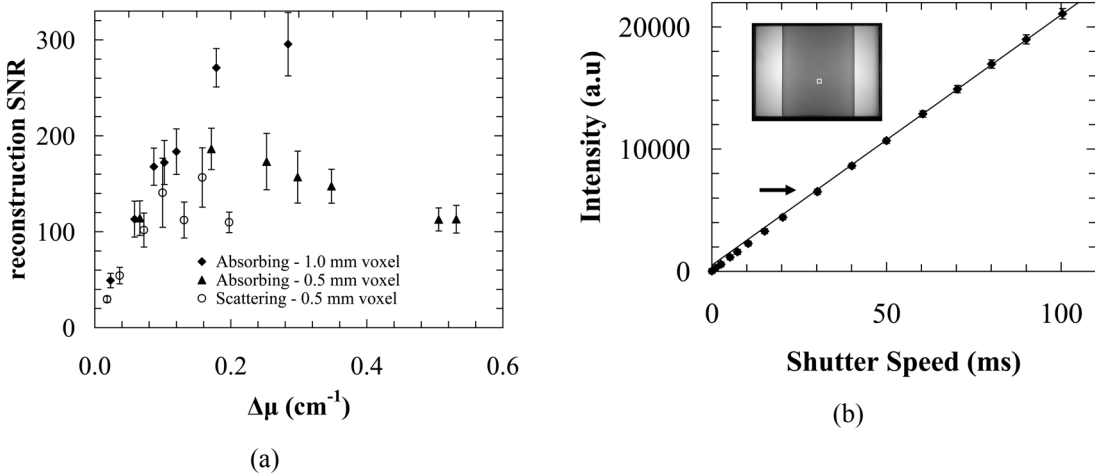


**Figure 2.12:** (a) Reconstructed mean to standard deviation signal to noise ratio for absorbing and scattering media-filled 1 L PETE jars imaged with the Vista scanner. Each data point represents the average of 9 measurements from a  $5 \times 5 \times 1$  voxel<sup>3</sup> ROI located at different positions in the jar region of the optical CT image. (b) Camera pixel response linearity for a  $20 \times 20$  pixel area in the projection image of a 0.74 mg/L absorbing solution. Some of the error bars are smaller than the symbol size. A linear fit to the data above 10000 au is shown in the plot. The arrow indicates the approximate point of departure from linearity.

The mean transmitted intensity value within a  $20 \times 20$  pixel area at a representative location in the projection image of a 0.74 mg/L absorbing solution (shown in figure 2.12b) was recorded over a range of camera shutter speeds under 590 nm illumination at f5 (figure 2.12b). A departure from linearity is observed at an intensity of  $\sim 6500$  arbitrary units (au), which is approximately 10% of the camera full scale intensity (65536 au).

## 2.4 Discussion

### 2.4.1 Cone Beam Geometry Validation

The results of the single point measurements from the cone beam CT validation experiments (figure 2.4c) suggest that there is some flexibility in the choice of camera lens aperture (f-stop) to satisfy the cone beam geometry condition in the imaged object space of the Vista scanner. A relatively broad range of f-stops from f4-f6.7 could be used. An f-stop of f5 was selected as the

default setting for the scanner in all subsequent imaging. This f-stop was deemed to be a good compromise between reasonable light collection efficiency and an appropriate depth of field covering the entire matching tank measurement volume. A rapid fall-off in the ratio of centre pixel pinhole-to-open-field intensity is observed for f-stops decreasing below f4, due to the fact that the depth of field does not fully cover the matching tank measurement volume, and moves outside the condition of cone beam geometry. Above f6.7, the ratio of centre pixel pinhole-to-open-field intensity decreases more slowly, but the light collection efficiency at the CCD detector is very low, causing a significant decrease in SNR (with a necessary increase in camera gain).

The two-dimensional evaluation of the projection image area using the 2 mm pinhole grid blocker (figure 2.5c) shows that most of the jar region in the map reaches a value near 95%. Lower values are obtained near the jar edge due to refractive index mismatch-driven re-direction of light at the matching fluid-jar wall interface. This is an unavoidable effect resulting from the use of PETE jars, which have an index of refraction of 1.575 at 590 nm. Raising the refractive index of the matching bath and gel dosimeter from the typical range of 1.34-1.36 at 590 nm and 21°C to that of PETE material is not practical, mainly due to the deleterious changes that would be required in the chemistry of the gel dosimeter in moving away from a primarily water-based formulation.

Despite this slight percentage variation within the jar region, the overall high percentage ratio of 95% indicates good conformation of the detected light to the preferred geometry within the ray path ‘light cone’ volume defined between the 2 mm diameter pinhole and each individual detector pixel. This indicates that the Vista scanner using 590 nm illumination reasonably satisfies the “narrow ray bundle” cone beam geometry description for imaging of absorbing solutions, at least up to the value of  $0.173 \pm 0.001 \text{ cm}^{-1}$  for the  $1.48 \text{ mgL}^{-1}$  patent blue violet dye solution.

### **2.4.2 Spatial Resolution**

The high resolution reconstruction capability of the Vista cone beam optical scanner has been, up to this point, assumed in the literature. The results shown in figure 2.6 now give a good basis for implementing  $0.5 \times 0.5 \times 0.5 \text{ mm}^3$  voxel size reconstruction of cone beam-imaged optically absorbing dosimeters, with a stringent requirement of a projection MTF value of 50% or greater at 2 line pairs  $\text{mm}^{-1}$  serving as the basis of this assessment (versus an MTF value of 10-20% or greater at 2 line pairs  $\text{mm}^{-1}$  discussed in other reports, for example, see Krstajic *et al*, 2007). The standard PETE dosimeter jar has a diameter of  $9.2 \pm 0.1 \text{ cm}$  and is held in position in the centre of the tank during scanning. The lowest projection image resolution will be obtained at the rear of the jar (referenced in terms of distance away from the detector), which is located 4.6 cm along the 7.6 cm total distance from the centre to the rear of the tank. Also, the MTF value decreases to 50% at an approximate line spacing of 3.2 line pairs  $\text{mm}^{-1}$  at the front of the tank, 2.5 line pairs  $\text{mm}^{-1}$  at the centre of the tank, and 1.8 line pairs  $\text{mm}^{-1}$  at the rear of the tank (see figures 2.6a-c). Given that the line spacing resolution falls off approximately linearly with distance from the front to the rear of the tank, the lowest resolution position in the PETE jar (i.e. at the rear of the jar) should then have an MTF value decreasing to 50% at approximately 2.1 line pairs  $\text{mm}^{-1}$ . This result satisfies the above criterion for imaging a optically absorbing media-filled PETE jar dosimeter positioned in the centre of the matching tank to a 0.5 mm cubic voxel resolution (at least from analysis of transmission projection images). As most absorbing gel dosimeters also exhibit optical scattering due to the gel matrix component (e.g., gelatin or agarose) used to spatially fix the dose, further reduction in spatial resolution is expected from the ‘ideal’ absorbing case due to convolution of a scatter kernel onto the transmission data. The scattering MTF result for the 5 wt% gelatin-in-water phantom indicates a slight degradation in the spatial resolution that is consistent with this assertion. However, the results from the gelatin phantom experiment still

indicate that a  $0.5 \times 0.5 \times 0.5 \text{ mm}^3$  voxel size reconstruction can be implemented for a cone beam-imaged optically absorbing, gelatin matrix-based gel dosimeter, given that the target position at the rear of the tank represents the lowest end of the spatial resolution range, and most of the imaged volume still has an MTF value greater than 50% at 2 line pairs  $\text{mm}^{-1}$ .

#### 2.4.3 Spatial Distortion

In the evaluation of geometric distortion, negligible radial distortion was expected in the case where the refractive indices of the matching tank and jar media were well-matched, but this was not the case. A small radial compression was observed (figure 2.8c), likely due to refractive index mismatch-derived distortion of light travelling through the dosimeter jar walls, and to a lesser extent, the matching tank windows. Further reduction in the radial compression can be achieved by lowering the refractive index of the tank media slightly below that of the jar media (typically by around 0.5%). Additional reduction in index beyond this point increases the spatial distortion.

Small day-to-day variations in index after matching is achieved are not deemed to be of great importance to geometric distortion throughout most of the image volume, since the average radial compression for matched tank and jar media refractive index was reported to be  $0.54 \pm 0.02\%$  for glycerol and  $0.84 \pm 0.02\%$  for propylene glycol at room temperature. This corresponds to geometric distortions in the range of 0.2-0.3 mm, which have a minimal impact on dose spatial accuracy. The worst result at the third pin had a total radial compression of  $\sim 0.6$  mm, which translates to only a single voxel shift, given that the reconstructed cubic voxel size is 0.5 mm. However, index mismatch can and does lead to problematic edge effects compromising the dosimetry near the container walls (for example, see the bottom two profiles in figure 2.11b). For this reason, regular attenuation should be given to bath-dosimeter index matching prior to imaging. On a final note, the results from this experiment are on par with previous results obtained using laser beam optical scanning system (Oldham and Kim 2004).

#### **2.4.4 Scanner Scatter Measurement**

The results in figure 2.9 indicate that the highest uncertainty region in the matching tank with and without the PETE jar was found to be at the top of the tank where there are reflections from the surface of the matching fluid solution or gelatin and the cone angle is great enough that there is reduced data coverage in the cone beam slice. In this situation of reduced data coverage, limitations in reconstruction using the cone beam algorithm are observed (Smith 1985, Kak and Slaney 1998). The region near the bottom of the tank is similar to that at the top of the tank, except that it experiences less stray light perturbation (primarily reflections from the bottoms of the jar and matching tank) than the region near top of the tank, hence has a lower standard deviation. The observed noise and artifacts are generally reduced throughout the rest of the tank.

Localized exceptions to this are stray-light derived optical artifacts along the jar axis of rotation and near the jar wall edges (Babic *et al* 2009). Reflections off the band pass filter in front of the camera lens have previously been identified as one source of stray light artifacts and are reduced by tilting the band pass filter (Jordan and Battista 2006a). Overall, the results indicate that an 8 cm diameter, 10 cm high cylindrical ROI centered in the 1 L PETE jar volume image is the best-behaved (lowest measurement uncertainty) region for future work in 3D gel dosimetry. As the outer diameter of the PETE jar is 9.2 cm and the total imaged height of the PETE jar is 13 cm, this corresponds to ~62% of the total imaged volume of the jar. This ROI still incorporates the reduced (but measurable) reflection artifact at the center of the projection area. As long as this is understood, 3D dose in this perturbed region can be correctly interpreted.

The cone beam scanner exhibits low scatter attenuation measurement accuracy compared to the ‘true’ spectrophotometer measurement (figure 2.10a), a result that is primarily due to artifacts such as cupping in the data. As there are different effects that can give rise to cupping artifact (Al Nowais and Doran 2009), careful conclusions need to be drawn on the source of the

cupping observed in figures 2.9c and 2.10b. It is likely that scatter effects are the dominant source of cupping artifact over most of the useful measurement range of the scanner. However, wall effects are also a source of cupping. A few of the profiles in figure 2.10b show evidence of incomplete cancellation near the wall, which is a source of cupping in the data.

The difference in reconstructed attenuation between the two imaging wavelengths of 590 nm and 633 nm in figure 2.9c indicates that the attenuation falls somewhere between a third order and fourth order dependence on wavelength (i.e. close to the Rayleigh approximation). This indicates that scattering is the primary mechanism of attenuation in the gelatin matrix, and consequently, that angled scatter could be at least a partial, if not the dominant contributor to the observed cupping artifact, given the diffuse light source. The degree of cupping also increases with scatter solution concentration (figure 2.10b), which is consistent with this conclusion. Lastly, cupping has previously been observed when imaging scattering volumes using the Vista scanner (for example, see Bosi et al 2007, Bosi et al 2009) and other optical CT scanners and effectively modeled as scatter perturbation (Oldham 2004, Bosi *et al* 2007, Bosi *et al* 2009). On this basis, it is safe to conclude that the major contributor to cupping artifact in cone beam optical CT imaging is angled scatter perturbation, and that this effect is the main source of the non-linear attenuation behavior shown in figure 2.10a. Since optically absorbing gel dosimeters incorporate a scattering gelatin or agarose matrix for spatial fixing of dose information, the extent to which the ‘matrix scatter’ source of uncertainty perturbs the data and limits of optical readout accuracy of absorbing gel dosimeters is critically important and will be addressed further in a later report addressing the management of stray light perturbation. The question of whether useful 3D dose information can be obtained from optically scattering dosimeters using the Vista scanner is also critical toward 3D readout of polymer gels using a cone beam optical scanner. Experimental work has been completed in this regard, and results indicate that under tightly controlled conditions cone beam

optical CT readout of small field deliveries to scattering polymer gels is feasible. These results are outside the scope of this work, however, and will be reported at a later date.

#### 2.4.5 Scanner Absorption Measurement

The near unity linear fit relationship between the 590 nm (RI 1.344) spectrophotometer and Vista scanner absorption measurements over the attenuation range of 0.0-0.2 cm<sup>-1</sup> in figure 2.11a gives good indication that the cone beam optical CT imaging provides accurate measurements of absorbing media. The fact that the slope of the data is approximately 3% below unity is mostly due to stray light perturbation, and to a lesser extent, spectral differences between the two imaging systems (Babic *et al* 2008b). One indicator of stray light perturbation in the system is the bowing artifact (Jordan and Battista 2006a), seen in the reconstructed profiles of the absorbing solutions (figure 2.11b). This effect becomes more pronounced at higher absorption values. The management of, and correction for, this and other stray light effects in cone beam optical CT imaging is a significant topic in itself, and hence will be addressed more completely in a companion paper to this work. As a side note, a slight change in the bath index from 1.344 to 1.388 under 590 nm Vista scanner illumination did not introduce a significant change in the slope of the linear fit away from that obtained for the 590 nm (RI 1.344) spectrophotometer and Vista scanner absorption measurement data (figure 2.11a). This indicates that small day-to-day variations in refractive index due to evaporation of matching tank fluid are not likely a major determinant of scanner measurement precision and accuracy throughout most of the dosimeter volume, with localized exceptions near the dosimeter jar walls, as previously mentioned.

At mean jar attenuations greater than approximately 0.3 cm<sup>-1</sup>, the relationship between Vista scanner and spectrophotometer absorption measurement significantly depart from linearity. For the 9.2 cm diameter scattering solution-filled 1 L PETE jar, this corresponds to a drop in transmission from reference to data scan through the centre of the jar to approximately 10% of the

full scale intensity in the CCD camera. This behavior is partly an effect of measurement at the lower end of the dynamic range of the camera, where pixel response to low light transmission becomes non-linear (see figure 2.12b). A quick calculation using the results from figure 12b indicates that this effect could account for 10-20% of the difference between the spectrophotometer and cone beam optical CT measured values. The rest is likely due to stray light effects, the source of which will be discussed further in the previously mentioned companion paper to this work.

Longer shutter times could be employed to raise the recorded intensity into the CCD chip, in order to avoid the non-linear behavior at the low end of the dynamic range. This is limited, however, by deleterious blooming effects from pixel saturation at the high end of the dynamic range (Krstajic and Doran 2007) in the regions outside the jar walls in the projection image. One way to extend the measurement range of the scanner to lower transmission values through the dosimeter (i.e. higher mean jar attenuation values) is to introduce absorbing dye into the matching tank fluid and increase camera shutter time and/or gain (Jordan and Battista 2009b). Another way is to employ a variable light field method described by Krstajic *et al* (2007).

Referring again to figure 2.10a, it can be noted that there was no definitive upward or downward trend in measured attenuation over the 16 months' measurement trial period. It should also be noted that more than three scans were completed for some of the jar concentrations; the 0.05 g/L and 0.10 g/L solutions in particular were scanned several more times in other characterization work. The lack of trend in the results, therefore, suggest the possibility that the variation may at least in part be due to the scan conditions, which if better controlled would yield higher measurement precision. When close attention was given to scanner warm-up time, keeping the light source on throughout both scans, and using the optional Vista software projection normalization region, the measurement variation was reduced to less than 1% inter-day precision

for a 1.48 mg/L absorbing solution, as reported in Table 2.1. The full investigation leading to the employment of these and other imaging protocols will be discussed more completely in a companion paper to this work.

Finally, the results presented in figure 2.12a indicate that a mean-to-standard deviation SNR of better than 100 is achieved in more than 60% of the jar volume image at attenuation values in the approximate range of  $0.06\text{-}0.50\text{ cm}^{-1}$  and  $0.07\text{-}0.20\text{ cm}^{-1}$  for absorbing and scattering media respectively at a 0.5 mm cubic voxel resolution. These data can be then be combined with the accuracy results obtained from the Vista scanner-spectrophotometer comparison, indicating an approximate 3% accuracy for absorbing media mean jar attenuation values of  $0.00\text{-}0.18\text{ cm}^{-1}$ . In this range, the standard deviation of the mean in-jar attenuation values was found to be on the order of 1.0-1.3%. Hence, an approximate 3-4% accuracy and SNR of 100 or greater is obtained for more than 60% of the jar volume in 0.5 mm cubic voxel resolution reconstructed optical CT images over the absorption range of  $0.06\text{-}0.18\text{ cm}^{-1}$ . The calibration scatter solution measurements, on the other hand, are nowhere near this level of accuracy over the entire range of measurement due to the observed non-linear behavior arising from angled scatter stray light perturbation (figure 2.10a).

Extending these results into gel dosimetry, a Fricke-xylenol-gelatin (FXG)-filled 1 L PETE jar dosimeter, with an absorption contrast mechanism and a low scattering gelatin matrix attenuation (which should mostly cancel out as the baseline between the reference and data scans, to be discussed further in later work), should achieve approximately the same SNR of 100 and 3-4% measurement accuracy in 60+% of the imaged dosimeter volume for mean jar attenuation coefficients in the range of  $0.06\text{-}0.18\text{ cm}^{-1}$ . The ‘dose resolution’ can then be calculated for a given FXG dosimeter sensitivity.

There are a few options available to improve the SNR at lower attenuation values. Multiple averages of each projection may possibly provide a slight improvement in the SNR, but come with the disadvantage of a longer scan time and will not remove the artifacts that mimic noise, such as refractive index mismatches, floating particles in the matching tank, scratches on the optics, etc. Post acquisition filtering of projection (sinogram) data and reconstructed images also can improve the SNR without too great negative impact in lower dose gradient regions (Jirasek and Hilts 2009), but can affect the measurement integrity at high dose gradients. Increased pre-reconstruction binning of the data in the Vista software may be another alternative. A higher pixel binning area does affect the 3D dose distribution at high dose gradients, but the tradeoff between SNR and spatial integrity of dose may be managed carefully to ensure data integrity. At present, the preferred option is to keep the same imaging parameters and as high a resolution as possible (i.e. 0.5 mm cubic voxel size) and work toward further reduction of the other artifacts that mimic noise in the measurement. To maximize the SNR, careful attention to the dose sensitivity of the gel dosimeter is required to ensure that the post-irradiation attenuation values in the dosimeter jar are as high as possible to maximize SNR, but not so high that the transmitted intensity falls below approximately 10% of full scale intensity (i.e. into the non-linear range of the detector) for any projection in the data scan.

## 2.5 Conclusions

With proper selection of camera lens aperture, the Vista cone beam CCD-based optical CT scanner conforms to the “narrow ray bundle” condition of cone beam geometry for 3D imaging of optically absorbing dosimeters. The system was demonstrated to be capable of imaging both absorbing and scattering media to a reconstructed voxel resolution of  $0.5 \times 0.5 \times 0.5 \text{ mm}^3$ . At this resolution, a reconstructed optical CT image of a standard-sized 1 L PETE jar dosimeter can be produced in less than 20 minutes total imaging and reconstruction time using a standard desktop

computer. Although the absorption measurements show evidence of stray light perturbation, the scanner was shown to be capable of imaging more than 60% of the volume within an absorbing media-filled 1 L PETE jar dosimeter to 0.5 mm cubic voxel resolution with minimal spatial distortion, an accuracy of 3-4%, and mean to standard deviation signal to noise ratio greater than 100 over an optical absorption range of  $0.06\text{-}0.18 \text{ cm}^{-1}$ . An inter-day scan precision of 1% was demonstrated for a representative absorbing media-filled 1 L PETE jar dosimeter with mean attenuation of  $0.173 \text{ cm}^{-1}$  near the upper end of the preferred range of  $0.06\text{-}0.18 \text{ cm}^{-1}$ . The absorption measurements in this work are in reasonable agreement with the benchmark  $1 \times 1 \times 1 \text{ mm}^3$  spatial resolution, 60 minutes imaging time, 3% accuracy and 1% precision criteria suggested by Oldham *et al* (2001) for comparing optical CT to the ‘gold standard’ of MRI. This indicates that cone beam optical CT is a viable option for 3D readout of absorbing gel dosimeters. Future work addressing the effects of stray light perturbation should hopefully improve the accuracy and range of cone beam optical CT absorption measurement further. In contrast, the scanner has been observed to have much more limited capability in 3D imaging of optically scattering media. Consistent with previous investigations, artifacts arising from angled scatter and other forms of stray light perturbation have been shown to compromise the accuracy of attenuation measurement over the entire volume of the scattering media-filled 1 L PETE jar dosimeter. Additional calibration, stray light reduction, or stray light correction schemes will have to be explored in order to yield improved data from cone beam optical CT imaging of optically scattering dosimeters.

## 2.6 References

- Al Nowais S and Doran S 2009 CCD-based optical CT scanning of highly attenuating phantoms. *J.Phys.: Conf.Ser.* 164 1-5.
- Babic S, Battista J and Jordan K 2008 Three-dimensional dose verification for intensity-modulated radiation therapy in the radiological physics centre head-and-neck phantom using optical computed tomography scans of ferrous xylene-orange gel dosimeters. *Int.J.Radiat.Oncol.Biol.Phys.* 70 1281-1291.
- Babic S, McNiven A, Battista J and Jordan K 2009 Three-dimensional dosimetry of small megavoltage radiation fields using radiochromic gels and optical CT scanning. *Phys.Med.Biol.* 54 2463-2481.
- Bayreder C, Schon R, Wieland M, Georg D, Moser E and Berg A 2008 The spatial resolution in dosimetry with normoxic polymer-gels investigated with the dose modulation transfer approach. *Med.Phys.* 35 1756-1769.
- Berg A, Pernkopf M, Waldhausl C, Schmidt W and Moser E 2004 High resolution MR based polymer dosimetry versus film densitometry: a systematic study based on the modulation transfer function approach. *Physics in Medicine & Biology* 49 4087-4108.
- Bosi S, Naseri P, Puran A, Davies J and Baldock C 2007 Initial investigation of a novel light-scattering gel phantom for evaluation of optical CT scanners for radiotherapy gel dosimetry. *Phys.Med.Biol.* 52 2893-2903.
- Bosi S G, Brown S, Sarabipour S, De Deene Y and Baldock C 2009 Modelling optical scattering artefacts for varying pathlength in a gel dosimeter phantom. *Phys.Med.Biol.* 54 275-283.
- DeJean P, Senden R J, McAuley K B, Rogers M and Schreiner L J 2006a Initial Experience with a commercial cone beam CT unit for polymer gel dosimetry I: optical dosimetry issues. *Journal of Physics: Conference Series* 56 179-182.
- DeJean P, Senden R J, McAuley K B, Rogers M and Schreiner L J 2006b Initial Experience with a commercial cone beam CT unit for polymer gel dosimetry II: clinical potential. *J.Phys.: Conf.Ser.* 56 183-186.
- Doran S and Krstajic N 2006 The history and principles of optical computed tomography for scanning 3-D radiation dosimeters. *J.Phys.: Conf.Ser.* 56 45-57.
- Doran S J, Koerkamp K K, Bero M A, Jenneson P, Morton E J and Gilboy W B 2001 A CCD-based optical CT scanner for high-resolution 3D imaging of radiation dose distributions: equipment specifications, optical simulations and preliminary results. *Phys.Med.Biol.* 46 3191-3213.
- Doran S J, Krstajic N, Adamovics J and Jenneson P M 2004 Optical CT scanning of PRESAGE(TM) polyurethane samples with a CCD-based readout system. *Journal of Physics: Conference Series* 3.

- Feldkamp L A, Davis L C and Kress J W 1984 Practical cone-beam algorithm. *J.Opt.Soc.Amer.* 1 612-619.
- Gore J C, Kang Y S and Schulz R J 1984 Measurement of radiation dose distributions by nuclear magnetic resonance (NMR) imaging. *Phys.Med.Biol.* 29 1189-1197.
- Gore J C, Ranade M, Maryanski M J and Schulz R J 1996 Radiation dose distributions in three dimensions from tomographic optical density scanning of polymer gels: I. Development of an optical scanner. *Phys.Med.Biol.* 41 2695-2704.
- Guan H and Gordon R 1996 Computed tomography using algebraic reconstruction techniques (ARTs) with different projection access schemes: a comparison study under practical situations. *Phys.Med.Biol.* 41 1727-1743.
- Hillier J 1949 Some remarks on the image contrast in electron microscopy and the two-component objective. *J.Bacteriol.* 57 313-317.
- Islam K T, Dempsey J F, Ranade M K, Maryanski M J and Low D A 2003 Initial evaluation of commercial optical CT-based 3D gel dosimeter. *Med.Phys.* 30 2159-2168.
- Jirasek A and Hilts M 2009 An overview of polymer gel dosimetry using x-ray CT. *J.Phys.: Conf.Ser.* 164 246-256.
- Jordan K and Battista J 2006a Linearity and image uniformity of the Vista<sup>TM</sup> optical CT scanner. *J.Phys.: Conf.Ser.* 56 217-220.
- Jordan K and Battista J 2006b Small, medium and large optical cone beam CT. *J.Phys.: Conf.Ser.* 214-216.
- Jordan K and Battista J 2009a Scatter measurements for optical cone-beam computed tomography. *J.Phys.: Conf.Ser.* 164 159-163.
- Jordan K and Battista J R 2009b A stable black-refractive-index-matching liquid for optical CT scanning of hydrogels. *J.Phys.: Conf.Ser.* 164 290-293.
- Kak A C and Slaney M 1998 *Principles of Computerized Tomographic Imaging*. Philadelphia: Society for Industrial and Applied Mathematics. 107
- Kelly B G, Jordan K J and Battista J J 1998 Optical CT reconstruction of 3D dose distributions using the ferrous- benzoic-xylenol (FBX) gel dosimeter. *Med.Phys.* 25 1741-1750.
- Krstajic N and Doran S J 2006 Focusing optics of a parallel beam CCD optical tomography apparatus for 3D radiation gel dosimetry. *Phys.Med.Biol.* 51 2055-2075.
- Krstajic N and Doran S J 2007 Characterization of a parallel-beam CCD optical-CT apparatus for 3D radiation dosimetry. *Phys.Med.Biol.* 52 3693-3713.

- Lopatiuk-Tirpak O, Langen K M, Meeks S L, Kupelian P A, Zeidan O A and Maryanski M J 2008 Performance evaluation of an improved optical computed tomography polymer gel dosimeter system for 3D dose verification of static and dynamic phantom deliveries. *Med.Phys.* 35 3847-3859.
- Marks D L, Stack R, Johnson A J, Brady D J and Munson D C 2001 Cone-beam tomography with a digital camera. *Appl.Opt.* 40 1795-1805.
- Maryanski M J, Gore J C, Kennan R P and Schulz R J 1993 NMR relaxation enhancement in gels polymerized and cross-linked by ionizing radiation: a new approach to 3D dosimetry by MRI. *Magn.Reson.Imaging* 11 253-258.
- Maryanski M J, Zastavker Y Z and Gore J C 1996 Radiation dose distributions in three dimensions from tomographic optical density scanning of polymer gels: II. Optical properties of the BANG polymer gel. *Phys.Med.Biol.* 41 2705-2717.
- Oldham M 2004 Optical-CT scanning of polymer gels. *Journal of Physics: Conference Series* 3 122-135.
- Oldham M and Kim L 2004 Optical-CT gel-dosimetry. II: Optical artifacts and geometrical distortion. *Med.Phys.* 31 1093-1104.
- Oldham M, Siewerdsen J H, Kumar S, Wong J and Jaffray D A 2003 Optical-CT gel-dosimetry I: basic investigations. *Med.Phys.* 30 623-634.
- Oldham M, Siewerdsen J H, Shetty A and Jaffray D A 2001 High resolution gel-dosimetry by optical-CT and MR scanning. *Med.Phys.* 28 1436-1445.
- Olding T, Holmes O and Schreiner L J 2009 Scatter Corrections for Cone Beam Optical CT. *J.Phys.: Conf.Ser.* 164 174-178.
- Olsson L E, Fransson A, Ericsson A and Mattsson S 1990 MR imaging of absorbed dose distributions for radiotherapy using ferrous sulphate gels. *Phys.Med.Biol.* 35 1623-1631.
- Olsson L E, Westrin B, Fransson A and Nordell B 1992 Diffusion of ferric ions in agarose dosimeter gels. *Phys.Med.Biol.* 37 2243-2251.
- Robb R A 1982 The Dynamic Spatial Reconstructor: An X-Ray Video-Fluoroscopic CT Scanner for Dynamic Volume Imaging of Moving Organs. *IEEE Trans.Med.Imaging* 1 22-33.
- Schreiner L J 2009 Where does gel dosimetry fit in the clinic? *J.Phys.: Conf.Ser.* 164 1-12.
- Schreiner L J and Olding T 2009 Gel Dosimetry. In: Rogers, D. W. and Cygler, J. E. *AAPM Medical Physics Monograph No. 34: Clinical Dosimetry Measurements in Radiotherapy*. Madison, WI, USA, Medical Physics Publishing.
- Smith B D 1985 Image reconstruction from cone-beam projections: necessary and sufficient conditions and reconstruction methods. *IEEE Trans.Med.Imaging* 4 14-25.

Tarte B J and van Doorn T 1995 Laser based tomographic scanning of gel volumes for applications in ionising radiation dosimetry. *10th Conference of the Australasian Optical Society, University of Queensland* .

Tarte B J and van Doorn T 1993 Optical scanning of ferrous sulphate gels for radiotherapy treatment dosimetry. *APSEM/BECON Australasian Conference on Physical Science and Engineering in Medicine /Biomedical Engineering Conference* .

van Doorn T, Bhat M, Rutten T P, Tran T and Costanzo A 2005 A fast, high spatial resolution optical tomographic scanner for measurement of absorption in gel dosimetry. *Australas.Phys.Eng Sci.Med.* 28 76-85.

Wolodzko J G, Marsden C and Appleby A 1999 CCD imaging for optical tomography of gel radiation dosimeters. *Med.Phys.* 26 2508-2513.

## **Chapter 3**

### **Imaging Protocols**

A version of this chapter has been submitted to Physics in Medicine and Biology as *Olding T and Schreiner L J “Cone beam optical computed tomography for gel dosimetry II: imaging protocols”*.

#### **3.1 Abstract**

This work develops imaging protocols for improved dose readout of a Fricke-xylenol orange-gelatin (FXG) gel-filled 1 L polyethylene terephthalate (PETE) jar dosimeter using a commercial Vista<sup>TM</sup> cone beam optical computed tomography (CT) scanner from Modus Medical Devices Inc (London, ON, Canada). To ensure good management of light source-detector stability, it was determined that: (a) a minimum of two hours warm-up time is necessary prior to dosimeter scanning, (b) the light source should be kept on until the completion of the last data scan except for the minimum amount of time required to acquire dark field images, and (c) the optional Vista software projection image normalization routine should be used in image reconstruction. The institution of dosimeter scan time and temperature controls was strongly indicated from the experiments. A standard post-irradiation wait time of 30 minutes measured to within  $\pm$  30 seconds was established to minimize the measurement uncertainties due to dosimeter development and diffusion. To alleviate thermochromic behavior leading to inaccurate dose readout, holding bath warm up and a pre-scan temperature adjustment procedures were developed to control dosimeter temperature to within  $\pm$  0.2°C. The possibility of stray light minimizing protocols was also investigated and deemed to be unnecessary. The largest significant sources of stray light in the system were identified as being due to angled scatter from the dosimeter gelatin

matrix and refraction from the jar wall interfaces. It was concluded that these phenomena would be better addressed through dosimeter modification and an inter-jar dose-to-attenuation calibration methodology, rather than by setting additional imaging protocols.

### **3.2 Introduction**

Since the emergence of gel dosimetry as a potential candidate for three-dimensional (3D) dose measurements in radiation therapy (Gore *et al* 1984, Olsson *et al* 1990), significant attention has been directed toward the use of magnetic resonance imaging (MRI) for gel dosimeter readout (Schreiner and Olding 2009). One reason for MRI being quickly established as the preferred modality for 3D dose readout was its prior development as a mature technology in other medical applications, which served as a good basis for the new task of gel dosimetry (Doran 2009).

The preferred dose contrast mechanism in MR imaging of gel dosimeters has typically been the change in R2 spin-spin relaxation rate, which can be calibrated to obtain a quantitative 3D dose distribution from the irradiated gel dosimeter. However, there was some confusion in the early development of this field which, in part, was sourced in the lack of standard protocols for MR imaging (Schreiner and Olding 2009). Following this early work were some investigations aimed toward the optimization of MRI parameters for gel dosimetry (De Deene and Baldock 2002, De Deene 2004), which helped to bring better consistency to the field. Other studies focused on a variety of other factors, such as dosimeter temperature at irradiation, post-irradiation time before scanning, and dosimeter temperature at time of scanning for different types of normoxic polymer gel (De Deene *et al* 2002, De Deene *et al* 2006). From these studies a number of recommendations have been developed (i.e. imaging protocols) for good practice in MRI-based gel dosimetry.

In the mid 1990's, optical computed tomography (CT) was introduced as an alternative 3D readout method for gel dosimeters (Tarte and van Doorn 1993, Tarte and van Doorn 1995,

Gore *et al* 1996). Unlike MR imaging, optical CT had not seen significant prior development as a quantitative 3D imaging tool, and to date much important characterization work remains to be done in this field. A number of scanner designs have been introduced since then, ranging from improved translate-rotate scanners (van Doorn *et al* 2005, Krstajic and Doran 2007a, Lopatiuk-Tirpak *et al* 2008), to faster area detection schemes (as opposed to point detection) based on cone beam (Wolodzko *et al* 1999, Babic *et al* 2008) and parallel beam (Doran *et al* 2001, Krstajic and Doran 2006, Krstajic and Doran 2007b) charge-coupled device (CCD) configurations. Each of these approaches to data acquisition has advantages and limitations that need to be understood and characterized in combination with the chemistry of the gel dosimeter in use.

In a previous work, some basic properties of the Vista<sup>TM</sup> cone beam optical CT scanner (Modus Medical Devices Inc) were characterized (Olding *et al* 2010) and the scanner shown to be capable of imaging optically absorbing media to the Resolution, Imaging time, Accuracy and Precision (RTAP) criteria that have been suggested for comparing the imaging modalities of MRI and optical CT (Oldham *et al* 2001). The experimental investigations presented in this report follow up on imaging issues raised in Olding *et al* (2010), and are particularly directed at cone beam optical CT imaging of a Fricke-xylenol-gelatin (FXG) gel dosimeter (Kelly *et al* 1998). This dosimeter has previously been shown to be a well suited dosimeter for use with optical cone beam imaging (Babic *et al* 2008, Babic *et al* 2009) since it benefits from optical absorption being the contrast mechanism for the dosimeter. In addition to establishing some of the necessary details for reliable cone beam optical imaging of an FXG gel dosimeter, this report is intended to serve as an illustrative example of the work that is required to move past basic scanner characterization to imaging a specific type of gel dosimeter with its own inherent strengths and limitations. As in Olding *et al* (2010), basic assessments are completed employing calibration scattering solutions, absorbing solutions, and gelatin phantoms that allow the optical

measurement to be separated from the uncertainties in dose delivery and gel dosimetry. Time and temperature imaging protocols are established for improved dosimeter readout. The main sources of stray light perturbation in the system are then assessed, and recommendations made for future improvement in the optical measurement of 3D dose.

### **3.3 Experiment**

This section starts with a general overview of the preparation and cone beam imaging of calibration solutions and FXG gel dosimeters. The first set of experiments is directed at setting a *scanner*-related protocol for improving measurement precision. Then, time and temperature-related attenuation variations in the FXG gel are investigated in order to establish corresponding *dosimeter*-related protocols for the gel formulation. The final set of experiments is aimed at understanding the sources of stray light perturbation in the system, and in this case, the investigations of the dosimeter- and scanner-related stray light sources are discussed together.

#### **3.3.1 Cone Beam Optical CT Imaging**

Three-dimensional imaging was performed using a Vista cone beam optical scanner (Modus Medical Devices Inc) employing a charged-coupled device (CCD) camera with the lens aperture set to f5, and either 633 or 590 nm LED diffuse light panel illumination (specified in each experiment). As a detailed description of the scanner and its operation has previously been reported (Olding *et al* 2010), only necessary details are repeated here. Matching tank solution for the scanner consisted of 10-12 wt% propylene glycol (Cat.No.134368, Sigma-Aldrich Ltd, Oakville, Canada) in water, the refractive index of which (1.344-1.346 ± 0.001 at 590 nm) was monitored over time using a handheld refractometer with a central measurement wavelength of 589 nm ( $r^2$  mini refractometer, Reichert Analytical Instruments, Depew, NY, USA) at room temperature ( $21 \pm 1^\circ\text{C}$ ). Temperature measurements were taken using a digital temperature probe

(TM99A-NA Digital Thermometer, Nuclear Associates, Carle Place, NY, USA). For each scan, a set of 410 light intensity transmission projections were acquired over 360° in approximately 4 minutes. Reference scans were completed on a 1 L PETE jar containing matching tank solution (or on a FXG gel-filled 1 L PETE dosimeter jar prior to irradiation) at the highest shutter exposure time possible without inducing camera pixel saturation and with the lowest gain setting. Data scans were acquired at the same camera settings as the reference scan in all of the imaging runs. Optical CT attenuation images were reconstructed to an isotropic voxel resolution of 0.5 mm or 1.0 mm. The default resolution was 0.5 mm, unless otherwise specified.

The calibration scattering solutions, absorbing solutions, and uniform 5 wt% gelatin-in-water phantoms used for investigating the possibility of standard imaging protocols were prepared according to Olding *et al* (2010). FXG gel dosimeters in this work were prepared according to the recipe suggested by Babic *et al* (2008), containing 0.3 mM ferrous ammonium sulphate (Cat.No.203505, Sigma-Aldrich Ltd, Oakville, Canada), 0.05 mM xylenol orange (Cat.No.398187, Sigma-Aldrich Ltd), 65 mM sulfuric acid (Cat.No.258105, Sigma-Aldrich Ltd), and 6 wt% gelatin (300 bloom Type A porcine gelatin, Cat.No.G2500, Sigma-Aldrich Ltd) in distilled, de-ionized water. After preparation, the heated FXG solutions were poured into 1 L PETE jars and allowed to set overnight prior to irradiation.

Line profiles and regions of interest (ROI) in absorbing, scattering, gelatin phantom and FXG dosimeter projection data and optical CT reconstructed 3D data sets were evaluated using ImageJ (National Institute of Health, Bethesda, MD, USA), Microview 2.1.2 (GE Healthcare, United Kingdom) or MatLab (Mathworks, Newark, NJ, USA) software.

### **3.3.2 Scanner Light Source-Detector Stability**

One of the key considerations for achieving a high precision Vista scanner measurement is to ensure that the light source-detector combination yields a stable signal over time. A default

projection image normalization region is employed by the cone beam reconstruction software toward this end (figure 3.1a inset). In the software routine, a mean projection intensity value is calculated in the normalization region-of-interest (ROI) for each reference and data projection image. The set of mean intensity ROI values for each scan is averaged to obtain a mean scan intensity value for each scan. The reference and data projection image sets are then divided by their respective global scan normalization value to account for any light source-detector variability at the time of image collection.

To test the efficacy of this method of managing light source-detector variability, a reference scan was taken of a 1 L PETE jar containing 12 wt% propylene glycol-in-water matching tank fluid immediately after the scanner was turned on, under 633 nm illumination. Data scans of a 0.1 g/L calibration scattering solution were then acquired at one hour intervals over a scanner warm-up period spanning 5 hours. The results (figure 3.1a) indicate a 2.5% drop in mean attenuation over the 5 hour period. Previous experiments have indicated that the most

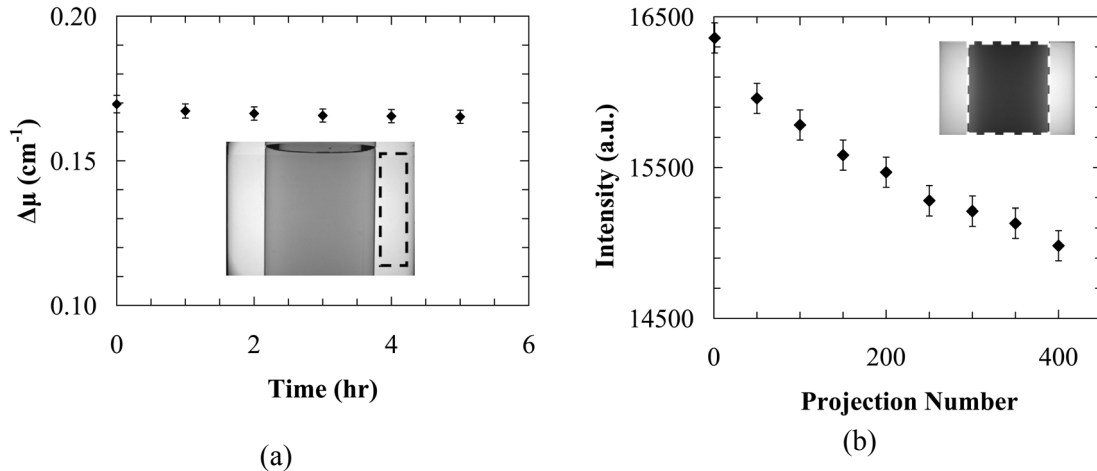


**Figure 3.1:** (a) Change in mean ROI attenuation of a uniform 0.10 g/L scattering solution with scanner warm up time. A slight drop is observed even with the use of a normalization region in the scan projection data (see inset). (b) Variation in the mean jar region projection intensity (see inset) observed in the first data scan of the 0.1 g/L calibration scattering solution.

accurate region for dosimetry within the jar is a cylindrical ROI covering the central 8 cm of the jar's diameter (i.e. to within 5 mm of the jar wall) and the central 10 cm in height (Olding *et al* 2010). This cylindrical ROI was set as the evaluation volume for the data in figure 3.1a.

Looking within the set of 410 projection images of the first data scan from figure 3.1a, a significant drop in the mean 'jar region' projection intensity is clearly evident (figure 3.1b).

The open field intensity of the light source was subsequently evaluated over a 16 hour time period using a photodiode detector (figure 3.2a) and was found to stabilize after approximately 2 hours with a slight sinusoidal ripple in magnitude over time. Similar mean open field intensity behaviour was observed when using the scanner camera for the measurement of intensity (figure 3.2b). However, if the scanner light source was turned off for more than a few seconds, a sharp increase in mean intensity was observed by the camera as the light source was turned on again (figure 3.2b), and the signal would then require additional time for stabilization.

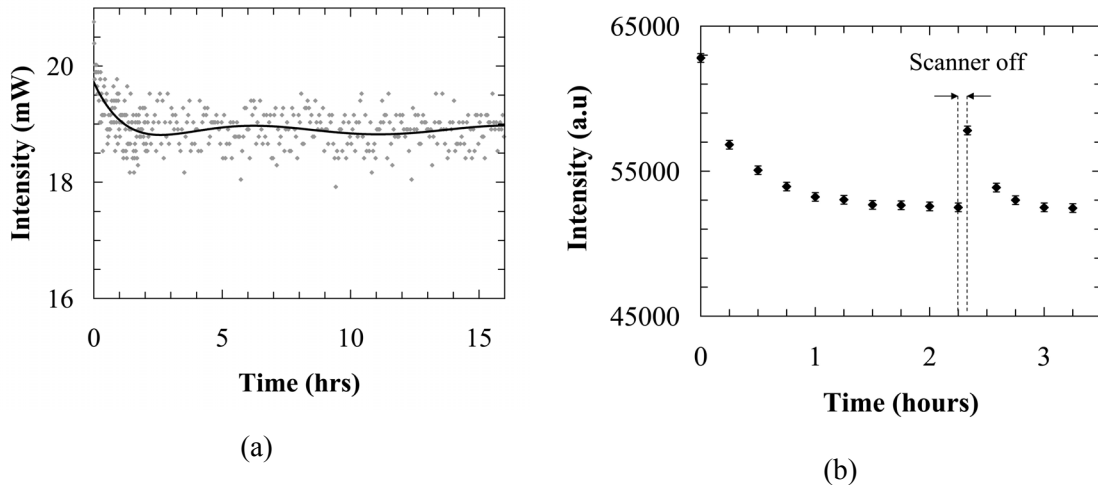


**Figure 3.2:** (a) An independent measurement of light source intensity over time using a photodiode detector indicates that the light source stabilizes in approximately 1-2 hours. Error bars are smaller than symbol size. (b) Mean open field intensity of the light source measured over time by the Vista scanner.

### 3.3.3 Scan Time Constraints

Moving beyond the evaluation of scattering and absorbing solutions to imaging FXG gel dosimeters leads to additional time constraints beyond that of a minimum scanner warm up time. A previous report has indicated that the FXG dosimeter can stabilize in ~40 minutes for a 200 cGy delivery (Kelly *et al* 1998), but a closer examination of the results from this work indicate that the attenuation is still increasing at a marginal rate of ~3% per hour relative to the value obtained at the 40 minute mark.

To investigate this further, a FXG gel dosimeter was irradiated to a superficial dose of 200 cGy on the day after manufacture using a Gulmay superficial x-ray therapy unit (Gulmay Medical Inc., Buford, GA, USA) with a 6 cm cone insert. The Gulmay unit was employed for the delivery in order to obtain a large variation in dose distribution within the gel volume. The dosimeter was then imaged on the Vista scanner at 590 nm over a 24 hour period after irradiation.

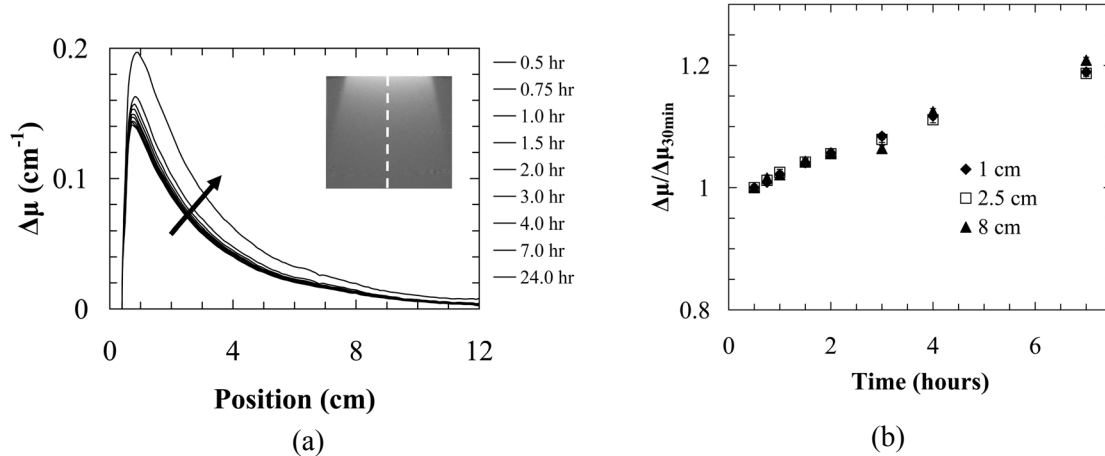


**Figure 3.3:** (a) Development of attenuation (depth dose) from an 80 kVp, 200 cGy, 6 cm cone Gulmay delivery. The arrow is directed toward increasing time. (b) Relative attenuation along the central axis at three positions along the central axis in the gel dosimeter (normalized to the attenuation value at 30 minutes). The error bars in (b) are smaller than symbol size.

The dosimeter and the scanner matching tank fluid were held at  $20.1 \pm 0.2^\circ\text{C}$  during this post-irradiation time period. The central axis depth attenuation curves corrected for auto-oxidation effects (Babic *et al* 2008) clearly show dose development over this time period (figure 3.3a). Attenuation data taken from three depths in the curves and normalized to the attenuation value at a post-irradiation time of 30 minutes indicate an attenuation increase of approximately 2.8-3.0% per hour at each depth (figure 3.3b).

Another factor that plays a role in the development of FXG dosimeter imaging protocols is the loss of spatial dose integrity over time due to diffusion of the ferric-xylenol orange ion complex (Harris *et al* 1996, Rae *et al* 1996, Baldock *et al* 2001). A line profile through the optical CT image of the 200 cGy Gulmay delivery at a depth of 1 cm (figure 3.4a, normalized to maximum attenuation) shows the effect of diffusion on spatial dose integrity over time. In an enlarged view near the top edge of the dose gradient (figure 3.4b), the normalized attenuation changes in magnitude at a rate up to  $\sim 0.4\%$  every 10 minutes at the fastest changing point along this attenuation (dose) profile.

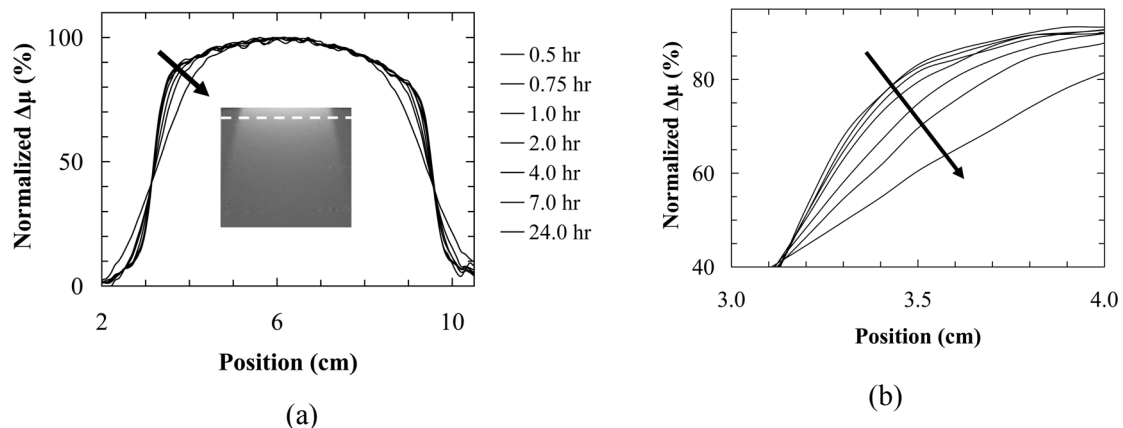


**Figure 3.4:** (a) Line profile through the central axis of the 200 cGy superficial (80 kVp) delivery at 1 cm depth. Increasing time is indicated by the arrow direction. (b) A close-up view of the arrow region in (a).

### 3.3.4 Scan Temperature Constraints

Representative 0.1 g/L acrylic scattering and 1.48 mg/L patent blue violet dye absorbing solution-filled 1 L PETE jars were cooled in the refrigerator prior to optical scanning at 633 nm. The mean reconstructed ROI attenuation coefficient of the cooled scatter solution-filled jar was found to be elevated by slightly more than 3% compared to the room temperature attenuation value. An evaluation of the mean transmitted intensity value within the jar region of the projection images indicates a slight trend of increasing intensity through the jar as it warms up (figure 3.5a). The measurements were repeated on the cooled absorbing solution, and less than 0.5% projection intensity variation was observed over the range of 10-21°C (figure 3.5a).

The FXG gel dosimeter was assessed to see if the iron-xylenol orange dye complex had a similar temperature response to that of the patent blue violet dye. Figure 3.5b shows the reconstructed central axis attenuation (depth dose) for a FXG gel irradiated with a 6 x 6 cm, 20 MeV electron beam to a dose of 200 cGy at a reference depth of 3 cm, using a Varian Clinac

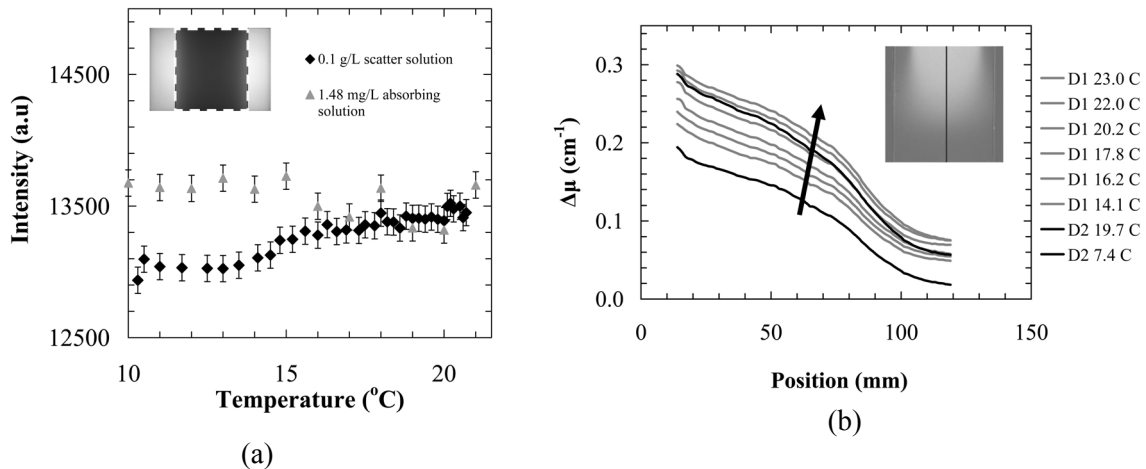


**Figure 3.5:** (a) Mean intensity of the open field projection data showing temperature dependence of uniform scattering acrylic and absorbing dye solutions. (b) Diffusion-perturbed central axis attenuation for a FXG gel dosimeter irradiated with a 200 cGy electron beam. Two sets of scans were obtained for this dosimeter on subsequent days (D1 in gray, D2 in black), with increasing temperature shown by the arrow direction.

21iX linear accelerator (Varian Medical Systems, Palo Alto, CA, USA), and refrigerated for 3 weeks to ensure reaction completion (i.e. dosimeter development is minimal at this point). The measured dosimeter data are known to be inconsistent with the planned delivery due to diffusion effects over the three week post-irradiation time period. However, the primary interest is in obtaining relative data measurements at temperature, so this is not a significant issue. Individual scans were acquired at 590 nm on the Vista scanner and auto-oxidation effects were taken into account (Babic *et al* 2008). Approximate temperature measurements of the dosimeter were taken prior to each scan by inserting the temperature probe 1 cm into the FXG gel. The temperature of the matching tank solution was held to  $22 \pm 1$  °C during the scans. The dosimeter was placed in a covered, warm water-filled tank between scans. The dosimeter jar was then returned to the refrigerator and re-scanned on the following day. The scan data are shown in figure 3.5b, with auto-oxidation effects between the two days accounted for in the data.

Some follow-up temperature experiments were then performed. A FX aqueous solution-filled 1 L PETE jar prepared according to Babic *et al* (2008), but not including the gelatin component, was irradiated through the top surface of the gel with an 1800 cGy, 6 x 6 cm, 6 MV photon beam (to the reference depth of 2 cm) and imaged at 590 nm and room temperature ( $21.4 \pm 0.1$  °C) at a post-irradiation time of 30 minutes. The jar was then cooled down in an ice bath and re-imaged over the next 2 hours at different warm-up temperatures, with temperature readings taken in the same manner as for the data presented in figure 3.5b. An FXG gel-filled 1 L PETE jar dosimeter was also prepared, irradiated with a 180 cGy, 6 x 6 cm, 6 MV photon beam, and similarly imaged. Mean ROI attenuation values for the region covering the central 8 cm in diameter and 10 cm in height of the imaged jars (reconstructed to 1 mm cubic voxel size) are shown in figure 3.6a. Finally, after overnight refrigeration, the two dosimeters were placed in a

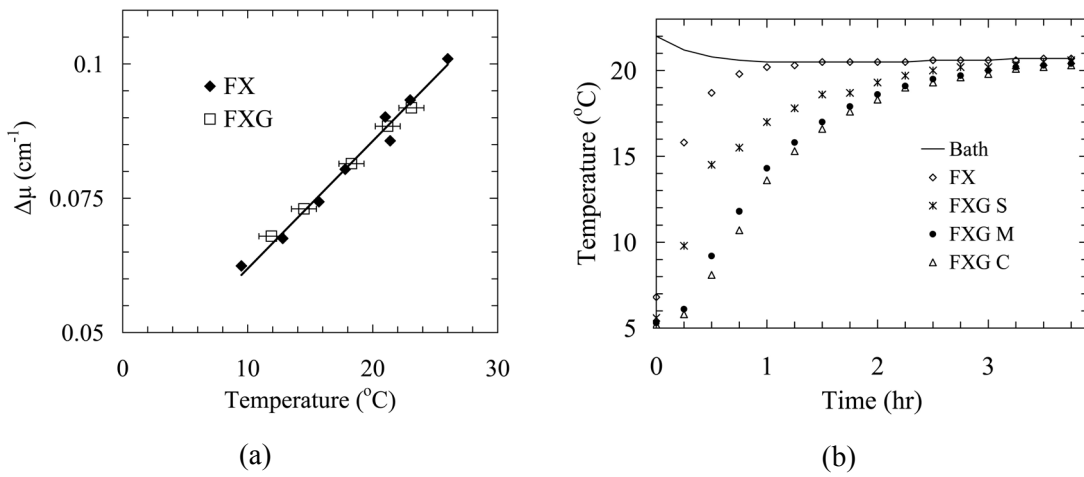


**Figure 3.6:** (a) Change in mean jar ROI attenuation values with temperature for (i) a FX solution-filled jar irradiated with an 1800 cGy 6 MV photon beam, and (ii) a FXG gel-filled jar irradiated with a 180 cGy 6 MV photon beam. (b) Temperature readings at the centre of the FX jar, and at the centre (C), mid-point along the radius (M), and side (S) of the FXG jar for a period of time after placing the refrigerated jars in a covered, 20 L warm-up bath. Some of the error bars are smaller than the symbol size.

warm-up bath at 22°C. Temperature readings were taken at 15 minute intervals over a period of 4 hours in the centre of the FX jar (figure 3.6b). Temperature readings were also acquired at 15 minute intervals over the same 4 hour period at three points in the FXG jar with the probe inserted 9 cm deep into the FXG gel (also shown in figure 3.6b). The selected positions were located approximately 0 cm, 2 cm and 4 cm from the centre of the 4.6 cm radius jar.

### 3.3.5 Stray Light Reduction

Cone beam optical CT imaging of absorbing and scattering solutions is known to be affected by optical artifacts due to stray light from a number of different sources (Jordan and Battista 2006, Bosi *et al* 2007, Bosi *et al* 2009, Jordan and Battista 2009, Olding *et al* 2010). Stray light perturbation occurs when light rays from the diffuse light source not originally travelling along a cone beam primary ray path reflect or scatter onto that ray path (i.e. within some finite sized ray bundle defined primarily by the camera lens aperture), typically prior to exiting the attenuating

media or when in transit through the camera lens optics. As light arriving along a primary ray path is indiscriminately focused onto the CCD chip regardless of the original path taken, stray light may be acquired as contaminant signal in the projection image recorded by the camera. The experiments in this section are therefore aimed toward describing the main sources of perturbation and considering the possibility of setting stray light-reducing protocols for improved FXG gel dosimetry. As the FXG gel dosimeter combines a low scattering attenuation gelatin matrix with an optical absorption dose contrast mechanism, evaluation of both scattering and absorbing solutions in the Vista scanner is required.

The fundamental relationship on which Feldkamp filtered back projection cone beam reconstruction (Feldkamp *et al* 1984) is based is Beer's Law. This law states that for a light intensity  $I_0$  incident at the surface of a uniform substance of linear attenuation coefficient  $\mu$ , the attenuated light intensity  $I$  at some depth  $x$  in the substance is given by  $I = I_0 e^{-\mu x}$ . The cone beam reconstruction calculations presume that light travels in straight lines along cone beam ray paths through the attenuating media. This "ray path" condition generally holds true for the lens-based camera detector in the Vista scanner, as the camera optics only focus light onto the CCD chip that is travelling in tight ray bundles along cone beam geometry ray paths toward the camera lens after exiting the attenuating media (Olding *et al* 2010).

One method of verifying the assumption of cone beam geometry described in Olding *et al* (2010) involves the acquisition of two-dimensional (2D) percentage intensity maps from the Vista scanner. These maps are obtained through use of a 2 mm pinhole grid blocker inserted at the light source side of the matching tank. Each pinhole can be thought of as passing a tight ray bundle of light. Then, the intensity of light reaching the centre pixel in the illuminated region at the detector with the pinhole blocker in place relative to the intensity reaching the same "centre" pixel under open field condition is effectively a measure of how much light reaching the camera is sourced in

that ray bundle (or light cone). Figures 3.7a and 3.7b show open field and pinhole blocker images of a 12 wt% propylene glycol-in-water fluid-filled 1 L PETE jar in the matching tank at 590 nm. The 1/32' thick aluminum matte-finished blocker used to obtain the image in figure 3.7b had 2 mm diameter pinholes, 11 mm (square) spacing between pinholes, and was inserted at the light source side of the matching tank. Figure 3.7c shows the measurements along the line of blocker pinholes highlighted in figure 3.7b, with and without the PETE jar inserted in the matching tank. The ratio varies less than 2% without the jar in place. When the 1 L PETE jar is in the matching tank, a significant level of perturbation up to 4-6% near the jar walls is observed in the projection image.

The projection image data is increasingly perturbed when imaging scattering media (Olding *et al* 2010). To explore this effect, the 2 mm diameter pinhole blocker grid experiment described in figure 3.7 was repeated with the matching tank fluid-filled jar replaced by a 5 wt% gelatin-in-water-filled jar (see figure 3.8). A bi-cubic spline function in MatLab was used to

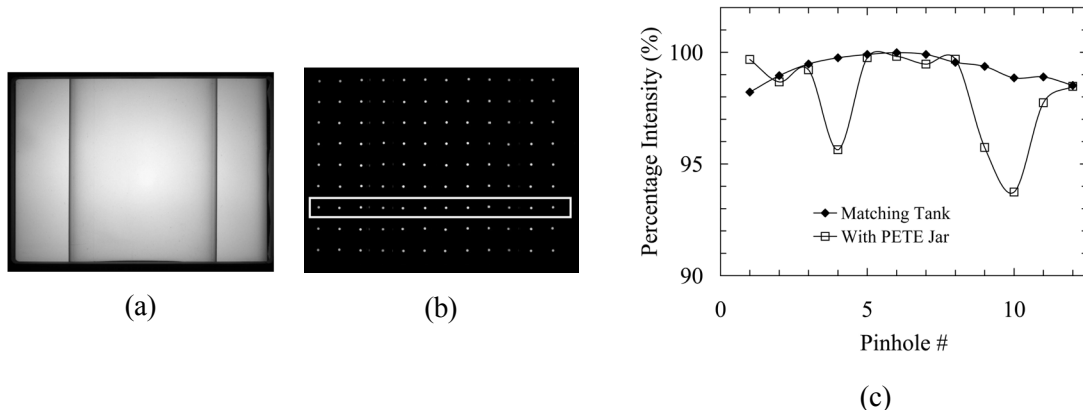


**Figure 3.7:** (a) Open field and (b) 2 mm diameter pinhole grid blocker projection images from the Vista scanner with a matching fluid-filled 1 L PETE jar in the matching tank. (c) Each pinhole blocker ‘centre pixel’ intensity is extracted from one line of pinholes in the image (highlighted in figure 3.7b) and expressed as a percentage of open field intensity at the same pixel from the open field projection image. The plot shows the data from this line of pinholes with and without the matching tank-fluid-filled 1 L PETE jar in the tank. Fitted curves to the data are included to aid the eye.

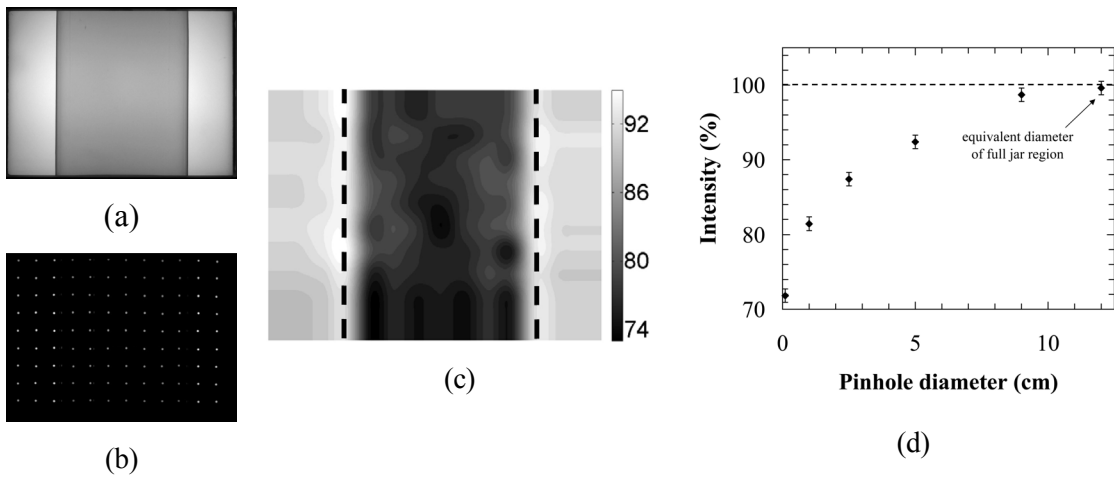


**Figure 3.8:** (a) Open field and (b) 2 mm diameter pinhole grid projection images from the Vista scanner with a 5 wt% gelatin-water filled 1 L PETE jar in the matching tank. (c) An interpolated percentage map is calculated from the measurements of peak pinhole intensity and open field intensity. The dotted lines show the jar edges. (d) Pinhole blocker ‘centre pixel’ intensity values are extracted from the ‘blocked’ image and expressed as a percentage of open field intensity at the same pixel from the open field projection image, for varied diameter single pinholes at f5 with the single pinhole blocker placed at the light source side of the matching tank.

interpolate between measured grid points to obtain a 2D percentage map for the full projection image. A reduced mean ‘jar region’ percentage intensity value of ~78% (figure 3.8c) is indicated. A series of increasing diameter single pinhole blockers (with the pinholes approximately centered in front of the jar) were then inserted at the light source side of the matching tank in order to determine the extent of angled scatter intensity reaching each CCD camera pixel (figure 3.8d).

When the experiments are extended from a gelatin ‘blank’ to imaging a FXG dosimeter (i.e. an absorption dose contrast mechanism combined with a scattering gelatin matrix), slight variations are observed in the background stray light scatter ‘wash’ of dosimeters irradiated with different dose distributions. For example, percentage maps calculated from open field and 2 mm pinhole grid blocker projection images acquired at 590 nm using the Vista scanner are shown in figure 3.9 for (b) an un-irradiated FXG dosimeter, (d) a 200 cGy electron beam-irradiated FXG dosimeter, and (f) a 200 cGy intensity modulated radiation therapy (IMRT)-irradiated FXG

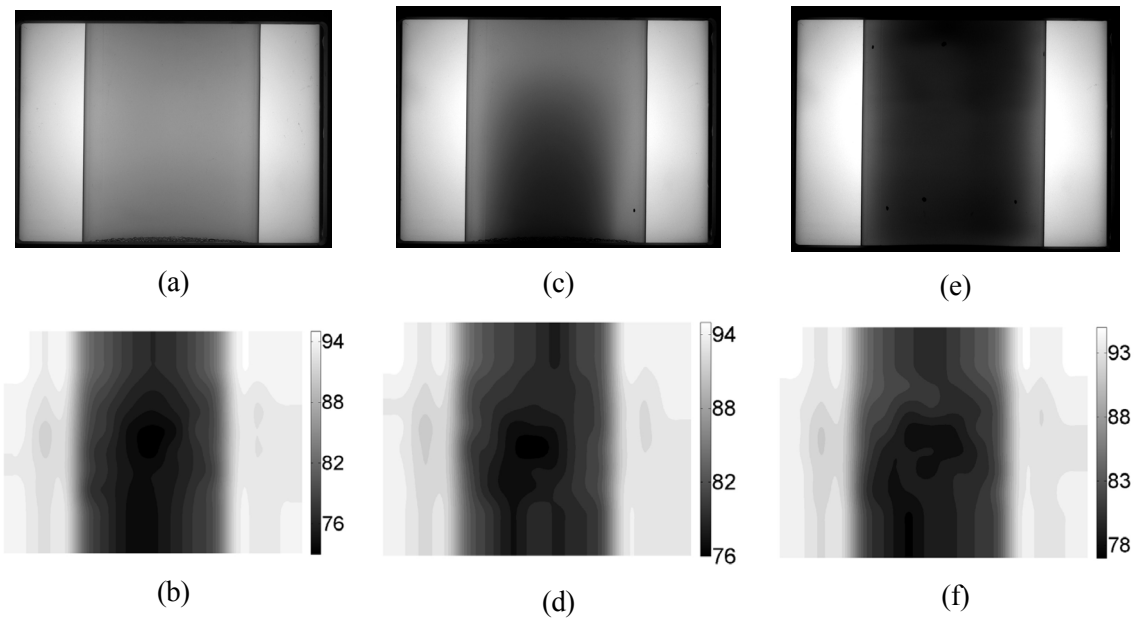


**Figure 3.9:** Projection images and 2 mm diameter pinhole blocker grid percentage maps for: (a),(b) an FXG dosimeter jar prior to irradiation with a calibration electron beam, (c),(d) a 200 cGy electron beam irradiated dosimeter and (e),(f) a test 200 cGy intensity modulated radiation therapy (IMRT) delivery.

dosimeter. The mean ‘jar region’ percentage values obtained for the three dosimeters were found to be 77.5%, 80.0% and 80.8% respectively.

The question is: can the level of stray light perturbation be meaningfully reduced through a hardware adjustment or imaging protocol? It is difficult to assign meaningful protocols compensating for stray light sources inherent to the *dosimeter*, such as the jar interfaces or the scattering gel matrix. However, there are other sources of stray light in the system related to the *scanner*. Perhaps the simplest perturbation to manage (and the final focal point of this work) is contaminant stray light travelling through the low scattering matching fluid regions on either side of the jar. Diffuse light from this region can refract at the jar-fluid interface onto a primary ray path in the jar region of the transmission projection image. It is possible then, that inserting

custom blockers on either side of the jar could reduce the overall level of stray light perturbation. To test this theory out, thick, black cardboard side blockers were inserted at the light source side of the matching tank, positioned 5 mm from the jar edges in the projection image (see figure 3.10a). Two reconstructed attenuation profiles across the jar region of a 1 L PETE jar containing 1.48 mg/L absorbing solution are shown in figure 3.10b, obtained with and without the side blockers in place in the Vista scanner (590 nm, 1.0 mm cubic voxel size). A projection image showing the placement of the side blockers is shown in the inset of figure 3.10b. A jar region-sized cardboard blocker was then placed in front of the 1.48 mg/L absorbing solution at the light source side of the tank and a single projection image recorded (figure 3.10c). Slight stray light impingement occurs into the blocked jar region of the projection image, with a mean transmitted intensity of ~450 arbitrary units (au) over the blocked jar region, ranging up to 1500 au near the

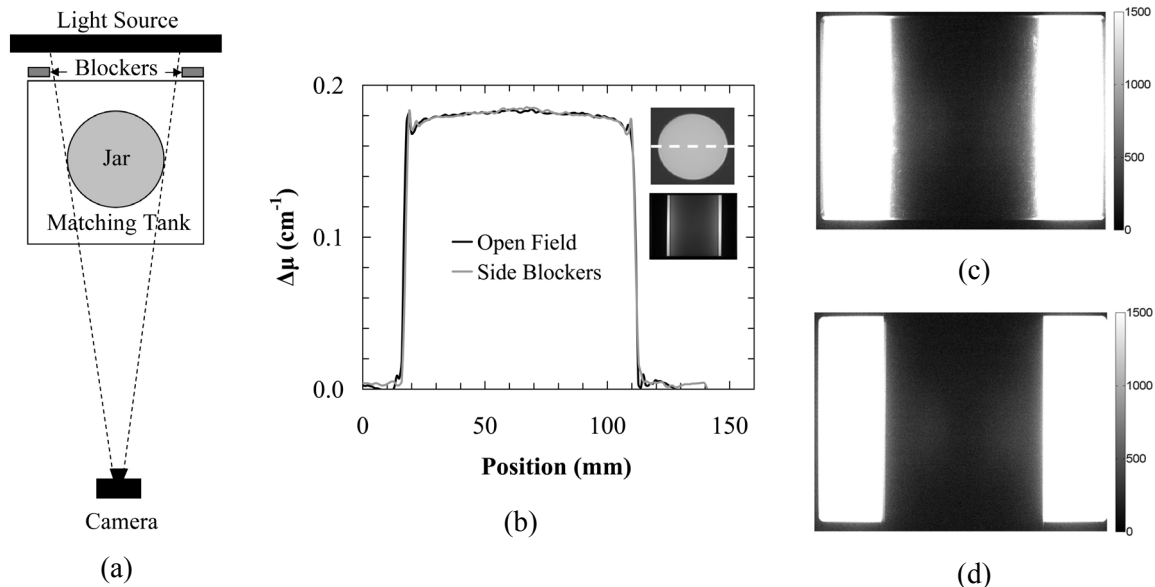


**Figure 3.10:** (a) Scanner set up with side blockers in place. (b) Profiles across the reconstructed images of a PETE jar containing 1.48 mg/L absorbing solution imaged on the Vista scanner, with and without side blockers at the light source side of the matching tank. Transmission projection images of the 1.48 mg/L absorbing solution with a blocker covering the jar region at (c) the light source side of, and (d) the camera side of the matching tank.

jar walls. Dark field images recorded by the camera typically have a mean intensity of ~25 au.

A second ‘blocked jar region’ projection image was taken of the 1.48 mg/L absorbing solution with the blocker at the *camera side* of the matching tank (figure 3.10d). A small stray light perturbation was again observed in the blocked jar region with a mean intensity of 400 au ranging up to ~900 au near the jar walls.

The stray light side blocker experiments were repeated under the same conditions as in figure 3.10a, replacing the jar containing 1.48 mg/L absorbing solution with jars containing 0.02 g/L and 0.10 g/L scattering solution. A slight reduction in reconstructed attenuation (that is particularly noticeable near the jar wall) is observed in the attenuation profiles without the side blockers in place (figure 3.11a). The effect is more clearly distinguished at the higher scattering

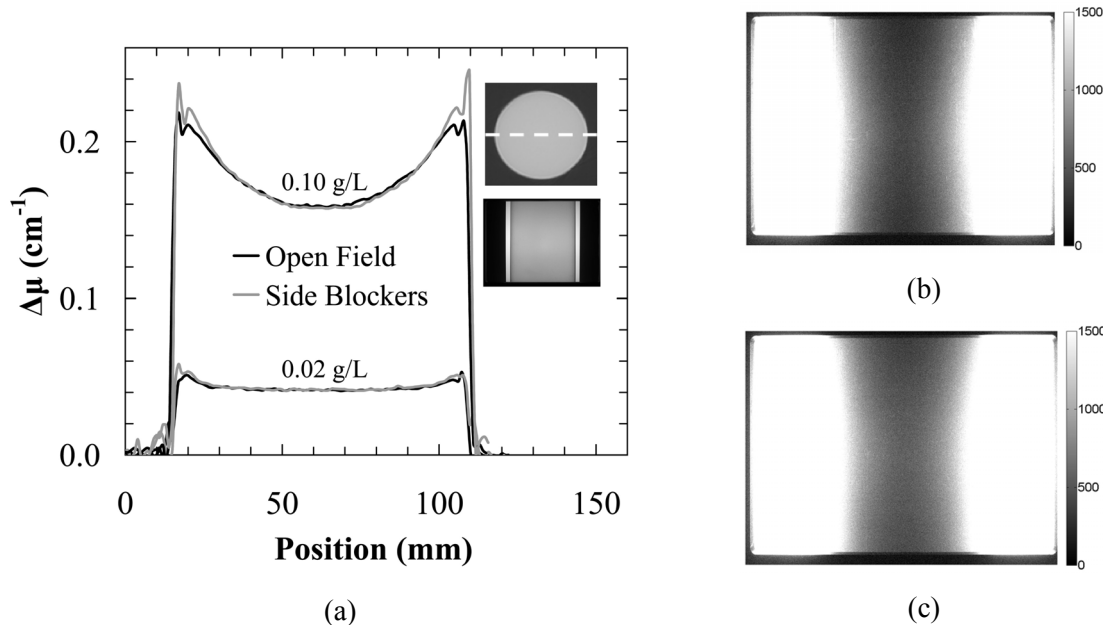


**Figure 3.11:** (a) Profiles across the reconstructed optical CT images of 1 L PETE jars containing 0.02 g/L and 0.10 g/L scattering solution imaged on the Vista scanner with and without side blockers at the light source side of the matching tank. Transmission projection images of: (b) 0.02 g/L, and (c) 0.10 g/L scattering solutions with a blocker covering the jar region at the light source side of matching tank.

concentration, where the ratio of stray light to primary transmitted light in the image is higher. Compared to the results in figure 3.10c, greater stray light impingement is observed into the blocked jar region of the projection image, increasing with scatter concentration (see figures 3.11b and 3.11c).

### **3.4 Discussion**

#### **3.4.1 Scanner Light Source-Detector Stability**

The reported decrease in mean jar attenuation value of the calibration 0.1 g/L scatter solution as the scanner warms up (figure 3.1a) implies that the use of the Vista scanner projection image normalization region does not fully account for light source-detector variation. Taking a closer look at the mean intensity value in the jar region of the projection images from the first data scan (figure 3.1b), there is a significant drop in recorded intensity within the time frame of the scan. The Vista software normalization methodology accounts for inter-scan but not intra-scan variation, hence the change in response results in a drop in reconstructed mean attenuation value.

The results show that the scanner light source essentially stabilizes within the first 1-2 hours after the light panel is turned on (see independent photodiode measurements in figure 3.2a). However, the sharp peak in recorded intensity observed after the light source is switched off for 5 minutes, then on again (figure 3.2b), indicates a “cool down” instability in the output of the light source. The Vista scan software up to this point in its development incorporated a procedure of acquiring a dark field image as the last projection image in both the reference and data scans by turning the light source off and leaving it off after the scan was completed. The software was henceforth modified to turn off the light source for the minimum amount of time required to acquire the dark field image, after which the light source was turned back on. This fast off-on operation was determined to have negligible effect on the stability of the light source signal.

As most of the light source instability leading to a calculated reduction in attenuation occurs in the first two hours of scanner warm-up, a protocol was established requiring: 1) a minimum of two hours warm-up time prior to dosimeter scanning and 2) that the light source be kept on until completion of the last data scan. The software normalization routine is then able to effectively account for the small, slow intensity variation observed over time as shown in figure 3.2a (on the order of less than 1%). Without this correction, a slight baseline difference between mean light source intensity for the reference and data scans could be observed if the two scans are initiated during the peak and valley of the sinusoidal ripple respectively, or vice versa. Intra-scan light variations are small if the scanner warm up time protocol is employed, but it is conceivable that a further small improvement in measurement precision may be realized if individual projection image normalizations are incorporated in the reconstruction software.

### **3.4.2 Scan Time Constraints**

The rate of FXG gel dosimeter development determined from the data presented in figure 3.3b is on par with the results reported by Kelly *et al* (1998). Since the rate of attenuation increase is roughly 3% per hour past the post-irradiation time of 30 minutes, and a typical 360°, 410 projection Vista scan takes 4-5 minutes, a mean increase in attenuation of approximately 0.25% happens between start and end of the scan. Also, the time frame for the dose delivery of complicated treatment plans can be on the order of 5 minutes, which introduces an additional (intra-scan) variable into consideration for accurate dosimeter readout. The importance of a fast scan time is highlighted through this result. Dosimeter development is prohibitive to FXG dosimeter readout when using a point detection scheme-based optical scanner (with scan time on the order of hours), unless a time-based correction is employed.

In order to reduce the uncertainties introduced by diffusion, it is desirable to minimize the time between irradiation and imaging of the dosimeter. However, the rate of dose development is

higher when imaging is performed before the 30 minute mark (Kelly *et al* 1998), resulting in increased intra-scan attenuation variation. An approximate balance between these two parameters of dosimeter development and spatial dose integrity is found at 15-30 minutes post-irradiation. Given that the effects of diffusion are less significant away from dose gradients, but that dose development variation occurs through the entire dosimeter, a standard post-irradiation imaging time of 30 minutes was established for FXG dosimeter readout. Further reductions in scan time in the future may lead to reducing this time toward to the 15-20 minute mark, which can be realistically achieved if the scanner is close in physical location to the irradiator in the clinic. Moving from a full scan over  $360^{\circ}$  to a half scan over  $180^{\circ}$  plus a fan angle of  $\sim 12^{\circ}$  to fully sample the Radon space (Kak and Slaney 2001) would be one logical step to take toward a shorter scan time, but with a tradeoff of decreased signal to noise. As in the case of dosimeter development, diffusion-related loss of spatial dose integrity over time also effectively prohibits the use of a point-detection optical scanner for FXG dosimeter readout due to its slow scan time. The accurate assessment of time between irradiation and scanning is important enough to specify the standard post-irradiation wait time of 30 minutes prior optical cone beam imaging to within  $\pm 30$  seconds, which is readily accomplished.

### **3.4.3 Scan Temperature Constraints**

In figure 3.5a, an increase in transmitted intensity (i.e. decrease in attenuation) is observed in the projection images of the scattering solution as the solution warms up to room temperature. This effect is likely due the decreasing difference between the refractive indices of the solvent and scattering particles with increasing temperature (Franklin and Wang 2002). Given that the 3% increase in measured attenuation occurs over a range of  $13^{\circ}\text{C}$ , a specification on scanner measurement temperature to within  $\pm 1^{\circ}\text{C}$  would control the uncertainty in measured attenuation due to the scattering gelatin matrix in the FXG gel dosimeter to  $\pm 0.25\%$ . The measurements of

the patent blue violet-based absorbing solution were essentially temperature-independent (figure 3.5a). At this point one may be tempted to leave the scan temperature specification at  $\pm 1^{\circ}\text{C}$ . This would effectively minimize the temperature dependent change in scatter attenuation from the gelatin matrix.

The results in figure 3.5b indicate, however, that unlike the patent blue violet dye solution, the FXG gel dosimeter exhibits significant optical attenuation temperature dependence. This thermochromic behavior is believed to be primarily sourced in d-orbital spin state crossover of the ferric ion in the ferric ion-xylenol-orange dye complex with increase in temperature (Wulfsberg 2000); this effect should be controlled for accurate dosimetry. The increase in attenuation with temperature was observed to be approximately 2.5% per degree Celsius (figure 3.6a) with or without the gelatin in solution. This gives strong indication that the ferric ion-xylenol-orange dye complex is the primary source of attenuation change with temperature, and that the dosimeter temperature should be strictly controlled to within the practical measurement limit of  $\pm 0.1^{\circ}\text{C}$  at the point of scanning (translating to an approximate dose measurement uncertainty of  $\pm 0.25\%$ ). This result is more severe than that observed in a previous experiment, where the effect of temperature on un-irradiated FXG samples indicates an increase in measured absorbance of  $\sim 5\%$  after warming the samples from  $5^{\circ}\text{C}$  up to  $30^{\circ}\text{C}$  (Bero and Kharita 2004). The two results are consistent, though, as the un-irradiated samples analyzed in Bero and Kharita's experiments primarily contain ferrous ions, and only a minimal quantity of the thermochromic behavior-inducing ferric ion.

In order to accomplish the necessary degree of temperature control, two additional protocols were introduced in the scan procedure. First, on the day of irradiation, the refrigerated dosimeter jars are placed in a large covered ‘holding’ water bath (typically adjusted to between  $20.0$ - $21.0 \pm 0.1^{\circ}\text{C}$  depending on the ambient temperature in the clinic) approximately 3-4 hours

before scanning to ensure temperature uniformity to within roughly  $\pm 0.2^{\circ}\text{C}$  in the gel dosimeter jar (figure 3.6b). The bath is covered to reduce ultraviolet light-driven reactions in the dosimeter. It is noteworthy that the presence of gelatin in solution significantly slows down temperature equalization in the gel. Second, the temperature of the scanner matching bath is adjusted to the temperature of the holding bath (e.g.  $20.0 \pm 0.1^{\circ}\text{C}$ ) immediately prior to the reference scan being performed. There are a few sources of heat in the scanner that can cause the matching bath to warm up over time (the stepper motor, the camera and to a small degree, the light source), so usually the matching bath needs to be cooled to the target temperature. To adjust the matching bath temperature, a PETE jar containing refrigerated water or hot water is placed in the bath under low agitation stirring for a short period of time while monitoring the temperature until the target point is reached. The dosimeter is then inserted in the scanner matching bath and the bath temperature is recorded before and after the reference scan is completed. The dosimeter jar is returned to the covered holding bath until the time of irradiation and returned to the bath after irradiation until the time of the data scan measurement. These two protocols, when followed, significantly reduce observed fluctuations in the measurement that were previously assumed to be due to variation in batch preparation (chemical amounts, sensitivity, process of manufacture, etc).

#### **3.4.4 Stray Light Reduction**

The results presented in figure 3.7c clearly indicate that refractive index (RI) mismatch-derived re-direction of light at jar wall interfaces is a primary source of stray light perturbation in the projection image data. There are two obvious approaches that could reduce this perturbation, both related to dosimeter manufacture. First, the PETE dosimeter jar could be replaced with another high optical clarity container derived from an acrylonitrile-based Barex<sup>TM</sup>, or a polymethyl-methacrylate (PMMA)-based polymer. However, the RI value at a wavelength of 590 nm is only marginally different when the PETE jar with an RI of  $\approx 1.58$  (Shabana 2004) is replaced with

Barex with an RI  $\approx$  1.51 (Islam *et al* 2003) or PMMA with an RI  $\approx$  1.49 (Groh and Zimmermann 1991). Given that the FXG gel has a refractive index of  $\approx$  1.345 at 590 nm, a slightly optically scattering fluoropolymer container material such as poly-tetrafluoroethylene (PTFE, e.g. Teflon) with an RI  $\approx$  1.35 at 590 nm, (Groh and Zimmermann 1991) would have to be used to provide a reasonable RI match between the gel and the jar material, as used in Babic *et al* (2008). Unfortunately, PTFE and its other fluoropolymer counterparts are comparatively expensive and are reasonably difficult to form into high quality, off-the-shelf dosimeter containers. Also, the question of whether optical scatter through the translucent PTFE container wall is more or less detrimental to stray light perturbation than refractive index-mismatch when using PETE has not been addressed to date.

The second option is to raise the RI of the gel and the matching tank fluid close to that of PETE. However, this involves a significant solvent replacement step that will compromise the water equivalence of the gel and may lead to deleterious changes in the radio-sensitivity of the dosimeter, as discussed previously (Olding *et al* 2010).

As RI mismatch-driven re-direction of light at jar wall interfaces is inherent to the physical structure of the dosimeter jar, it is difficult to set imaging protocols that will reduce this form of stray light perturbation in FXG gel dosimetry. Although it has not been confirmed, this effect is the likely source of bowing artifact observed in previous work with the Vista scanner (Jordan and Battista 2006, Olding *et al* 2010).

The second, and perhaps the most significant source of stray light perturbation observed in cone beam imaging of FXG gel dosimeters is angled scatter from the gelatin matrix. The results shown in figures 3.8c and 3.8d indicate that over 20% of the light arriving at each pixel throughout most of the jar region is scattered onto the primary ray path from a much larger region than that observed in the case of the absorbing solution. Contaminant light intensity at each

detector pixel is scattered onto that pixel's primary cone beam ray path from varied paths throughout the full jar volume (figure 3.8d). Without further consideration, this contaminant light intensity appears to compromise the measurement accuracy of the system.

In another report, cone beam optical CT-based FXG gel dosimetry has been shown to have good accuracy in the measurement of 3D dose (Babic *et al* 2008, see tables 1 and 2). To explain this result, two lines of thinking come into play. First, the scattering gelatin background does not significantly change during irradiation and hence there may be a partial cancellation in the low spatial variation scatter ‘wash’ background signal (see figure 3.8c) between reference and data scan, due to the fact that the ratio of reference and data scan projection intensities is taken during image reconstruction. This stray light perturbation will not be entirely cancelled in the reconstruction (due to the fact that the ratio is logarithmic in nature), but the resulting effect on reconstructed attenuation may be relatively small. Second, the dose response of the ‘measurement’ FXG gel dosimeter in Babic *et al* (2008) is calibrated using the attenuation-to-dose relationship obtained from a second well-characterized electron beam-irradiated FXG gel dosimeter. If the angled scatter-based stray light perturbation is consistent between the calibration and measurement dosimeters, its effects may be calibrated out of the volume attenuation data. The results presented by Babic *et al* indicate that the image attenuation data is still slightly perturbed by stray light, but that a single value measured stray light correction applied to the projection data prior to image reconstruction appears to adequately manage this perturbation.

Looking at the projection image percentage maps presented in figure 3.9, the variation in mean scatter contribution between the three jars is seen to be relatively small. The differences are likely related to the degree to which scatter-sourced stray light is attenuated through optical absorption in the dosimeter. That is, stray light is attenuated least in the low absorbing un-irradiated dosimeter, more so in the electron beam dosimeter and most in the highest absorbing

IMRT dosimeter. There are no straightforward imaging protocols for reducing stray light perturbation due to angled scatter. The other Vista scanner imaging wavelength of 633 nm could be used (instead of 590 nm) to reduce the scatter contribution by ~30%, as optical scattering through the dosimeter follows an approximate 3<sup>rd</sup> to 4<sup>th</sup> order inverse wavelength dependence (Olding *et al* 2010). However, a new radio-sensitive dye would have to be identified, as the response of the iron-xylenol orange complex drops significantly at 633 nm compared to 590 nm (Kelly *et al* 1998). At present, the 590 nm imaging wavelength provides the best ratio of optical absorption response-to-scatter background signal.

Moving on to the third source of stray light perturbation considered in this work, the two attenuation profiles in figure 3.10b are observed to be very similar. This indicates that the overall stray light perturbation from the low scattering matching fluid regions on either side of the jar is minimal when imaging absorbing media. That is, most of the bowing artifact observed in the imaging of uniform absorbing media-filled jars (Jordan and Battista 2006, Olding *et al* 2010) is due to small angle re-direction of light travelling through the jar, not high angle re-direction of light originating from the regions on either side of the jar. Presumably, the stray light signal observed in the blocked jar region with the blocker at the light source side of the matching tank (figure 3.10c) is mostly cancelled in the ratio of reference and data images during image reconstruction, giving the matched profiles in figure 3.10b.

The stray light signal recorded in the blocked jar region of the projection image when the blocker is placed at the camera side of the matching tank (figure 3.10d) requires further explanation. This form of stray light perturbation would not be expected to be derived from the negligible light scattering that occurs during travel through the air to the camera. The source of this effect is believed instead to be in the camera optics. In photography, there is a tendency for bright objects in the field of view to reduce the contrast everywhere within the image. This is

termed ‘veiling glare’, a global illumination effect that arises from multiple scattering in the camera lens optics system (Williams 1999). The standard method for glare measurement involves photographing a dark target surrounded by bright illumination. For high attenuation absorbing solutions such as the 1.48 mg/L solution in question, the transmission projection image acquired by the camera fits this description well. It is possible that veiling glare could be a significant source of stray light-induced bowing artifact in the case where the absorbing solution has comparatively high optical absorbance compared to the surrounding matching tank fluid. One approach to reducing veiling glare would be to use a higher quality CCD camera-lens system in the scanner, to prevent multiple scattering in the lens optics. Another tactic to reduce this form of perturbation would be to replace the scanner light source. A variable intensity light source with high area intensity through the jar media and lower area intensity through the low scattering matching fluid regions on either side of the jar would act to both increase the dynamic range of the imaging system and decrease the bright-next-to-dark variability leading to veiling glare. Both of these hardware changes are considered to be outside the scope of this work.

When the absorbing media-filled jar is replaced with a scattering media-filled 1 L PETE jar in the matching tank, the management of high angle re-directed light originating from the regions on either side of the jar becomes more important. This is likely because this light can be further scattered by particles in the scattering media-filled jar onto a cone beam primary ray path to the CCD detector. Referring to figure 3.11a, the level of perturbation is sufficiently different between the reference jar containing matching tank fluid and the jars containing scattering media, that a slight reduction in reconstructed attenuation (which is particularly noticeable near the PETE jar wall) is observed in the attenuation profiles without the side blockers in place. The effect is more clearly distinguished at the higher scattering concentration, where the ratio of stray light to primary transmitted light in the image is higher. Since there is an observable difference in

scattering systems, the question of whether the use of side blockers (baffles) in the Vista scanner (Babic *et al* 2008, Babic *et al* 2009) should become standard practice in the imaging of FXG gel dosimeters (incorporating a scattering gelatin matrix) is important.

The 0.02 g/L scattering solution in figure 3.11 was chosen for evaluation because it is a close match in mean attenuation ( $\sim 0.42 \text{ cm}^{-1}$ ) to a 5 wt% gelatin-in-water-filled 1 L PETE jar imaged at 590 nm ( $\sim 0.45 \text{ cm}^{-1}$ , see Olding *et al* 2010), giving a quantitative sense of the stray light perturbation due to the gelatin matrix. The average difference in reconstructed attenuation within the central 90% of the 0.02 g/L cross-jar profiles in figure 3.11a was found to be less than 0.5%. This represents the worst case scenario for the magnitude of stray light perturbation, with little cancellation between the essentially non-scattering matching-tank fluid filled 1 L PETE reference scan and the 0.02 g/L scattering-solution filled jar used for the data scan. The FXG gel dosimeter, on the other hand, has a relatively unchanging gelatin matrix in both the reference and data scans, and hence, should see greater cancellation of gelatin scatter signal between the two scans. Thus, stray light perturbation sourced from the regions on either side of the jar should reduce the shift in attenuation to much less than 0.5%. Even with this in mind, the side blockers could be left in if there were no other considerations to account for. However, the insertion of these blockers prevents the use of the projection image normalization software correction discussed in section 3.1. The normalization region corrects for global differences in light source intensity that may be as much as 0.5-1.0% between the reference and data scan. The variability in light source-detector stability over time is comparatively a more significant source of uncertainty. Hence, the decision was made to adhere to the protocol of employing the standard projection image normalization routine, and forego the use of side blockers in the scanner. While a smaller normalization region could be obtained between the jar edge and side blocker edge if side blockers were in place, the use of the larger standard normalization region is at present preferred.

This preference is mostly due to the possibility of greater refractive light intensity variations near the dosimeter jar wall.

Overall, the results presented in this report suggest some general conclusions for the implementation of optical CT-based gel dosimetry. First, most gel dosimeters will contain a gel-forming matrix material that is (a) inhomogeneous in refractive index against the surrounding aqueous media, and (b) not well-matched in refractive index to the dosimeter container material. As these differences in refractive index are dependent on, and may be accentuated by, changes in temperature, it is prudent to have some form of temperature control in the optical imaging system. It is also important to establish temperature controls for the actual container size and gel recipe (for example, the weight percentage of gelatin in solution changes the temperature response, see figure 3.6b) being used for the dosimetry.

Second, most gel dosimeters will exhibit some degree of ongoing dose development at the time of optical imaging. This suggests the implementation of a time control in the imaging. As a matter of standard practice, the post-irradiation time prior to imaging should be optimized for signal-to-noise, spatial dose integrity, and the speed of results (for each type of dosimeter). Beyond this, the goal should then be to complete the optical scan in as fast a time as possible to minimize intra-scan variations without compromising the quality of the raw intensity data.

Third, since the optical data will inherently be contaminated by stray light perturbation due to angled scatter from the gel-forming matrix material and refractive index mismatch at the container interface, the use of a second calibration gel dosimeter prepared in an identically sized container of the same material and filled with gel from the same batch is strongly indicated. The calibration and measurement dosimeter jars should then be irradiated and imaged under as closely matched time and temperature conditions as possible. The reasoning behind this conclusion is linked to the idea that most of the stray light perturbation will then be effectively cancelled in the

dose-to-attenuation calibration relationship applied between the two dosimeters and the environmental variations between dosimeters will be minimized.

### **3.5 Conclusions**

Improved FXG dosimeter readout using the Vista cone beam optical scanner can be realized through particular attention to the management of light source-detector stability, the wait time between irradiation and scan measurement, the overall scan time, and dosimeter scan temperature. Imaging protocols are established in this report that increases the level of control in each of these areas without compromising the practicality of fast optical cone beam FXG gel dosimeter readout. The identification of thermochromic behavior in the FXG gel, in particular, is an important step forward in improving its dosimetry. The largest sources of stray light perturbation in the system were identified as being due to angled scatter from the dosimeter gelatin matrix and refraction from the jar wall interfaces, both of which are better addressed through future work on dosimeter modification and an inter jar dose-to-attenuation calibration methodology, rather than by additional imaging protocols. The use of custom side blockers for stray light reduction is not considered to be critical, and it prevents the use of an important software projection image normalization routine. Hence, specific imaging protocols were not realized in this work for the management of stray light perturbation in this scanner-dosimeter combination. Future effort in this regard should be primarily directed toward substitution of the FXG dosimeter gelatin matrix and dosimeter container materials with stray-light reducing alternatives.

### **3.6 References**

- Babic S, Battista J and Jordan K 2008 Three-dimensional dose verification for intensity-modulated radiation therapy in the radiological physics centre head-and-neck phantom using optical computed tomography scans of ferrous xylenol-orange gel dosimeters. *Int.J.Radiat.Oncol.Biol.Phys.* 70 1281-1291.
- Babic S, McNiven A, Battista J and Jordan K 2009 Three-dimensional dosimetry of small megavoltage radiation fields using radiochromic gels and optical CT scanning. *Phys.Med.Biol.* 54 2463-2481.
- Baldock C, Harris P J, Piercy A R and Healy B 2001 Experimental determination of the diffusion coefficient in two-dimensions in ferrous sulphate gels using the finite element method. *Australas.Phys.Eng Sci.Med.* 24 19-30.
- Bero M A and Kharita M H 2004 Effects of ambient temperature on the FXG radiochromic gels used for 3-D dosimetry. *J.Phys.: Conf.Ser.* 3 236-239.
- Bosi S, Naseri P, Puran A, Davies J and Baldock C 2007 Initial investigation of a novel light-scattering gel phantom for evaluation of optical CT scanners for radiotherapy gel dosimetry. *Phys.Med.Biol.* 52 2893-2903.
- Bosi S G, Brown S, Sarabipour S, De Deene Y and Baldock C 2009 Modelling optical scattering artefacts for varying pathlength in a gel dosimeter phantom. *Phys.Med.Biol.* 54 275-283.
- De Deene Y 2004 Fundamentals of MRI measurements for gel dosimetry. *J.Phys.: Conf.Ser.* 3 87-114.
- De Deene Y and Baldock C 2002 Optimization of multiple spin-echo sequences for 3D polymer gel dosimetry. *Phys.Med.Biol.* 47 3117-3141.
- De Deene Y, Hurley C, Venning A, Vergote K, Mather M, Healy B J and Baldock C 2002 A basic study of some normoxic polymer gel dosimeters. *Phys.Med.Biol.* 47 3441-3463.
- De Deene Y, Vergote K, Claeys C and De Wagter C 2006 The fundamental radiation properties of normoxic polymer gel dosimeters: a comparison between a methacrylic acid based gel and acrylamide based gels. *Phys.Med.Biol.* 51 653-673.
- Doran S 2009 The history and principles of optical computed tomography for scanning 3-D radiation dosimeters: 2008 update. *J.Phys.: Conf.Ser.* 164 98-119.
- Doran S J, Koerkamp K K, Bero M A, Jenneson P, Morton E J and Gilboy W B 2001 A CCD-based optical CT scanner for high-resolution 3D imaging of radiation dose distributions: equipment specifications, optical simulations and preliminary results. *Phys.Med.Biol.* 46 3191-3213.
- Feldkamp L A, Davis L C and Kress J W 1984 Practical cone-beam algorithm. *J.Opt.Soc.Amer.* 1 612-619.

- Franklin J and Wang Z Y 2002 Refractive Index Matching: A General Method for Enhancing the Optical Clarity of a Hydrogel Matrix. *Chem.Mater.* 14 4487-4489.
- Gore J C, Kang Y S and Schulz R J 1984 Measurement of radiation dose distributions by nuclear magnetic resonance (NMR) imaging. *Phys.Med.Biol.* 29 1189-1197.
- Gore J C, Ranade M, Maryanski M J and Schulz R J 1996 Radiation dose distributions in three dimensions from tomographic optical density scanning of polymer gels: I. Development of an optical scanner. *Phys.Med.Biol.* 41 2695-2704.
- Groh W and Zimmermann A 1991 What is the lowest refractive index of an organic polymer? *Macromolecules* 24 6660-6663.
- Harris P J, Piercy A and Baldock C 1996 A method for determining the diffusion coefficient in Fe(II/III) radiation dosimetry gels using finite elements. *Phys.Med.Biol.* 41 1745-1753.
- Islam K T, Dempsey J F, Ranade M K, Maryanski M J and Low D A 2003 Initial evaluation of commercial optical CT-based 3D gel dosimeter. *Medical Physics*. 30 2159-2168.
- Jordan K and Battista J 2006 Linearity and image uniformity of the Vista<sup>TM</sup> optical CT scanner. *J.Phys.: Conf.Ser.* 56 217-220.
- Jordan K and Battista J 2009 Scatter measurements for optical cone-beam computed tomography. *J.Phys.: Conf.Ser.* 164 159-163.
- Kak A C and Slaney M 2001 *Principles of Computerized Tomographic Imaging*. Philadelphia: Society for Industrial and Applied Mathematics. 327.
- Kelly B G, Jordan K J and Battista J J 1998 Optical CT reconstruction of 3D dose distributions using the ferrous- benzoic-xylenol (FBX) gel dosimeter. *Med.Phys.* 25 1741-1750.
- Krstajic N and Doran S J 2006 Focusing optics of a parallel beam CCD optical tomography apparatus for 3D radiation gel dosimetry. *Phys.Med.Biol.* 51 2055-2075.
- Krstajic N and Doran S J 2007a Fast laser scanning optical-CT apparatus for 3D radiation dosimetry. *Phys.Med.Biol.* 52 N257-N263.
- Krstajic N and Doran S J 2007b Characterization of a parallel-beam CCD optical-CT apparatus for 3D radiation dosimetry. *Phys.Med.Biol.* 52 3693-3713.
- Lopatiuk-Tirpak O, Langen K M, Meeks S L, Kupelian P A, Zeidan O A and Maryanski M J 2008 Performance evaluation of an improved optical computed tomography polymer gel dosimeter system for 3D dose verification of static and dynamic phantom deliveries. *Med.Phys.* 35 3847-3859.
- Oldham M, Siewersden J H, Shetty A and Jaffray D A 2001 High resolution gel-dosimetry by optical-CT and MR scanning. *Med.Phys.* 28 1436-1445.

- Olding T, Holmes O and Schreiner L J 2010 Cone beam optical computed tomography for gel dosimetry I: scanner characterization. *Phys.Med.Biol.* 55 2819-2840.
- Olsson L E, Fransson A, Ericsson A and Mattsson S 1990 MR imaging of absorbed dose distributions for radiotherapy using ferrous sulphate gels. *Phys.Med.Biol.* 35 1623-1631.
- Rae W I, Willemse C A, Lotter M G, Engelbrecht J S and Swarts J C 1996 Chelator effect on ion diffusion in ferrous-sulfate-doped gelatin gel dosimeters as analyzed by MRI. *Med.Phys.* 23 15-23.
- Schreiner L J and Olding T 2009 Gel Dosimetry. In: Rogers, D. W. and Cygler, J. E. *AAPM Medical Physics Monograph No. 34: Clinical Dosimetry Measurements in Radiotherapy*. Madison, WI, USA, Medical Physics Publishing.
- Shabana H M 2004 Refractive index-structure correlation in chemically treated polyethylene terephthalate fibres. *Polymer Testing* 23 291-297.
- Tarte B J and van Doorn T 1995 Laser based tomographic scanning of gel volumes for applications in ionising radiation dosimetry. *10th Conference of the Australasian Optical Society, University of Queensland* .
- Tarte B J and van Doorn T 1993 Optical scanning of ferrous sulphate gels for radiotherapy treatment dosimetry. *APSEM/BECON Australasian Conference on Physical Science and Engineering in Medicine /Biomedical Engineering Conference* .
- van Doorn T, Bhat M, Rutten T P, Tran T and Costanzo A 2005 A fast, high spatial resolution optical tomographic scanner for measurement of absorption in gel dosimetry. *Australas.Phys.Eng Sci.Med.* 28 76-85.
- Williams T J 1999 Veiling glare. *The optical transfer function of imaging systems*. Bristol, UK, Institute of Physics Publishing. 405.
- Wolodzko J G, Marsden C and Appleby A 1999 CCD imaging for optical tomography of gel radiation dosimeters. *Med.Phys.* 26 2508-2513.
- Wulfsberg G 2000 *Inorganic chemistry*. Sausalito, CA: University Science Books. 368

## **Chapter 4**

### **IMRT Treatment Plan Quality Assurance Using FXG Gels**

A version of this chapter has been prepared for submission to Medical Physics as: *Olding T, Darko J and Schreiner L J “Evaluation of IMRT treatment plans using cone beam optical CT-based FXG gel dosimetry”.*

#### **4.1 Abstract**

An approach is described in this report for the three-dimensional (3D) evaluation of intensity modulated radiation therapy (IMRT) deliveries using a Fricke-xylenol orange-gelatin (FXG) gel dosimeter in combination with the fast, easily accessible optical readout tool of cone beam optical computed tomography (CT). The dose response linearity, same batch inter-jar dose response reproducibility, and megavoltage energy independence of the FXG gel dosimeter were assessed to set the calibration basis for IMRT delivery evaluation. A wax-filled reproduction of the head-and-neck from a Kyoto SBU-4 Rando anthropomorphic phantom (Capintec, Ramsey, NJ) was prepared for the IMRT study, with a custom cavity designed to fit a standard-sized (1 L) FXG-gel filled dosimeter. Following imaging on the CT simulator and subsequent contouring, a test six field, 6 MV, 200 cGy IMRT plan was generated and delivered to the custom head-and-neck phantom. After consideration of the uncertainties involved in the IMRT treatment planning, the calibrated FXG gel dose results indicate a systematic negative shift up to 5-6% in gel dose compared to the treatment plan dose, likely due to stray light perturbation in the optical readout. In an effort to reduce stray light perturbation in the system, the standard porcine skin gelatin matrix component of the FXG gel dosimeter was replaced with a bovine bone gelatin and the IMRT delivery was repeated. A comparison of the 3D Low's gamma function analyses of the two

deliveries indicates significant improvement in the dosimetry after gelatin substitution. The porcine gelatin-based dosimeter demonstrated 88% voxel agreement between treatment plan to gel-measured dose using 5% dose difference and 3 mm distance-to-agreement criteria, while the bovine gelatin-based dosimeter achieved 95% voxel agreement using more restrictive 3% dose difference and 3 mm distance-to-agreement gamma criteria.

## 4.2 Introduction

Cancer treatments using conformal or intensity modulated radiation therapy (IMRT) involve complex three-dimensional (3D) dose distributions that are characterized by large dose changes over small spatial displacements. A further complication in IMRT treatments is that the dose is delivered dynamically, so that specific points in the irradiated volumes receive their final dose only over a total treatment time. Therefore, full dose verification of an IMRT delivery is labor intensive and often impractical with traditional dosimetry techniques employing ion chambers, diodes, thermo-luminescent dosimeters (TLD), or film.

Gel dosimetry is a promising candidate for high resolution 3D dose verification of sophisticated radiation therapy delivery options such as IMRT. The majority of recent gel studies evaluating conformal or IMRT deliveries with gel dosimetry have employed polymer gel formulations and magnetic resonance imaging (MRI) (Oldham *et al* 1998, Low *et al* 1999, De Neve *et al* 1999, De Deene *et al* 2000, Vergote *et al* 2003, Gustavsson *et al* 2003, Vergote *et al* 2004, Ceberg *et al* 2008) or optical computed tomography (CT) dose readout (Ibbott *et al* 2002, Xu *et al* 2004, Oldham *et al* 2005, Wuu and Xu 2006, Lopatiuk-Tirpak *et al* 2008). One study has been completed using a Fricke-xylenol orange-gelatin (FXG) dosimeter and optical CT readout (Babic *et al* 2008b). A non-tissue-equivalent radiochromic polyurethane-based dosimeter (PRESAGE<sup>TM</sup>) has also been developed for optical CT readout and utilized for IMRT treatment

verification (Guo *et al* 2006a, Guo *et al* 2006b, Oldham *et al* 2008, Sakhalkar *et al* 2009a, Sakhalkar *et al* 2009b).

There are advantages and disadvantages associated with each gel dosimeter-readout modality combination. The general practice for polymer gel-MRI evaluation of dose deliveries has been to calibrate the relationship between absorbed dose and R2 spin-spin relaxation rate with small vials irradiated to known doses covering the dose range of the IMRT delivery. This calibration is then applied to the larger IMRT dosimeter, and the IMRT gel-measured dose is most often normalized to a well-measured reference point in the delivery to achieve a relative dose distribution. One parameter for evaluating the delivery is Low's gamma function (Low *et al* 1998, Low and Dempsey 2003), which quantifies the agreement of the combined metrics of dose difference and distance-to-agreement between two dose distributions into a single 'gamma' value. The gamma function assigns a value less than 1 in regions where dose difference and distance to agreement are within set criteria, for example, 3% dose and 3 mm distance between points in the treatment planning system-calculated and gel-measured dose distributions. Values greater than 1 are understood as having failed the criteria. Relative dose distributions from polymer gel-MRI measurement have been observed in multiple studies as achieving full volume gamma value agreement greater than 90% between a well-known reference dose and gel-measured dose for 3% and 3mm criteria. With a high level of care, 99.5% agreement for 4% and 5 mm comparison criteria without gel dose normalization to a reference point has been reported (Vergote *et al* 2004). However, while these high resolution, dose distribution comparisons represent a significant step forward in 3D dose verification, limited accessibility to MRI prevents the use of 3D polymer gel-MRI dosimetry in most clinics.

Polymer gel-optical CT measurement of IMRT dose distributions involves a relatively low cost scanner that is widely accessible. The challenge with this type of measurement is that the

scan data is perturbed by angled scatter and other stray light effects (Oldham *et al* 2003, Oldham and Kim 2004) which affect the gel measurement accuracy of complex IMRT dose distributions. Also, as in the case of polymer gel-MRI measurement, results are not acquired quickly. A 12-hour period between irradiation and measurement is typically observed to ensure full dosimeter development, and the scan, reconstruction, and analysis time is also on the order of several hours.

Although optical CT-based gel dosimetry is still not as well-developed its MRI counterpart, sustained development of this technology (Doran and Krstajic 2006, Doran 2009) has led to new possibilities in optical absorption-based gel dosimetry. Fast area detection optical CT scanners based on cone beam (Wolodzko *et al* 1999, Babic *et al* 2008b) and parallel beam (Doran *et al* 2001, Krstajic and Doran 2006, Krstajic and Doran 2007) charge-coupled-device (CCD) configurations have been introduced that promise to address the previously limiting time sensitive diffusion effects affecting spatial integrity of dose in the optically absorbing FXG dosimeter (Kelly *et al* 1998, Babic *et al* 2009). Also, in another approach, the change in chemistry to a PRESAGE dosimeter reduces diffusion in its optically absorbing matrix (Guo *et al* 2006a, Guo *et al* 2006b). This enables the use of the less stray-light-perturbed laser beam-photodiode point detection-based optical CT scanners with this type of dosimeter, albeit with a tradeoff of non-tissue equivalence and longer scan times.

The FXG gel dosimeter-cone beam optical CT imaging system is the focus of this work. This combination has the advantage of simple non-toxic dosimeter preparation, high dose sensitivity, fast response and scan times leading to same day results, and accurate readout without normalization to a relative gel-measured dose distribution (Babic *et al* 2008b). In the report by Babic *et al* (2008b), a 6 x 6 cm 12 MeV electron beam-irradiated FXG gel imaged with a laser beam point detection scanner is used to establish the relationship between dose and optical absorption. A 6 field IMRT plan is delivered to a second FXG dosimeter inserted in the

Radiological Physics Centre (RPC) head-and-neck phantom and scanned with the Vista<sup>TM</sup> cone beam optical CT scanner (Modus Medical Ltd, London, ON, Canada). A single value stray light correction related to cone beam readout is applied prior to image reconstruction and IMRT gel dose is then determined using the electron beam dose-to-attenuation calibration relationship.

The investigations in this report build on the understanding and application of FXG gel-cone beam optical CT dosimetry, making use of previous work on scanner characterization and imaging protocols (Olding and Schreiner 2010, Olding *et al* 2010). To simplify equipment requirements from that of Babic *et al* (2008), the Vista scanner is used exclusively for both gel calibration and IMRT gel dosimetry. An additional motivation for using the same scanner in both cases is to hopefully improve the dosimetry by minimizing the differences between the calibration and IMRT dose measurement conditions. The dose calibration linearity, intra-batch reproducibility, and megavoltage range energy independence of the FXG dosimeter are established, serving as the basis for IMRT evaluation. An approach is described for head-and-neck IMRT plan evaluation using a standard FXG-filled 1 L PETE jar in phantom. A dosimeter modification is then introduced that reduces stray light perturbation in gel imaging and hence improves the absolute IMRT measurement capabilities of the FXG gel dosimeter in combination with cone beam optical CT.

### **4.3 Materials and Methods**

#### **4.3.1 FXG Gel Preparation**

FXG dosimeters were prepared according to the recipe outlined by Babic *et al* (2008), with final concentrations of 0.3 mM ferrous ammonium sulphate (Cat.No.203505, Sigma-Aldrich Ltd, Oakville, Canada), 0.05 mM xylenol orange (Cat.No.398187, Sigma-Aldrich Ltd), 65 mM sulfuric acid (Cat.No.258105, Sigma-Aldrich Ltd), and 6 wt% gelatin in distilled, de-ionized

water. The gelatin was added to a portion of the water and allowed to swell for 15 minutes at room temperature. The mixture was then heated to 45°C, and held for 5-20 minutes at that temperature to dissolve the gelatin. The other components were dissolved in the remaining portion of the water, and then added to the dissolved gelatin-water mixture cooled to 35°C. Two different gelatin sources were investigated, the standard 300 bloom Type A porcine skin gelatin, (Cat.No.G2500, Sigma-Aldrich Ltd), and a photographic quality 300 Bloom bovine bone gelatin (ZA-A300, Eastman Gelatine Corp., Peabody, MA, USA). The cooled solutions were poured into 1 L PETE jars or standard 10 mm poly-methyl methacrylate (PMMA) spectrophotometer cuvettes and allowed to set overnight in a refrigerator prior to irradiation. FXG dosimeters in this report were prepared with the standard porcine gelatin, unless otherwise specified.

#### **4.3.2 Optical Imaging**

Three-dimensional imaging of FXG gel-filled 1 L PETE jar dosimeters was performed at a wavelength of 590 nm using the Vista cone beam optical CT scanner. For each scan, a set of 410 light intensity transmission projections were acquired over 360° by a 1024 x 768 pixel, 12-bit CCD camera using a 2/3" diameter, 12 mm focal length lens set to the preferred aperture setting of f5 (Olding *et al* 2010). The FXG gel dosimeters were warmed according to protocol to the Vista scanner bath temperature in a covered (light blocking) holding tank (Olding and Schreiner 2010), and pre-irradiation reference scans and post-irradiation data scans were acquired at a matched temperature (i.e. within ± 0.1°C of each other) in the range of 20.0-21.0°C. Temperature agreement to within the practical measurement limit of ± 0.1°C was required between the calibration electron beam and IMRT measurement dosimeters for both the reference and data scans.

Reference scans were completed on each FXG dosimeter jar close to the time of irradiation, at the highest shutter exposure time possible without inducing camera pixel saturation,

and the lowest gain setting. Data scans were acquired using the same camera settings as the reference scan at the preferred post-irradiation time of  $30 \pm 0.2$  minutes on the FXG dosimeters (Olding and Schreiner 2010). The data scan camera settings were automatically set to the reference scan settings by the VistaScan software. Reconstructed 3D linear optical attenuation data sets were obtained using the natural logarithmic ratio of the data and reference scans through use of the VistaRecon software, employing the Feldkamp filtered back-projection reconstruction algorithm with a Hamming filter (Feldkamp *et al* 1984). Dark field images were acquired for and subtracted from each of the reference and data scans prior to image reconstruction at a cubic voxel resolution of 0.5 mm. Reference and data scans were acquired over a period of 4.5 minutes and high resolution (0.5 mm) reconstruction of the  $12.8 \times 12.8 \times 12.8$  cm<sup>3</sup> volume was completed in 10 minutes on a standard desktop computer. Matching tank solution for the scanner consisted of a 10 wt% propylene glycol-water mixture, the refractive index of which ( $1.344 \pm 0.001$  at 590 nm) was monitored over time using a handheld refractometer with a central measurement wavelength of 589 nm (r<sup>2</sup> mini refractometer, Reichert Analytical Instruments, Depew, NY, USA) at room temperature ( $21 \pm 1^\circ\text{C}$ ). Temperature measurements were taken using a digital temperature probe (TM99A-NA Digital Thermometer, Nuclear Associates, Carle Place, NY, USA). Line profiles and regions of interest (ROI) in FXG dosimeter projection data and optical CT reconstructed 3D data sets were evaluated using Microview 2.1.2 (GE Healthcare, United Kingdom) or MatLab (Mathworks, Newark NJ) software.

Single value FXG gel-filled cuvette optical attenuation measurements (at 590 nm) were acquired at a post irradiation time of  $30 \pm 5$  minutes and a temperature of  $23.0 \pm 0.2^\circ\text{C}$  using an Ultrospec 1000 UV/Visible spectrophotometer (Biochrom Ltd, Cambridge UK) at 590 nm.

#### 4.3.3 FXG Gel Response Calibration

Gel irradiations were completed on the day after manufacture using a Varian Clinac 21iX linear accelerator (Varian Medical Systems, Palo Alto, CA, USA), a T780C Co-60 radiotherapy unit (Best Theratronics, Kanata, ON), or a Gulmay superficial x-ray therapy system (Gulmay Medical Inc., Buford, GA, USA). Depth fiducials were marked on the calibration FXG gel dosimeters in permanent red marker, as reference points for registration of depth dose to attenuation in the reconstructed optical CT image. Calibration 6 x 6 cm electron beams (6, 12, and 20 MeV) were delivered through the top gel surface in the PETE jar with the lid off (figure 4.1a), typically to a maximum dose of 180-220 cGy using the Clinac irradiator. The 6 MV and 15 MV photon beam calibrations were delivered similarly. A 200 cGy superficial delivery was performed using the Gulmay unit at 80 kVp, employing a 6 cm cone set to the gel surface.

Calibration photon beam central axis depth dose data were obtained from  $0.13 \text{ cm}^3$  ionization chamber-water tank measurements (CC13/TNC ionization chamber, Scanditronix-Wellhofer North America, Bartlett, TN, USA). Calibration electron beam central axis depth dose

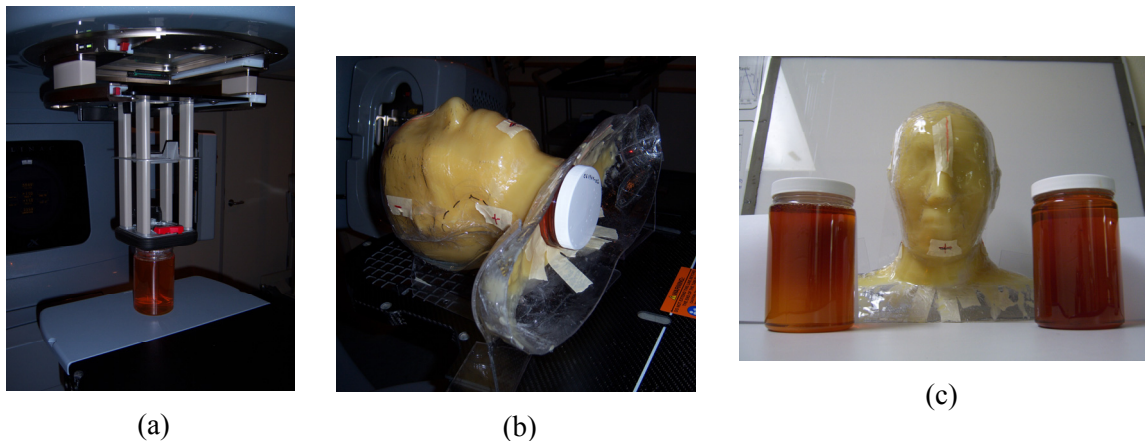


**Figure 4.1:** (a) Calibration gel dosimeter electron beam setup at the treatment unit. (b) A wax-filled reproduction of the head and neck from a Kyoto SBU-4 Rando anthropomorphic phantom (Capintec, Ramsey, NJ) prepared at the CCSEO, with a cavity for insertion of a 1 L PETE gel dosimeter jar. (c) Another view of the wax Rando reproduction, with a measurement jar for a test IMRT plan on the right, and an electron beam-irradiated FX gel calibration jar on the left.

data were acquired from diode-water tank measurements (DEB002-3727, DEB022-3608, Scanditronix-Wellhofer North America). The dose data are considered to be accurate to within an uncertainty of  $\pm$  0.5% based on standard deviation of measurement. The irradiator room temperature was not specified, but the gel dosimeters were kept in a covered holding tank filled with water maintained to  $20.0\text{--}21.0 \pm 0.2^\circ\text{C}$  until the point of irradiation. Given that the yield of the dose contrast-producing  $\text{Fe}^{3+}$  ions in aqueous solution increases with solution temperature by about 0.12% per degree Celsius (Shortt 1989), the variation in dosimeter response with temperature at the time of irradiation was considered to be minimal, and hence the room temperature was not strictly monitored.

A full dose range investigation was performed using a series of FXG gel-filled 10 mm PMMA spectrophotometer cuvettes. The cuvettes were inserted at known positions in a custom-built water tank and irradiated with a well-calibrated 10 x 10 cm field from the T780C Co-60 radiotherapy unit, rotating the cuvettes by  $180^\circ$  halfway through the irradiation. Auto-oxidation effects in the FXG gel were characterized by using the Vista scanner to image an un-irradiated 1 L FXG gel-filled PETE jar dosimeter at 30 minute intervals over a period of 5 hours. The dosimeter jar was removed between scans and stored at room temperature in the dark.

#### **4.3.4 IMRT Dose Evaluation**

A wax-filled reproduction of the head-and-neck from a Kyoto SBU-4 Rando anthropomorphic phantom (Capintec, Ramsey, NJ) was prepared at the Cancer Centre of Southeastern Ontario (CCSEO) for the IMRT study, with a custom cavity designed to fit the standard 1 L PETE jar gel dosimeter (figure 4.1b). A CT data set was acquired for the wax Rando reproduction with a FXG gel dosimeter inserted in the phantom cavity on a Picker PQ 5000 Philips CT scanner (Philips Medical Systems, Andover, MA, USA). Steel 1 mm beads and permanent marker fiducial marks were added to the wax-filled reproduction as reference points for positioning at the treatment unit.

The FXG gel dosimeter scanned using x-ray CT was not used further for IMRT dose measurement. However, all IMRT gel dosimeters in subsequent experiments were filled to the same jar height as the original CT scanned dosimeter to ensure accurate dose calculation.

A 6 field, 6 MV IMRT treatment plan was generated in Eclipse (Varian Medical, Palo Alto CA) using approximated target contours applied to the phantom CT data set, and a single fraction (prescription dose of 200 cGy) scheduled to the treatment unit. The irradiator used in all IMRT and electron beam calibration deliveries was a Varian Clinac 21iX linear accelerator with Advanced OBI (On-Board Imaging). Two gel dosimeters were used in each IMRT evaluation, filled from a single batch of gel (figure 4.1c). One container was irradiated with a well characterized electron beam and used for calibration. The other container was inserted into the wax-filled Rando reproduction. Fiducials on the Rando reproduction from the CT scan were utilized for set up of the IMRT delivery at the treatment unit. Cone beam x-ray CT (CBCT) imaging of the phantom was completed at a 1 mm cubic voxel resolution according to the standard head protocol (100kVp/145mAs, half scan with full bowtie filter), and 3D-3D planning CT-onboard CBCT matching was performed. The treatment fraction was then delivered with the phantom positioned on the head-and-neck S frame. The full IMRT delivery evaluation was then repeated with the phantom positioned directly on the treatment couch.

Optical CT gel-measured IMRT dose data were registered to Eclipse (Varian Medical, Palo Alto CA) planning data in MatLab (Mathworks, Newark NJ), for viewing in the Computational Environment for Radiotherapy Research (CERR) developed at Washington State University, St.Louis, MO, USA (Deasy *et al* 2003). First, a permanent red marker was used to indicate 6 fiducials (two sets of three fiducials marked on separate parallel planes) on the exterior surface of the PETE jar, to fix the spatial position of the optical CT volume data. Steel 1 mm diameter beads were then affixed with tape on top of the permanent marker fiducials to provide

positioning information from the 3D-3D planning CT matched onboard CBCT scan. The beads were removed from the jar after the irradiation, before optical CT scanning. An in-house registration routine written in MATLAB (Holmes 2008) was used to align the optical CT and CBCT fiducial data points through an affine transformation solid body rotation, and register the optical CT dose data to the planning CT. The mean CBCT scan dose to the gel dosimeter was separately determined by ion chamber measurements as  $0.8 \pm 0.1$  cGy, and was appropriately accounted for. Dose evaluations between the reference Eclipse planning dose and optical CT gel-measured dose were completed using in-house developed routines in MatLab and contouring tools in the CERR environment for full 3D voxel-by-voxel Low's gamma function (Holmes 2008) and dose difference histogram analysis.

#### **4.3.5 Modified Dosimeter Characterization**

One method of assessing stray light perturbation in the Vista scanner projection image data involves the calculation of two-dimensional (2D) transmission percentage maps from the scanner projection data, described in more detail elsewhere (Olding *et al* 2010). Briefly, two 5 wt% gelatin-in water-filled 1 L PETE jars were prepared, one using a porcine gelatin from Sigma-Aldrich Ltd, and the other using a bovine gelatin from Eastman Gelatine Corp. Projection images were acquired of the two gelatin-in-water-filled jars using the Vista scanner, with and without a 2 mm pinhole grid blocker (16 mm square spacing between pinholes) in place at the light source side of the matching tank. Note that each pinhole can be thought of as passing a small ray bundle of light. Then, the intensity of light reaching the center pixel in the illuminated region at the detector with the pinhole blocker in place relative to the intensity reaching the same “center” pixel under open field condition is effectively a measure of how much light reaching the camera is sourced in that ray bundle. A full 2D transmission percentage map showing the effects of stray light perturbation was then obtained for each gelatin type by evaluating the data at the pinhole

coordinates in the open field and ‘blocked’ projection images, and interpolating between the points using a bi-cubic spline interpolation routine in MatLab.

The molecular weight distributions of both types of gelatin were assessed by size exclusion chromatography using an external analytical testing service provided through Eastman Gelatine Corp.

## 4.4 Results

### 4.4.1 FXG Gel Response Calibration

Figure 4.2a shows the spectrophotometer-measured attenuation response from the series of gel-filled 10 mm square PMMA cuvettes irradiated to set dose values in the range of 0-50 Gy. In the range of 0-5 Gy, the dose sensitivity can be well-calibrated to a linear relationship (see figure 4.2a inset), with a  $R^2$  correlation coefficient of 0.9994. Figure 4.2b shows the effect of auto-oxidation in the FXG gel, a slow reaction over time that increases the optical attenuation background in the dosimeter (Kelly *et al* 1998, Babic *et al* 2008a). As the dosimeter stabilizes in temperature

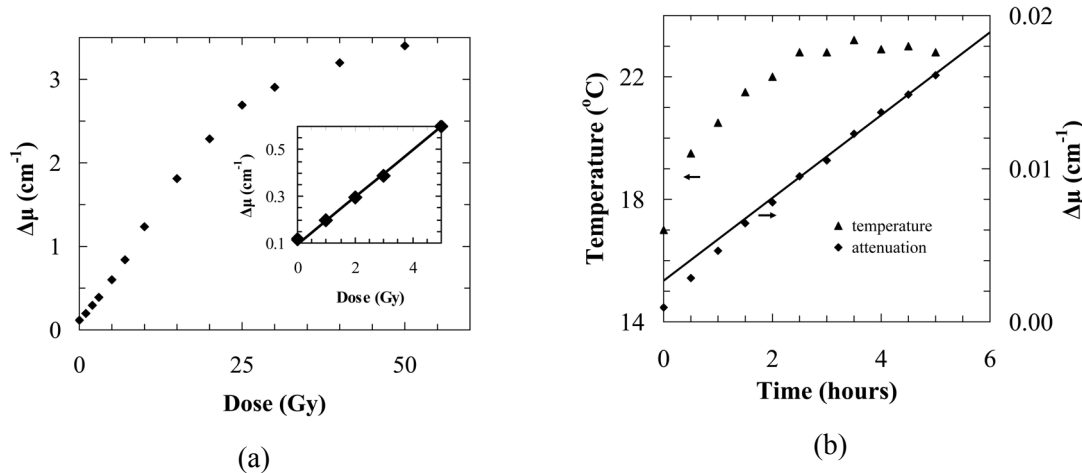


**Figure 4.2:** (a) Dose response of the FXG gel recipe into the saturation range. (b) Auto-oxidation rate of the FXG dosimeter under room temperature conditions. The mean attenuation values reported in (b) were determined from an 8 cm diameter, 10 cm high region-of interest centered in volume of the FXG gel-filled 1 L PETE jar. A linear fit to the attenuation data obtained at a dosimeter temperature greater than 22°C is also shown in the plot.

near  $23^{\circ}\text{C}$  over time, the rate of auto-oxidation becomes linear at  $0.00270 \pm 0.00005 \text{ cm}^{-1} \text{ hr}^{-1}$ . This study was repeated at a lower temperature, and the auto-oxidation rate was found to be  $0.00150 \pm 0.00003 \text{ cm}^{-1} \text{ hr}^{-1}$  when the 1 L FXG gel dosimeter was stored in a covered water-filled holding tank at  $21.0 \pm 0.2^{\circ}\text{C}$  prior to optical scanning and between scans.

Figure 4.3a shows raw calibration depth dose data over a range of energies in the FXG gel dosimeter, corrected for auto-oxidation during the time between the reference and data scans. Optical CT scans of calibration electron and photon beams were acquired at  $30 \pm 0.2$  minutes post-irradiation in the temperature range of  $20.8\text{-}21.2 \pm 0.1^{\circ}\text{C}$ . Each attenuation data point was obtained as the mean value of a 5 mm diameter single slice circular region of interest (ROI) on the central depth dose axis of the electron beam in the optical CT volume image ( $\sim 75$  pixels). The dose is considered to be uniform over this region across the lateral and superior-inferior profiles

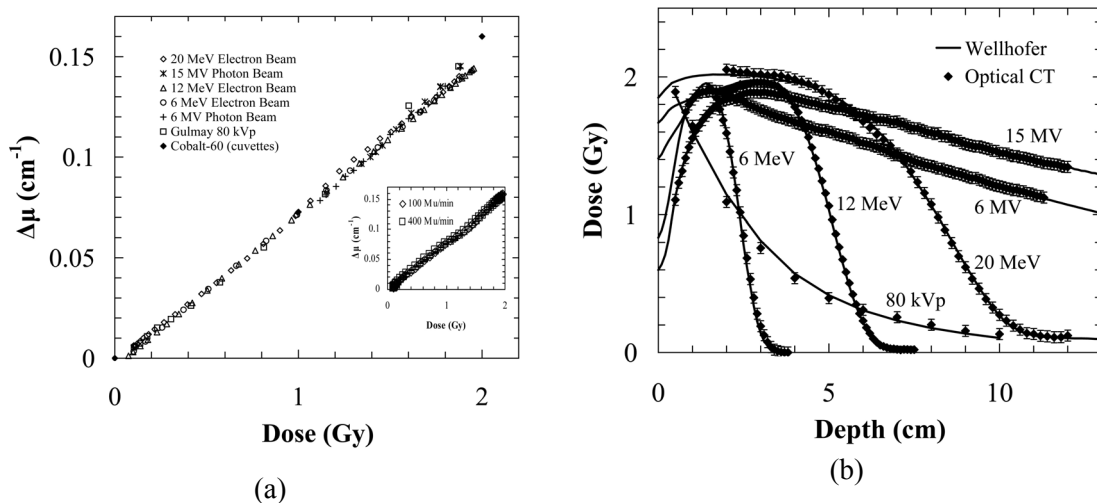
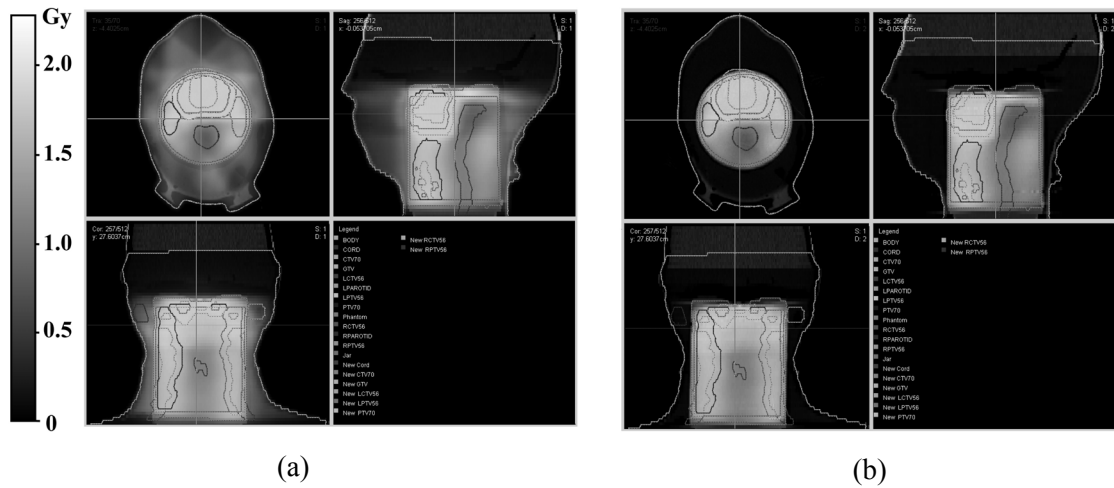


**Figure 4.3:** (a) Calibration data corrected for auto-oxidation, showing the reproducibility and energy dependence of the FX gel dosimeter. The inset plot shows the 20MeV electron beam calibration of two FXG 1 L PETE dosimeters from same gel batch, delivered at different dose rates. (b) Depth dose curves of the different treatment beams from (i) the Wellhofer measurements in a water tank and (ii) the calibrated FXG dosimeter (assuming a linear calibration relationship between absorbed dose and optical attenuation). For the purpose of clarity, only the line through the Wellhofer depth dose data is shown in this plot.

of the electron beam gel delivery (Babic *et al* 2008b), and taking the mean value in this region improves the signal-to-noise ratio. The Co-60 irradiated cuvette-spectrophotometer attenuation measurements are also reported in figure 4.3a for comparison, normalized with a temperature correction (for a 2°C scan temperature difference) to 21°C (Olding and Schreiner 2010). Electron beam calibrations for two FXG 1 L PETE jar dosimeters prepared from the same gel batch and irradiated with a 200 cGy, 6 x 6 cm, 20 MeV electron beam at two different dose rates are also shown in figure 4.3a (inset). At each depth, the mean optical attenuation values from these two dosimeters were observed to be in agreement within error over the full dose-to-attenuation calibration range. Figure 4.3b shows the agreement between the Wellhofer ion chamber-measured and linear dose-to-attenuation fit calibrated FXG gel (optical CT) depth dose curves.

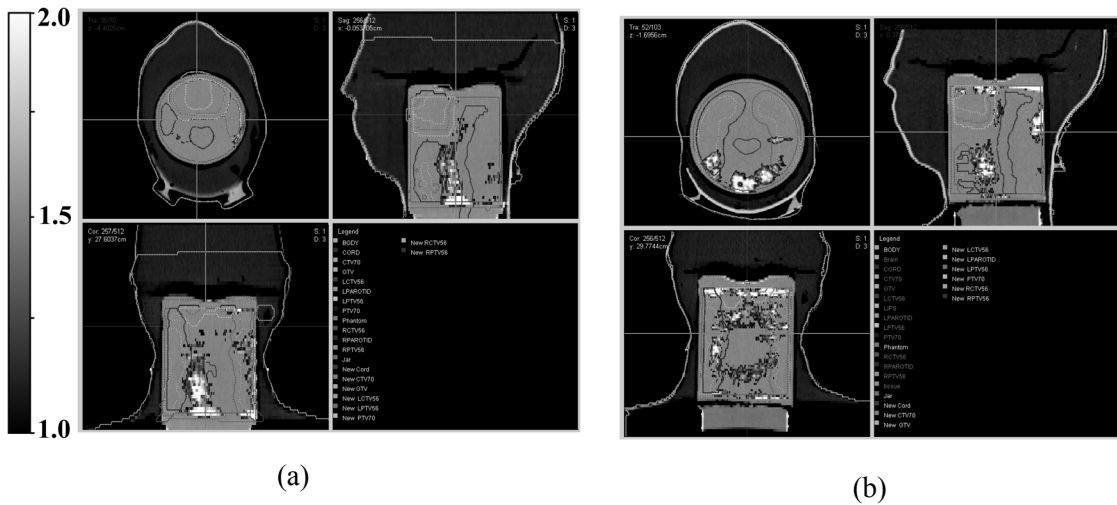
#### 4.4.2 IMRT Delivery Evaluation

Figure 4.4 shows 3D visualizations in the CERR environment of the (a) treatment plan and (b) gel-measured dose distributions overlaid on the contoured planning CT images for a six field,



**Figure 4.4:** (a) Eclipse treatment planning dose and (b) gel-measured dose (right) for a test 6 field 200 cGy IMRT plan delivered to the wax-filled Rando reproduction.

6MV, 200 cGy (single fraction) IMRT plan delivery. IMRT gel dose was calibrated with a 200 cGy, 20MeV gel dose electron beam delivery, as described previously. Figure 4.5a presents the results of 3D Low's gamma function voxel-by-voxel comparison of gel-measured dose against the reference Eclipse dose for the above IMRT delivery, employing 5% dose difference and 3 mm distance-to-agreement criteria. The phantom in this case was positioned on the couch-fitting head-and-neck S-frame used for planning CT scanning and treatment plan dose calculations. The percentage of treatment plan dose and measured gel dose voxels in agreement (i.e. gamma value less than 1) was 88.8%, within the ROI dose evaluation volume covering the central 8 cm in diameter and 10 cm in height of the jar. Regions failing the 3D gamma function criteria are represented in figure 4.5a as a grayscale wash overlaid on the planning CT image data and passing regions in the jar are not plotted, for clarity. Observed failures are primarily localized to lower dose regions in the delivery near the spinal cord contour and the left lateral jar edge. The



**Figure 4.5:** Fully 3D Low's gamma function comparisons (5%, 3mm) between reference treatment planning dose calculated in Eclipse™ and gel-measured dose delivered to the wax-filled Rando reproduction with a 1L PETE jar FXG gel dosimeter insert. In (a), the head-and-neck S-frame employed in the planning CT and dose calculations was employed in the IMRT delivery. In (b), the phantom was placed directly on the treatment couch during delivery of the same IMRT irradiation.

regions of failure outside the dosimeter jar and at the superior end of the jar are the result of gamma function comparison outside the extent of the gel dose data. The same IMRT irradiation was then repeated, but in this case the fraction was delivered with the phantom positioned directly on the treatment couch, instead of on the head-and-neck S-frame. The percentage voxel agreement within the 5%, 3mm 3D gamma function criteria was reduced in this case to 81.6% (figure 4.5b).

Figure 4.6a shows the dose difference histogram (plan dose minus gel-measured dose) for the ROI volume of the FXG gel IMRT delivery employing the head-and-neck S-frame, including close to a million voxels of spatial dose data. A clear shift in magnitude is observed between the Eclipse plan and gel dose distributions, with an overall mean value calculated to be  $-9.8 \pm 9.5$  cGy. In comparison, a mean shift of  $-11.9 \pm 9.6$  cGy was determined from the dose difference

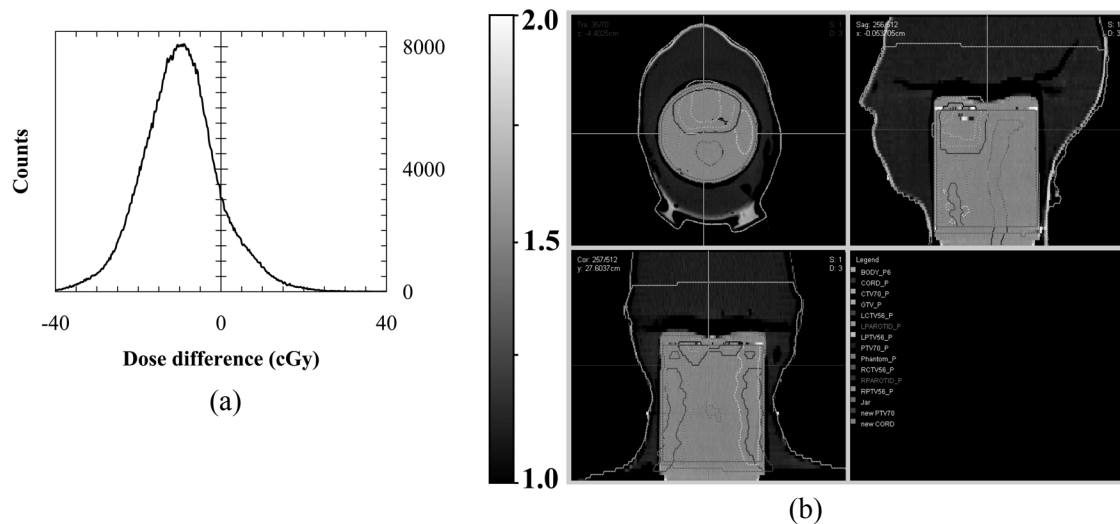


**Figure 4.6:** (a) Dose difference histogram in the ROI volume of the FXG gel IMRT delivery employing the head-and-neck S-frame. (b) A Low's gamma function comparison (3%, 3mm) between reference treatment planning dose calculated in Eclipse<sup>TM</sup> and gel-measured dose, with a 10 cGy shift added to the gel-measured dose data.

histogram for the IMRT delivery directly through the couch. When a positive mean shift of 10 cGy is applied to the S-frame IMRT delivery gel dose data, the agreement between the plan dose and gel-measured dose greatly increases to passing 98.7% of the ROI voxels in a 3%, 3mm 3D gamma function comparison (figure 4.6b).

The 6 field, 6MV, 200 cGy single fraction IMRT delivery using the couch-fitted head-and-neck S-frame was repeated as described previously, with the standard 300 bloom porcine skin gelatin replaced with 300 bloom bovine bone gelatin in the gel batch used to prepare the FXG gel-filled 1 L PETE jar calibration and IMRT measurement dosimeters. IMRT dose was calibrated with a 200 cGy, 12 MeV gel dose electron beam delivery.

Figure 4.7a shows the dose difference histogram in the ROI volume of the bovine gelatin-based FXG gel dosimeter for this IMRT delivery. In this case, the mean value of the histogram

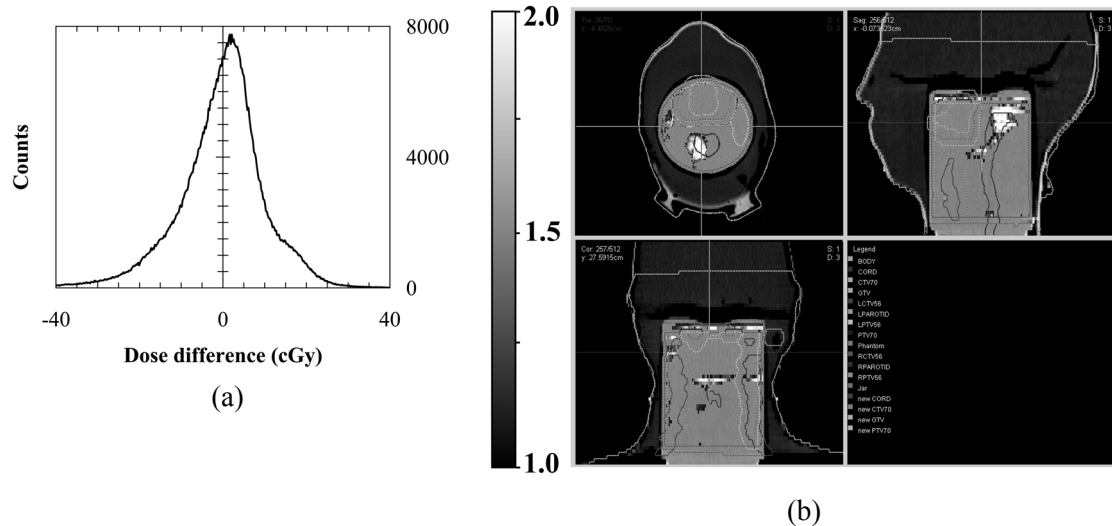


**Figure 4.7:** (a) Dose difference histogram in the ROI volume of the bovine-based FXG gel dosimeter IMRT delivery employing the head-and-neck S-frame. (b) A Low's gamma function comparison (3%, 3mm) between reference treatment planning dose calculated in Eclipse<sup>TM</sup> and gel-measured dose.

was determined to be  $-0.5 \pm 10.8$  cGy, indicating a significant reduction in mean dose shift between the plan and measurement. Figure 4.7b shows a CERR-based visualization of a voxel-to-voxel gamma function comparison (3%, 3mm) between reference treatment planning dose calculated in Eclipse<sup>TM</sup> and gel-measured dose delivered to the wax-filled Rando reproduction. Within the ROI volume of the FXG dosimeter, 95%+ of the voxels satisfy the 3% dose difference and 3mm distance-to-agreement criteria between the plan dose and gel-measured IMRT dose. Most of the failure occurs in the low dose region falling within or near the spinal cord contour.

#### 4.4.3 Modified Dosimeter Characterization

Figure 4.8a shows the profiles across two 5 wt% gelatin-water-filled 1 L PETE jars imaged in the Vista scanner at 590 nm and reconstructed (against a reference scan of a 1 L PETE jar filled with matching tank solution) to a cubic voxel resolution of 0.5 mm. One of the gelatin-water-filled jars was prepared using the standard 300 bloom porcine skin gelatin (Gelatin 1, black line) and the other from 300 bloom bovine bone gelatin (Gelatin 2, grey line).

Figures 4.8b and 4.8c show percentage transmission maps for the two 1L gelatin-filled PETE jars from figure 4.8a, derived from open field and 2 mm pinhole grid blocker projection images. The mean percentage transmission values in the jar region of the map are  $78 \pm 3\%$  and  $88 \pm 2\%$  for the porcine gelatin-based and bovine gelatin-based matrices respectively.

One key parameter that influences the optical transmission of the gelatin matrix is its effective particle size distribution. Figure 4.9a shows the molecular weight distributions of the porcine and bovine gelatin materials determined by particle size exclusion chromatography (analysis completed by a third party through Eastman Gelatine Corp). These molecular weight distributions are indirectly measured through a process of hydrodynamic volume sizing against known standards, and hence have a direct correlation to effective particle size distribution. That

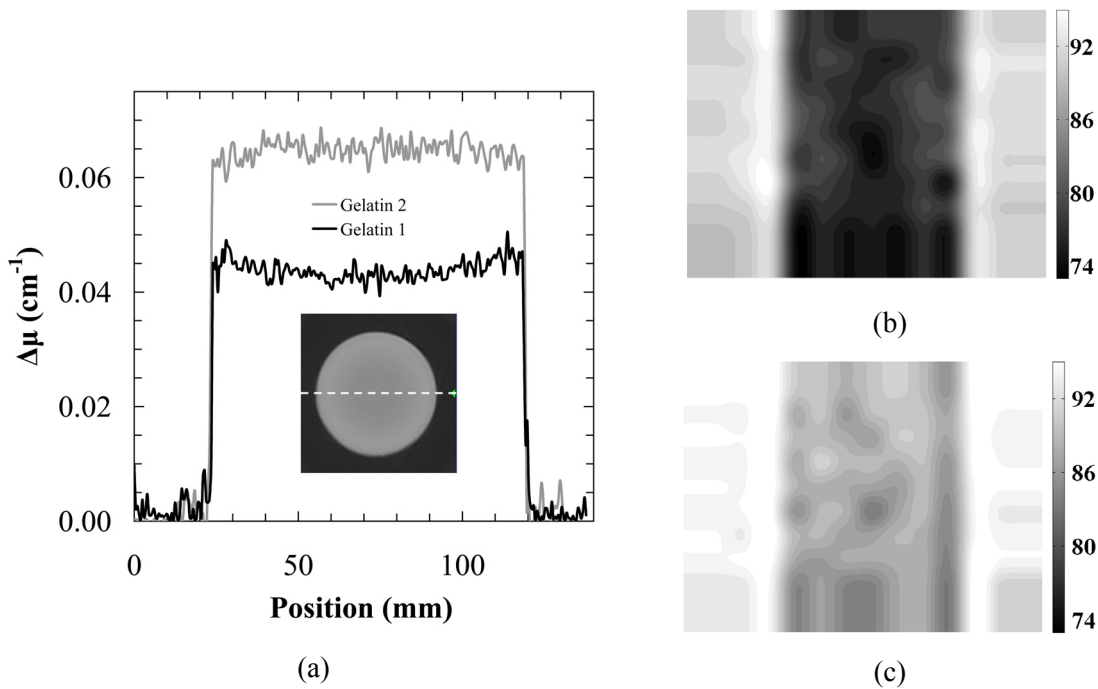


**Figure 4.8:** (a) Profiles across the reconstructed optical CT images of the 5 wt% gelatin-in water-filled 1 L PETE jars, prepared using standard 300 bloom porcine skin gelatin (Gelatin 1, black line) and 300 bloom bovine bone gelatin (Gelatin 2, grey line) and imaged on the Vista scanner. Interpolated percentage maps are also shown, derived from open field and ‘blocked’ pinhole grid projection image data of the (b) porcine and (c) bovine gelatin-in-water-filled 1L PETE jars in the Vista scanner.

is, the ‘effective size’ of the particle generally increases with molecular weight, but the magnitude of increase depends on the structure of the particle (random coil, rigid rod, hard sphere, etc.). The time at which the signal is observed (figure 4.9a) is correlated against the behavior of the known standards to infer the molecular weight. Regions 1-5 in figure 4.9a correspond to the molecular weight ranges of >250 kilodaltons (kDa), 250-150 kDa, 150-50 kDa, 50-20 kDa, and 20-4 kDa respectively. Figure 4.9b shows a representative angular optical scattering diagram for small and large particles in aqueous colloidal suspension, with the positive x-axis indicating forward scattering and the y-axis oriented to 90° side scattering of visible light through a small sample (diameter) of the scattering media. The distributions in figure 4.9b show a well-known angular

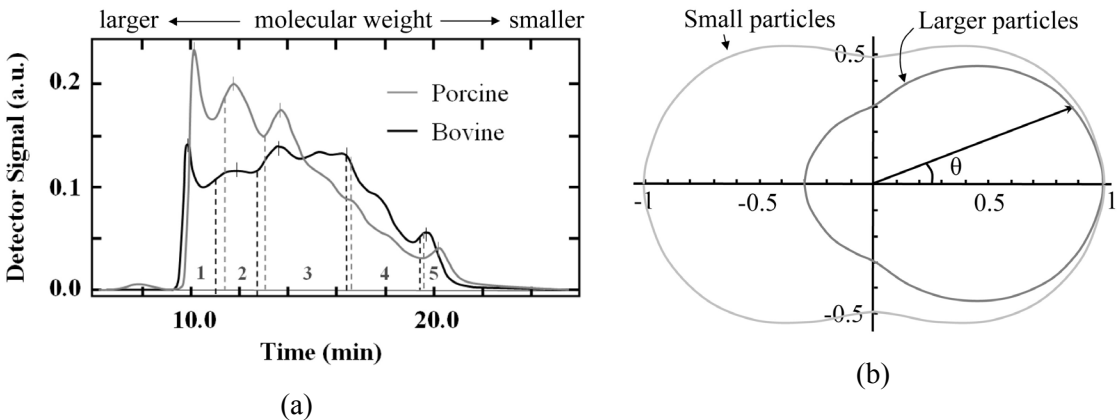


**Figure 4.9:** (a) Overlaid size exclusion chromatograms of the gel dosimetry standard 300 bloom porcine skin gelatin (Sigma-Aldrich Canada Ltd) and the proposed alternative 300 bloom bovine bone gelatin (Eastman Gelatine Corp). (b) Asymmetry in scattering intensity as a function of scattering angle for two small (sub-micron) particle sizes.

variation between the two (sub-micron size range) scattering particle sizes, with increasing forward scattering bias as the particle size increases.

## 4.5 Discussion

### 4.5.1 FXG Gel Response Calibration

Referring to figure 4.2a, a small threshold dose in the range of 0.1-0.2 Gy is evident, which is consistent with the results of an earlier investigation using this FXG gel recipe(Babic *et al* 2008a). The starting point for dose saturation behavior appears to be roughly 20 Gy, so single fraction typical IMRT doses of 2 Gy are well within the optimal response range of the dosimeter. The fact that the dose sensitivity can be well-calibrated to a linear relationship over the range of 0-5 Gy (see figure 4.2a inset) is consistent with the predicted theoretical relationship between dose, radiation chemical yield G(X) and optical attenuation coefficient found in literature (Schreiner and Olding 2009). The increase in the slope observed past ~5 Gy may partially be due

to dose development in the cuvettes during the increasing time span of the dose delivery, which was not accounted for in the results. To be clear, while the cuvette-based calibration was used to verify the assumption of linearity over the electron beam calibration dose range, it was not employed further for IMRT gel calibration. The time and temperature specifications in this particular experiment were not controlled to the levels ( $\pm 0.1^\circ\text{C}$ ,  $30 \pm 0.5$  minutes post-irradiation time) previously suggested for accurate dosimetry (Olding and Schreiner 2010). They were, however, considered to be adequate for identifying the practical dosimetry range and establishing the assumption of a linear calibration relationship between attenuation and dose.

The reduction in auto-oxidation rate with temperature observed between the two studies reported in section 4.4.1 is consistent with previous work (Caldeira *et al* 2007, Babic *et al* 2008a). The apparent increase in rate at lower temperatures in figure 4.2b can be explained by an overall attenuation shift with temperature induced by thermochromic behavior in the FXG gel (Olding and Schreiner 2010) combined with a ‘masked’ decrease in auto-oxidation rate at the lower temperatures.

Looking at figure 4.3a, most of the dose-to-attenuation calibration data are seen to visually overlap in the plot. Given that only the 6 MeV and the 12 MeV data in this plot were from the same gel batch, and normalization corrections were not employed, this suggests a reasonable level of response reproducibility (~1-2%) between gel batches for FXG gel-filled 1 L PETE jar dosimeter calibrations. Further work would be required, however, to confirm that this is the case. On the other hand, the fact that the dose-to-attenuation calibration data presented in the inset of figure 4.3a agree within the ROI attenuation measurement standard deviation of  $\pm 0.002 \text{ cm}^{-1}$  gives good indication that an IMRT measurement dosimeter can be well-calibrated by a second FXG gel-filled 1 L PETE jar dosimeter prepared from the same gel batch.

The observable difference between the cuvette and PETE jar attenuation values at the dose level of 2 Gy (in figure 4.3a) highlights the well-known challenge of using different sizes of dosimeter containers for gel calibration and dose measurement (De Deene *et al* 2007). For this reason, all IMRT measurements and electron beam dosimeter calibrations in this work were completed in identically sized 1 L PETE jars filled with FXG gel from the same batch and stored under as close to the same environmental conditions as possible (Schreiner and Olding 2009, Olding *et al* 2010).

Accurate optical measurement near the surface of the gel can be problematic, as the data are perturbed by stray light reflections from the surface of the matching fluid solution or gelatin. Also, the cone angle is great enough in this region that there is reduced data coverage in the cone beam slice and limitations in reconstruction using the cone beam algorithm are observed (Olding *et al* 2010). For this reason, data points from a depth greater than approximately 1.5 cm in the gel are preferred for establishing the calibration relationship. Another approach to avoiding this high uncertainty region (not employed in this work) would be to use calibration and measurement gel dosimeters of shorter height, held at a lower vertical position during imaging in the Vista scanner (Babic *et al* 2008b, Babic *et al* 2009).

In addition to indicating good reproducibility, the calibration data for the different beam energies shown in figure 4.3a also suggest that the FXG gel dosimeter is approximately energy independent into the kilovoltage energy range. This conclusion makes sense, since 1) the reported ratios of water-to-Fricke-gelatin (FG) gel restricted stopping power and mass-energy absorption coefficient calculated by Monte Carlo methods vary less than ~1% from unity for a standard FG gel recipe over the energy range of 0.01-50 MeV (Rogers 2009), indicating water equivalence in the FG gel for these energies, 2) water equivalence implies approximate energy independence over this energy range, and 3) the FXG gel in this work is similar to the aforementioned FG gel

**Table 4.1:** Fricke-Based Gel Atomic Compositions

	H(%)	C(%)	N(%)	O(%)	S(%)	Cl(%)	Na(%)	Fe(%)	Total
FG	10.948	2.096	0.762	86.006	0.177	0.003	0.002	0.006	100.0
FXG	10.898	2.519	0.912	85.446	0.223	0.000	0.000	0.002	100.0

recipe in atomic composition (see table 4.1) and hence, water equivalent. An IMRT measurement dosimeter can be hence be well-calibrated by a second FXG gel-filled 1 L PETE jar dosimeter prepared from the same gel batch and irradiated with different treatment beam energy.

#### 4.5.2 IMRT Dose Evaluation

The FXG gel response calibration factors discussed in section 4.5.1 (i.e. dose calibration linearity, temperature dependent auto-oxidation rate, same batch inter-jar dose response reproducibility, and energy independence in the megavoltage treatment energy range) establish the IMRT evaluation.

Looking at figure 4.4, the selected planar views of the treatment plan and gel-measured dose distributions from the first IMRT delivery show reasonable qualitative agreement, as a first point of reference. However, a 5%, 3mm 3D Low's gamma function comparison of the two dose distributions (figure 4.5a) indicates that there is room for improvement. The observed agreement (approximately 89%) and relaxed gamma criteria (5%, 3 mm) do not satisfy the preferred target level of 95% voxel agreement using the metrics of 3% dose difference and 3 mm distance-to-agreement. The preferred level of agreement was based on a review of the proceedings of the international DosGel conferences on gel dosimetry, the last four of which are available on the internet through the *Journal of Physics: Conference Series* publications.

First, even without achieving the desired level of dose comparison, useful comparisons between deliveries can be made. For example, when the same IMRT delivery is repeated with the

fraction was delivered with the phantom positioned directly on the treatment couch, instead of on the head-and-neck S-frame, the percentage of voxel agreement using 5%, 3mm 3D Low's gamma function criteria was reduced to approximately 82%. Referring to figure 4.5b, a concentrated region of failure is observed near the posterior side of the FXG dosimeter jar (in the sagittal and axial slice views) which is roughly consistent in location and magnitude of dose difference (up to ~2-3%) with published report regarding the attenuation of the posterior oblique fields through the treatment couch (Poppe *et al* 2007). This example highlights the ability of gel dosimetry, with reasonable simplicity, to effectively capture slight modifications in the measured 3D dose distribution as changes in delivery are introduced.

Second, the dose shift recorded in figure 4.6a may, in fact, be a systematic error in the measurement. If it is, then selected dose points could be well-quantified by ion chamber measurements and the dose distribution normalized to those measurements. The 3%, 3mm Low's gamma function analysis in figure 4.6b (assuming a shift of 10 cGy in the single dose point measurement) then indicates an acceptable calculated plan-to-measured gel dose comparison. However, the intent in this work is to move away from normalization corrections and gain an overall better understanding of the contributing factors to this dose shift.

A number of variables need to be addressed when considering the source(s) of the shift in the cone beam optical CT-FXG gel system. First, previously established protocols addressing measurement variations due to CCD detector-light source variability and dosimeter scan temperature were employed in the IMRT delivery assessment that minimize the uncertainty in the calibration between FXG dosimeter jars (Olding and Schreiner 2010). Second, the effects of gel auto-oxidation and additional CBCT scan dose have been quantified in this work and accounted for. Third, diffusion in the FXG gel after irradiation can cause localized variations on the order of 2-3%, particularly near dose gradients, but has been minimized through the use of a fast scanner

and would not account for a global shift in the response of the dosimeter. Fourth, uncertainties in the delivery are assumed to be on the order of 1-2%, but not up the level of the observed 10 cGy (5%) shift. Finally, it is possible that the calculated IMRT plan used in this investigation is not as accurate as assumed. To investigate this further, a new (and reasonably different) 7 field, 6 MV IMRT delivery was planned and delivered to the wax-filled Rando reproduction with a 1 L FXG gel-filled dosimeter jar insert, as before. The shift in the mean of the dose difference histogram between plan dose and gel-measured dose was found to be  $-10.3 \pm 7.3$  cGy. A three-dimensional portal image-based dose reconstruction methodology was then utilized as an independent quality assurance (QA) check of the IMRT treatment plan (Ansbaecher 2006) and the results found to be acceptable. As the mean shift between treatment plan dose and gel-measured dose was again found to be approximately 10 cGy (for a completely different QA-verified treatment plan) the cause of is shift is likely not found in the plan calculations.

The next leading candidate capable of causing a shift in the Vista scanner-based dosimetry is stray light perturbation in the calibration and measurement dosimeters, investigated previously (Babic *et al* 2008b, Olding *et al* 2010). A primary uncontrolled source of perturbation limiting the accuracy of dosimetry has been suggested to be scattered light from the gelatin matrix (Olding *et al* 2010), and its reduction is the focus of dosimeter modification in this work. Several approaches were contemplated toward achieving a suitable reduction in scattered light. Finding an alternative radiosensitive dye with good response at a higher imaging wavelength (633 nm) is one option. Given that the attenuation of the gelatin matrix has between a third and fourth order dependence on wavelength, an approximate reduction of 30% in scatter attenuation (perturbation) could be realized by changing the measurement wavelength if a suitable dye could be found. Another route would be to replace a significant portion of the water in the recipe with a higher refractive index solvent such as glycerol or propylene glycol or a higher index dissolved

material such as sucrose to reduce scattering at the interfaces of the gelatin particles (Franklin and Wang 2002). This is problematic in that the base FXG gel chemistry would be changed, affecting the energy dependence of the gel. Also, the reduction in scatter perturbation is small, even for replacement of up to 50% of the water by weight in the recipe with a higher index solvent. A third option would be to reduce the amount of gelatin in the FXG gel recipe or replace it with a less scattering alternative water soluble, gel forming material. This was considered to be the most viable option for further investigation.

The outcome of the IMRT delivery evaluation using two same batch bovine gelatin-based FXG gel-filled 1 L PETE jar dosimeters for calibration and IMRT indicates a significant improvement following gelatin substitution. The results presented in figure 4.7 (for the modified bovine gelatin-based FXG gel dosimeter) were obtained without dose normalization and satisfy the previously indicated target 95% voxel agreement between the reference and measurement dose distributions for 3%, 3 mm. gamma function criteria. The rationale behind the selection and use of this gelling agent is presented in the following section.

#### **4.5.3 Modified Dosimeter Characterization**

A wide range of commercially available gel-forming hydrocolloids were reviewed as possible 300 Bloom porcine gelatin replacement materials. The criteria for candidate selection were water solubility, gel forming capability and strength at room temperature, optical transparency, and ability to function in an acidic aqueous environment. On this basis, most of the reviewed gel-forming materials were deemed unsuitable for use. Two carrageenan-based gel formers and a Type A (acid processed) 300 bloom bovine bone (ossein) gelatin were selected for further investigation.

Early-stage trials testing for optical transparency indicated that the carrageenan-based products increased the gel matrix-derived stray light perturbation compared to the 300 bloom

porcine skin gelatin, and were hence disqualified from use. The bovine bone gelatin, on the other hand, was found to have promising optical properties, as seen in figure 4.8. While the mean optical attenuation of the bovine bone gelatin matrix is greater in magnitude than that of the porcine skin gelatin (figure 4.8a), there is a noticeable absence of cupping artifact in the bovine bone gelatin optical CT image profile compared to the profile for the porcine skin gelatin, suggesting a reduction in stray light perturbation from angular scattering in the gel (Olding *et al* 2010). A follow-up percentage transmission map evaluation of the two gelatin types (figure 4.8b and 8c) indicates better conformation of the detector-recorded light to the cone beam ray path geometry (Olding *et al* 2010) when using the bovine gelatin. This again suggests a reduction in angled scatter-sourced stray light perturbation. Overall, the results presented in figure 4.8 give weight to the hypothesis that stray light perturbation in the measurement system is substantially responsible for shifting the dose readout, in agreement with Babic *et al* (2008). Replacement of the standard porcine gelatin with reduced angle scatter-inducing bovine gelatin reduces the need for applying a corrective shift to the gel-measured dose. To be clear, the result in figure 4.7a does not imply that stray light perturbation has been completely removed from the measurement system. Rather, the level of perturbation has been reduced to the point where it is relatively consistent in the imaging of the calibration and IMRT measurement dosimeter jars, and hence it is mostly cancelled out in the application of the IMRT dose-to-attenuation calibration relationship.

A comparison of molecular weight distributions indicates that the porcine gelatin contains a larger fraction of high molecular weight chains than the bovine gelatin (figure 4.9a). This higher molecular weight roughly translates into a larger effective mean particle size of the porcine gelatin material. Given that the light transmitted through the FXG gel-filled 1 L PETE jar dosimeter can experience multiple scattering events, the scattering diagram in figure 4.9b then suggests a stronger bias in the porcine gelatin-based dosimeter (versus the bovine gelatin-based

dosimeter) toward the acquisition of low angle forward scattered stray light by the CCD detector. This would explain the reduction in cupping artifact in the imaging of the bovine gelatin-based dosimeter (figure 4.8a) due to the higher percentage of detected signal conforming to cone beam geometry (i.e. reduced percentage of ‘stray light’ signal in figure 4.8b compared to figure 4.8c).

Future work aimed toward additional reduction of stray light arising from low angled scatter through the gel-forming matrix material should hence give strong consideration to both the optical clarity and the effective particle size distribution of the gel-former in aqueous solution.

#### 4.6 Conclusions

Clinically accessible 3D evaluations of intensity modulated radiation therapy (IMRT) deliveries are feasible using a Fricke-xylenol orange-gelatin (FXG) gel dosimeter in combination with cone beam optical computed tomography (CT). The dose-to-optical attenuation response of the FXG gel dosimeter is linear over the range of 0-5 Gy and approximately energy-independent in the megavoltage treatment energy range. Substitution of standard 300 Bloom porcine skin gelatin with a high optical clarity 300 Bloom bovine bone gelatin in the FXG gel dosimeter formulation has the effect of reducing stray light perturbation in the optical measurement system, and leads to an improvement in the Low’s gamma function comparison of calculated treatment plan and gel-measured IMRT dose. Following gelatin substitution, the preferred target level of 95% voxel agreement was observed in the IMRT plan-to-delivery evaluation using 3% dose difference and 3 mm distance-to-agreement gamma criteria, without further need for a dose normalization correction. This result indicates the viability of cone beam optical CT-based FXG gel dosimetry as an accessible tool for 3D dose verification of IMRT treatment plans in the cancer clinic.

## 4.7 References

- Ansbacher W 2006 Three-dimensional portal image-based dose reconstruction in a virtual phantom for rapid evaluation of IMRT plans. *Med Phys* 33 3369-3382.
- Babic S, Battista J and Jordan K 2008a An apparent threshold dose response in ferrous xylanol-orange gel dosimeters when scanned with a yellow light source. *Phys.Med.Biol.* 53 1637-1650.
- Babic S, Battista J and Jordan K 2008b Three-dimensional dose verification for intensity-modulated radiation therapy in the radiological physics centre head-and-neck phantom using optical computed tomography scans of ferrous xylanol-orange gel dosimeters. *Int.J.Radiat.Oncol.Biol.Phys.* 70 1281-1291.
- Babic S, McNiven A, Battista J and Jordan K 2009 Three-dimensional dosimetry of small megavoltage radiation fields using radiochromic gels and optical CT scanning. *Phys.Med.Biol.* 54 2463-2481.
- Caldeira A M, Neto A M, Bento A C, Baesso M L, Silva M A and de Almeida A 2007 Behavior of oxidation in the radiochromic gel dosimeter through photoacoustic technique measurements. *Appl.Radiat.Isot.* 65 605-609.
- Ceberg S, Karlsson A, Gustavsson H, Wittgren L and Back S A 2008 Verification of dynamic radiotherapy: the potential for 3D dosimetry under respiratory-like motion using polymer gel. *Phys.Med.Biol.* 53 N387-N396.
- De Deene Y, De Wagter C, Van Duyse B, Derycke S, Mersseman B, De Gersem W, Voet T, Achten E and De Neve W 2000 Validation of MR-based polymer gel dosimetry as a preclinical three-dimensional verification tool in conformal radiotherapy. *Magn Reson.Med.* 43 116-125.
- De Deene Y, Pittomvils G and Visalatchi S 2007 The influence of cooling rate on the accuracy of normoxic polymer gel dosimeters. *Phys.Med.Biol.* 52 2719-2728.
- De Neve W, De Gersem W, Derycke S, De Meerleer G, Moerman M, Bate M T, Van Duyse B, Vakaet L, De Deene Y, Mersseman B and De Wagter C 1999 Clinical delivery of intensity modulated conformal radiotherapy for relapsed or second-primary head and neck cancer using a multileaf collimator with dynamic control. *Radiother.Oncol.* 50 301-314.
- Deasy J O, Blanco A I and Clark V H 2003 CERR: a computational environment for radiotherapy research. *Med.Phys.* 30 979-985.
- Doran S 2009 The history and principles of optical computed tomography for scanning 3-D radiation dosimeters: 2008 update. *J.Phys.: Conf.Ser.* 164 98-119.
- Doran S and Krstajic N 2006 The history and principles of optical computed tomography for scanning 3-D radiation dosimeters. *J.Phys.: Conf.Ser.* 56 45-57.

- Doran S J, Koerkamp K K, Bero M A, Jennesson P, Morton E J and Gilboy W B 2001 A CCD-based optical CT scanner for high-resolution 3D imaging of radiation dose distributions: equipment specifications, optical simulations and preliminary results. *Phys.Med.Biol.* 46 3191-3213.
- Feldkamp L A, Davis L C and Kress J W 1984 Practical cone-beam algorithm. *J.Opt.Soc.Amer.* 1 612-619.
- Franklin J and Wang Z Y 2002 Refractive Index Matching: A General Method for Enhancing the Optical Clarity of a Hydrogel Matrix. *Chem.Mater.* 14 4487-4489.
- Guo P, Adamovics J and Oldham M 2006a A practical three-dimensional dosimetry system for radiation therapy. *Med.Phys.* 33 3962-3972.
- Guo P Y, Adamovics J A and Oldham M 2006b Characterization of a new radiochromic three-dimensional dosimeter. *Med.Phys.* 33 1338-1345.
- Gustavsson H, Karlsson A, Back SA, Olsson L E, Haraldsson P, Engstram P and Nystram H 2003 MAGIC-type polymer gel for three-dimensional dosimetry: intensity-modulated radiation therapy verification. *Med.Phys.* 30 1264-1271.
- Holmes O *Validation of Conformal Radiation Therapy Treatments in 3D Using Polymer Gel Dosimeters and Optical Computed Tomography* (M.Sc., Queen's University, 2008).
- Ibbott G, Beach M and Maryanski M 2002 An anthropomorphic head phantom with a BANG polymer gel insert for the dosimetric evaluation of intensity modulated radiation therapy treatment delivery. *Standards and Codes of Practice in Medical Radiation Dosimetry: Proceedings of an International Symposium* 2 361.
- Kelly B G, Jordan K J and Battista J J 1998 Optical CT reconstruction of 3D dose distributions using the ferrous- benzoic-xylenol (FBX) gel dosimeter. *Med.Phys.* 25 1741-1750.
- Krstajic N and Doran S J 2006 Focusing optics of a parallel beam CCD optical tomography apparatus for 3D radiation gel dosimetry. *Phys.Med.Biol.* 51 2055-2075.
- Krstajic N and Doran S J 2007 Characterization of a parallel-beam CCD optical-CT apparatus for 3D radiation dosimetry. *Phys.Med.Biol.* 52 3693-3713.
- Lopatiuk-Tirpak O, Langen K M, Meeks S L, Kupelian P A, Zeidan O A and Maryanski M J 2008 Performance evaluation of an improved optical computed tomography polymer gel dosimeter system for 3D dose verification of static and dynamic phantom deliveries. *Med.Phys.* 35 3847-3859.
- Low D A and Dempsey J F 2003 Evaluation of the gamma dose distribution comparison method. *Med.Phys.* 30 2455-2464.

- Low D A, Dempsey J F, Venkatesan R, Mutic S, Markman J, Haacke E M and Purdy J A 1999 Evaluation of Polymer gels and MRI as a 3-D dosimeter for intensity-modulated radiation therapy. *Med.Phys.* 26 1542-1551.
- Low D A, Harms W B, Mutic S and Purdy J A 1998 A technique for the quantitative evaluation of dose distributions. *Med.Phys.* 25 656-661.
- Oldham M, Baustert I, Lord C, Smith T A, McJury M, Warrington A P, Leach M O and Webb S 1998 An investigation into the dosimetry of a nine-field tomotherapy irradiation using BANG-gel dosimetry. *Phys.Med.Biol.* 43 1113-1132.
- Oldham M and Kim L 2004 Optical-CT gel-dosimetry. II: Optical artifacts and geometrical distortion. *Med.Phys.* 31 1093-1104.
- Oldham M, Kim L and Hugo G 2005 Optical-CT imaging of complex 3D dose distributions. *J.Phys.* 5745 138-146.
- Oldham M, Sakhalkar H, Guo P and Adamovics J 2008 An investigation of the accuracy of an IMRT dose distribution using two- and three-dimensional dosimetry techniques. *Med.Phys.* 35 2072-2080.
- Oldham M, Siewerdsen J H, Kumar S, Wong J and Jaffray D A 2003 Optical-CT gel-dosimetry I: basic investigations. *Med.Phys.* 30 623-634.
- Olding T, Holmes O and Schreiner L J 2010 Cone beam optical computed tomography for gel dosimetry I: scanner characterization. *Phys.Med.Biol.* 55 2819-2840.
- Olding T and Schreiner L J 2010 Cone Beam Optical Computed Tomography for Gel Dosimetry II: Imaging protocols. *Phys.Med.Biol.* submitted for publication.
- Poppe B, Chofor N, Ruhmann A, Kunth W, Djouguela A, Kollhoff R and Willborn K C 2007 The effect of a carbon-fiber couch on the depth-dose curves and transmission properties for megavoltage photon beams. *Strahlenther.Onkol.* 183 43-48.
- Rogers D W 2009 Stopping-Power Ratios, Ratios of Mass-Energy Absorption Coefficients and CSDA Ranges of Electrons. In: Rogers, D. W. and Cygler, J. E. *AAPM Medical Physics Monograph No. 34: Clinical Dosimetry Measurements in Radiotherapy*. Madison, WI, USA, Medical Physics Publishing. 1097.
- Sakhalkar H, Sterling D, Adamovics J, Ibbott G and Oldham M 2009a Investigation of the feasibility of relative 3D dosimetry in the Radiologic Physics Center Head and Neck IMRT phantom using presage/optical-CT. *Med.Phys.* 36 3371-3377.
- Sakhalkar H S, Adamovics J, Ibbott G and Oldham M 2009b A comprehensive evaluation of the PRESAGE/optical-CT 3D dosimetry system. *Med.Phys.* 36 71-82.

- Schreiner L J and Olding T 2009 Gel Dosimetry. In: Rogers, D. W. and Cygler, J. E. *AAPM Medical Physics Monograph No. 34: Clinical Dosimetry Measurements in Radiotherapy*. Madison, WI, USA, Medical Physics Publishing.
- Shortt K 1989 The temperature dependence of  $G(\text{Fe}^{3+})$  for the Fricke dosimeter. *Phys.Med.Biol.* 34 1923-1926.
- Vergote K, De Deene Y, Claus F, De Gersem W, Van Duyse B, Paelinck L, Achten E, De Neve W and De Wagter C 2003 Application of monomer/polymer gel dosimetry to study the effects of tissue inhomogeneities on intensity-modulated radiation therapy (IMRT) dose distributions. *Radiother.Oncol* 67 119-128.
- Vergote K, De Deene Y, Duthoy W, De Gersem W, De Neve W, Achten E and De Wagter C 2004 Validation and application of polymer gel dosimetry for the dose verification of an intensity-modulated arc therapy (IMAT) treatment. *Physics in Medicine & Biology*. 49(2):287-305.
- Wolodzko J G, Marsden C and Appleby A 1999 CCD imaging for optical tomography of gel radiation dosimeters. *Med.Phys.* 26 2508-2513.
- Wuu C S and Xu Y 2006 Three-dimensional dose verification for intensity modulated radiation therapy using optical CT based polymer gel dosimetry. *Med.Phys.* 33 1412-1419.
- Xu Y, Wuu C S and Maryanski M J 2004 Performance of a commercial optical CT scanner and polymer gel dosimeters for 3-D dose verification. *Med.Phys.* 31 3024-3033.

## **Chapter 5**

### **Small Field Dose Delivery Evaluations Using Polymer Gels**

A version of this chapter has been submitted to the Indian Journal of Medical Physics as: *Olding T, Holmes O, DeJean P, McAuley K, Nkongchu K, Santyr G, and Schreiner L J “Small Field Dose Delivery Evaluations Using Cone Beam Optical Computed Tomography-Based Polymer Gel Dosimetry”.*

#### **5.1 Abstract**

This article explores the combination of cone beam optical computed tomography (CT) with an N-isopropylacrylamide (NIPAM)-based polymer gel dosimeter for three-dimensional (3D) dose imaging of small field deliveries. Initial investigations indicate that cone beam optical imaging of polymer gels is complicated by scattered stray light perturbation. This can lead to significant dosimetry failures in comparison to dose readout by magnetic resonance imaging (MRI). The dosimetry is improved after modifications to the dosimeter preparation, matching its performance with the imaging capabilities of the optical scanner. Analysis of a test 500 cGy pencil beam dose distribution delivered to the modified 1 L-sized NIPAM dosimeter indicates 99.5% voxel agreement between treatment plan and gel-measured dose in the central plane of the dose delivery for two-dimensional (2D) Low's gamma function analysis criteria of 3% dose and 3 mm distance-to-agreement. The fitted inter-jar dose responses of modified NIPAM dosimeters prepared (a) from the same gel batch, and (b) from different gel batches prepared on the same day were found to be in agreement to within 3.6% and 3.8% respectively over the full dose range. This indicates that intra-batch or inter-batch dosimeters prepared on the same day are suitable for dose sensitivity calibration.

## 5.2 Introduction

Since gel dosimetry first emerged as a prospective candidate for high resolution, 3D dose measurements in radiation therapy, a number of systems have been employed for readout of gel dose. These systems have primarily been based on the imaging modalities of magnetic resonance imaging (Gore *et al* 1984, Olsson *et al* 1990), optical CT (Gore *et al* 1996), and x-ray CT (Hilts *et al* 2000), each of which has its disadvantages and advantages. Optical CT, in particular, has the disadvantage of stray light perturbation affecting optical dose readout accuracy (for example, see (Oldham *et al* 2003, Oldham and Kim 2004)). However, this modality also has a key advantage of accessibility in most clinical environments, as these scanners are low cost, compact and usually portable (Doran and Krstajic 2006, Doran 2009). In addition, fast 3D imaging has been realized through the use of either a cone beam (Wolodzko *et al* 1999, Babic *et al* 2008) or parallel beam (Doran *et al* 2001, Krstajic and Doran 2006, Krstajic and Doran 2007) charge coupled device (CCD) optical scanner configuration. The much reduced imaging time of these area detection-based scanners is an important step forward toward the use of Fricke-based gels for 3D dosimetry, which are limited by diffusion-related loss of spatial dose integrity over time (Olsson *et al* 1992, Baldock *et al* 2001).

The performance capabilities of the commercially available Vista<sup>TM</sup> cone beam optical CT scanner (Modus Medical Devices Inc, London, ON, Canada) have been investigated and found to be suitable for readout of optically absorbing gel dosimeters (Olding *et al* 2010). The Fricke-xylenol orange-gelatin (FXG) absorbing gel dosimeter in particular, can be employed for three-dimensional (3D) verification of intensity modulated radiotherapy (IMRT) dose distributions (Babic *et al* 2008). However, diffusion effects in the FXG dosimeter, which have a reasonably small effect on spatial dose integrity within most of the imaged volume of IMRT dose distributions over time, become more problematic when examining high dose gradients such as

those found in small field dosimetry. Post-imaging correction schemes become necessary in order to obtain accurate dose measurements (Babic *et al* 2009).

The focus of this investigation is to determine whether an optically scattering polymer gel dosimeter could be used in combination with cone beam optical CT for evaluation of high gradient dose distributions such as those in small field deliveries. Polymer gels have high resolution dose contrast response and do not suffer from the diffusion effects found in the Fricke-based gels (Maryanski *et al* 1993, Maryanski *et al* 1996). Hence, these gels should be appropriate for investigating small field dose distributions. However, cone beam optical CT readout of polymer gels has previously been shown to be significantly perturbed by contaminant stray light (DeJean *et al* 2006a, DeJean *et al* 2006b, Bosi *et al* 2007, Olding *et al* 2010) that greatly affects the measurement accuracy of this approach.

The main task in this work is to establish whether the effects of stray light can be reduced or managed to the point where an acceptable level of dosimetry is achieved for small field deliveries to a polymer gel dosimeter imaged with the Vista cone beam optical CT scanner. The accuracy of this combination of gel dosimeter and readout method could be assessed by a comparison between reference ('true') and measured (polymer gel-cone beam optical CT) dose distributions using dose difference maps. However, such maps are particularly sensitive to differences in the high dose gradients of the small field pencil beam delivery, since small spatial errors in either data set can lead to large dose differences between the measured and planned distributions. A better comparison of spatial dose distributions can be obtained through use of Low's gamma function (Low *et al* 1999, Low and Dempsey 2003), which quantifies the agreement of the combined metrics of dose difference and distance-to-agreement between two dose distributions into a single 'gamma' value. The gamma function assigns values less than 1 in regions where dose difference and distance-to-agreement are within set criteria, for example, 3%

dose and 3 mm distance between points in the treatment planning system-calculated and gel-measured dose distributions. Values greater than 1 are understood as having failed the criteria. The target level in this investigation was set to be 95% voxel agreement between reference and measured dose distributions for 3% dose difference and 3 mm distance-to-agreement gamma function criteria.

An N-isopropylacrylamide (NIPAM)-based chemistry (Senden *et al* 2006) was employed in the preparation of all polymer gel dosimeters in this report. This formulation was originally developed as a lower toxicity alternative to the more widely used acrylamide-based polymer gel (Maryanski *et al* 1993, Maryanski *et al* 1996). Results in this paper present an initial comparison of cone beam optical CT and the ‘gold standard’ of MRI in the dosimetric readout of a test small field dose delivery to a standard formulation NIPAM gel-filled 1 L PETE jar dosimeter. Following this comparison is an independent assessment of the optical CT scanner using calibration hybrid acrylic-gelatin scattering gel phantoms. The use of these phantoms separates the measurement from the uncertainties of polymer gel dosimeter preparation and dose delivery. The NIPAM gel dosimeter formulation and preparation procedure are then evaluated and modified to match the scanner’s performance limitations. Finally, the dosimetry of the improved formulation/preparation is evaluated and different calibration methodologies investigated for practical use.

## 5.3 Experiment

### 5.3.1 Gel Dosimeter Preparation

Dosimeters in this study were prepared under atmospheric (normoxic) conditions according to one of two preparation procedures referred to as procedures A and B, which differ primarily in the mixing order of chemicals and temperature at the time of NIPAM monomer addition. In

procedure A, gels containing 5 wt% gelatin (300 bloom Type A porcine gelatin, Cat.No.G2500, Sigma-Aldrich Ltd, Oakville, Canada), 3 wt% N,N'-methylene-bis-acrylamide (BIS) cross-linking monomer (Cat.No.146072, Sigma-Aldrich Ltd), 3 wt% N-isopropylacrylamide (NIPAM) monomer (Cat.No.415324, Sigma-Aldrich Ltd) and 10 mM of tetrakis hydroxymethyl phosphonium chloride (THPC, Cat.No.404861, Sigma-Aldrich Ltd) in aqueous solution, were prepared according to a standard approach reported in literature (Senden *et al* 2006). These polymer gels are henceforth identified according to literature convention as 6%T, 50%C NIPAM, where T refers to the total weight percent of monomer, and C is the percentage of cross-linking monomer in the gel. As all dosimeters in this report have a cross-linking monomer percentage of 50%, the 50%C designation is assumed from this point forward. The gelatin was allowed to swell in 80 wt% of the total amount of de-ionized water at room temperature for 15 minutes and the solution was then heated to 50°C while stirring. BIS cross-linker was added under stirring and the solution temperature held at 50°C until the cross-linker was fully dissolved. The solution was allowed to cool to approximately 37°C and the NIPAM monomer was added under stirring until the monomer was dissolved. A dilute solution of THPC antioxidant was prepared with the remaining 20 wt% of the water and added to the solution at a temperature of approximately 35°C. The solutions were poured into 1 L PETE jars and refrigerated for 24 hours prior to irradiation.

In the alternative approach (procedure B), polymer gel dosimeters with total monomer concentrations between 3-6% T were prepared by allowing 5 wt% of gelatin to swell in 70 wt% of the de-ionized water at room temperature for 10 minutes and heating the solution to 50°C as before. The BIS cross-linker was added under stirring at 50°C until dissolved. The BIS-gelatin-water solution was then cooled to 34°C. Separately, the NIPAM monomer and THPC were dissolved in the remaining water at room temperature. The NIPAM-THPC-water solution was then added to the cooled BIS-gelatin-water solution, mixed for 1-2 minutes then poured into 1 L

PETE containers, and refrigerated for 24 hours prior to irradiation. The 3%T, 3.5%T, 4%T and 6% T dosimeters contained 5 mM, 5.83 mM, 6.67 mM and 10 mM of THPC, respectively.

### 5.3.2 Optical CT Imaging

Optical readout of the dosimeters was completed under room temperature conditions at an illumination wavelength of 633 nm and camera lens aperture of f5 using the Vista<sup>TM</sup> cone beam optical CT scanner (Modus Medical Devices Inc, London, ON, Canada). A full description of the imaging and reconstruction process for the Vista scanner has previously been reported (Olding *et al* 2010), so only the necessary details are repeated here. Matching tank solution for the scanner consisted of a 12 wt% propylene glycol-in-water mixture, the refractive index of which ( $1.346 \pm 0.001$  at 590 nm) was monitored over time using a handheld refractometer with a central measurement wavelength of 589 nm (r<sup>2</sup> mini refractometer, Reichert Analytical Instruments, Depew, NY, USA) at room temperature ( $21 \pm 1^\circ\text{C}$ ). Room temperature measurements were taken using a digital temperature probe (TM99A-NA Digital Thermometer, Nuclear Associates, Carle Place, NY, USA).

Reference scans were completed on each dosimeter close to the time of irradiation, at the highest shutter exposure time possible without inducing camera pixel saturation, and the lowest gain setting. Data scans were acquired using the same camera settings as the reference scan at a post-irradiation time of ~12 hours, unless otherwise specified. As the dosimeter reacts over a period of several hours after the irradiation (Senden *et al* 2006), the wait time of 12 hours prior to optical CT scanning was chosen to ensure that the polymerization reaction was near completion at the time of imaging. For each scan, a set of 410 light intensity transmission projections were acquired over 360° in approximately 5-6 minutes. High resolution ( $0.5 \times 0.5 \times 0.5 \text{ mm}^3$  voxel) images, with a volume of  $12.8 \times 12.8 \times 12.8 \text{ cm}^3$  incorporating the imaged dosimeter, were reconstructed in 10 minutes using a standard desktop computer.

### 5.3.3 Initial Optical CT-MRI Comparison

Note that this experimental section was completed by Paul DeJean and Ken Nkongchu under the supervision of L. John Schreiner and Giles Santyr, as recorded in the co-authorship section of this thesis. A comparison of the polymer gel imaging capabilities of cone beam optical CT and MRI was completed by using both modalities to image the same irradiated NIPAM dosimeter. A 6%T cylindrical dosimeter with outer jar diameter of 9.2 cm prepared according to procedure A was used in this investigation. This dosimeter was irradiated with a 500 cGy calibration distribution consisting of three pencil beams of different beam weights delivered in a well-defined “A” dose pattern (figure 5.1a). The dosimeter was also irradiated with a 25 field, 500 cGy “K” pattern used as an evaluation dose distribution (figure 5.1b). The calibration “A” and measurement “K” patterned pencil beam deliveries were forward planned with a modified Milan Bentley dose

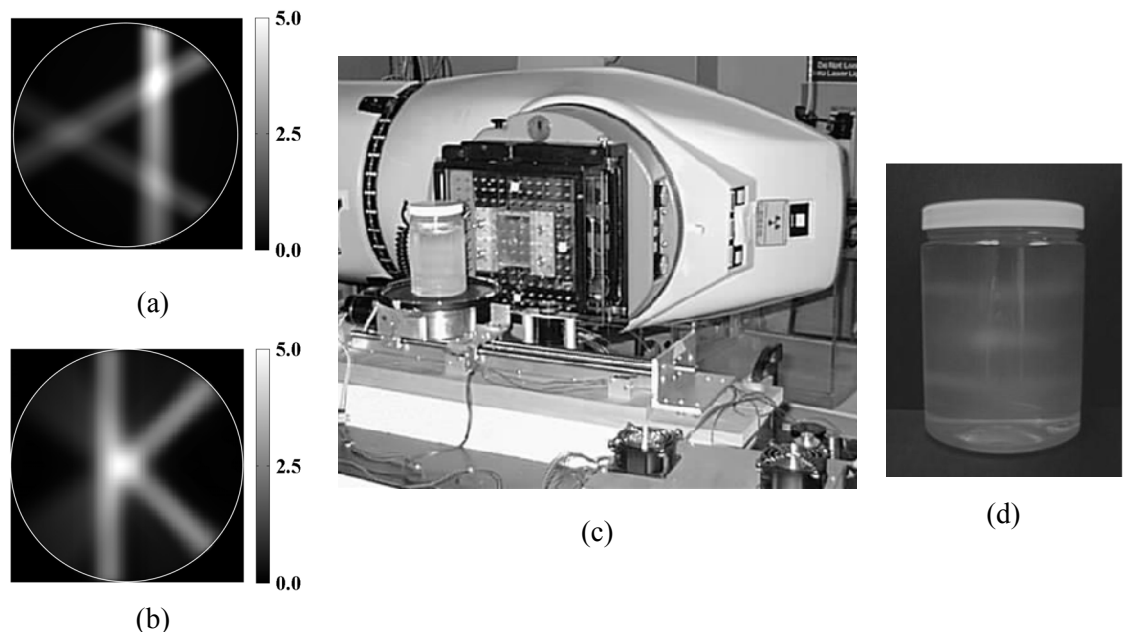


**Figure 5.1:** (a), (b) Test 500 cGy “A” and “K” patterned pencil beam treatment plans (c) The tomotherapy benchtop apparatus used to perform the pencil beam deliveries. (d) The irradiated NIPAM dosimeter.

calculation algorithm verified with Monte Carlo calculations (Milan and Bentley 1974, Dhanesar 2008). The plans were delivered to the dosimeter through use of an in-house-built tomotherapy apparatus with pencil beam collimation customized to a T780C cobalt-60 radiotherapy unit (Best Theratronics, Kanata, ON), shown in figure 5.1c. The irradiated dosimeter (figure 5.1d) containing two “A” calibration distribution and one “K” measurement distribution was imaged ~12 hours after delivery using optical CT, and on a subsequent day using MRI.

MR imaging of the dosimeters was performed at a static field strength of 1.89 T (Magnex Scientific, Abingdon, Oxon, England) using a transmit/receive bird-cage coil (Morris Instruments Inc. Ottawa, ON, Canada) having a 12 cm internal diameter and a multiple spin-echo, multi-slice pulse sequence. The dosimeters were placed in the magnet room for ~24 hours prior to scanning to allow the gel time to reach room temperature. Centric k-space acquisition minimized the errors in spin-spin relaxation rate ( $R_2$ ) due to radiofrequency power deposition-related temperature increases, notably in the area of high dose gradients (De Deene and De Wagter 2001). The refocusing 180° radiofrequency pulse phase was  $\pi$ -shifted for successive phase encoding lines. This caused centre-line artifacts (i.e. ‘zipper’ artifacts) due to stimulated echoes to be located at the edges of the image, for ease of removal during post-processing (Graumann *et al* 1986). The sequence used an echo time of 40 ms. The optimum number of echoes predicted to obtain an optimal dose resolution for an echo time of 40 ms and the expected  $R_2$  range (1.50-1.85 s<sup>-1</sup>) of the gel was ~32 (Lepage *et al* 2001, Baldock *et al* 2001b, De Deene and Baldock 2002). In practice, however, reducing the number of echoes from 32 to 26 gave little change in  $R_2$  value. All image acquisition was therefore done with 26 echoes. A 128 mm field of view was used and 17 slices were acquired with thicknesses of 5 mm each with a matrix of 128 x 128 to give a spatial resolution of 1 mm x 1 mm x 5 mm with 2 averages taken per scan.  $R_2$  maps were obtained by performing a pixel-by-pixel exponential fit to the image data (Nkongchu 2006).

Distortions due to non-linear gradients and static field inhomogeneities of up to 10 mm were corrected to within 1 mm using a combined method adapted from two previous reports(Kawanaka and Takagi 1986, Chang and Fitzpatrick 1992). The measured distortions in all three orthogonal imaging directions (x,y,z) were fitted to a three-variable (x,y,z) third-order polynomial and then used to correct subsequent images acquired using the imaging system. The distortion mapping and correction used simple grid phantoms with known physical dimensions filled with gels of approximately the same concentration to simulate the induced inhomogeneities expected in the dosimeters (Nkongchu 2006).

#### **5.3.4 Scanner Assessment**

Optical cone beam imaging of scattering media (such as the NIPAM polymer gel dosimeter) has been shown to be non-linearly affected by angled scatter stray light perturbation that compromises the accuracy of absolute measurement (Olding *et al* 2010). However, the possibility exists that a well-behaved range of linear, *relative* scatter attenuation measurements could be established under some set of limiting conditions. To investigate this possibility, hybrid scattering acrylic emulsion-gelatin phantoms were manufactured in 1 L PETE jars using a similar approach to a previous investigation (Bosi *et al* 2007). These phantoms separate the optical measurement from the uncertainties of dosimeter manufacture and dose delivery. For each phantom, a gelatin mixture was prepared by adding 5 wt% gelatin (Cat.No.G2500, Sigma-Aldrich Ltd) to room temperature distilled, de-ionized water. The mixture was allowed to swell for 15 minutes at room temperature, heated to 45°C, and held for 5 minutes at that temperature to dissolve the gelatin. A suitable quantity of propylene glycol was then added to the heated gelatin-water solution for refraction matching to a typical 6%T NIPAM gel dosimeter recipe. After preparation, the heated propylene glycol-gelatin-water solution was poured into a 1 L PETE jar with a rigid finger-shaped container fixed in the jar to form the mould shape. The jar was then placed in the

refrigerator overnight to set the mould. On the following day, hot water at a temperature of 40–50°C was poured into the finger-shaped container, melting the gelatin mould slightly near the walls, and allowing the container to be removed. Calibration scattering solutions of varied concentration prepared according to Olding *et al* (2010) were poured into the mould cavity. This hybrid scattering acrylic emulsion-gelatin phantom was then imaged on the Vista scanner at each concentration of scattering solution.

### **5.3.5 Dosimeter Assessment & Modification**

To separate the optical scattering attenuation of the gelatin matrix from the other chemical components in the NIPAM gel dosimeter, a 5 wt% gelatin-in-water-filled 1 L PETE jar was imaged on the Vista scanner against a reference 1 L PETE jar containing matching tank solution. The phantom was prepared by adding the gelatin (Cat.No.G2500, Sigma-Aldrich Ltd) to room temperature distilled, de-ionized water. The mixture was allowed to swell for 15 minutes and then heated to 45°C for 5 minutes to dissolve the gelatin. The heated solution was poured into a 1 L PETE container and placed in the refrigerator overnight to set the gelatin. The gelatin-filled jar was then brought to room temperature conditions prior to optical scanning.

The contribution of reacted monomers in solution to background optical scatter attenuation was then considered. A reference scan was taken of a 1 L PETE jar filled with matching tank fluid. Data scans and corresponding optical CT images were then acquired for an un-irradiated 6%T dosimeter prepared according to procedure A, and two un-irradiated 4%T dosimeters prepared according to: (a) procedure A, and (b) the proposed alternative procedure B.

### **5.3.6 Modified Dosimeter Evaluation & Use**

To evaluate the changes in formulation and preparation procedure, test 500 cGy “A” and “K” dose distributions were delivered to 6%T and 4%T dosimeters prepared according to procedure

B. An independent dosimetric assessment of the “K” pattern was completed using Gafchromic film, with the film positioned at the central “K” slice and the delivery scaled down to 300 cGy. In this case, the “K” pattern was planned and delivered (using the same tomotherapy benchtop and cobalt-60 irradiator) to an in-house built polystyrene phantom with the film placed at one of the 7 possible plane positions, and an independent calibration of the film optical density-to-dose response was applied (Dhanesar 2008). Finally, different calibration approaches were assessed by delivering intersecting pencil beam “A” patterns at different heights in four 4%T NIPAM gel dosimeters prepared in two batches (two dosimeter jars per batch) according to procedure B.

## 5.4 Results

### 5.4.1 Initial Optical CT-MRI Comparison

In the optical CT-MRI comparison, the relationship between optical CT attenuation and dose was calibrated from the central slice in the “A” pattern dose distribution as shown in figure 5.2a. The

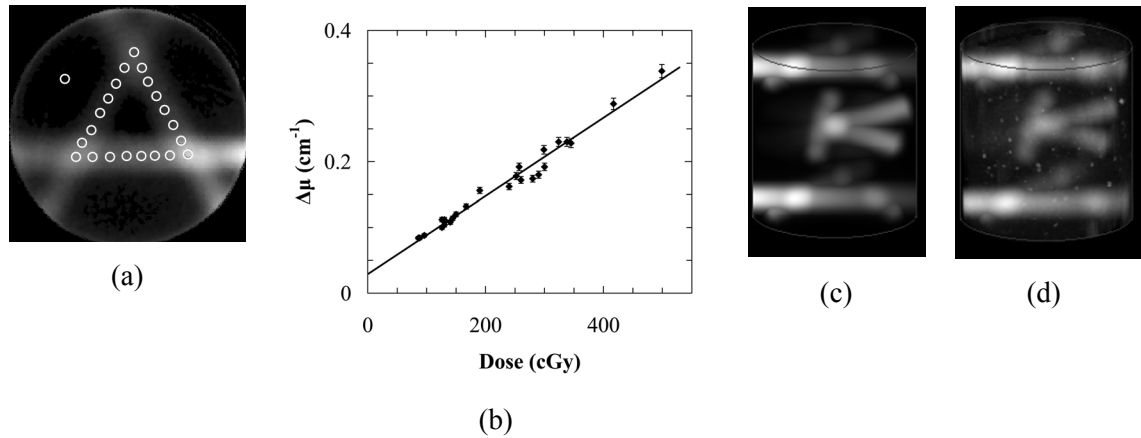


**Figure 5.2:** NIPAM gel dosimeters prepared according to procedure A were irradiated using (a) a standard pencil beam “A” pattern. (b) A linear fit calibration curve is obtained by registering and correlating well determined points on the plan and optical CT slice. (c) A volume image of a treatment plan containing two calibration “A” patterns and one measurement “K” pattern, and (d) the corresponding NIPAM gel dosimeter-measured optical CT image.

treatment plan dose and gel-measured attenuation patterns were first visually (manually) registered, and specific points covering the full dose-to-attenuation range were selected along the beam axes in the central slice of the “A” pattern. The dose and optical attenuation values at these points in the treatment plan dose and optical CT-measured attenuation distributions respectively were then fit to a linear relationship (figure 5.2b). This linear fit relationship was then applied to calibrate the full dosimeter image volume. A similar process was used for MRI R2-to-dose calibration. Figures 5.2c and 5.2d show volume images of the treatment plan dose and optical CT measured attenuation distributions respectively. Note that the initial, manual approach to optical dose-to-attenuation registration was later modified to yield an improved calibration methodology, as described in a later section in this paper.

Figures 5.3a and 5.3b present two-dimensional (2D) maps of a 3%, 3 mm Low’s gamma function voxel-by-voxel comparison of gel-measured dose against the reference treatment plan dose in the central plane of the calibrated “K” pencil beam delivery, for cone beam optical CT and MRI dose readout respectively. Significant disagreement between treatment plan dose and gel-measured dose was observed over most of the central slice of the optical CT-imaged “K” dose distribution, with only 60.2% of the voxels passing the 3%, 3mm agreement criteria. In comparison, most of the voxels (92.8%) in the central slice of the MR-imaged “K” dose distribution were in agreement with treatment plan dose when the same gamma function criteria are applied.

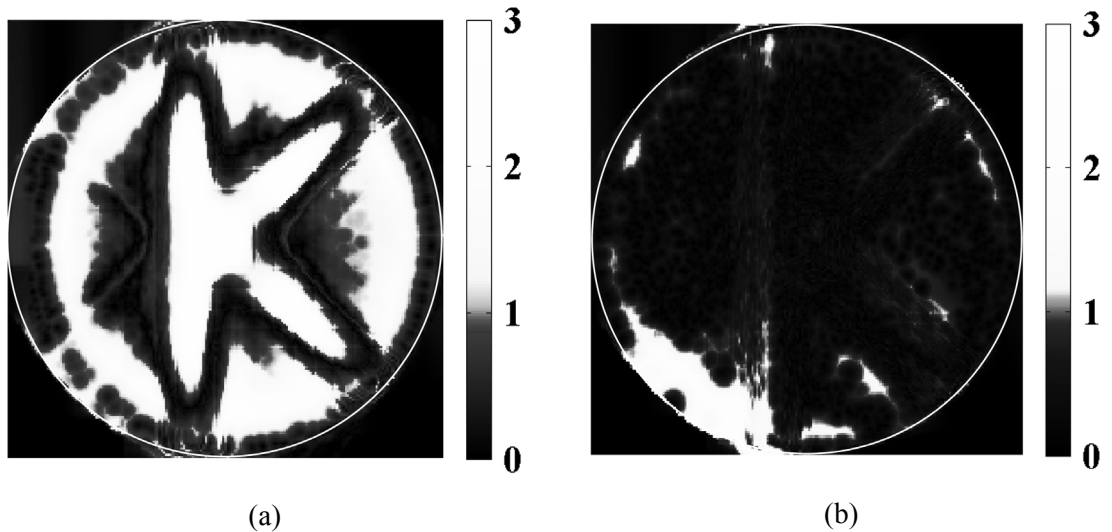


**Figure 5.3:** The central slice of a 500 cGy “K” treatment plan delivered to the 6%T NIPAM gel dosimeter prepared according to procedure A was calibrated with the dose-to-attenuation relationship determined from the “A” pattern, and evaluated using a Low’s gamma function analysis with 3% dose and 3 mm distance-to-agreement gamma function criteria. Two-dimensional gamma maps are shown comparing treatment plan dose to gel-measured dose obtained from (a) optical CT and (b) MR imaging.

#### 5.4.2 Scanner Assessment

Figures 5.4a-c show projection images of 9.2 cm diameter PETE jar phantoms incorporating: (a) a gelatin matrix surrounding a 1.6 cm diameter scattering finger, (b) a gelatin matrix surrounding a 5 cm diameter scattering finger, and (c) a uniform scattering solution, acquired by the Vista scanner. The phantom incorporating a 1.6 cm diameter scattering finger indicates linearity in mean attenuation value up to at least  $0.6 \text{ cm}^{-1}$  for a 1 cm diameter, 8 cm high cylindrical region of interest (ROI) centered in the scattering finger region (figure 5.4d). The phantom incorporating the 5 cm diameter scattering finger displays non-linearity at  $\sim 0.26 \text{ cm}^{-1}$  for a 4 cm diameter, 8 cm high measurement ROI centered in the scattering finger region. Both of these upper limits well exceed that for the scattering solution-filled jar phantom at  $0.125 \text{ cm}^{-1}$  within an 8 cm diameter, 10 cm high measurement ROI centred in the jar volume.

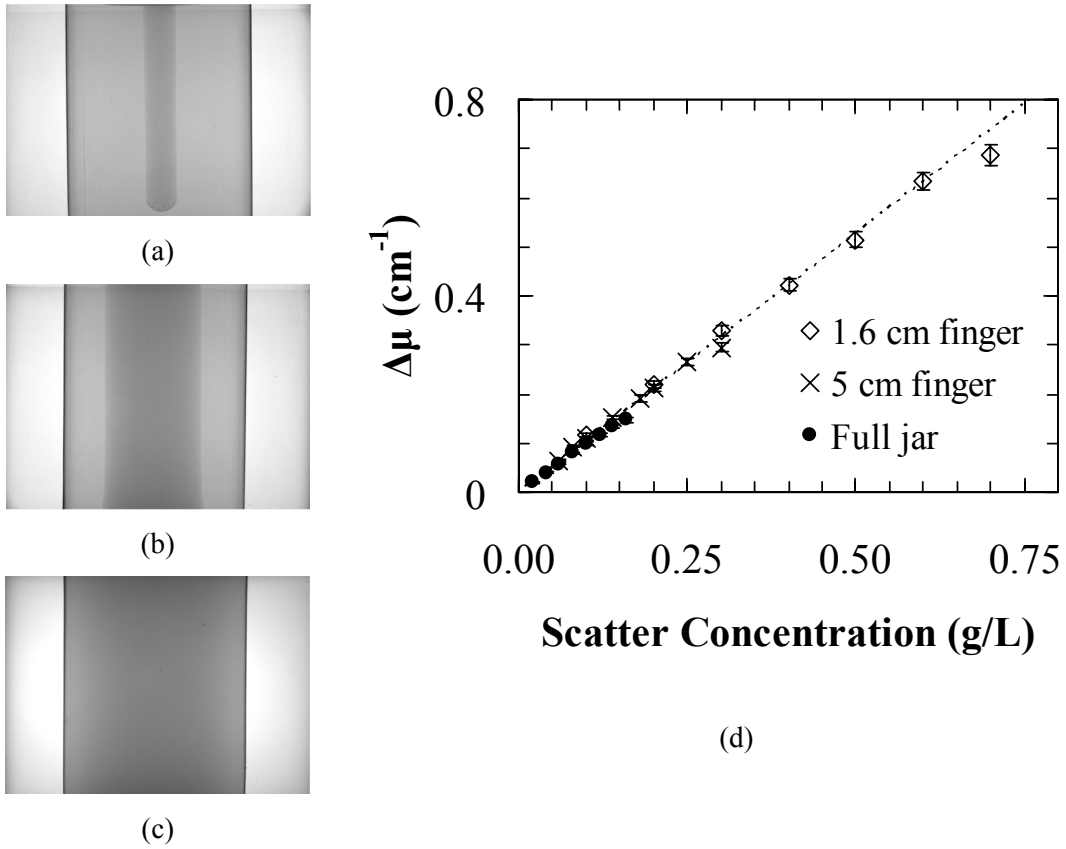


**Figure 5.4:** Vista scanner projection images from (a) a 1.6 cm diameter scattering finger-gelatin phantom, (b) a 5 cm diameter scattering finger-gelatin phantom, and (c) a scattering solution –filled jar phantom. (d) Vista mean attenuation value versus scatter concentration, measured within the scattering finger region of interest for the different phantoms, indicating the range of approximately linear behavior for each size of scattering region. Some of the error bars are smaller than symbol size.

#### 5.4.3 Dosimeter Assessment & Modification

In the evaluation of the sources of dosimeter background scatter attenuation, the mean attenuation of the 5 wt% gelatin-in-water matrix was found to be  $0.030 \pm 0.005$  cm<sup>-1</sup> in a cylindrical region of interest (ROI) covering the central 8 cm in diameter (i.e. within 5 mm of the jar walls) and central 10 cm in height of jar volume (Olding *et al* 2010). The ROI attenuations of the un-irradiated 6%T

and 4%T dosimeters prepared according to procedure A were found to be  $0.10 \pm 0.02 \text{ cm}^{-1}$  and  $0.074 \pm 0.008 \text{ cm}^{-1}$  respectively.

A reduced ROI background attenuation ( $0.050 \pm 0.002 \text{ cm}^{-1}$ ) was observed after the change in the 4%T dosimeter preparation procedure (to procedure B). Figures 5.5a and 5.5b show vertical slices through the reconstructed optical CT images of the 6%T and 4%T dosimeters prepared according to procedure A. Figure 5.5c shows the same vertical slice through the optical CT image of the 4%T dosimeter prepared according to procedure B.

Dose data from the central plane of calibration “A” patterns delivered to four NIPAM dosimeters (3%T, 3.5%T 4%T, and 6%T) prepared according to procedure B are shown in figure 5.6. The data were selected according to a modified calibration approach compared to that described in figure 2a. Registration of gel-measured dose to treatment plan dose was

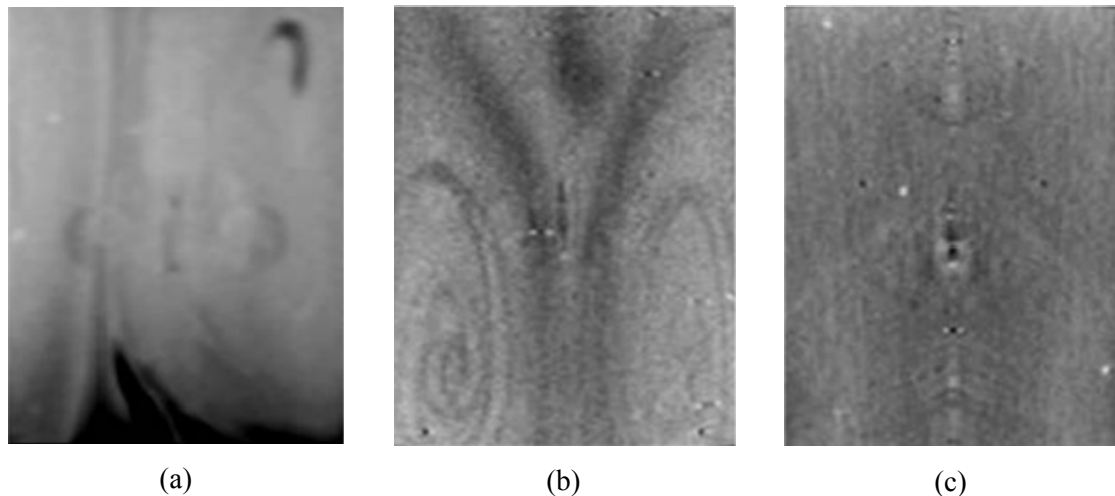


**Figure 5.5:** Reconstructed image data showing the qualitative variation in dosimeter background attenuation with manufacture procedure. Both the (a) 6%T and (b) 4%T dosimeters can have significant irregularities in dosimeter background. These irregularities and the overall background opacity can be reduced as seen in (c) a 4%T dosimeter produced by a modified preparation method. The central axis artifacts seen in (c) are not features in the dosimeter but are related to other stray light effects from scanner imaging. The slice in (c) is windowed at a significantly higher level of contrast than (a) and (b) to show these artifacts.

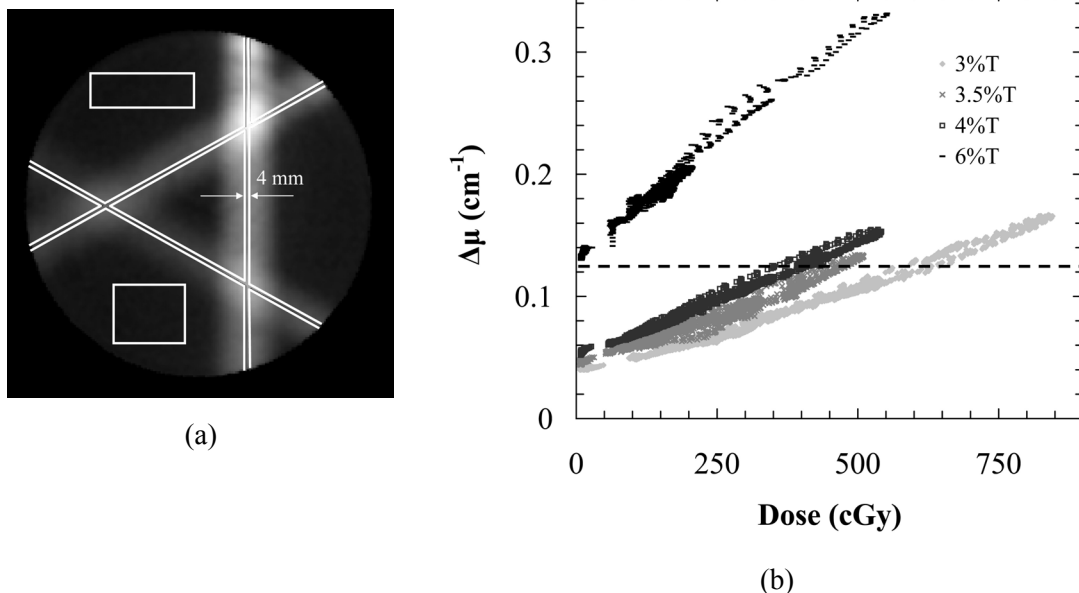


**Figure 5.6:** (a) The attenuation to dose calibration region of interest (ROI) for a 4%T NIPAM-based dosimeter prepared according to procedure B and irradiated using a standard intersecting pencil beam “A” pattern. (b) Dose data from the central plane of calibration “A” patterns delivered to four NIPAM-based polymer gel dosimeters prepared according to procedure B with total monomer in the range of 3-6%T. The dotted line indicates the approximate limit of well-behaved readout of well-characterized scattering solution-filled 1 L PETE jar dosimeters.

accomplished using an automatic computer selected point based registration tool written in MATLAB (Holmes 2008). A larger number of data points ( $> 3000$ ) were used in the dose-to-attenuation second order polynomial fit calibration, taken from the marked regions in figure 5.6a. The dashed line shown in the plot (figure 5.6b) indicates a mean attenuation value of  $0.125 \text{ cm}^{-1}$ , assessed as the point of significant departure from linearity of the scattering solution-filled 1 L PETE jar cone beam image data in the previous section (figure 5.4d).

#### 5.4.4 Modified Dosimeter Evaluation & Use

Figure 5.7a shows an evaluation of the 4%T dosimeter prepared according to procedure A. The 3%,3 mm 2D Low’s gamma function analysis of the central “K” slice calibrated with the “A” pattern-derived dose-to-attenuation relationship indicates improved dosimetry over the initial

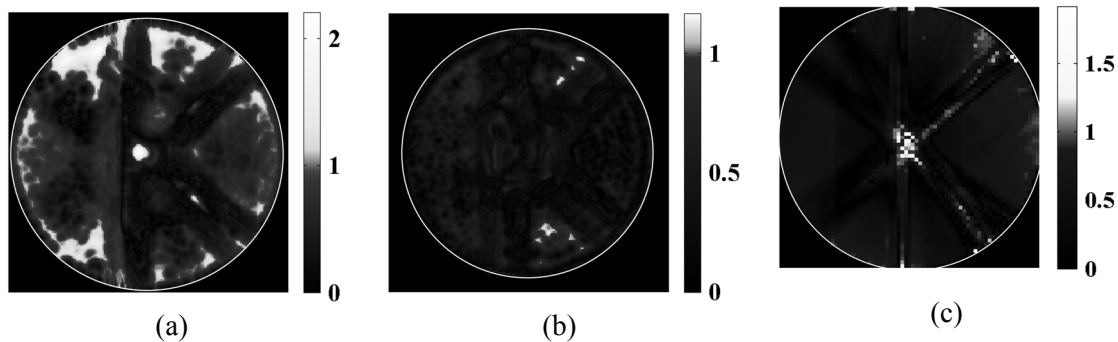


**Figure 5.7:** Gamma function evaluations (3%, 3mm) of a 500 cGy “K” treatment plan delivered to (a) a 6%T dosimeter, (b) a 4%T dosimeter and (c) Gafchromic film (300 cGy).

optical CT results presented in figure 5.2b, with an increased 89.2% voxel agreement between gel-measured dose. However, regions of significant failure are still indicated in both high and low dose regions in the dosimetry due to operation outside the approximate upper limit of the Vista scanner. When the experiment was repeated on a 4%T dosimeter prepared according to procedure B, an improved 99.5% voxel agreement is observed between gel-measured dose and treatment plan dose using the same gamma comparison criteria (figure 5.7b). The 3%, 3mm 2D Low’s gamma function analysis of the independent Gafchromic film measurement shown in figure 5.7c indicates 98.6% voxel agreement between treatment plan dose and film dose. Most of the observed failure in the central region was due to mechanical abrasion of the film in phantom.

Calibration data were obtained from the central plane of each intersecting pencil beam irradiation according to the method in figure 5.5a. The intra-batch dose response (i.e. response between two dosimeter jars prepared from the same gel batch) was investigated through calculation of second-order polymer fits to the “A” patterns in these jars, shown in figure 5.8a. The fitted dose responses were found to be in agreement to within 3.6 % of the dose maximum value over the full dose range (figure 5.8a). The average difference between fits was 1.5%, falling within the combined standard error of the fits of ~4.0%.

The inter-batch dose response was investigated in a similar manner. In this case, the polynomial fits to the “A” patterns in two dosimeter jars prepared from different gel batches differed by as much as 3.8% (see figure 5.8b). The average difference of 1.6% between fits was also within the combined standard error of the fits (~4.5 %), and was only slightly worse than the result from intra-batch calibration. Both these gel batches were prepared on the same day using

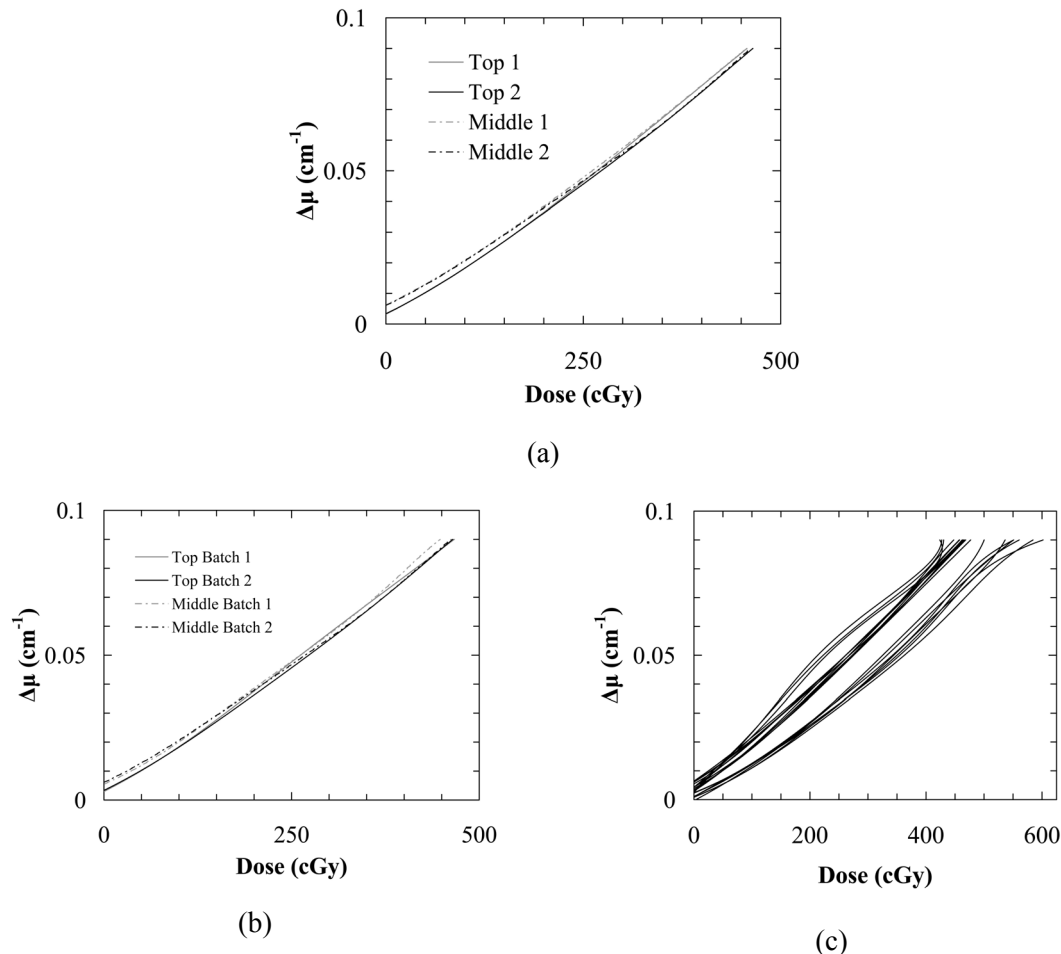


**Figure 5.8:** Second order polynomial dose-to-attenuation fits to calibration “A” patterns delivered to two 4%T, 50%C NIPAM-based polymer gel dosimeters prepared (a) from the same gel batch, (b) on the same day from different gel batches, according to procedure B, and (c) from multiple batches prepared on different days using multiple chemical lots.

the same chemicals. They also were irradiated and scanned within a short time period of each other. When the day of preparation, chemical lot, or irradiation & scan times are varied, the “A” pattern calibration fits varied considerably, as shown in figure 5.8c.

## 5.5 Discussion

### 5.5.1 Initial Optical CT-MRI Comparison

On preliminary examination, the calibration data in figure 5.2b indicates that the NIPAM dosimeter has a well-behaved linear dose response, without obvious stray light perturbation due to angled scatter signal. However, a 2D gamma function analysis of the optical CT-imaged (and “A” pattern-calibrated) “K” dose distribution (figure 5.3a) reports an unacceptable level of disagreement between treatment plan dose and gel-measured dose in the central slice of the dose distribution. Without further investigation, these results seem to indicate that cone beam optical CT is unsuitable for readout of scattering polymer gel dosimeters. A large percentage of the failure observed from MRI (figure 5.3b) can be attributed to susceptibility artifacts near the jar edge. With this effect accounted for, the performance of the gold standard of MRI is both acceptable and clearly superior to that of cone beam optical CT for accurate polymer gel dosimeter readout. Note that due to time constraints, it was necessary to scan the irradiated dosimeter using MRI on a subsequent day. However, since an in-jar (or intra-jar) “A” calibration of attenuation-to-dose was performed for both readout modalities then applied to the “K” dose distribution, the differences in dosimeter scan temperature and dosimeter development time are well-accounted for in the calibrated “K” dose distribution

The observed failure in optical CT imaging is consistent with results presented in a previous report indicating that, despite the conformation of the data to a linear fit, the Vista scanner scatter attenuation measurements exhibit non-linear behavior compared to ‘true’

spectrophotometer attenuation measurements (Olding *et al* 2010). This prior work concludes that artifacts arising from angled scatter and other forms of stray light perturbation compromise the accuracy of attenuation measurement over the entire volume of the scattering media-filled 1 L PETE jar dosimeter. The results (figure 10a in Olding *et al* 2010) also show that the accuracy of the cone beam optical scatter measurement reduces significantly with increasing mean scatter attenuation within the 1 L PETE jar dosimeter. A second conclusion from Olding *et al.* (2010) was that angled scatter and other forms of stray light perturbation need to be better managed or corrected for in order for the combination of polymer gel dosimetry and cone beam optical CT imaging to be viable.

### **5.5.2 Scanner Assessment**

Cone beam imaging data from the hybrid acrylic-gelatin scattering finger phantoms (figure 5.4d) shows that the point at which the scanner scatter attenuation measurement significantly depart from linearity varies with the size and shape of the scattering region. The results also indicate that the *relative* attenuation measurements show reasonable linearity and reproducibility over a range of scatter concentrations and scattering region volumes. This range increases as the size of the scattering region decreases. A benchmark upper limit on the well-behaved linear fit range of (relative) scatter attenuation measurement for small field dose deliveries to a NIPAM-gel filled 1 L PETE jar dosimeter can therefore be roughly established as  $0.125 \text{ cm}^{-1}$ . This value represents the worst case scenario, where the full PETE jar volume exhibits this scatter attenuation.

The goal, therefore, is to reduce the overall dosimeter response so that all post-irradiation attenuation values from the dosimeter fall within this well-behaved linear fit range of attenuation measurement. The simplest approaches to reduction of angled scatter-sourced stray light perturbation include increasing the scanner light source wavelength into the infrared and/or reducing the dose contrast sensitivity and scatter attenuation background of the NIPAM gel.

Dosimeter modification was selected as the route of choice as it was easiest to adjust, and was estimated as being capable of greater reduction in stray light perturbation. Both routes involve a necessary tradeoff of lower signal-to-noise ratio.

### **5.5.3 Dosimeter Assessment & Modification**

The imaged mean attenuation values for the 5% gelatin-in-water-filled jar and a typical 6%T dosimeter indicate that most of the background scatter attenuation in the dosimeter is not from the gelatin matrix. The remaining background scatter attenuation is likely sourced from independent polymerization reactions involving the BIS and NIPAM monomers. It is conceivable that a small reduction in background could be achieved by lowering the gelatin content in the dosimeter to 3-4 wt%. However, a larger reduction in background may be possible through better control of monomer reactions in solution, if there are monomer-based polymerization reactions occurring prior to irradiation.

Unpublished results from the testing of the BIS and NIPAM monomers have indicated that the NIPAM monomer in particular may undergo some form of polymerization reaction after the addition of THPC oxygen scavenger to a NIPAM-water mixture. This has been evidenced by a clear-to-cloudy reversible phase transition observed in the NIPAM-water-THPC solution as the temperature of solution is raised and lowered past the temperature range of 25-30°C. This clear-to-cloudy reversible transition is consistent with reports in literature (Kara *et al* 2002, Takata *et al* 2002) describing the de-swelling behavior of polymerized NIPAM in solution at a lower critical solution temperature in the temperature range of 25-30°C, accompanied by a measureable increase in turbidity. In basic polymer science literature, an initiator is generally used to cause polymerization of the NIPAM monomer in solution. In the case of the NIPAM-water-THPC mixture, the initiator is not known, but it may possibly be some combination of ultraviolet light exposure, chemical contaminants, or heat. There is some time hysteresis in this reversible

temperature-dependent phase transition, such that de-swelled polymerized NIPAM in solution may remain as “frozen-in” scattering particles in the polymer gel dosimeter after it has transitioned to solid gel state under refrigeration. This is believed to be the source of the increase in scatter background with monomer addition. This conclusion is consistent with the results obtained when the gels are prepared with acrylamide monomer replacing the NIPAM monomer (but keeping the same BIS cross-linking monomer). The replacement of the NIPAM monomer leads to a lower polymer gel background scatter attenuation background of 0.05-0.06 cm<sup>-1</sup> (unpublished results), much closer to that measured for the gelatin matrix. Unlike the NIPAM monomer, no evidence of lower critical solution temperature behavior is indicated for acrylamide in the literature.

To determine the contribution to scatter background attenuation by the suspected NIPAM monomer polymerization and de-swelling behavior at elevated temperatures, two changes were made to the manufacturing process. First, the total amount of monomer and cross-linker was lowered from 6%T to 4%T. A corresponding decrease in background attenuation was measured with the reduction in total monomer concentration, supporting the conclusion that monomer polymerization is the second, and major source of background scatter attenuation in the NIPAM polymer gel dosimeter. Second, both the 6%T dosimeter and the 4%T dosimeter prepared according to procedure A have been observed to have irregular backgrounds (see figures 5.5a and 5.5b). This feature is likely due to thermal currents during spatial fixing of scattering particles in the gelation process. These irregular backgrounds can also cause problems with the dosimetry if the jar is even slightly shifted between reference and data scans. To address this issue, a second change was made to dosimeter preparation, as described in procedure B.

Undesirable polymerization-deswelling behavior of the NIPAM monomer can mostly be avoided by dissolving NIPAM separately in room-temperature water, then adding THPC to this

mixture at the last possible moment before addition of the NIPAM-THPC-water solution to the BIS-gelatin-water solution at 33-34°C. This procedure yields a final solution temperature of approximately 30°C which is sufficiently above the gelatin set point of roughly 26-28°C so that the solution can be poured into the dosimeter jar without the formation of entrapped bubbles. The dosimeter jar is immediately placed in a dark refrigerator to prevent the suspected UV light initiation of polymerization. This preparation procedure (i.e. procedure B) advantageously reduces both the irregularities and the overall level of the dosimeter background scatter attenuation from around  $0.075 \pm 0.008 \text{ cm}^{-1}$  (figure 5.5b) to as little as  $0.050 \pm 0.002 \text{ cm}^{-1}$  for a 4%T NIPAM-based polymer gel dosimeter (figure 5.5c). The reduced background attenuation of the 3-4%T polymer gels, combined with the lower irradiation gel dosimeter sensitivity, then results in irradiated dosimeter attenuation values that are below this approximate upper limit on mean jar scatter attenuation linearity from the cone beam optical CT scanner (figure 5.6b).

#### **5.5.4 Modified Dosimeter Evaluation & Use**

The gamma function analyses presented in figure 5.7 indicate that the target 95% voxel agreement between treatment plan and cone beam optical CT NIPAM gel-measured dose distributions using 3% dose and 3 mm distance-to-agreement gamma function criteria is satisfied using the 4%T NIPAM gel-filled dosimeter. This shows that careful dosimeter selection enables the evaluation of small field dose deliveries using cone-beam optical CT-based polymer gel dosimetry. While the limitations on what constitutes a small field have not strictly been specified, pencil beam deliveries of 1-2 cm field edge width are certainly possible using the standard-sized 1 L 4%T NIPAM dosimeter.

The results from figure 5.8a indicate that a same-batch, inter-jar calibration methodology for evaluation of small field dose deliveries using cone beam optical CT-based NIPAM polymer gel dosimetry is feasible. It was expected that using a ‘calibration’ and a ‘measurement’

dosimeter prepared from the same gel batch, in the same container size, and under the same environmental conditions (De Deene *et al* 2007) would clearly be the best approach. The approximately equivalent performance from inter-batch dosimeter calibration when the batches were prepared on the same day (see figure 5.8b) was a surprising result. However, only a single set of experimental results are presented in each of figures 5.8a and 5.8b, so definitive conclusions cannot be drawn in this regard. Also, while a cobalt-60 irradiator is utilized in this experiment, a similar pencil beam pattern could be well-characterized for linear accelerator delivery in cancer centers that do not have access to a cobalt-60 unit. Additional scatter management and/or correction strategies are required for inter-batch calibration and dosimeter readout of larger volume irradiations where scatter perturbation from the irradiated volume suppresses the measured attenuation values in a non-linear manner.

## 5.6 Conclusions

With appropriate attention to gel chemistry and manufacture, normoxic NIPAM polymer gel dosimeters can be used in combination with cone beam optical computed tomography dose readout for assessment of small field dose deliveries. Relative, linearly-related optical scatter attenuation measurements are obtained for different scattering volumes in a standard-sized NIPAM gel-filled 1 L PETE jar dosimeter up to an approximate upper limit of  $0.125 \text{ cm}^{-1}$ . These attenuation measurements can be calibrated to dose using a well-determined dose distribution, and used for small field dose delivery evaluation. Under the condition of intra-batch calibration, the target level of 95% voxel agreement between treatment plan and gel-measured dose distributions is realized for 3% dose and 3 mm distance-to-agreement gamma function criteria. Clinical utility is therefore well indicated. Inter-batch calibration is also possible, but requires further attention to the chemical lot, manufacture and environmental conditions of the dosimeter prior to irradiation.

## 5.7 References

- Babic S, Battista J and Jordan K 2008 Three-dimensional dose verification for intensity-modulated radiation therapy in the radiological physics centre head-and-neck phantom using optical computed tomography scans of ferrous xylene-orange gel dosimeters. *Int.J.Radiat.Oncol.Biol.Phys.* 70 1281-1291.
- Babic S, McNiven A, Battista J and Jordan K 2009 Three-dimensional dosimetry of small megavoltage radiation fields using radiochromic gels and optical CT scanning. *Phys.Med.Biol.* 54 2463-2481.
- Baldock C, Harris P J, Piercy A R and Healy B 2001a Experimental determination of the diffusion coefficient in two-dimensions in ferrous sulphate gels using the finite element method. *Australas.Phys.Eng.Sci.Med.* 24 19-30.
- Baldock C, Lepage M, Back S A, Murry P J, Jayasekera P M, Porter D and Kron T 2001b Dose resolution in radiotherapy polymer gel dosimetry: effect of echo spacing in MRI pulse sequence. *Phys.Med.Biol.* 46 449-460.
- Bosi S, Naseri P, Puran A, Davies J and Baldock C 2007 Initial investigation of a novel light-scattering gel phantom for evaluation of optical CT scanners for radiotherapy gel dosimetry. *Phys.Med.Biol.* 52 2893-2903.
- Chang H and Fitzpatrick J M 1992 A technique for accurate magnetic resonance imaging in the presence of field inhomogeneities. *IEEE Trans.Med.Imaging* 11 319-329.
- De Deene Y and Baldock C 2002 Optimization of multiple spin-echo sequences for 3D polymer gel dosimetry. *Phys.Med.Biol.* 47 3117-3141.
- De Deene Y and De Wager C 2001 Artefacts in multi-echo T2 imaging for high-precision gel dosimetry: III. Effects of temperature drift during scanning. *Phys.Med.Biol.* 46 2697-2711.
- De Deene Y, Pittomvils G and Visalatchi S 2007 The influence of cooling rate on the accuracy of normoxic polymer gel dosimeters. *Phys.Med.Biol.* 52 2719-2728.
- DeJean P, Senden R J, McAuley K B, Rogers M and Schreiner L J 2006a Initial Experience with a commercial cone beam CT unit for polymer gel dosimetry I: optical dosimetry issues. *Journal of Physics: Conference Series* 56 179-182.
- DeJean P, Senden R J, McAuley K B, Rogers M and Schreiner L J 2006b Initial Experience with a commercial cone beam CT unit for polymer gel dosimetry II: clinical potential. *J.Phys.: Conf.Ser.* 56 183-186.
- Dhanesar S *Conformal Radiation Therapy with Cobalt-60 Tomotherapy* (M.Sc. Thesis, Queen's University, 2008).
- Doran S 2009 The history and principles of optical computed tomography for scanning 3-D radiation dosimeters: 2008 update. *J.Phys.: Conf.Ser.* 164 98-119.

- Doran S and Krstajic N 2006 The history and principles of optical computed tomography for scanning 3-D radiation dosimeters. *J.Phys.: Conf.Ser.* 56 45-57.
- Doran S J, Koerkamp K K, Bero M A, Jenneson P, Morton E J and Gilboy W B 2001 A CCD-based optical CT scanner for high-resolution 3D imaging of radiation dose distributions: equipment specifications, optical simulations and preliminary results. *Phys.Med.Biol.* 46 3191-3213.
- Gore J C, Kang Y S and Schulz R J 1984 Measurement of radiation dose distributions by nuclear magnetic resonance (NMR) imaging. *Phys.Med.Biol.* 29 1189-1197.
- Gore J C, Ranade M, Maryanski M J and Schulz R J 1996 Radiation dose distributions in three dimensions from tomographic optical density scanning of polymer gels: I. Development of an optical scanner. *Phys.Med.Biol.* 41 2695-2704.
- Graumann R, Oppelt A and Stetter E 1986 Multiple-spin-echo imaging with a 2D Fourier method. *Magn Reson.Med.* 3 707-721.
- Hilts M, Audet C, Duzenli C and Jirasek A 2000 Polymer gel dosimetry using x-ray computed tomography: a feasibility study. *Phys.Med.Biol.* 45 2559-2571.
- Holmes O *Validation of Conformal Radiation Therapy Treatments in 3D Using Polymer Gel Dosimeters and Optical Computed Tomography* (M.Sc. Thesis, Queen's University, 2008).
- Kara S, Sayil C and Okay O 2002 Real Time Temperature and Photon Transmission Measurements for Monitoring Phase Separation during the Formation of Poly(N-isopropylacrylamide) Gels. *J.Appl.Polym.Sci.* 86 3589-3595.
- Kawanaka A and Takagi N 1986 Estimation of static magnetic field and gradient fields from NMR image. *J.Phys E: Sci.Instrum* 19 871-875.
- Krstajic N and Doran S J 2006 Focusing optics of a parallel beam CCD optical tomography apparatus for 3D radiation gel dosimetry. *Phys.Med.Biol.* 51 2055-2075.
- Krstajic N and Doran S J 2007 Characterization of a parallel-beam CCD optical-CT apparatus for 3D radiation dosimetry. *Phys.Med.Biol.* 52 3693-3713.
- Lepage M, Jayasakera P M, Back S A J and Baldock C 2001 Dose resolution optimization of polymer gel dosimeters using different monomers. *Phys.Med.Biol.* 46 2665-2680.
- Low D A and Dempsey J F 2003 Evaluation of the gamma dose distribution comparison method. *Med.Phys.* 30 2455-2464.
- Low D A, Dempsey J F, Venkatesan R, Mutic S, Markman J, Haacke E M and Purdy J A 1999 Evaluation of Polymer gels and MRI as a 3-D dosimeter for intensity-modulated radiation therapy. *Med.Phys.* 26 1542-1551.

Maryanski M J, Gore J C, Kennan R P and Schulz R J 1993 NMR relaxation enhancement in gels polymerized and cross-linked by ionizing radiation: a new approach to 3D dosimetry by MRI. *Magn.Reson.Imaging* 11 253-258.

Maryanski M J, Zastavker Y Z and Gore J C 1996 Radiation dose distributions in three dimensions from tomographic optical density scanning of polymer gels: II. Optical properties of the BANG polymer gel. *Phys.Med.Biol.* 41 2705-2717.

Milan J and Bentley R E 1974 The storage and manipulation of radiation dose data in a small digital computer. *Br.J.Radiol.* 47 115-121.

Nkongchu K, "Magnetic resonance imaging approaches to gel dosimetry for validation of conformal radiotherapy treatment plans" (Ph.D. Thesis, Carleton University, 2006).

Oldham M and Kim L 2004 Optical-CT gel-dosimetry. II: Optical artifacts and geometrical distortion. *Med.Phys.* 31 1093-1104.

Oldham M, Siewerdsen J H, Kumar S, Wong J and Jaffray D A 2003 Optical-CT gel-dosimetry I: basic investigations. *Med.Phys.* 30 623-634.

Olding T, Holmes O and Schreiner L J 2010 Cone beam optical computed tomography for gel dosimetry I: scanner characterization. *Phys.Med.Biol.* 55 2819-2840.

Olsson L E, Fransson A, Ericsson A and Mattsson S 1990 MR imaging of absorbed dose distributions for radiotherapy using ferrous sulphate gels. *Phys.Med.Biol.* 35 1623-1631.

Olsson L E, Westrin B, Fransson A and Nordell B 1992 Diffusion of ferric ions in agarose dosimeter gels. *Phys.Med.Biol.* 37 2243-2251.

Senden R J, De Jean P, McAuley K B and Schreiner L J 2006 Polymer gel dosimeters with reduced toxicity: a preliminary investigation of the NMR and optical dose-response using different monomers. *Phys.Med.Biol.* 51 3301-3314.

Takata S, Suzuki K, Norisuye T and Shibayama M 2002 Dependence of shrinking kinetics of poly(N-isopropylacrylamide) gels on preparation temperature. *Polymer* 43 3101-3107.

Wolodzko J G, Marsden C and Appleby A 1999 CCD imaging for optical tomography of gel radiation dosimeters. *Med.Phys.* 26 2508-2513.

## **Chapter 6**

### **Treatment Process Quality Assurance Using Polymer Gels**

A version of this chapter is in the process of being prepared for submission to Medical Physics as:

*Olding T, Holmes O, McAuley K, Darko J, and Schreiner L J “Treatment Process Quality Assurance Using Cone Beam Optical CT-Based Polymer Gel Dosimetry.”*

#### **6.1 Abstract**

This work explores the improvement of the combination of cone beam optical computed tomography (CT) with an N-isopropylacrylamide (NIPAM)-based polymer gel dosimeter for three-dimensional (3D) dose measurements in treatment process quality assurance. Results are presented from the imaging of non-uniform calibration scattering phantoms (incorporating varied size and varied attenuation scattering regions) that illustrate the complicating effects of scatter-derived stray light perturbation in the system. Different scatter management and correction strategies are applied in an attempt to improve the accuracy of measurement. Modification of the scanner to a fan beam configuration is shown to be a viable route forward, as the polymer gels are relatively insensitive to the increased scan time required for fan beam data acquisition. Stray light corrections of the projection image data using beam stop array measurements are shown to have limited application in the imaging of relatively uniform dose deliveries. Finally, even without achieving a high level of dosimetric accuracy, cone beam optical CT-based polymer gel dosimetry can provide useful 3D dose evaluations. In this report, a treatment process quality assurance methodology using a NIPAM gel in-phantom is described, and results are presented from an example conformal delivery that clearly identify a mis-alignment in the delivery when a first order global dose sensitivity normalization correction is applied to the dose data.

## 6.2 Introduction

Polymer gels were introduced over a decade ago (Maryanski *et al* 1993, Maryanski *et al* 1994) as promising high resolution, tissue-equivalent chemical dosimeters for full three-dimensional (3D) measurement of complex radiation therapy dose distributions. The long-term stability of spatial dose information in the polymer gel was a key advancement in the field of gel dosimetry. The widespread accessibility of polymer gels was also an exciting prospect, due to the possibility of using relatively inexpensive optical computed tomography (CT) scanners for 3D dose readout (Maryanski *et al* 1996, Doran and Krstajic 2006). However, optical readout of 3D dose (Gore *et al* 1996) has been challenged by the confounding effects of stray light perturbation arising from angled scatter and other forms of contaminant light (Oldham *et al* 2003, Oldham and Kim 2004). These effects are particularly problematic when employing a fast area-based imaging apparatus, such as the Vista<sup>TM</sup> cone beam optical CT scanner (Modus Medical Devices Inc, London, ON, Canada).

The question addressed in this work is whether stray light perturbation can be reduced or corrected for so that the measurement from cone beam optical CT-based polymer gel dosimetry can be improved for use in treatment process quality assurance (QA). Various pre- and post-processing scatter management strategies have been employed in cone beam x-ray CT that may be applied to cone beam optical CT (Rinkel *et al* 2007). One approach employs anti-scatter grids to reduce X-ray scatter signal in the projection image (Endo *et al* 2001, Siewerssen *et al* 2004). Another tactic, referred to as the beam stop method, is to acquire projection images with and without an array of opaque disks inserted at the x-ray source side of the scanner (Siewerssen and Jaffray 2001, Ning *et al* 2004). Scatter measurements are extracted from the centre point of each disk in the projection image, and the grid of point measurements is interpolated to form a scatter map. These corrective maps (or a mean scatter value) are then subtracted from each image in the

projection set prior to reconstruction. This method has been used in the determination of single point measurement stray light value corrections in primarily optically absorbing media (Jordan and Battista 2006).

The stray light reduction schemes explored in this work include: a) insertion of optical anti-scatter grids (i.e. polarizer sheets) in the imaging apparatus, b) increasing the object to detector distance in the scanner, and c) limiting the area of image acquisition to fan beam geometry. In addition, the scatter correction capabilities and limitations of an optical beam stop array (BSA) method (Olding *et al* 2009) for uniform and high dose gradient regions are investigated. Independent calibration scattering solutions, scattering gel phantoms and absorbing solutions are employed in the stray light reduction and correction assessments (Olding *et al* 2010) that allow the uncertainties of stray light perturbation to be separated from those arising from gel preparation and dose delivery. An N-isopropylacrylamide (NIPAM)-based recipe (Senden *et al* 2006) was employed in the preparation of the polymer gel dosimeters used for treatment process quality assurance in this report. This formulation was originally developed as a lower toxicity alternative to the more widely used acrylamide-based polymer gel (Maryanski *et al* 1993, Maryanski *et al* 1996), and was chosen for this reason.

## 6.3 Methods and Materials

### 6.3.1 Calibration Solution and Gel Dosimeter and Preparation

Calibration scattering solutions were prepared through addition of small amounts of an acrylic latex emulsion (Duramax B-1000, Rohm & Haas, Philadelphia, PA, USA) to mixtures of 12 wt% propylene glycol (Cat.No.134368, Sigma-Aldrich Ltd) in water. These solutions were then poured into 1 L polyethylene terephthalate (PETE) containers with an outer diameter of 9.2 cm. Calibration absorbing solutions were similarly prepared through addition of small amounts of

patent blue violet dye (Cat.No.198218, Sigma-Aldrich Ltd) to mixtures of 12 wt% propylene glycol in water and poured into 1 L PETE containers. The calibration solutions were stored at room temperature prior to optical scanning.

Heated scattering acrylic emulsion-gelatin phantoms were manufactured in 1 L PETE containers using a similar approach to that described by Bosi *et al* (2007). The 5 wt% gelatin-in-water-based mould was prepared with a rigid ‘finger’-shaped container positioned into the 1 L PETE jar during gel setting in the refrigerator overnight. On the following day, hot water at a temperature of 40-50°C was poured into the finger-shaped container, melting the gelatin slightly near the walls, thus allowing the container to be removed. A calibration scattering solution was poured into the mould cavity and the hybrid scattering acrylic emulsion-gelatin phantom was imaged on the Vista scanner. These last two steps were then repeated for a series of varied concentration scattering solutions.

NIPAM polymer gel dosimeters were prepared under atmospheric (normoxic) conditions containing 5 wt% gelatin (300 bloom Type A porcine gelatin, Cat.No.G2500, Sigma-Aldrich Ltd), 2 wt% N,N'-methylene-bis-acrylamide (BIS) crosslinking monomer (Cat.No.146072, Sigma-Aldrich Ltd), 2 wt% N-isopropylacrylamide (NIPAM) monomer (Cat.No.415324, Sigma-Aldrich Ltd) and 5 mM of tetrakis hydroxymethyl phosphonium chloride (THPC, Cat.No.404861, Sigma-Aldrich Ltd) in a balance of water. The dosimeters were prepared by allowing the gelatin to swell in 70 wt% of the de-ionized water at room temperature for 10 minutes and heating the solution to 50°C. The BIS cross-linker was added under stirring at 50°C until dissolved. The BIS-gelatin-water solution was then cooled to 34°C. Separately, the NIPAM monomer and THPC were dissolved in the remaining water at room temperature. The NIPAM-THPC-water solution was then added to the cooled BIS-gelatin-water solution, mixed for 1-2 minutes, poured into 1 L PETE containers, and refrigerated for 24 hours prior to irradiation.

### **6.3.2 Cone Beam Optical CT Imaging**

Optical CT imaging was completed under room temperature conditions at an illumination wavelength of 633 nm and camera lens aperture of f5 in the Vista<sup>TM</sup> cone beam optical scanner (Modus Medical Devices Inc). A full description of the imaging and reconstruction process for the Vista scanner has previously been reported (Olding *et al* 2010), so only the necessary details are repeated here. Matching tank solution for the scanner consisted of a 12 wt% propylene glycol-in-water mixture, the refractive index of which ( $1.346 \pm 0.001$  at 590 nm) was monitored over time using a handheld refractometer with a central measurement wavelength of 589 nm (r<sup>2</sup> mini refractometer, Reichert Analytical Instruments, Depew, NY, USA) at room temperature ( $21 \pm 1^\circ\text{C}$ ). Room temperature measurements were taken using a digital temperature probe (TM99A-NA Digital Thermometer, Nuclear Associates, Carle Place, NY, USA).

Reference scans were completed on the NIPAM gel dosimeters close to the time of irradiation, at the highest shutter exposure time possible without inducing camera pixel saturation, and the lowest gain setting. Data scans were acquired using the same camera settings as the reference scan at a post-irradiation time of ~12 hours, unless otherwise specified. As the dosimeter reacts over a period of several hours after the irradiation (Senden *et al* 2006), the wait time of 12 hours prior to optical CT scanning was chosen to ensure that the polymerization reaction was near completion at the time of imaging.

Calibration solutions and phantoms were similarly imaged, with a 1 L PETE jar filled with matching tank fluid used for their reference scans. The 12 hour post-irradiation wait time imposed for the imaging of NIPAM dosimeters was not required for the calibration solutions and phantoms, which were imaged immediately following the reference scans. For each scan, a set of 410 light intensity transmission projections were acquired over  $360^\circ$  in approximately 5-6 minutes. High resolution ( $0.5 \times 0.5 \times 0.5 \text{ mm}^3$  voxel) images with a volume of  $12.8 \times 12.8 \times 12.8$

$\text{cm}^3$  incorporating the imaged 1 L PETE jar, were reconstructed in 10 minutes using a standard desktop computer.

### 6.3.3 Stray Light Reduction

Three different hardware adjustments were explored with the goal of achieving stray light reduction in the system. In the first configuration, polarizing films (TECHSPEC<sup>TM</sup> polarizing film, Cat.No. R45-669, Edmund Optics, Barrington, NJ, USA) were placed at the front and rear of the Vista scanner matching tank (see figure 6.1a). Optical CT imaging was then completed on varied concentration scattering solution-filled 1 L PETE jars at room temperature over a concentration range of 0.01-0.08 g/L. Spectrophotometer measurements were also obtained by separating small portions of the varied concentration calibration solutions into 10 mm polymethyl-methacrylate (PMMA) cuvettes and evaluating these samples using an Ultrospec 1000 UV/Visible spectrophotometer (Biochrom Ltd, Cambridge, UK). As the spectrophotometer provides better than 0.5-1.0% accuracy in transmission measurement, its data were considered to be a reasonably ‘true’ assessment of calibration solution attenuation (Olding *et al* 2010).

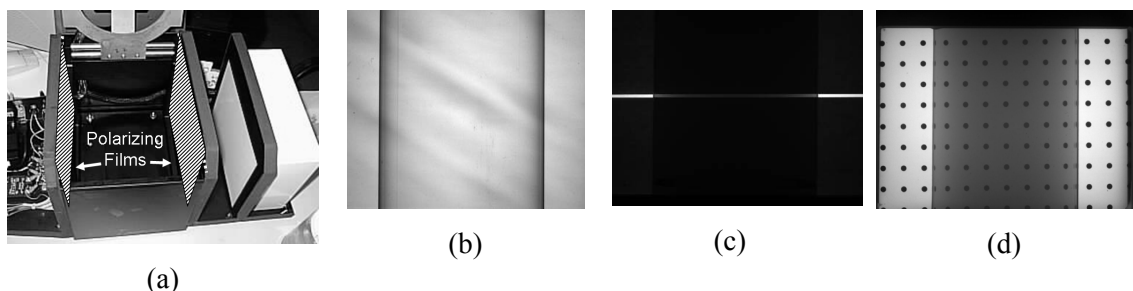


**Figure 6.1:** (a) A photograph showing the positions of the polarizing films in the Vista scanner. (b) A projection image of a matching tank fluid-filled 1 L PETE jar in the Vista scanner with the polarizing films in place. (c) A fan beam projection image of a 0.15 g/L calibration solution-filled 1 L PETE jar in the Vista scanner. (d) A projection image of a 0.10 g/L calibration solution-filled 1 L PETE jar with a BSA blocker placed at the light source side of the matching tank (4 mm diameter dots, 16 mm grid spacing).

In the second stray light reduction scheme, a blocker containing a slit of 5 mm width at a height near the centre of the projection image was inserted in front of the scanner light panel to modify the light source to a fan beam configuration (see figure 6.1c). Optical CT imaging was completed on varied concentration scattering solution-filled 1 L PETE jars at room temperature over a concentration range of 0.01-0.20 g/L.

The third configuration examined the effect of increasing object-to-detector distance on stray light reduction. The thought was that the increased distance may result in improved rejection of angled scatter signal. Representative 0.05 g/L and 0.10 g/L scatter solution-filled PETE jars were imaged using the normal scanner configuration (with a detector-to object axis distance  $D_{ad}$  of  $57 \pm 0.2$  cm). The camera lens was then replaced with a 2/3" diameter, 12-36 mm focal length zoom lens (Computar M3Z1228C-MP, Commack, NY, USA), the scanner re-calibrated at a  $D_{ad}$  of  $156 \pm 0.2$  cm, and the two jars re-imaged.

#### **6.3.4 Stray Light Correction**

The feasibility of beam stop array (BSA) measurement-based stray light corrections was investigated by first acquiring optical CT scans of a series of 0.01-0.40 g/L scattering solution-filled 1 L PETE jars, with and without a BSA blocker in place at the light source side of the matching tank in the Vista scanner. In this case, a high print quality 4 mm diameter blocker size BSA with 16 mm spacing between blockers was used. A script written in MatLab was then used to acquire the mean light intensity from a 2 x 2 pixel region located at the center of each blocker in the projection image (see example projection image acquired with the BSA blocker in place, shown in figure 6.1d), compare it to the mean light intensity for the same region in the projection image taken without the blocker in place, and extract a stray light intensity value. A bi-cubic spline interpolation function in MatLab was then used to interpolate between the stray light intensity value grid points and generate a two-dimensional (2D) stray light intensity map over the

full projection image area, expressed either in units of intensity or as a percentage of the raw projection image intensity data. Each of the raw projection images in both the reference and data scans was corrected with its corresponding stray light intensity map (in MatLab) prior to optical CT volume image reconstruction.

Moving to a more complicated scenario, a 5 cm diameter 0.10 g/L hybrid scattering finger-gelatin phantom was prepared in a 1 L PETE jar. Optical CT scans were completed on the scattering finger phantom with and without a BSA blocker in place as before. In this case, however, a higher grid density blocker (with 1 mm diameter dots and 8 mm grid spacing) was employed.

### **6.3.5 Treatment Process Quality Assurance**

A simple image guided adaptive radiation therapy (IGART) process quality assurance (QA) experiment was completed as outlined in figure 6.2. This experiment was intended to explore the capabilities of cone beam optical CT-based polymer gel dosimetry for full radiation therapy treatment process QA. The phantom was treated through the IGART process as if it were a patient undergoing prostate cancer treatment.

A set of two 1 L PETE jars were filled from a single batch of NIPAM gel. The gel dosimeter irradiations were completed on the day after manufacture using a Varian Clinac 21iX linear accelerator with On-Board cone beam Imaging (Advanced OBI) capability (Varian Medical Systems, Palo Alto, CA, USA). One jar was irradiated with a well-characterized 20 MeV electron beam to a dose of 600 cGy at a reference depth of 2 cm. The other jar was inserted into an AQUA geometric torso phantom (from Modus Medical Devices Inc, see figure 6.2) as the ‘measurement’ dosimeter. Depth fiducials were marked in permanent red marker on the electron beam-irradiated calibration gel dosimeter as reference points for registration of depth dose to attenuation in the reconstructed optical CT image.

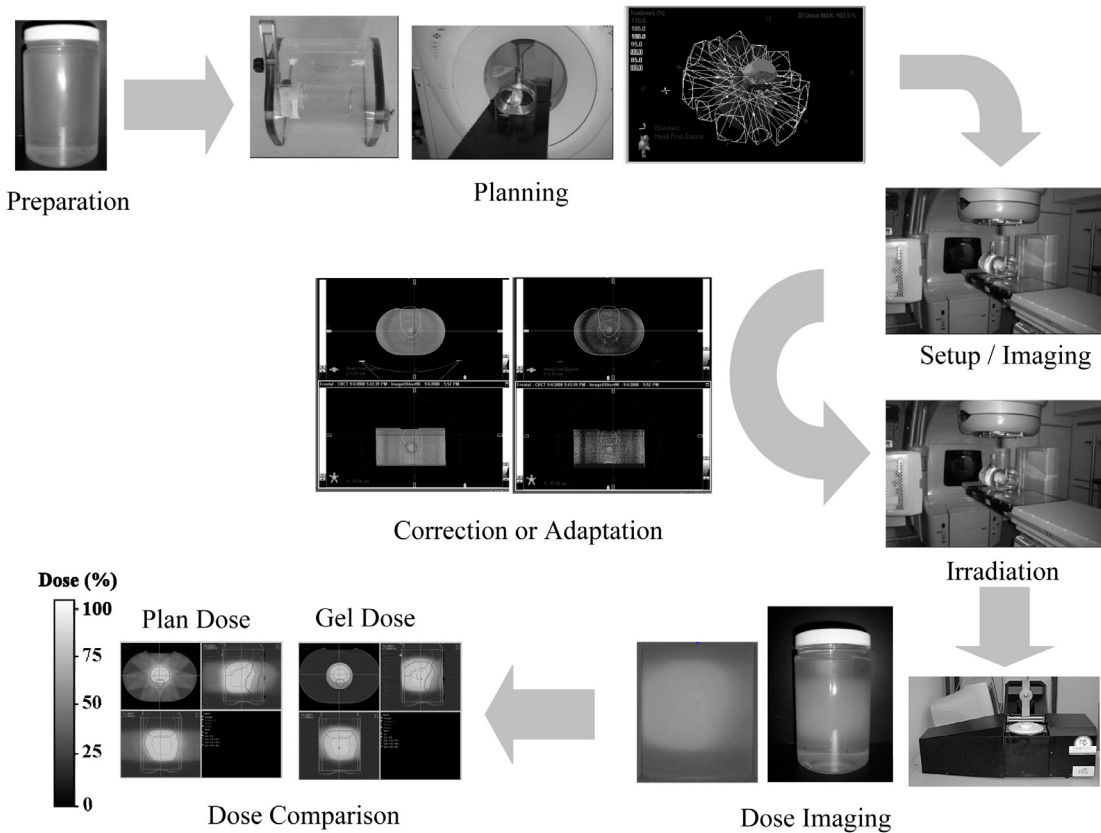


**Figure 6.2:** Evaluation of a simple image guided adaptive radiation therapy process using an AQUA geometric torso phantom (from Modus Medical Devices Inc) and cone beam optical CT-based polymer gel dosimetry.

To register the spatial position of the optical CT volume data from the measurement dosimeter, six fiducials were marked in red permanent marker on the exterior surface of the PETE jar. Two sets of three fiducials marked on separate parallel planes were adequate for this purpose. Steel 1 mm diameter beads were then attached with tape on top of the marker fiducials to provide positioning information in the planning CT and on-board cone beam computed tomography (CBCT) scans. The fiducial-marked measurement dosimeter was inserted in the AQUA phantom and imaged on a Picker PQ 5000 Philips CT simulator (Philips Medical Systems, Andover, MA,

USA). A 7 field, 6 MV conformal treatment plan was generated in Eclipse (Varian Medical, Palo Alto, CA, USA) using approximated target contours applied to the phantom CT data set, and a single 300 cGy treatment fraction scheduled to the treatment unit.

At the treatment unit, CBCT imaging of the phantom was completed at a 1 mm cubic voxel resolution according to the standard head-and-neck protocol (100kVp/145mAs, half scan with full bowtie filter). 3D-3D matching was performed between the planning CT and onboard CBCT images and an adaptation/correction step was then executed. In this investigation, a simple patient setup verification and setup correction step with CBCT on the treatment unit prior to delivery was the process under test. The treatment fraction was then delivered under a condition of failure, ignoring a required shift in the setup. After treatment, the dosimeter was removed for imaging and subsequent analysis. The steel bead fiducials were removed from the jar prior to optical CT scanning.

The gel-measured dose data from the measurement dosimeter were registered to Eclipse planning data in MatLab (Mathworks, Newark NJ), for viewing in the CERR (Washington State, St Louis, MO, USA) environment (Deasy *et al* 2003). An in-house registration routine written in MATLAB (Holmes 2008) was used to align the optical CT and CBCT fiducial data positions. Gel dose was compared to treatment plan dose using a full 3D voxel-by-voxel gamma function analysis (Low *et al* 1998, Low and Dempsey 2003).

Previous work exploring the possibility of using cone beam optical CT in combination with optically scattering gel dosimeters (Olding *et al* 2010) has indicated that the reconstructed attenuation data are suppressed by angled scatter stray light perturbation. Since both the calibration and measurement dosimeter data are affected, a normalization approach applied between the two dosimeter data sets (similar in concept to that found in the literature, for example, see (Oldham *et al* 2008, Sakhalkar *et al* 2009a, Sakhalkar *et al* 2009b)) was utilized in

this work. As a first order approximation, a normalization correction was applied to the ‘measurement’ dosimeter optical CT attenuation data, assuming differing attenuation-to-dose sensitivities between the calibration and measurement jars. This global correction term was obtained by normalizing the reconstructed attenuation values in the calibration and measurement dosimeter jars at 300 cGy (at well-determined points in the two dose distributions). The measurement dosimeter data was then normalized during calibration to the fitted attenuation-to-dose relationship.

## 6.4 Results

### 6.4.1 Stray Light Perturbation

Figure 6.3 shows reconstructed attenuation profiles from the two sets of hybrid scattering phantoms incorporating different sized 0.1 g/L (figure 6.3a) and 0.04 g/L (figure 6.3b) acrylic emulsion-based scattering regions imaged with the Vista scanner. While the attenuation values should be consistent within each concentration series of phantoms, the results show that scattering volume attenuation decreases with increasing size of scattering region, from the single 1.6 cm diameter scattering ‘finger’ to the pair of 1.6 cm diameter fingers (in the 0.1 g/L scattering solution series), to the 5 cm diameter finger, to the full jar scattering solution. This effect has previously been shown to be primarily due to angled scatter stray light perturbation in the system (Olding *et al* 2010).

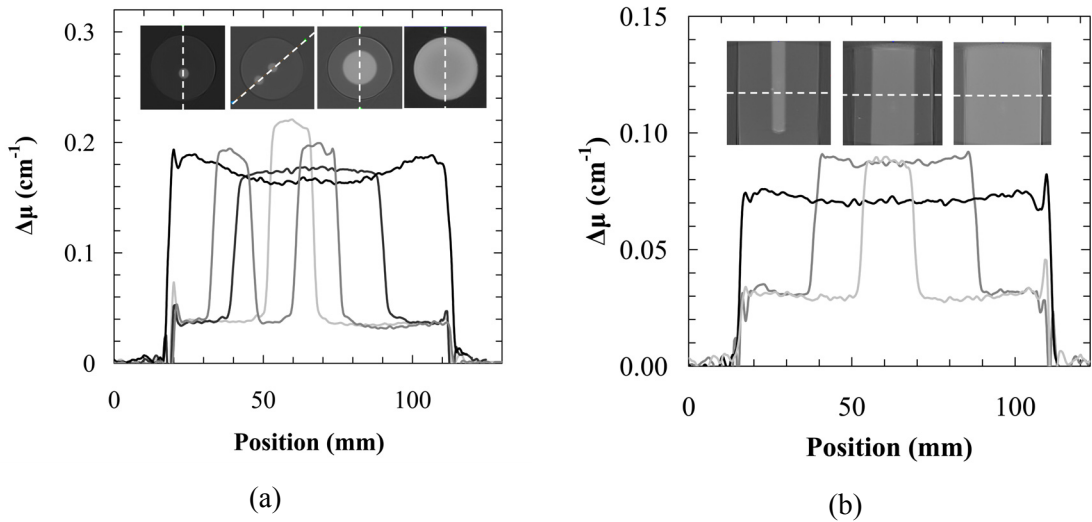


**Figure 6.3:** (a) Profiles of a 1 L PETE jar phantom containing 0.10 g/L scattering finger regions surrounded by a gelatin matrix. Global suppression of attenuation values is observed due to multiple scatter. (b) Profiles of a 1 L PETE jar phantom containing 0.04 g/L scattering finger regions in a gelatin matrix. Top and side slice views of the scattering regions are presented in (a) and (b) respectively for the purpose of improved visualization.

#### 6.4.2 Stray Light Reduction

For the polarizing film study, mean optical attenuation values were obtained for each imaged jar from an 8 cm diameter, 10 cm high region-of-interest (ROI) centered in the imaged jar volume. This ROI has been previously determined to be the best-behaved measurement region for 1 L PETE jar dosimeters in the Vista scanner (Olding *et al* 2010). Mean ROI optical attenuation values were also obtained under normal scanner conditions from the full range of calibration scattering and absorbing solution-filled 1 L PETE jars (using the same ROI). The Vista scanner measurements are presented in figure 6.4a against spectrophotometer attenuation measurements of the same calibration solutions.

Single plane mean optical attenuation values (evaluated from an 8 cm diameter slice ROI centered in the jar volume) from the fan beam study are similarly reported in figure 6.4b, along

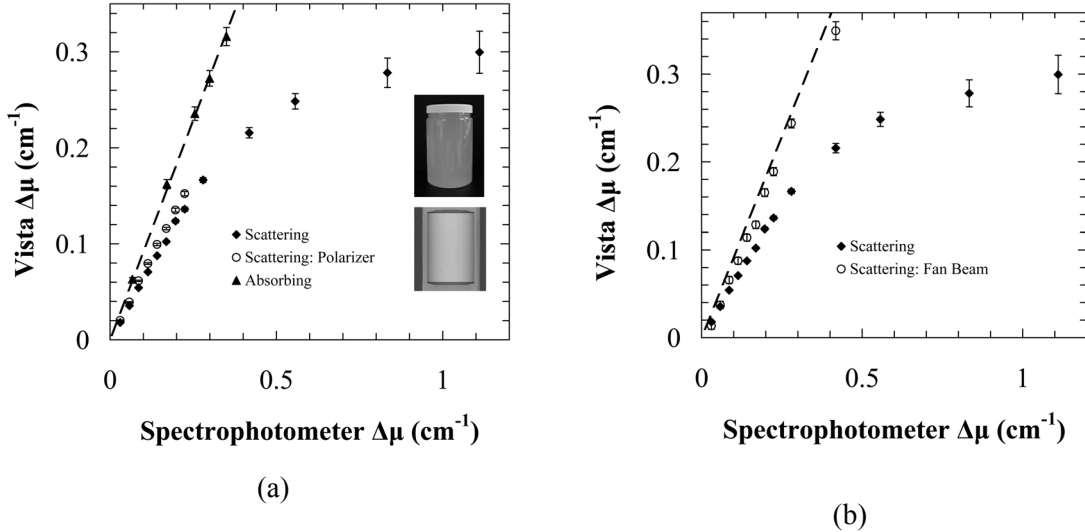


**Figure 6.4:** (a) Mean optical attenuation coefficients of calibration solution-filled 1 L PETE jars (top right inset) with and without the polarizing films in the Vista scanner, and spectrophotometer measurements using 10 mm PMMA cuvettes. A linear fit to the absorbing solution data in the range of  $0.00$ - $0.35\text{cm}^{-1}$  is shown in the plot. An 8 cm diameter, 10 cm high cylindrical region-of-interest (ROI, lower right inset) centered in the jar image volume was used in the evaluation of the Vista scanner data. (b) Mean ROI optical attenuation coefficients of the calibration solution-filled 1 L PETE jars with and without the fan beam blocker in the Vista scanner. An 8 cm diameter slice was used for evaluating the mean optical attenuation values from the fan beam data. Some error bars are smaller than symbol size.

with the ROI values for the calibration scattering solutions and the linear fit to the absorbing solutions from before.

Mean ROI optical attenuation values from the varied object axis-to-detector distance ( $D_{ad}$ ) experiment (using the same ROI as in figure 6.4a) are presented in table 6.1.

**Table 6.1:** Effect of Increasing Object-to-Camera Distance

Solution	$D_{ad} = 57 \text{ cm}$	$D_{ad} = 156 \text{ cm}$
0.05 g/L	$0.093 \pm 0.001 \text{ cm}^{-1}$	$0.092 \pm 0.001 \text{ cm}^{-1}$
0.1 g/L	$0.166 \pm 0.003 \text{ cm}^{-1}$	$0.168 \pm 0.003 \text{ cm}^{-1}$

### 6.4.3 Stray Light Correction

A representative interpolated 2D percentage stray light correction map is shown in figure 6.5a. This map was obtained from the open field and beam stop array (BSA) blocker grid (4 mm diameter, 16 mm blocker dot spacing) projection image data of a 0.10 g/L calibration solution-filled 1 L PETE jar in the Vista scanner. Mean ROI optical attenuation values from the uncorrected and BSA-corrected reconstructed optical CT image data over a range of scatter solution concentrations are reported in figure 6.5b.

A projection image of the 5 cm diameter 0.10 g/L hybrid scattering finger-gelatin phantom with the higher grid density BSA blocker in place (1 mm diameter dots, 8 mm grid spacing) is shown in figure 6.6a. Uncorrected and BSA-corrected attenuation profiles are shown

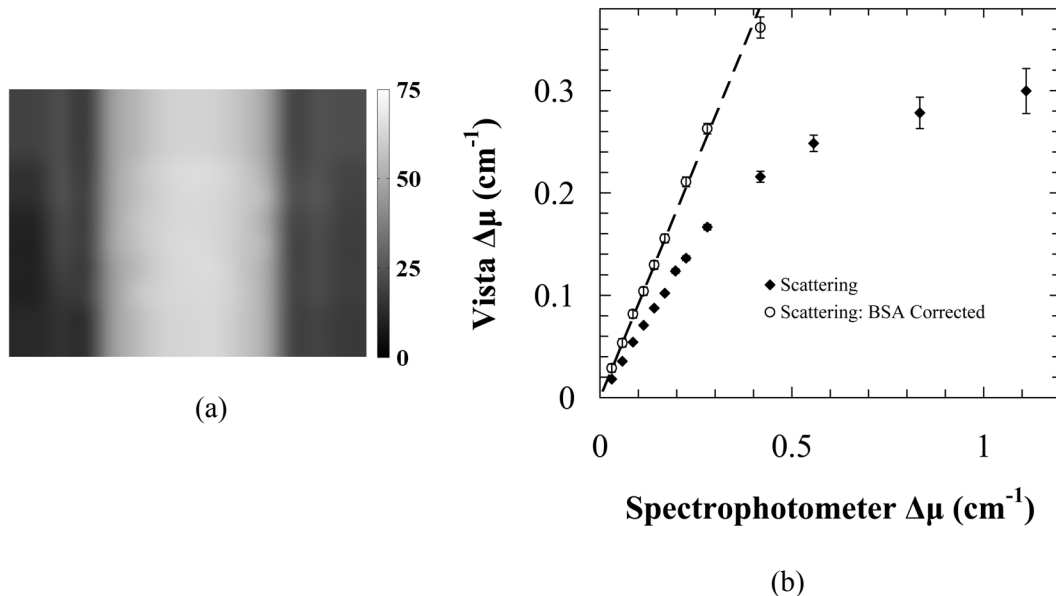


**Figure 6.5:** (a) A representative interpolated percentage stray light correction map obtained from the image data of a 0.10 g/L calibration solution-filled 1 L PETE jar in the Vista scanner (b) Mean ROI optical attenuation coefficients of uncorrected and BSA-corrected calibration solution-filled 1 L PETE jars. The ROI is the same as in figure 6.4a, with the absorbing solution linear fit from figure 6.4a included in the plot for the purpose of comparison. Some error bars are smaller than symbol size

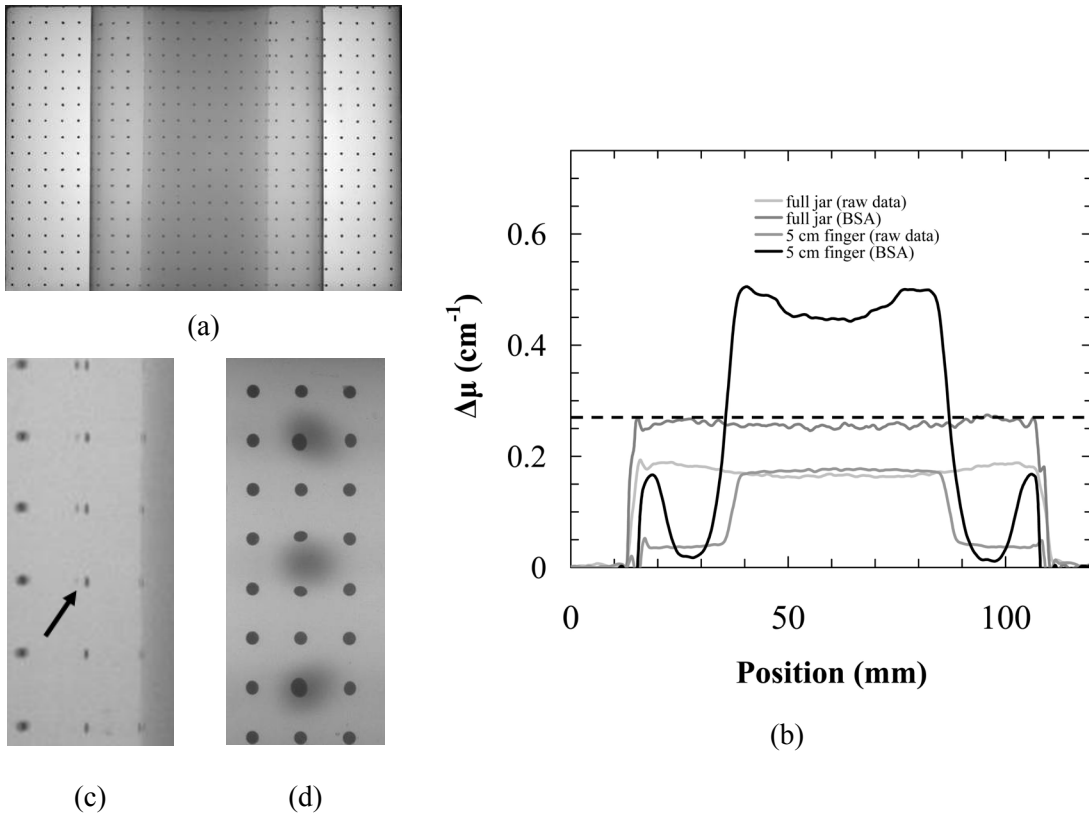


**Figure 6.6:** (a) A representative BSA-blocked projection image of the hybrid 5 cm 0.10 g/L scattering finger-gelatin phantom (b) Reconstructed attenuation profiles of the uncorrected and BSA-corrected 1) scattering finger-gelatin phantom and 2) 0.10 g/L scatter solution-filled 1 L PETE jar. (c) A section of a selected BSA-blocked scattering finger-gelatin phantom projection image, showing blocker dot distortion due to light refraction from the PETE jar seam. (d) A section of a selected 4 mm diameter BSA-blocked projection image. This image shows a NIPAM gel-filled 1 L PETE jar dosimeter irradiated with 3 pencil beam patterns, and indicates distortion of the blockers near the pencil beams.

in figure 6.6b across the jar diameter of: 1) the 5 cm scattering finger-gelatin phantom and 2) a 0.10 g/L scattering solution-filled 1 L PETE jar from the data series presented in figure 6.3c. Figure 6.6c presents a section of a selected BSA-blocked scattering finger-gelatin phantom projection image, showing blocker dot distortion due to light refraction from the PETE jar seam. Figure 6.6d shows a section of a selected BSA-blocked projection image from a full projection image scan set of three separate pencil beam deliveries to a NIPAM gel-filled 1 L PETE jar

dosimeter. An in-house tomotherapy benchtop with pencil beam collimation customized to a T780C cobalt-60 radiotherapy unit (Best Theratronics, Kanata, ON) was used for the pencil beam deliveries.

#### 6.4.4 Treatment Process Quality Assurance

Figures 6.7a and 6.7b show CERR-based visualizations of the treatment plan and normalized gel-measured dose (from the process in figure 6.2) in a central coronal slice, when a 0.8 cm inferior-direction phantom shift observed in 3D-3D matching was not corrected for. The plan and measurement distributions are visibly different. Figure 6.7c presents the results of 3D Low's gamma function pixel-by-pixel comparison of gel-measured dose against the reference Eclipse treatment plan dose, employing 3% dose difference and 3 mm distance-to-agreement criteria (again, in the CERR environment). Regions failing the 3D gamma function criteria are represented as a grayscale wash on top of the CT slice, and passing regions in the jar are not

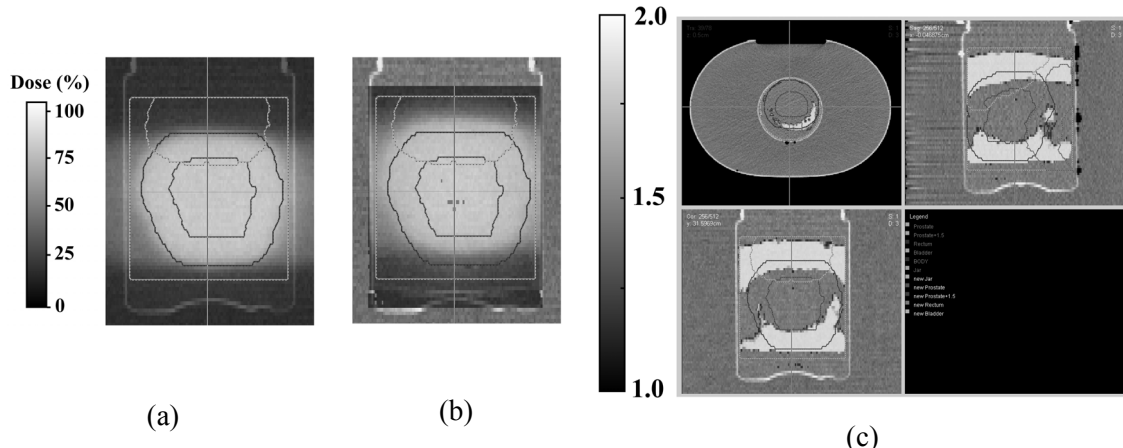


**Figure 6.7:** CERR-based visualizations of (a) the treatment plan and (b) normalized gel-measured dose in a central coronal slice, when a required 0.8 cm inferior-direction phantom shift assessed from CBCT-planning CT matching was not applied. (c) A corresponding 3D Low's gamma function comparison showing regions of failure for 3%, 3 mm gamma criteria between reference treatment planning dose calculated in Eclipse™ and gel-measured dose delivered to the AQUA phantom with a NIPAM gel-filled 1L PETE jar dosimeter insert.

plotted, for clarity. The percentage of treatment plan dose and measured gel dose pixels in agreement (i.e. gamma value < 1) was less than 60% within a region-of-interest (ROI ) dose evaluation volume covering the central 10 cm height of the jar and 8 cm of the jar diameter.

## 6.5 Discussion

### 6.5.1 Stray Light Reduction

Stray light perturbation occurs when light rays from the diffuse light source reflect or scatter onto a cone beam primary ray path (i.e. within some finite sized ray bundle defined primarily by the camera lens aperture), typically prior to exiting the attenuating media or when in transit through the system of camera lens optics. Light arriving along a primary ray path is indiscriminately focused onto the camera detector chip regardless of the original path taken. Hence, stray light may be acquired as contaminant light intensity in the projection image data. Its effects clearly perturb the cone beam measurement of optically scattering media (i.e. polymer gels), as illustrated by the phantom study results in figure 6.3, and become more problematic at higher scatter attenuations and with larger scattering volumes.

Looking at the results presented in figure 6.4a, it is clear that ‘anti-scatter grid’ polarizing films do not substantially reduce contaminant stray light in the measurement. That is, the insertion of the polarizer films in the scanner does not shift the scatter measurement data significantly closer to the near unity linear relationship between Vista and spectrophotometer measurement observed from imaging absorbing media (agreement within 3% over mean jar attenuation range of 0.0-0.2 cm<sup>-1</sup>, see Olding *et al* 2010). This result makes sense, as the polarizing film on the detector side of the matching tank would not be expected to provide much greater rejection of angled scatter along the cone beam ray paths than the camera lens aperture itself. The lens aperture accepts light primarily from a small cone angle of approximately 1° to

each detector pixel when imaging absorbing (near ideal) media (Olding *et al* 2010). Then, the only meaningful reduction in scatter-sourced stray light would come from the conditioning of the diffuse light source by the polarizing film at the light source side of the tank to reject higher angle diffuse light from the system. The potential of introducing streaks in the projection data can be a significant issue (see figure 6.1b), and is a secondary reason for not proceeding with the use of this type of polarizing ‘anti-scatter’ film.

A negligible difference is reported in table 6.1 between the normal distance and extended object-to-detector distance mean attenuation values of the representative 0.05 g/L and 0.10 g/L scattering solutions. Hence, moving the detector back has almost no effect in reducing stray light perturbation of the image data. Intuitively, one can see how moving the detector away from the object should result in the rejection of slightly angled stray light. However, the ‘primary’ ray bundle of transmitted light recorded at each detector pixel also has a slight angular distribution which will also change with object-to-detector distance. Moving the detector further away therefore reduces the recorded intensity of both primary and stray light transmission, keeping their ratio relatively the same. This explanation fits the observation of negligible overall stray light reduction with increased object-to-detector separation distance.

The fan beam data in figure 6.4b indicates improved agreement to the expected near unity relationship between Vista scanner and spectrophotometer measurement. The slope of a linear fit to the fan beam data is within 10% of the value from the linear fit to the absorbing data. This is due to the reduced area of the light source from which stray light could be derived. The obvious drawback with this approach is the increased scan time. A fan beam system represents a compromise between the fast scan time of the cone beam scanner and the improved scatter rejection of point-detection rotate-translate optical scanners. While this route is not preferred, it is definitely a viable option for imaging polymer gels, since these dosimeters are relatively

unaffected by spatial dose degradation over time (due to diffusion). A normalization correction would still be required for the fan beam data, since the absolute accuracy of fan beam attenuation measurement would still not be at an acceptable level for direct application to 3D dosimetry.

### 6.5.2 Stray Light Correction

For cone beam optical CT reconstruction to yield accurate data, most of the detector-recorded light should travel within tight ray bundles along the cone beam ray path from the light source through the object space to each detector pixel. However, the BSA-derived percentage map in figure 6.5a indicates that, on average, slightly over 60% of the light in the ‘jar region’ of the Vista scanned 0.10 g/L scattering solution projection image arrives from a starting point outside of the 4 mm diameter blocker region at the light source side of the matching tank. This means that a significant portion of the detector-recorded light does not conform to the preferred tight ray bundle condition through the object space. After application of the percentage map corrections to the raw projection image data, the full range of BSA-corrected mean ROI optical attenuation coefficients are within 5% agreement to the absorbing data (near ideal) linear fit relationship (figure 6.5b).

A profile across the reconstructed image of the BSA-corrected 0.10 g/L scattering solution-filled 1 L PETE jar (figure 6.6b) shows close agreement between the Vista and ‘true’ spectrophotometer attenuation values (spectrophotometer value shown by the dashed line in the plot) for the scattering solution. The scatter solution filled jar represents the simplest case of a uniform dose delivery to the 1 L PETE jar dosimeter.

Moving to the more complicated scenario of a non-uniform, high dose gradient delivery represented by the hybrid 0.10 g/L scattering finger-gelatin phantom introduces new challenges. In this case, a higher resolution BSA blocker with 8 mm grid spacing was used to obtain stray light measurements. The diameter of the individual blocker dots was also reduced to 1 mm to

minimize the overall blocked area of the light source (to approximately 1.3% of the light-source illuminated area in the projection image). If a higher blocker area is used, then the measured stray light value reads lower than expected.

Looking at the reconstructed BSA-corrected finger phantom profile in figure 6.6b, cupping is evident in the scattering finger region of the data. In addition, scattering finger attenuation values much greater than the expected attenuation of  $\sim 0.26 \text{ cm}^{-1}$  are reported. Two aspects of the BSA correction scheme are responsible for this inaccuracy. First, the grid resolution is not high enough to track the variation in stray light contribution at the edge of the scattering finger region. The interpolated percentage map then overcorrects for stray light in this region (in the spacing between the grid blocker point measurements), leading to cupping in the reconstructed attenuation data. Second, the individual 1 mm diameter blocker dots (at the light source side of the matching tank) are smaller in diameter than the area of the cone beam geometry ‘ray bundle’ of light from the light source that reaches each detector pixel, using a camera lens aperture setting of f5. Referring to the basic premise/approximation of cone beam imaging geometry, there is a small ray bundle of light centered on each primary ray path from the diffuse light source to the CCD detector chip that is actually focused through the camera lens aperture onto each CCD pixel. Approximately 10% of the ‘primary’ light recorded at each detector pixel through an absorbing (near ideal) media object space has been shown to arrive from outside the ray bundle ‘light cone’ defined by a 1 mm diameter base (i.e. grid blocker) at the light source side of the tank, vertex at the detector pixel, and the cone base-to-vertex distance of  $66.0 \pm 0.1 \text{ cm}$  (Olding *et al* 2010). The use of a 1 mm diameter blocker size therefore gives a mixed measurement of stray light *and* primary transmitted light. When this measurement is applied, it leads to overcorrection of the reconstructed image data, as observed in figure 6.6b.

The projection images in figures 6.6c and 6.6d highlight two additional factors that need to be considered when applying a BSA correction. Refraction at the jar seams of the 1 L PETE jar can cause the small 1 mm diameter blockers to mostly disappear from the projection image as the seam rotates past each column of blockers (figure 6.6c). This causes a severe overestimation of the stray light measurement(s) in the projection images at the points where this occurs, leading to streaking artifacts in the reconstructed optical CT image. Similarly, light refracts at the higher refractive index boundary of the irradiated pencil beam (Maryanski *et al* 1996) adjacent to the lower indices of the un-irradiated gel and matching tank solution, causing ‘stretching’ and ‘contraction’ distortions of the (4 mm diameter) BSA blockers in the projection image (figure 6.6d). This leads to misreads of the stray light contribution for the affected blockers. The jar seam effect can be managed by applying appropriate stray light contribution limits in the MatLab-based projection image correction routine. BSA grid distortions near refractive index boundaries and/or steep gradients, on the other hand, are not easily corrected for.

Overall, the BSA correction methodology does indicate some capability of stray light correction for relatively low spatial variation scatter (dose) distributions. This method does not, however, effectively track stray light contributions near high dose gradients. This is due to the limitations in resolution when using this approach. It is possible that some sort of fast electronic sliding beam stop blocker such as a liquid crystal display could be used to obtain higher resolution stray light data. However, if this hardware approach is possible without comprising the fast cone beam scanning time, then it would likely be better to use it as a sliding *beam pass* window for primary light measurement of each projection image, circumventing the need for a second projection image scan. Although outside the scope of this work, this fast scanning sliding window concept may lead to a viable stray light reduction scheme for cone beam optical CT-based polymer gel dosimetry.

### **6.5.3 Treatment Process Quality Assurance**

Conventional tools may be more convenient and appropriate than gel dosimetry to QA individual steps in IGART, such as field fluence patterns for a particular patient, or CBCT and planning CT 3D-3D matching. However, these QA tests validate only user-specified spatial points. The IGART process involves a number of instances where professional judgment is required (for example, to assess whether a patient is to be repositioned or if re-planning is necessary). These decision points and the overall process itself are not easily tested by conventional means.

In the ideal scenario, the IGART process QA would not exclusively be performed by the physics team. Instead, a physics team member would prepare the gel dosimeter and insert it into an anthropomorphic phantom. The phantom would then be given to the radiation therapy team to process as a patient. Planning therapists would perform CT simulation, oncologists might contour structures which could be delineated in the target, planners or dosimetrists would plan the delivery on the treatment planning system, and treatment therapists would deliver the treatment using the IGART approach(es) being assessed. In the proof of concept investigation outlined in figure 6.2, the approach was limited to simple patient setup with CBCT. This test could easily be made more challenging by introducing internal shifts of the dosimeter. Then, after irradiation and completion of the process, the phantom would go back to physics for dosimeter removal and analysis. Many of the same tools used for the comparison of treatment plans, for example dose volume histograms, gamma index and are well-suited to assessing the delivery of the adaptive treatment.

The image guided approach tested in this investigation indicates that gels can provide useful information on the dose delivery at the treatment unit. With the application of a dose sensitivity normalization correction between calibration and measurement dosimeter data, gel dosimetry results from the IGART experiments clearly showed when a simple spatial shift from

3D-3D planning CT-CBCT matching was not implemented as intended (see figure 6.7c). However, the simple assumption of a single normalization value correction applied throughout the jar volume between the calibration and ‘prostate’ measurement dosimeters will not adequately correct the dosimetry in most cases. Non-uniform stray light perturbation throughout the dosimeter volume becomes more evident as the scatter concentration (i.e. the level of dose) and scatter volume (i.e. treatment volume) increases (see figure 6.3). In order for cone beam optical CT-based polymer gel dosimetry to attain a higher level of dosimetric accuracy in treatment process QA, it non-uniform stray light perturbation in the measurement system would still have to be reduced or corrected for.

## 6.6 Conclusions

Gel dosimeters are uniquely suited to the assessment of IGART schemes in the clinic. The dosimetry is relatively simple to implement and, once procedures are established, is easy to maintain and continue. Gel dosimetry can enable new quality control tests for the clinical program that are not easily performed with by conventional methods. Useful information may be acquired from cone beam optical CT-based polymer gel dosimetry through application of a dose sensitivity normalization correction between calibration and measurement dosimeter jars. For example, simple spatial shifts in the treatment process setup may be tested. It is also anticipated that other variations in the treatment process may also be effectively evaluated by inter-dosimeter comparison. However, the quality of the dose data needs to be further improved in order to reach the target capability of 95% pixel agreement between a well-known reference dose distribution and the gel-measured dose distribution for 3% dose and 3 mm distance-to-agreement 3D Low’s gamma function criteria. While the stray light reduction and correction strategies explored in this work did not reach this target level of agreement, the fan beam approach indicated a significant reduction of stray light perturbation in the measurement, and hence is worthwhile of further

investigation. The beam stop array correction strategy also shows some merit for correction of relatively low spatial variation scatter (dose) distributions. Although not tested in this work, this scanner-dosimeter combination may possibly be extended in its capability by integrating a fast electronic sliding beam pass liquid crystal display blocker with the diffuse light source.

## 6.7 References

- Deasy J O, Blanco A I and Clark V H 2003 CERR: a computational environment for radiotherapy research. *Med.Phys.* 30 979-985.
- Doran S and Krstajic N 2006 The history and principles of optical computed tomography for scanning 3-D radiation dosimeters. *J.Phys.: Conf.Ser.* 56 45-57.
- Endo M, Tsunoo T, Nakamori N and Yoshida K 2001 Effect of scattered radiation on image noise in cone beam CT. *Med.Phys.* 28 469-474.
- Gore J C, Ranade M, Maryanski M J and Schulz R J 1996 Radiation dose distributions in three dimensions from tomographic optical density scanning of polymer gels: I. Development of an optical scanner. *Phys.Med.Biol.* 41 2695-2704.
- Holmes O *Validation of Conformal Radiation Therapy Treatments in 3D Using Polymer Gel Dosimeters and Optical Computed Tomography* (M.Sc., Queen's University, 2008).
- Jordan K and Battista J 2006 Linearity and image uniformity of the Vista<sup>TM</sup> optical CT scanner. *J.Phys.: Conf.Ser.* 56 217-220.
- Low D A and Dempsey J F 2003 Evaluation of the gamma dose distribution comparison method. *Med.Phys.* 30 2455-2464.
- Low D A, Harms W B, Mutic S and Purdy J A 1998 A technique for the quantitative evaluation of dose distributions. *Med.Phys.* 25 656-661.
- Maryanski M J, Gore J C, Kennan R P and Schulz R J 1993 NMR relaxation enhancement in gels polymerized and cross-linked by ionizing radiation: a new approach to 3D dosimetry by MRI. *Magn.Reson.Imaging* 11 253-258.
- Maryanski M J, Schulz R J, Ibbott G S, Gatenby J C, Horton D and Gore J C 1994 Magnetic resonance imaging of radiation dose distributions using a polymer-gel dosimeter. *Phys.Med.Biol.* 39 1437-1455.
- Maryanski M J, Zastavker Y Z and Gore J C 1996 Radiation dose distributions in three dimensions from tomographic optical density scanning of polymer gels: II. Optical properties of the BANG polymer gel. *Phys.Med.Biol.* 41 2705-2717.
- Ning R, Tang X and Conover D 2004 X-ray scatter correction algorithm for cone beam CT imaging. *Med.Phys.* 31 1195-1202.
- Oldham M and Kim L 2004 Optical-CT gel-dosimetry. II: Optical artifacts and geometrical distortion. *Med.Phys.* 31 1093-1104.
- Oldham M, Sakhalkar H, Guo P and Adamovics J 2008 An investigation of the accuracy of an IMRT dose distribution using two- and three-dimensional dosimetry techniques. *Med.Phys.* 35 2072-2080.

- Oldham M, Siewerdsen J H, Kumar S, Wong J and Jaffray D A 2003 Optical-CT gel-dosimetry I: basic investigations. *Med.Phys.* 30 623-634.
- Olding T, Holmes O and Schreiner L J 2009 Scatter Corrections for Cone Beam Optical CT. *J.Phys.: Conf.Ser.* 164 174-178.
- Olding T, Holmes O and Schreiner L J 2010 Cone beam optical computed tomography for gel dosimetry I: scanner characterization. *Phys.Med.Biol.* 55 2819-2840.
- Rinkel J, Gerfault L, Esteve F and Dinten J M 2007 A new method for x-ray scatter correction: first assessment on a cone-beam CT experimental setup. *Phys.Med.Biol.* 52 4633-4652.
- Sakhalkar H, Sterling D, Adamovics J, Ibbott G and Oldham M 2009a Investigation of the feasibility of relative 3D dosimetry in the Radiologic Physics Center Head and Neck IMRT phantom using presage/optical-CT. *Med.Phys.* 36 3371-3377.
- Sakhalkar H S, Adamovics J, Ibbott G and Oldham M 2009b A comprehensive evaluation of the PRESAGE/optical-CT 3D dosimetry system. *Med.Phys.* 36 71-82.
- Senden R J, De Jean P, McAuley K B and Schreiner L J 2006 Polymer gel dosimeters with reduced toxicity: a preliminary investigation of the NMR and optical dose-response using different monomers. *Phys.Med.Biol.* 51 3301-3314.
- Siewerdsen J H and Jaffray D A 2001 Cone-beam computed tomography with a flat-panel imager: magnitude and effects of x-ray scatter. *Med.Phys.* 28 220-231.
- Siewerdsen J H, Moseley D J, Bakhtiar B, Richard S and Jaffray D A 2004 The influence of antiscatter grids on soft-tissue detectability in cone-beam computed tomography with flat-panel detectors. *Med.Phys.* 31 3506-3520.

## **Chapter 7**

### **Conclusions**

#### **7.1 Viability & Use**

The careful establishment of and adherence to set imaging protocols and dosimeter preparation procedures enables reproducible and accurate 3D dose measurements from cone beam optical computed tomography (CT)-based gel dosimetry (chapters 2 and 3). This imaging modality is clearly well-suited to the readout of optically absorbing dosimeters (chapters 2-4), but has limited capability in the 3D measurement of optically scattering dosimeters (chapters 2, 5 and 6). The identification of thermochromic behaviour in the Frick-xylenol orange-gelatin (FXG) optically absorbing gel (chapter 3), and lower critical solution temperature behaviour in the N-isopropylacryamide (NIPAM) optically scattering polymer gel (chapter 5), are important steps to improving their dosimetry. Moving the dosimeter response into the optimal performance ranges of the scanner is also significantly important (chapters 2 and 5). While the constraints required for reliable cone beam optical CT-based gel dosimetry are strict, they are not prohibitive to the practical uptake of this technique in the clinic. Other conventional dosimeters commonly used in the clinic such as film, diodes, and thermo-luminescent diodes (TLDs), require a comparable attention to detail for proper implementation.

It is strongly recommended that the imaging capabilities of the cone beam scanner be characterized for each type of dosimeter chemistry, and that a standard size dosimeter container is used in the characterization. This recommendation is exemplified in chapters 2 and 3 of this thesis. The imaging protocols and performance assessment obtained from one container size may not apply to a different container size. Confounding effects in this regard include the various

forms of stray light perturbation as well as the environmental conditions and response of the gel (chapters 3 and 6).

It is considered good practice to calibrate the dose response for each dosimetry run. The differences between the calibration and measurement dosimeter may be limited by preparing them in identically-sized containers for the same gel batch and storing them in the same conditions prior to irradiation. This reduces any concerns related to the slight variations in the manufacturing process. In this thesis, the practical details of an electron/photon beam calibration approach for the FXG gel (chapter 4) and a pencil (photon) beam pattern calibration approach for the NIPAM gel (chapter 5) are outlined. Although it has been implicitly assumed throughout this work and so not discussed explicitly, optical readout requires that the optics, light source diffuser, matching tank windows, matching tank fluid, and dosimeter container surfaces be kept clean and scratch-free (i.e. are well-maintained and minimally handled).

Cone beam optical CT-based gel dosimetry is best used in situations that are difficult to handle using a conventional type of dosimeter. These situations include (Schreiner 2009):

- i. the commissioning of a new radiation therapy technique such as brachytherapy, radiosurgery, and intensity modulated radiation therapy (IMRT) in the clinic. To be clear, the technique being evaluated may not be new within the field of radiation therapy, but may be new to the clinic at which it is being commissioned.
- ii. the commissioning of a new treatment planning system in the clinic.
- iii. the dosimetric characterization of small radiation fields
- iv. the periodic validation of a full treatment process (particularly a process with an image-guided adaptive step) .

Various aspects of situations i, iii, and iv have been investigated and are described in chapters 4, 5 and 6 of this thesis respectively. At present, the application of cone beam optical CT-based FXG gel dosimetry as a secondary quality assurance (QA) tool for the evaluation of IMRT treatment plans (chapter 4) is perhaps the furthest along in its development for clinical use.

At present, patient-specific QA is applied in the evaluation of IMRT plans at the Cancer Centre of Southeastern Ontario (CCSEO) by two means. First, the individual fields of the plan are cumulatively delivered at a gantry angle of 0° to an ImRT Matrixx (Scanditronix Wellhöfer, Bartlett, TN, USA). The aggregate Matrixx-measured dose and aggregate plan dose are then compared using a two-dimensional (2D) Low's gamma function evaluation with 3% dose difference and 3 mm distance-to-agreement criteria (Low and Dempsey 2003). Second, portal image data is acquired from the delivery of the each IMRT plan field at the treatment unit without a patient present. The 3D dose delivered to a cylindrical virtual phantom on the treatment couch is calculated using a back-projection technique-based software package termed 'Epidose' (Ansbacker 2006). The plan dose and Epidose-measured dose are then compared using a weighted dose difference chi ( $\chi$ ) test (Bakai *et al* 2003), also employing 3%, 3mm criteria.

Although most of the IMRT treatment plan evaluations completed at the CCSEO to date have satisfied the agreement criteria between the treatment plan dose and Epidose-measured dose, occasional failures are observed. In these cases additional QA and/or re-planning is required. Cone beam optical CT-based FXG gel dosimetry has been demonstrated in chapter 4 to be capable of meeting the 3%, 3 mm gamma function comparison requirements for IMRT treatment plan evaluation. Hence, FXG gel dosimetry could readily be used as a secondary check in patient-specific IMRT QA at the CCSEO. The gel can be prepared and ready for imaging in 12 hours or less, the CT acquisition and plan registration takes less than 1 hour, the scan and reconstruction time under 30 minutes, and the analysis time 3-4 hours. The secondary 3D dose verification could

therefore be completed within 18-24 hours from the point of request. The discussion of next steps for this clinical application is continued in the next section on future work.

Moving on to polymer gels, the long-term stability and spatial dose integrity of the NIPAM polymer gel formulation give it a distinct advantage over the FXG gel (which suffers from the effects of auto-oxidation and diffusion) in treatment process QA, where the gel is in phantom for a long period of time. This advantage also applies to small field dosimetry. In these two situations, however, cone beam optical CT-based NIPAM polymer gel dosimetry is limited by the accuracy of the measurement. The reproducibility of the response appears to be sufficient to enable repetitive, relative measurements (for example, to assess slight changes in the delivery). Unfortunately, the stray light reduction and correction strategies explored in this thesis (chapter 6) did not improve the measurement of complex dose distributions as much as was anticipated. The fan beam approach is perhaps the most promising, but it comes with the tradeoff of increased scan time. This is perhaps not as much of an issue with the slow-developing NIPAM gel, and thus remains a possibility to explore further, particularly if fast electronic windowing of the scanner light source can be realized.

The goals of this thesis were to: (a) establish the performance capabilities and limitations of the two main classes of cone beam optical CT-based gel dosimetry, (b) improve their measurement, and (c) apply them to the evaluation of clinically relevant complex dose distributions. From the above discussion, it is evident that these goals were well-satisfied for both FXG gels and NIPAM gels, but that the optically absorbing FXG gel-cone beam optical CT system holds more promise for long-term clinical application.

## 7.2 Future Work

The possibility of FXG gel-based IMRT QA presented in the previous section has led to its being included in plans for an in-depth investigation of the Epidose analysis at the CCSEO, extending beyond the ion chamber and film commissioning already performed. A new cylindrical, acrylic phantom has been built with a custom cavity for insertion of a 1 L FXG gel dosimeter. The direct gel-based measurement of complex 3D distributions in the Epidose cylindrical geometry is anticipated to provide additional insight into the occasional failures observed from the Epidose analysis of IMRT treatment plans.

One of the remaining primary tasks in the development of cone beam optical CT-based FXG gel dosimetry is to formalize the approach and software package for dose registration, calibration, analysis and results presentation in each clinical application, with supporting documentation. Otherwise, its use will suffer from the perception of being an art.

Another primary task for cone beam optical CT-based FXG gel dosimetry is to improve its measurement by reducing the various forms of stray light perturbation. Some changes are hardware-related, such as minimizing side scatter signal through use of a variable intensity light source, or reducing the veiling glare by selection of higher quality optical components. The most important changes to be made, however, are inherent to the dosimeter. The jar wall interfaces and the scattering gel-forming matrix are the two most significant forms of stray light perturbation in the system (chapter 3). Chapter 4 exemplifies the gain in accuracy that can be realized through use of an alternative gel-former. It is hoped that further improvements can be made in both these regards. Alternatively, there is good indication that the stray light perturbation in the readout of FXG gels may be well-managed by a normalization correction (chapter 4). The substitute gel former in the FXG gel dosimeter (chapter 4) may also be used in the NIPAM gel formulation to improve its measurement.

The motivation for completing all of these tasks is supported by the belief that the ongoing development of easily accessible, fast optical readout tools such as cone beam optical CT, and regular engagement in the sideline activity of using cone beam optical CT-based gel dosimetry for selected clinical treatment plan evaluations, will help to establish 3D gel measurement as a viable tool in the cancer clinic.

### 7.3 References

- Ansbacher W 2006 Three-dimensional portal image-based dose reconstruction in a virtual phantom for rapid evaluation of IMRT plans. *Med Phys* 33 3369-3382.
- Bakai A, Alber M and Nusslin F 2003 A revision of the gamma-evaluation concept for the comparison of dose distributions. *Phys.Med.Biol.* 48 3543-3553.
- Low D A and Dempsey J F 2003 Evaluation of the gamma dose distribution comparison method. *Med.Phys.* 30 2455-2464.
- Schreiner L J 2009 Where does gel dosimetry fit in the clinic? *J.Phys.: Conf.Ser.* **164** 1-12.

## Appendices

### A. Permission to reproduce copyrighted material in Chapter 2

To: "Olding, Tim" <Tim.Olding@krcc.on.ca>  
Cc:  
Bcc:  
Subject: Re: Copyright permission

---

"Olding, Tim" Hello, 08/07/2010 19:44:12

 Copyright permission

Olding, Tim to: permissions 08/07/2010 19:44

---

Hello,

I am looking to reproduce a version of the following paper

Ref: PMB/338312/PAP  
TITLE: Cone beam optical computed tomography for gel dosimetry I: scanner characterization  
AUTHORS: Dr T Olding et al  
Phys. Med. Biol. 55 (2010) 2819-2840

as a chapter in my doctoral thesis in the Dept. of Physics, Engineering Physics and Astronomy at Queen's University, Kingston, Ontario, Canada, and am seeking your copyright permission to do so. Please let me know if there is further information you require from me for this request.

Regards,

Tim Olding  
Dept. of Physics  
Queen's University

PERMISSION TO REPRODUCE AS REQUESTED  
IS GIVEN PROVIDED THAT:

(a) ~~the consent of the author(s) is obtained~~  
(b) the source of the material including author/editor,  
title, date and publisher is acknowledged.\*

IOP Publishing Ltd  
Dirac House  
Temple Back  
BRISTOL BS1 6BE Date 27/7/2010 Rights & Permissions

\*Please include the IOP Copyright line, mention the journal's homepage at:

iopscience.org/pmb

and provide a link back to the article's abstract on our website from the electronic version of your thesis (if applicable).

Thank you.